High-Latitude Climate, Ice Sheet, and Oceanographic Evolution During the Miocene

By

Jared Ethan Nirenberg

M.Sc. Brown University, Providence, RI, 2022

B.S. Rice University, Houston, TX, 2020

B.A. Rice University, Houston, TX, 2020

A dissertation submitted in partial fulfillment of the requirements for the degree of Doctor of Philosophy in the Department of Earth, Environmental, and Planetary Sciences at Brown University

Providence, Rhode Island, USA

February 2026

This dissertation by Jared E. Nirenberg is accepted in its present form by the Department of Earth, Environmental, and Planetary Sciences as satisfying the dissertation requirement for the degree of Doctor of Philosophy.

Date DECEMBER 5, 2025 ______________________

Timothy Herbert, PhD, Advisor

Recommended to the Graduate Council

Date 12/5/25 ______________________

Daniel Ibarra, PhD, Reader

Date 12/5/25 ______________________

James Russell, PhD, Reader

Date 12/5/25 ______________________

Victor Tsai, PhD, Reader

Date 12/5/25 ______________________

Jordan Abell, PhD, External Reader

Approved by the Graduate Council

Date______________ ______________________

Janet Blume, Interim Dean of the Graduate School

CURRICULUM VITAE

Jared E. Nirenberg

Education

M.Sc. in Earth, Environmental, and Planetary Sciences, Brown University, 2022
Thesis, "Miocene Sea Surface Temperature in the High-Latitude North Pacific: Long-term trends and orbital-scale variability"
B.S. in Earth Science with a concentration in geochemistry, Rice University, 2020
Honors Thesis: "Glacially-controlled variations in the biological pump of the Ross Sea in the Mid-to-Late Pliocene"
Honors: *Magna cum laude*, Distinction in Research and Creative Work
B.A. in Chemistry, Rice University, 2020
Honors: Inducted into Phi Beta Kappa

Publications

1. **J.E. Nirenberg** & T.D. Herbert (2025). North Pacific warmth synchronous with the Miocene Climatic Optimum, *Geology*, https://doi.org/10.1130/G52432.1
2. G. Piccione, **J.E. Nirenberg**, J.B. Novak, A. Hawthorn, P. Northrup, T. Blackburn, & D.E. Ibarra (In review). Thermogenic Methane Production in Antarctic Subglacial Hydrocarbon Seeps. *Geology*, https://doi.org/10.31223/X5HM89
3. F. Zhu, J. Zhu, W. Si, **J.E. Nirenberg**, T.D. Herbert, J.E. Tierney, R.P. Acosta, N.J. Burls, & D. Evans (In review). Model-data synthesis of benthic isotopes suggests a warmer Miocene Climatic Optimum. *Nature Communications*, https://doi.org/10.21203/rs.3.rs-7124543/v1
4. W. Si, J.B. Novak, N. Richter, P. Polissar, R. Ma, E. Santos, **J.E. Nirenberg**, T.D. Herbert, & M.P. Aubry (2024). Alkenone-derived estimates of Cretaceous $p\mathrm{CO_2}$. *Geology*, https://doi.org/10.1130/G51939.1
5. B. Hoegler* & **J.E. Nirenberg*** (2023). Scientific Ocean Drilling is necessary for climate studies, natural hazards research, and inspiring future scientists. *Perspectives of Earth and Space Scientists*. https://doi.org/10.1029/2023CN000224

*indicates co-first authorship

Manuscripts in preparation

1. **J.E. Nirenberg** & T.D. Herbert. East Antarctic ocean-ice sheet interactions during Miocene warmth. In preparation.
2. **J.E. Nirenberg**, S. Gilroy, J.T. Abell & T.D. Herbert. Controls on subpolar North Pacific productivity during the Early-Middle Miocene. In preparation.
3. **J.E. Nirenberg**, D.E. Ibarra & T.D. Herbert. Plant waxes record East Antarctic hydroclimate during Miocene global warmth. In preparation.

Conference abstracts

1. **J.E. Nirenberg** & T.D. Herbert (2025). Forcings of East Antarctic Ice Sheet expansion and stabilization during the Miocene. Poster presentation at AGU 2025.

2. **J.E. Nirenberg**, D.E. Ibarra, & T.D. Herbert (2024). Plant waxes record East Antarctic hydroclimate during Miocene global warmth. Oral presentation at AGU 2024.
3. S. Gilroy, **J.E. Nirenberg**, J.B. Novak, W. Si, K. Kimble, & T.D. Herbert (2024). North Pacific Deep Ocean Circulation during the Early Miocene. Poster presentation at AGU 2024.
4. I.M. Browne, M.O. Patterson, T. Barbelet, G. King, A.R. Lam, M.A. Berke, **J.E. Nirenberg**, G.R. Grant, G.H. Browne, R.M. McKay, B. Duncan, & D.K. Kulhanek (2024). Early to Middle Miocene Sedimentologic and Oceanographic Changes at ODP Site 1123, Chatham Rise, New Zealand. Poster presentation at AGU 2024.
5. **J.E. Nirenberg** & T.D. Herbert (2024). High-latitude ocean temperature evolution during the Miocene. Oral presentation at Miocene Climate Workshop and University of Arizona.
6. **J.E. Nirenberg**, T.D. Herbert, & D.E. Ibarra (2023). Miocene Evolution of Polar Southern Ocean Temperatures and Their Implications for Benthic Oxygen Isotopes. Oral presentation at AGU 2023.
7. **J.E. Nirenberg** & T.D. Herbert (2022). North Pacific Sea Surface Temperatures Evolved Synchronously with Antarctic Ice Volume during the Miocene. Poster presentation at AGU 2022.
8. **J.E. Nirenberg** & T.D. Herbert (2021). Middle Miocene Sea Surface Temperatures in the High-Latitude North Pacific. Poster presentation at AGU 2021.
9. **J.E. Nirenberg**, B.W. Romans, M.O. Patterson, D. Kulhanek, L. DeSantis, R. McKay, J. Ash, & IODP Expedition 374 Scientists (2020). Glacially-controlled variations in the biological pump of the Ross Sea in the Mid-to-late Pliocene. Poster presentation at GSA 2020.

Invited talks and seminars

1. Paleoclimate seminar at Woods Hole Oceanographic Institution (2025). "Miocene climate evolution in East Antarctica and the polar Southern Ocean".
2. Department seminar at Binghamton University, State University of New York (2024). "Miocene climate evolution in East Antarctica and the polar Southern Ocean".
3. Biology and paleoenvironments seminar at Columbia University (2023). "Earth's coldest waters in a past warmer climate: High-latitude ocean temperature evolution during the Miocene".
4. COOL-FRES Climate-Tectonics Workshop at the Massachusetts Institute of Technology (2023). "Miocene Warmth in the North Pacific Evolved Synchronously with Benthic Oxygen Isotopes".
5. Miocene meeting at Utrecht University (2023). "The Miocene Climatic Optimum in the Subpolar North Pacific: Synchrony of Sea Surface Temperatures with Antarctic Ice Volume".

Honors, Awards, and Grants

1. Outstanding Student Presentation Award at AGU 2024
2. Schlanger Ocean Drilling Fellowship from the U.S. Science Support Program 2023-2024
3. Honorable mention for the NSF Graduate Research Fellowship, 2022
4. Graduate Research, Training, and Travel Award from the Institute at Brown for Environment and Society, Fall 2021 and Spring 2023
5. Presidential Fellowship from Brown University, 2020-2023

6. Outstanding Undergraduate Student Award from the Rice University Department of Earth, Environmental, and Planetary Sciences, 2020
7. Houston Geological Society Undergraduate Scholarship, 2020
8. Torkild Rieber Award in Earth Science from the Rice University Department of Earth, Environmental, and Planetary Sciences, 2019
9. Eugen Merten Memorial Prize in Geology and Geophysics, the Rice University Department of Earth, Environmental, and Planetary Sciences, 2018

Teaching experience

1. Teaching assistant, "Earth: Evolution of a Habitable Planet". Brown University Department of Earth, Environmental, and Planetary Sciences, Spring 2024.
2. Teaching assistant, "Fire and Ice: A Journey Through Rhode Island's Climate History". Brown University Pre-College Programs, Summer 2023.

Students mentored

1. Sofía Gilroy, Brown University undergraduate, 2023-2025
2. Emily Clements, Brown University undergraduate, 2022-2024
3. Alexandra Coia, Brown University undergraduate, 2023
4. Jonah Bernstein-Schalet, Brown University undergraduate, 2022
5. Apollonia Arellano, Leadership Alliance REU intern, 2022
6. Valencia Ajeh, Leadership Alliance REU intern, 2022
7. Duncan Jurayj, Brown University undergraduate, 2021
8. El Hebert, Brown University undergraduate, 2021

Workshop participation

1. PaleoCAMP, Summer 2024.
2. Glacial sedimentation school at Oregon State University, Summer 2022.

Other academic and volunteer activities

1. Reviewer for *Paleoceanography and Paleoclimatology* and *Geophysical Research Letters*
2. Mentor for Leadership Alliance REU, Summer 2022
3. President of Brown DEEPS Geoclub, 2021-2022

ACKNOWLEDGEMENTS

First, I would like to wholeheartedly thank my family. My parents and grandparents have always been the biggest supporters of my education. They worked tirelessly so that I would be able to do anything I set my mind to, and I am eternally grateful. I could never have done this without their unwavering support over 27 years, nor would I ever want to.

Next, I would like to thank my amazing colleagues and friends from the Brown University Department of Earth, Environmental, and Planetary Sciences. They have provided an incredibly supportive community, whether we were manually injecting samples on a isotope ratio mass spectrometer or playing trivia at Narragansett Brewery. My labmates Anson Cheung, Bryce Mitsunaga, Kristin Kimble, and Weimin Si were always there to help me. I learned the most from them and other members of the paleoclimate groups in our department, such as Sloane Garelick, Meredith Parish, Andrea Mason, and Sarah McGrath, who were always incredibly generous with their time and support. It has truly been an honor to be part of such a kind, caring, and brilliant community.

I am deeply grateful to all of my mentors over many years. I would have never even known about PhD opportunities in science without the immense support of Jeanine Ash and Sylvia Dee, who guided me towards research as an undergraduate. I would like to also thank all of my teachers and professors over my lifetime of education. I was incredibly fortunate to have many passionate teachers in my life, and they have inspired my love for education. I am very thankful for everyone who has ever taken their time to write a letter of recommendation for me. Finally, I would like to thank my PhD advisor, Tim Herbert. Thank you for giving me the opportunity and guidance to accomplish my crazy and ambitious ideas.

I could not have done the work in this dissertation without the technical support of Marcelo Alexandre, Jamie Pahigian, and Ewerton Santos. I cannot thank them enough for their hard work keeping the lab and instruments running. I would also like to thank all of the undergraduate students that I have mentored who contributed to this dissertation. This work was assisted by Sofía Gilroy, Emily Clements, and Jonah Bernstein-Schalet.

I would also like to thank the scientists and crew of scientific ocean drilling expeditions over the past 50 years. Their hard work recovering, describing, and analyzing mud from the bottom of the ocean has inspired generations of scientists, including myself, and numerous fields of research. I am also very grateful for the hard work of the staff at the Gulf Coast Repository, who provided me copious amounts of sample material for this dissertation.

Finally, I would like to thank all of my friends and colleagues across the world who supported me during my PhD. I am lucky to be part of such a wonderful global scientific community. My frequent discussions with Imogen Browne, Emily Kaiser, Bella Duncan, and Emily Tibbett were invaluable for thinking about biomarkers and moral support. PaleoCAMP and GLASS introduced me to many friends around the world. I was supported by many friends at Brown, but nobody supported me more than Andrea Mason, for which I am forever grateful.

TABLE OF CONTENTS

LIST OF TABLES

LIST OF FIGURES

CHAPTER 1

Introduction

Jared E. Nirenberg[1]

[1]Department of Earth, Environmental, and Planetary Sciences, Brown University, Providence, Rhode Island, USA

Earth's polar regions are rapidly transforming due to anthropogenic climate change. Rising temperatures as a result of increasing atmospheric greenhouse gas concentrations are reshaping both the polar oceans and land surfaces into states that would have been unrecognizable just a century ago. Sea ice extent has declined to record lows in both the Arctic and Antarctic (Meier & Stroeve, 2022; Raphael & Handcock, 2022). Vegetated areas in both the Arctic (Frost et al., 2025) and Antarctic (Roland et al., 2024) are expanding at an accelerating pace, causing a rapid 'greening' of polar landscapes. While these changes are unprecedented within the timespans of modern instrumental and satellite observations, Earth's polar regions have been warm, ice-free, and vegetated during past warm climate intervals found within the geologic record.

Paleoclimate records present a unique and powerful opportunity to understand the response of Earth's polar regions to elevated greenhouse gas concentrations and warmer temperatures from the past as potential analogs for global warmth expected by the end of this century and beyond. Sediment core records recovered through scientific ocean drilling expeditions are invaluable resources for these explorations of the past. Their ability to continuously capture climate variability on a wide range of past timescales, from hundreds of years to over one hundred million years, is unparalleled by any other archive. Sediment cores recovered from ocean drilling not only provide records of past oceans, but also of terrestrial environments and polar ice sheets. High-latitude oceans, land, and ice, as well as the interactions between them, are all explored in this dissertation.

From research on thousands of sediment archives over decades, Earth's high-latitude regions stand out as the most dramatically different from modern during past warm climate intervals. Fossils and temperature reconstructions show that conditions similar to the modern subtropics have been present as far north as the Arctic (Sluijs et al., 2006; Willard et al., 2019). Antarctica, which is almost fully covered by ice sheets today, was once ice-free and inhabited with temperate ecosystems (Anderson et al., 2011; Poole et al., 2001; Warny et al., 2009, 2019). Temperatures in the high-latitudes warm by more than the global average, and this enhanced degree of temperature variability is known as polar amplification. Past warm climates were not simply similar to our present climate system but only uniformly warmer. Rather, fundamental reorganizations of Earth's climate systems, from ocean currents to atmospheric circulation to the global carbon cycle, occurred as a result of, and even contributed to, warmer global temperatures. However, the mechanisms driving such dramatic polar amplification as observed in geologic records have been elusive. Simulations from global climate models often fail to reproduce such a large degree of polar-amplified warming (Lunt et al., 2024). Geologic observations from the polar regions during past warm climate intervals provide targets for model simulations (Lunt et al., 2024), which provide full global climate reconstructions and inform past climate dynamics.

The Miocene Epoch (5.3 to 23 million years ago) is an ideal target interval for studies of past global warmth. A wide range of warmer than modern climate states occurred during the Miocene, including the most recent interval of wide-scale bipolar deglaciation during the warmest interval, the Miocene Climatic Optimum (MCO), between about 14 and 17 million years ago. Atmospheric carbon dioxide concentrations were higher than modern (Cenozoic CO_2 Proxy Integration Project (CENCO$_2$PIP) Consortium, 2023), and global temperatures were likely similar to those predicted by the end of the century under moderate to high carbon emissions scenarios (Steinthorsdottir, Coxall, et al., 2021; Westerhold et al., 2020). The Miocene also contains several intervals of global cooling, the most prominent of which are the Middle

Miocene Climate Transition (MMCT), about 14 million years ago, and the late Miocene cooling interval, about 6 to 7.5 million years ago (Herbert et al., 2016). These cooling intervals are some of the most prominent in the Cenozoic (Westerhold et al., 2020; Zachos et al., 2001), and several modern features of the Earth system, ranging from widespread grassland ecosystems in continental interiors to Earth's largest ice sheet in East Antarctica, have their origins in Miocene cooling intervals. During the Miocene, Earth's climate transformed from dramatically warmer than modern to only slightly warmer than modern (Herbert et al., 2016; Westerhold et al., 2020). However, there are many basic features of the Miocene climate system that are not yet well-constrained, such as just how hot global temperature were during peak Miocene warmth of the MCO as well as the timing and magnitude of subsequent cooling as Earth's climate transitioned out of this geologically-recent greenhouse state and towards the modern icehouse world.

In this dissertation, I present novel reconstructions to constrain aspects of Earth's high-latitude climate system during the Miocene using a diverse range of measurements on ocean sediment cores. Together, these studies quantify the degree of high-latitude ocean warming during the Miocene and constrain the response of these high-latitude regions to Miocene warmth and subsequent global cooling and ice sheet expansion.

The Miocene Climatic Optimum

Oxygen isotopes of benthic foraminifera (benthic $\delta^{18}O$) indicate that the MCO was the warmest interval over the past 34 million years (Westerhold et al., 2020), and nowhere was this warmth more apparent than in the high-latitude regions. During the MCO, ice sheets on Antarctica retreated, leaving the continent inhabited with temperate and tundra ecosystems

(Lewis et al., 2008; Sangiorgi et al., 2018; Warny et al., 2009). Insects and mosses thrived in lakes in the McMurdo Dry Valleys (Lewis et al., 2008), one of the most desolate environments on Earth today. In the Northern Hemisphere, there is no evidence for the presence of continental-scale ice sheets during the MCO (Thiede & Myhre, 1996). Rather, Arctic terrestrial records reconstruct a warm and wet landscape dominated by large forests at latitudes far north of the modern tree line (Williams et al., 2008). Thermophilic reptiles typical of the modern tropics and subtropics such as alligators, crocodiles, and tortoises inhabited regions as far north as 51°N in Germany and Poland (Böhme, 2003; Górka et al., 2025).

Despite these qualitative indicators of high-latitude warmth, very few quantitative constraints on the temperatures surrounding these drastic environmental changes exist. While continuous temperature proxy records are available in most regions of the global ocean over the past 12 million years (Figure 1), proxy data prior to 12 Ma is quite spatially and temporally sparse. This lack of quantitative temperature constraints is particularly apparent in the Southern high-latitudes near Antarctica, where no Miocene records using a commonly-applied sea surface temperature (SST) proxy, $U^{k'}_{37}$, existed prior to the work presented in this dissertation. Quantitative temperature reconstructions from the high-latitudes are necessary for determining the sensitivity of polar ice sheets and environments to temperature and greenhouse gas forcing. For example, if polar ice sheets exhibited wide-scale retreat during the MCO with only little warming at high latitudes, as some studies argue (Mejia Ramirez et al., 2024), this would imply a very high sensitivity of these environments to warming. Conversely, if polar warming was more extreme during the MCO, polar ice sheets and environments may be less susceptible to a long-term return to fully deglaciated conditions under low or moderate greenhouse gas emissions scenarios. Geologic evidence provides undisputable evidence of polar environments much warmer and wetter than modern during the MCO, but the temperatures at which these changes occurred are largely unconstrained.

While the MCO was warm on average, a large degree of orbital-scale variability in benthic $\delta^{18}O$ suggests a highly variable global climate and/or polar ice sheet extent during the MCO. Lithologies from ocean sediment cores in the Ross Sea confirms large variabilities in Antarctic ice sheet extent during the MCO, with reconstructed environments ranging from ice-proximal conditions to lacking evidence for nearby marine-terminating glaciers at all (Levy et al., 2016; McKay et al., 2024). Prior to beginning this dissertation, it was generally unknown whether a large degree of temperature variability accompanied this large amplitude of variability in Antarctic ice sheet extent and benthic $\delta^{18}O$ as well, as previous temperature proxy records did not have high enough sampling resolution to fully resolve orbital cyclicity. The degree of orbital-scale temperature variability during the MCO has implications for the partitioning of benthic $\delta^{18}O$ into temperature and ice volume signals as well as the sensitivity of the Miocene climate system, particularly at high-latitudes, to insolation changes due to orbital forcing and/or greenhouse gas forcing. I quantify these orbital-scale temperature variations using biomarker temperature proxies in Chapters 2 and 4.

The Middle Miocene Climate Transition and Mi3 glaciation

Warm and deglaciated conditions on Antarctica came to an end during the MMCT with the dramatic expansion of the East Antarctic Ice Sheet (EAIS) about 13.8-13.9 million years ago. EAIS expansion during this interval is recorded by many archives, including terrestrial records in the Transantarctic Mountains (Lewis et al., 2008), pulses of iceberg-rafted debris across the

Antarctic margin found in marine sediment records (Pierce et al., 2017), and a ~1‰ enrichment of benthic $\delta^{18}O$ observed globally (Holbourn et al., 2005, 2014, 2024; Shevenell et al., 2004). Miller et al. (1991) deemed this large enrichment of benthic $\delta^{18}O$ "Mi3", as the third major glacial event of the Miocene according to the records available then. Further work on compilations of high-resolution benthic $\delta^{18}O$ records that came after would reveal that the MMCT was not only a glacial event on Antarctica, but rather a broad reorganization of global climate in the Cenozoic evolution towards permanent polar glaciation (De Vleeschouwer et al., 2017; Westerhold et al., 2020).

Outside of Antarctica, global climate and ecosystems shifted from equable conditions during the MCO towards steeper meridional temperature gradients (Flower & Kennett, 1994) and greater terrestrial aridity (Pound et al., 2012) during the MMCT. However, there is disagreement on the timing of these changes. While some define the MMCT as beginning at ~14.7 Ma (Holbourn et al., 2014) due to increasing glacial maxima in benthic $\delta^{18}O$, we find that these glacials prior to 13.9 Ma are transient, and there is little change in the mean state relative to other periods of the MCO until Mi3. As such, in this dissertation, we define the MCO as extended until ~13.95 Ma and the MMCT beginning with the Mi3 glaciation. However, this definition is arbitrary and is not critical to the conclusions of this work or others. While we acknowledge, and the novel work presented in this dissertation confirms, the presence of transient glacial intervals on Antarctica prior to 13.9 Ma, Mi3 and the MMCT mark the establishment of a permanent presence of ice sheets on Antarctica. The extent of Antarctic ice sheets was certainly variable after the MMCT, but glacial retreats were not as extensive as those during the MCO.

While the significance of the MMCT in Cenozoic climate evolution is clear, it is far less clear what the causes of this transition were. High-resolution benthic $\delta^{18}O$ records indicate that EAIS expansion occurred during an ~80 kyr period of relatively invariant summer insolation in the Southern high-latitudes due to low 100-kyr eccentricity and low amplitude of 41-kyr obliquity variations (Holbourn et al., 2005). While a favorable orbital configuration may explain the precise timing of the MMCT, orbital parameters vary cyclically, so other factors are needed in conjunction to explain why this permanent climate transition occurred in the Middle Miocene. Conditions on Antarctica during the Middle Miocene are often assumed from benthic $\delta^{18}O$ at sites far from the continent due to the sparse availability of proxy data near Antarctica. Temperature proxy records that existed prior to this dissertation from the Antarctic margin during the MCO and MMCT had very low temporal resolution (1 sample per 100s of thousands of years), which cannot resolve the context of orbital-scale variability and are therefore difficult to compare with much higher resolution benthic $\delta^{18}O$ and known oscillations in orbital parameters. High-resolution temperature proxy data from sites both near Antarctica and elsewhere are needed to assess the global trends and regional variations in temperature variability with EAIS expansion during the MMCT. Temperature proxy records spanning the MMCT that fully resolve orbital-cyclicity are presented in Chapters 2 and 4.

Late Miocene cooling

After the MMCT, Miocene cooling intensified again after about 8 million years ago, culminating in a global climate and ecosystems similar to modern. Ocean temperatures across the global ocean declined between about 8 and 6 Ma, with cooling amplified at higher latitudes (Herbert et al., 2016). With global cooling, terrestrial ecosystems transformed from more equable distributions to steeper meridional gradients more similar to modern (Pound et al., 2012). Vast portions of continental interiors became more arid as forests were replaced with grassland ecosystems in Africa (Dupont et al., 2013), Asia (Quade et al., 1989), and North America (Wang et al., 1994), and the Sahara Desert was first established (Schuster et al., 2006).

In the polar regions, aridification and glaciation accompanied late Miocene global cooling. During the late Miocene, cold polar desert conditions became established over much of Antarctica. While parts of Antarctica have experienced hyperaridity and a total lack of weathering processes continuously since the MMCT (Lewis et al., 2007; Spector & Balco, 2020), other high-elevation regions experienced periodic returns to warmer and wetter conditions after the MMCT, which ceased about 6 million years ago (Verret et al., 2023) after late Miocene cooling. In addition to aridification, continental-scale ice sheets began to develop outside of Antarctica, with evidence for glaciation in Greenland (Larsen et al., 1994), Alaska (Rea et al., 1995), and Patagonia (Mercer & Sutter, 1982) dating to the late Miocene. Though these incipient glaciations proved to be ephemeral and did not persist through Pliocene warming, the initiation of glaciation in the high-latitudes of both hemispheres by the end of the Miocene represents a culmination of Miocene climate evolution from a nearly fully deglaciated MCO to near modern by ~6 Ma.

Despite all of the geologic and geochemical evidence for late Miocene cooling and glacial expansion, there are little to no shifts in benthic $\delta^{18}O$ during this interval (Figure 2, Westerhold et al., 2020). Benthic $\delta^{18}O$ should reflect high-latitude cooling and increase global ice volume, so the lack of any notable features during the late Miocene cooling interval is perplexing. One potential solution for this problem could be that low and mid latitude ocean temperatures cooled, but not high-latitude surface waters which would be imprinted into benthic

$\delta^{18}O$ as the regions of deep water formation (Herbert et al., 2016). However, there were no continuous ocean temperature records from the Southern high-latitudes spanning the late Miocene to test this hypothesis prior to the work in this dissertation. In Chapter 4, I show that the polar Southern Ocean cooled dramatically between 6 and 8 Ma, synchronously with global cooling during the late Miocene and the permanent establishment of hyperarid polar desert conditions on Antarctica. While these records further demonstrate the global nature of late Miocene cooling, which is likely indicative of its forcing, the mystery of why benthic $\delta^{18}O$ does not reflect this late Miocene cooling remains unsolved.

Biomarker paleotemperature proxies

Biomarkers are molecules produced by past organisms that are preserved in the sedimentary record and serve as powerful tools for reconstructing past environments. While we cannot directly measure temperatures in the geologic past, we can measure biological responses to temperature as changes in the lipid compositions of past organisms where these molecules are preserved in the sedimentary record. Alkenones and isoprenoid glycerol dialkyl glycerol tetraethers (GDGTs) are produced by marine organisms, and indices calculated from these lipid biomarkers, $U^{k'}_{37}$ and TEX_{86}, respectively, are widely-used proxies for reconstructing past SSTs. A strength of these biomarker proxies over inorganic paleotemperature proxies such as magnesium to calcium ratios and oxygen isotopes of foraminifera is that they are completely independent of calcite preservation, which is often poor at high-latitudes, and assumptions of past seawater chemistry.

Alkenones are long-chain, unsaturated ketones produced by certain species of haptophyte algae in the order Isochrysidales (Wang et al., 2021). The degree of unsaturation, or relative number of double bonds, of C_{37} alkenones is tightly correlated with the temperature of the water in which these algae live (Prahl & Wakeham, 1987; Prahl et al., 1988). Alkenone concentrations are highest in marine surface waters (Hamanaka et al., 2000), making $U^{k'}_{37}$ a proxy for sea surface temperatures (SSTs). Core-top calibrations of $U^{k'}_{37}$ reveal a strong linear relationship between $U^{k'}_{37}$ and mean annual SST of the overlying location (Müller et al., 1998). While there is debate over the linearity (or lack thereof) of the calibration at higher temperatures near saturation ($U^{k'}_{37}$ approaches 1), there is no statistically significant difference between calibrations below 24°C (Müller et al., 1998; Prahl & Wakeham, 1987; Tierney & Tingley, 2018), which encapsulates the temperature range observed at high-latitude sites, even during the warmest intervals of the MCO. However, $U^{k'}_{37}$ is not always representative of mean annual SST and can be biased towards seasonal temperatures (Tierney & Tingley, 2018), particularly in the high-latitudes where light is limited or unavailable during winter months. A key limitation of the $U^{k'}_{37}$ is its inability to capture temperature variability above ~29°C, when the proxy reaches saturation. While these temperatures are rare in the modern ocean (Locarnini et al., 2024), mean annual SSTs above 29°C were much more widespread during past warm climates such as the Miocene. Other proxies are needed to quantitatively reconstruct temperature variability at these high temperatures.

Isoprenoid GDGTs (isoGDGTs) in the ocean are produced by archaea as membrane lipids (De Rosa & Gambacorta, 1988). These large tetraethers have varying numbers of rings within their lipid cores, and the number of rings increases with increasing temperature (Gliozzi et al., 1983; Uda et al., 2001). TEX_{86} was originally developed as an index to quantify the degree of cyclization of isoGDGTs (Schouten et al., 2002), but other indices are now being explored (Ishii et al., 2025) as well as the full distribution of isoGDGTs (Dunkley Jones et al., 2020) for temperature reconstructions. One feature of TEX_{86} and other isoGDGT-based proxies is that they do not reach saturation at natural temperatures, unlike alkenones. As such, they are often the biomarker temperature proxy of choice during past warm climate intervals (Hollis et al., 2019). However, the ammonia-oxidizing archaea that produce marine isoGDGTs do not live exclusively in near-surface waters (Karner et al., 2001), unlike alkenone producers. Because of isoGDGT production at depth, TEX_{86} temperatures are often interpreted as an integrated temperature over a range of depths up to hundreds or thousands of meters from the surface (Ho & Laepple, 2016). In addition, isoGDGT distributions are affected by factors other than temperature, and several indices have been created to screen marine isoGDGT data for these non-thermal impacts (Hopmans et al., 2004; Taylor et al., 2013; Zhang et al., 2011, 2016). Furthermore, TEX_{86} has proven more difficult to calibrate to temperature than $U^{k'}_{37}$, with significantly greater disagreement between calibrations and higher uncertainties (Dunkley Jones et al., 2020; Kim et al., 2010; Schouten et al., 2002; Tierney & Tingley, 2014).

These two biomarker temperature proxies, $U^{k'}_{37}$ and TEX_{86}, are natural compliments to each other for multi-proxy comparison as they can easily be measured in the same organic extracts from sediment samples. In fact, due to the different depth habitats of the producing organisms, differences in $U^{k'}_{37}$ and TEX_{86}-based temperatures can even inform surface-subsurface temperature gradients (Lawrence et al., 2020). In this dissertation, I utilize $U^{k'}_{37}$ as the backbone for SST reconstruction due to its significantly lower calibration uncertainty (~1.5°C vs. 2.5-4°C for TEX_{86}) and less complex application due to the lack of screening indices for quality control. In Chapter 4, I apply both proxies in the same samples for direct comparison, as well as to compare with other site locations in the polar Southern Ocean, where TEX_{86} has been traditionally exclusively applied (Duncan et al., 2022; Levy et al., 2016; Sangiorgi et al., 2018; Shevenell et al., 2011). Together, I use these biomarker proxies in this dissertation to constrain high-latitude temperature evolution during the Miocene and evaluate thermal forcing of the responses of other climate and oceanographic variables, such as surface ocean productivity (Chapter 3) and terrestrial precipitation isotopes (Chapter 5).

Role of greenhouse gas forcing in Miocene climate change

While Miocene cooling from the MCO to the end of the Miocene is clear from many lines of geologic and geochemical evidence, the forcings of Miocene climate evolution are debated. Changes in atmospheric greenhouse gas concentrations are often theorized as a primary driver of Miocene climate due to the global nature of temperature and ecosystem shifts, which was known for at least the late Miocene. However, proxy reconstructions of past atmospheric greenhouse gas concentrations show wide disagreement in not only absolute concentrations, but also trends over time (Figure 2). Carbon isotopes of alkenones reconstruct unrealistically low concentrations of atmospheric CO_2 during the MCO, with the first estimates near concentrations observed during the Last Glacial Maximum, about 180 ppm (Pagani et al., 1999). Others reconstruct CO_2 concentrations somewhat higher than preindustrial (~400 ppm), but relatively invariant over the Miocene despite large changes in climate (Zhang et al., 2013). Reconstructions from boron isotopes of planktonic foraminifera suggest large changes in atmospheric CO_2 concentrations on orbital timescales during the MCO (Greenop et al., 2014), which would seem to be more consistent with large changes in global climate on these timescales (Holbourn et al., 2014, 2015). Newer records from carbon isotopes of other phytoplankton biomarkers reconstruct atmospheric CO_2 over 1000 ppm during the MCO (Witkowski et al., 2024). While some proxy records show declining atmospheric CO_2 concentrations during the global cooling intervals of the late Miocene (Brown et al., 2022; Tanner et al., 2020) and MMCT (Badger et al., 2013; Super et al., 2018), others do not and estimates of absolute concentrations vary by over an order of magnitude (Cenozoic CO_2 Proxy Integration Project (CENCO$_2$PIP) Consortium, 2023).

While direct CO_2 proxy reconstructions current yield an ambiguous verdict on the role of greenhouse gas forcing of Miocene climate, globally-distributed temperature records provide an indirect line of evidence for greenhouse gas forcings. The widespread, polar-amplified, and globally synchronous nature of SST decline during the late Miocene (Herbert et al., 2016) implies a global forcing, and atmospheric greenhouse gas concentrations provide one of the few realistic mechanisms for such a global forcing. However, little was known regarding the timing and amplitude of high-latitude temperatures changes during the Early and Middle Miocene due to a lack of SST records prior to the work in this dissertation. While records from the North Atlantic had demonstrated the bihemispheric nature of MCO warmth (Herbert et al., 2016, 2020; Sangiorgi et al., 2021; Super et al., 2020), the precise timing and magnitude of global high-latitude warming associated with the onset of the MCO and cooling associated with the MMCT were unclear. In this dissertation, I present high-resolution temperature reconstructions from the subpolar North Pacific and polar Southern Ocean to show that the MCO was globally-synchronous maximum of SSTs in the high-latitude regions. While I do not present any direct atmospheric CO_2 reconstructions, the synchronous timing and polar amplification of temperature changes in both hemispheres provides strong circumstantial evidence for greenhouse gas forcing of global climate during these intervals, which is further discussed in Chapters 2 and 4.

Overview and conclusions

In this dissertation, I present novel geochemical records from ocean drilling sites to provide a fuller picture of global high-latitude climate evolution during the Miocene. Particular emphasis is given to continuous, high-resolution paleotemperature reconstructions to quantify the degree of Miocene warmth across high-latitude regions as well as to help constrain global temperature evolution over the past 18 million years. In addition, I utilize other geochemical proxies at the same sites to constrain the response of polar terrestrial hydrologic cycling and surface ocean productivity during this warmer than modern interval in the geologic record. I utilize the sediment recovered from two deep ocean drilling sites with continuous sedimentation spanning Miocene climate transitions and relatively high sedimentation rates in order to reconstruct changes on orbital timescales. I focus on the subpolar North Pacific Ocean (Chapters 2 and 3) at Ocean Drilling Program (ODP) Site 884 and the polar Southern Ocean (Chapters 4 and 5) at ODP Site 1165, as previous proxy records from these regions were sparse or non-existent during the Early and Middle Miocene. Together with previous work in the North Atlantic Ocean (Herbert et al., 2016; Sangiorgi et al., 2021; Super et al., 2020), my work in this dissertation provides clarity on the temperature response of the high-latitude ocean to peak Neogene warmth and subsequent cooling over the past 18 million years.

In Chapter 2, I present an orbitally-resolved surface temperature record from Site 884 which spans the entire MCO and MMCT. Using this record, I demonstrate the synchrony of temperature changes between the Northern and Southern high-latitude regions surrounding the MCO as well as the persistently asymmetrical nature of warmth between the North Atlantic and North Pacific basins throughout the Miocene. In Chapter 3, I use X-ray fluorescence scanning of cores from Site 884 constrained with geochemical measurements to quantify sediment composition at high resolution. Combining biogenic sediment fluxes with other proxies for surface productivity and SSTs from Chapter 2, I explore the controls on biologic productivity in the subpolar North Pacific during the Early and Middle Miocene. In Chapter 4, I present ocean temperature reconstructions using multiple biomarker proxies from the polar Southern Ocean at Site 1165 spanning most of the Miocene (5 to 19 Ma). By comparing these temperatures with evidence of the evolution of the East Antarctic Ice Sheet, I constrain interactions between the ocean and ice sheet, finding a strong response of the marine ice margin to ocean temperature forcing but a more complex, threshold response of terrestrial ice volume. In Chapter 5, I reconstruct precipitation isotopes in East Antarctica over the Miocene as recorded by plant waxes preserved at Site 1165. I find a strong, though complex, relationship between temperatures in the polar Southern Ocean and terrestrial hydrology in East Antarctica, which defies straightforward application of modern Antarctic temperature-precipitation isotope relationships.

Together, these studies present a significant advancement in the quantity and resolution of temperature records during critical global climate transitions during the Miocene. In addition, interpreting other proxy and sedimentological data in the context of these temperature records constrains the response of several aspects of the high-latitude Earth system, such as polar ice sheets, terrestrial hydrology, and ocean surface productivity, to past temperature changes in a much warmer than modern climate state, but perhaps suggestive of the future. The work presented in this dissertation demonstrates the highly dynamic nature of the Miocene climate system to changes on timescales from thousands to millions of years. Future work to further advance the availability and quality of high-resolution records will be critical to understanding the implications of Miocene climate systems as analogs for future global warmth.

Figures

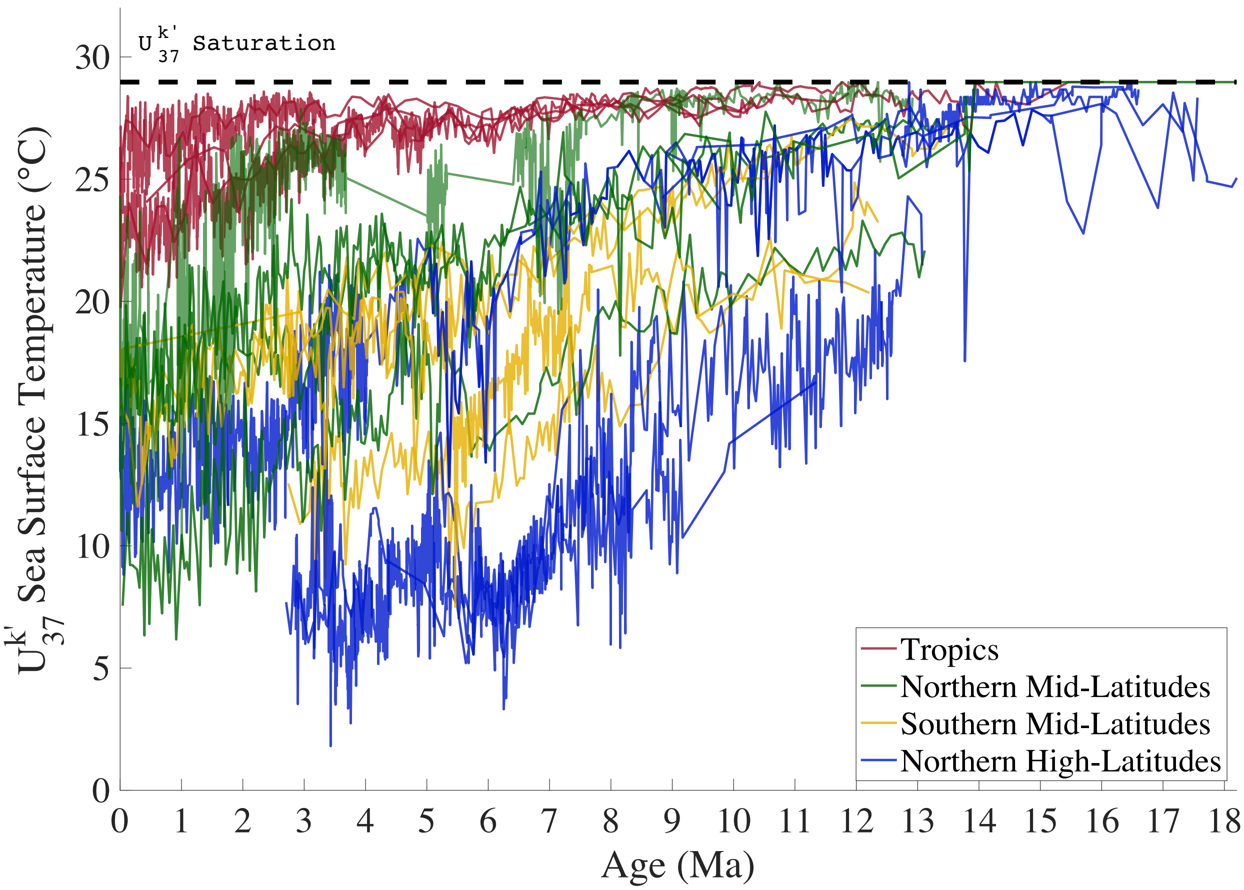

Figure 1. Miocene $U^{k'}_{37}$ records available prior to the work in this dissertation. $U^{k'}_{37}$ is calibrated to SST using the calibration of Müller et al. (1998). Lines are colored according to the latitude of the site location, with tropics (30°S-30°N) in red, northern mid-latitudes (30-50°N) in green, southern mid-latitudes (30-50°S) in yellow, and northern high-latitudes (>50°N) in blue. No records from the southern high-latitudes were available. $U^{k'}_{37}$ data is from Herbert et al. (2016, 2020), Huang et al. (2007), LaRiviere et al. (2012), Lawrence et al. (2020), Rommerskirchen et al. (2011), Rousselle et al. (2013), Sangiorgi et al. (2021), Seki et al. (2012), Super et al. (2020), and Zhang et al. (2014).

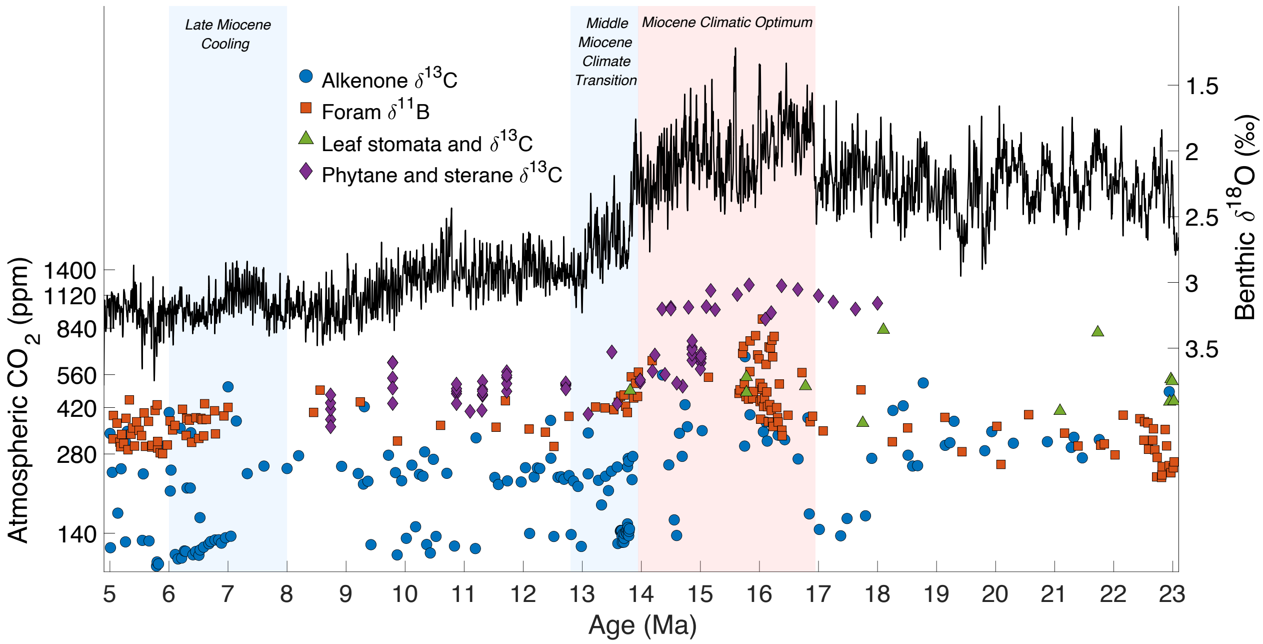

Figure 2. Benthic foraminiferal $\delta^{18}O$ and atmospheric pCO_2 proxies during the Miocene. Benthic $\delta^{18}O$ (black line) is from Westerhold et al. (2020). CO_2 proxy data is colored by the specific proxy, with carbon isotopes of alkenones in green, boron isotopes of planktonic foraminifera in orange, leaf stomatal indices and leaf carbon isotopes in green, and phytane and sterane carbon isotopes in purple. CO_2 data is from Badger et al. (2013), Bolton et al. (2016), Brown et al. (2022), Greenop et al. (2014), Kürschner et al. (2008), Liang et al. (2022), Londoño et al. (2018), Rae et al. (2021), Seki et al. (2010), Sosdian et al. (2018), Steinthorsdottir et al. (2021), Super et al. (2018), Tanner et al. (2020), Wang et al. (2015), Zhang et al. (2013, 2017).

References

Anderson, J. B., Warny, S., Askin, R. A., Wellner, J. S., Bohaty, S. M., Kirshner, A. E., et al. (2011). Progressive Cenozoic cooling and the demise of Antarctica's last refugium. *Proceedings of the National Academy of Sciences*, *108*(28), 11356–11360. https://doi.org/10.1073/pnas.1014885108

Badger, M. P. S., Lear, C. H., Pancost, R. D., Foster, G. L., Bailey, T. R., Leng, M. J., & Abels, H. A. (2013). CO_2 drawdown following the middle Miocene expansion of the Antarctic Ice Sheet. *Paleoceanography*, *28*(1), 42–53. https://doi.org/10.1002/palo.20015

Böhme, M. (2003). The Miocene Climatic Optimum: evidence from ectothermic vertebrates of Central Europe. *Palaeogeography, Palaeoclimatology, Palaeoecology*, *195*(3), 389–401. https://doi.org/10.1016/S0031-0182(03)00367-5

Bolton, C. T., Hernández-Sánchez, M. T., Fuertes, M.-Á., González-Lemos, S., Abrevaya, L., Mendez-Vicente, A., et al. (2016). Decrease in coccolithophore calcification and CO_2 since the middle Miocene. *Nature Communications*, *7*(1), 10284. https://doi.org/10.1038/ncomms10284

Brown, R. M., Chalk, T. B., Crocker, A. J., Wilson, P. A., & Foster, G. L. (2022). Late Miocene cooling coupled to carbon dioxide with Pleistocene-like climate sensitivity. *Nature Geoscience*, *15*(8), 664–670. https://doi.org/10.1038/s41561-022-00982-7

Cenozoic CO_2 Proxy Integration Project (CENCO$_2$PIP) Consortium. (2023). Toward a Cenozoic history of atmospheric CO_2. *Science*, *382*(6675), eadi5177. https://doi.org/10.1126/science.adi5177

De Rosa, M., & Gambacorta, A. (1988). The lipids of archaebacteria. *Progress in Lipid Research*, *27*(3), 153–175. https://doi.org/10.1016/0163-7827(88)90011-2

De Vleeschouwer, D., Vahlenkamp, M., Crucifix, M., & Pälike, H. (2017). Alternating Southern and Northern Hemisphere climate response to astronomical forcing during the past 35 m.y. *Geology*, *45*(4), 375–378. https://doi.org/10.1130/G38663.1

Duncan, B., McKay, R., Levy, R., Naish, T., Prebble, J. G., Sangiorgi, F., et al. (2022). Climatic and tectonic drivers of late Oligocene Antarctic ice volume. *Nature Geoscience*, *15*(10), 819–825. https://doi.org/10.1038/s41561-022-01025-x

Dunkley Jones, T., Eley, Y. L., Thomson, W., Greene, S. E., Mandel, I., Edgar, K., & Bendle, J. A. (2020). OPTiMAL: a new machine learning approach for GDGT-based palaeothermometry. *Clim. Past*, *16*(6), 2599–2617. https://doi.org/10.5194/cp-16-2599-2020

Dupont, L. M., Rommerskirchen, F., Mollenhauer, G., & Schefuß, E. (2013). Miocene to Pliocene changes in South African hydrology and vegetation in relation to the expansion of C4 plants. *Earth and Planetary Science Letters*, *375*, 408–417. https://doi.org/10.1016/j.epsl.2013.06.005

Flower, B. P., & Kennett, J. P. (1994). The middle Miocene climatic transition: East Antarctic ice sheet development, deep ocean circulation and global carbon cycling. *Palaeogeography, Palaeoclimatology, Palaeoecology*, *108*(3), 537–555. https://doi.org/10.1016/0031-0182(94)90251-8

Frost, G. V., Bhatt, U. S., Macander, M. J., Berner, L. T., Walker, D. A., Raynolds, M. K., et al. (2025). The changing face of the Arctic: four decades of greening and implications for tundra ecosystems. *Frontiers in Environmental Science*, *13*. https://doi.org/10.3389/fenvs.2025.1525574

Gliozzi, A., Paoli, G., De Rosa, M., & Gambacorta, A. (1983). Effect of isoprenoid cyclization on the transition temperature of lipids in thermophilic archaebacteria. *Biochimica et Biophysica Acta (BBA) - Biomembranes*, *735*(2), 234–242. https://doi.org/10.1016/0005-2736(83)90298-5

Górka, M., Březina, J., Chroust, M., Kowalski, R., López-Torres, S., & Tałanda, M. (2025). Crocodylian remains from the Miocene of the Fore-Carpathian Basin and its foreland—including the world's northernmost Neogene crocodylian. *Acta Palaeontologica Polonica*, *70*(2), 225–251. https://doi.org/10.4202/app.01194.2024

Greenop, R., Foster, G. L., Wilson, P. A., & Lear, C. H. (2014). Middle Miocene climate instability associated with high-amplitude CO_2 variability. *Paleoceanography*, *29*(9), 845–853. https://doi.org/10.1002/2014PA002653

Hamanaka, J., Sawada, K., & Tanoue, E. (2000). Production rates of C_{37} alkenones determined by ^{13}C-labeling technique in the euphotic zone of Sagami Bay, Japan. *Organic Geochemistry*, *31*(11), 1095–1102. https://doi.org/10.1016/S0146-6380(00)00118-2

Herbert, T. D., Lawrence, K. T., Tzanova, A., Peterson, L. C., Caballero-Gill, R., & Kelly, C. S. (2016). Late Miocene global cooling and the rise of modern ecosystems. *Nature Geoscience*, *9*(11), 843–847. https://doi.org/10.1038/ngeo2813

Herbert, T. D., Rose, R., Dybkjær, K., Rasmussen, E. S., & Śliwińska, K. K. (2020). Bihemispheric Warming in the Miocene Climatic Optimum as Seen From the Danish North Sea. *Paleoceanography and Paleoclimatology*, *35*(10), e2020PA003935. https://doi.org/10.1029/2020PA003935

Ho, S. L., & Laepple, T. (2016). Flat meridional temperature gradient in the early Eocene in the subsurface rather than surface ocean. *Nature Geoscience*, *9*(8), 606–610. https://doi.org/10.1038/ngeo2763

Holbourn, A., Kuhnt, W., Schulz, M., & Erlenkeuser, H. (2005). Impacts of orbital forcing and atmospheric carbon dioxide on Miocene ice-sheet expansion. *Nature*, *438*(7067), 483–487. https://doi.org/10.1038/nature04123

Holbourn, A., Kuhnt, W., Lyle, M., Schneider, L., Romero, O., & Andersen, N. (2014). Middle Miocene climate cooling linked to intensification of eastern equatorial Pacific upwelling. *Geology*, *42*(1), 19–22. https://doi.org/10.1130/G34890.1

Holbourn, A., Kuhnt, W., Kochhann, K. G. D., Andersen, N., & Sebastian Meier, K. J. (2015). Global perturbation of the carbon cycle at the onset of the Miocene Climatic Optimum. *Geology*, *43*(2), 123–126. https://doi.org/10.1130/G36317.1

Holbourn, A., Kuhnt, W., Kulhanek, D. K., Mountain, G., Rosenthal, Y., Sagawa, T., et al. (2024). Re-organization of Pacific overturning circulation across the Miocene Climate Optimum. *Nature Communications*, *15*(1), 8135. https://doi.org/10.1038/s41467-024-52516-x

Hollis, C. J., Dunkley Jones, T., Anagnostou, E., Bijl, P. K., Cramwinckel, M. J., Cui, Y., et al. (2019). The DeepMIP contribution to PMIP4: methodologies for selection, compilation and analysis of latest Paleocene and early Eocene climate proxy data, incorporating version 0.1 of the DeepMIP database. *Geoscientific Model Development*, *12*(7), 3149–3206. https://doi.org/10.5194/gmd-12-3149-2019

Hopmans, E. C., Weijers, J. W. H., Schefuß, E., Herfort, L., Sinninghe Damsté, J. S., & Schouten, S. (2004). A novel proxy for terrestrial organic matter in sediments based on branched and isoprenoid tetraether lipids. *Earth and Planetary Science Letters*, *224*(1), 107–116. https://doi.org/10.1016/j.epsl.2004.05.012

Huang, Y., Clemens, S. C., Liu, W., Wang, Y., & Prell, W. L. (2007). Large-scale hydrological change drove the late Miocene C_4 plant expansion in the Himalayan foreland and Arabian Peninsula. *Geology*, *35*(6), 531–534. https://doi.org/10.1130/G23666A.1

Ishii, H., Seki, O., Yamamoto, M., & Duncan, B. (2025). New isoprenoid GDGT index as a water mass and temperature proxy in the Southern Ocean. *EGUsphere*, 1–24. https://doi.org/10.5194/egusphere-2025-4281

Karner, M. B., DeLong, E. F., & Karl, D. M. (2001). Archaeal dominance in the mesopelagic zone of the Pacific Ocean. *Nature*, *409*(6819), 507–510. https://doi.org/10.1038/35054051

Kim, J.-H., van der Meer, J., Schouten, S., Helmke, P., Willmott, V., Sangiorgi, F., et al. (2010). New indices and calibrations derived from the distribution of crenarchaeal isoprenoid tetraether lipids: Implications for past sea surface temperature reconstructions. *Geochimica et Cosmochimica Acta*, *74*(16), 4639–4654. https://doi.org/10.1016/j.gca.2010.05.027

Kürschner, W. M., Kvaček, Z., & Dilcher, D. L. (2008). The impact of Miocene atmospheric carbon dioxide fluctuations on climate and the evolution of terrestrial ecosystems. *Proceedings of the National Academy of Sciences*, *105*(2), 449–453. https://doi.org/10.1073/pnas.0708588105

LaRiviere, J. P., Ravelo, A. C., Crimmins, A., Dekens, P. S., Ford, H. L., Lyle, M., & Wara, M. W. (2012). Late Miocene decoupling of oceanic warmth and atmospheric carbon dioxide forcing. *Nature*, *486*(7401), 97–100. https://doi.org/10.1038/nature11200

Larsen, H. C., Saunders, A. D., Clift, P. D., Beget, J., Wei, W., & Spezzaferri, S. (1994). Seven Million Years of Glaciation in Greenland. *Science*, *264*(5161), 952–955. https://doi.org/10.1126/science.264.5161.952

Lawrence, K. T., Pearson, A., Castañeda, I. S., Ladlow, C., Peterson, L. C., & Lawrence, C. E. (2020). Comparison of Late Neogene $U^{k'}_{37}$ and TEX_{86} Paleotemperature Records From the Eastern Equatorial Pacific at Orbital Resolution. *Paleoceanography and Paleoclimatology*, *35*(7), e2020PA003858. https://doi.org/10.1029/2020PA003858

Levy, R., Harwood, D., Florindo, F., Sangiorgi, F., Tripati, R., Eynatten, H. von, et al. (2016). Antarctic ice sheet sensitivity to atmospheric CO_2 variations in the early to mid-Miocene. *Proceedings of the National Academy of Sciences*, *113*(13), 3453–3458. https://doi.org/10.1073/pnas.1516030113

Lewis, Adam R., Marchant, D. R., Ashworth, A. C., Hedenäs, L., Hemming, S. R., Johnson, J. V., et al. (2008). Mid-Miocene cooling and the extinction of tundra in continental Antarctica. *Proceedings of the National Academy of Sciences*, *105*(31), 10676–10680. https://doi.org/10.1073/pnas.0802501105

Lewis, A.R., Marchant, D. R., Ashworth, A. C., Hemming, S. R., & Machlus, M. L. (2007). Major middle Miocene global climate change: Evidence from East Antarctica and the Transantarctic Mountains. *GSA Bulletin*, *119*(11–12), 1449–1461. https://doi.org/10.1130/0016-7606(2007)119%255B1449:MMMGCC%255D2.0.CO;2

Liang, J.-Q., Leng, Q., Höfig, D. F., Niu, G., Wang, L., Royer, D. L., et al. (2022). Constraining conifer physiological parameters in leaf gas-exchange models for ancient CO_2 reconstruction. *Global and Planetary Change*, *209*, 103737. https://doi.org/10.1016/j.gloplacha.2022.103737

Locarnini, R. A., Mishonov, A. V., Baranova, O. K., Reagan, J. R., Boyer, T. P., Seidov, D., et al. (2024). World Ocean Atlas 2023, Volume 1: Temperature. https://doi.org/10.25923/54BH-1613

Londoño, L., Royer, D. L., Jaramillo, C., Escobar, J., Foster, D. A., Cárdenas-Rozo, A. L., & Wood, A. (2018). Early Miocene CO_2 estimates from a Neotropical fossil leaf assemblage exceed 400 ppm. *American Journal of Botany*, *105*(11), 1929–1937. https://doi.org/10.1002/ajb2.1187

Lunt, D. J., Otto-Bliesner, B. L., Brierley, C., Haywood, A., Inglis, G. N., Izumi, K., et al. (2024). Paleoclimate data provide constraints on climate models' large-scale response to past CO_2 changes. *Communications Earth & Environment*, *5*(1), 419. https://doi.org/10.1038/s43247-024-01531-3

McKay, R., Cockrell, J., Shevenell, A. E., Laberg, J. S., Burns, J., Patterson, M., et al. (2024). Miocene ice sheet dynamics and sediment deposition in the central Ross Sea, Antarctica. *GSA Bulletin*, *137*(3–4), 1267–1291. https://doi.org/10.1130/B37613.1

Meier, W. N., & Stroeve, J. (2022). An Updated Assessment of the Changing Arctic Sea Ice Cover. *Oceanography*, *35*(3/4), 10–19.

Mejia Ramirez, L. M., Bernasconi, S. M., Fernandez, A., Zhang, H., Guitián, J., Jaggi, M., et al. (2024). Modest, not extreme, northern high latitude amplification over the Mid to Late Miocene shown by coccolith clumped isotopes [Application/pdf], 16 p. https://doi.org/10.3929/ETHZ-B-000715205

Mercer, J. H., & Sutter, J. F. (1982). Late miocene—earliest pliocene glaciation in southern Argentina: implications for global ice-sheet history. *Palaeogeography,* *Palaeoclimatology, Palaeoecology*, *38*(3), 185–206. https://doi.org/10.1016/0031-0182(82)90003-7

Miller, K. G., Wright, J. D., & Fairbanks, R. G. (1991). Unlocking the Ice House: Oligocene-Miocene oxygen isotopes, eustasy, and margin erosion. *Journal of Geophysical Research: Solid Earth*, *96*(B4), 6829–6848. https://doi.org/10.1029/90JB02015

Müller, P. J., Kirst, G., Ruhland, G., von Storch, I., & Rosell-Melé, A. (1998). Calibration of the alkenone paleotemperature index $U_{37}^{K'}$ based on core-tops from the eastern South Atlantic and the global ocean (60°N-60°S). *Geochimica et Cosmochimica Acta*, *62*(10), 1757–1772. https://doi.org/10.1016/S0016-7037(98)00097-0

Pagani, M., Freeman, K. H., & Arthur, M. A. (1999). Late Miocene Atmospheric CO_2 Concentrations and the Expansion of C_4 Grasses. *Science*, *285*(5429), 876–879. https://doi.org/10.1126/science.285.5429.876

Pierce, E. L., van de Flierdt, T., Williams, T., Hemming, S. R., Cook, C. P., & Passchier, S. (2017). Evidence for a dynamic East Antarctic ice sheet during the mid-Miocene climate transition. *Earth and Planetary Science Letters*, *478*, 1–13. https://doi.org/10.1016/j.epsl.2017.08.011

Poole, I., Hunt, R. J., & Cantrill, D. J. (2001). A Fossil Wood Flora from King George Island: Ecological Implications for an Antarctic Eocene Vegetation. *Annals of Botany*, *88*(1), 33–54. https://doi.org/10.1006/anbo.2001.1425

Pound, M. J., Haywood, A. M., Salzmann, U., & Riding, J. B. (2012). Global vegetation dynamics and latitudinal temperature gradients during the Mid to Late Miocene (15.97–5.33Ma). *Earth-Science Reviews*, *112*(1), 1–22. https://doi.org/10.1016/j.earscirev.2012.02.005

Prahl, F. G., & Wakeham, S. G. (1987). Calibration of unsaturation patterns in long-chain ketone compositions for palaeotemperature assessment. *Nature*, *330*(6146), 367–369. https://doi.org/10.1038/330367a0

Prahl, Fredrick G, Muehlhausen, L. A., & Zahnle, D. L. (1988). Further evaluation of long-chain alkenones as indicators of paleoceanographic conditions. *Geochimica et Cosmochimica Acta*, *52*(9), 2303–2310. https://doi.org/10.1016/0016-7037(88)90132-9

Quade, J., Cerling, T. E., & Bowman, J. R. (1989). Development of Asian monsoon revealed by marked ecological shift during the latest Miocene in northern Pakistan. *Nature*, *342*(6246), 163–166. https://doi.org/10.1038/342163a0

Rae, J. W. B., Zhang, Y. G., Liu, X., Foster, G. L., Stoll, H. M., & Whiteford, R. D. M. (2021). Atmospheric CO_2 over the Past 66 Million Years from Marine Archives. *Annual Review of Earth and Planetary Sciences*, *49*(Volume 49, 2021), 609–641. https://doi.org/10.1146/annurev-earth-082420-063026

Raphael, M. N., & Handcock, M. S. (2022). A new record minimum for Antarctic sea ice. *Nature Reviews Earth & Environment*, *3*(4), 215–216. https://doi.org/10.1038/s43017-022-00281-0

Rea, D. K., Basov, La., Scholl, D. W., & Allan, J. F. (Eds.). (1995). *Proceedings of the Ocean Drilling Program, 145 Scientific Results* (Vol. 145). Ocean Drilling Program. https://doi.org/10.2973/odp.proc.sr.145.1995

Roland, T. P., Bartlett, O. T., Charman, D. J., Anderson, K., Hodgson, D. A., Amesbury, M. J., et al. (2024). Sustained greening of the Antarctic Peninsula observed from satellites. *Nature Geoscience*, *17*(11), 1121–1126. https://doi.org/10.1038/s41561-024-01564-5

Rommerskirchen, F., Condon, T., Mollenhauer, G., Dupont, L., & Schefuss, E. (2011). Miocene to Pliocene development of surface and subsurface temperatures in the Benguela Current system. *Paleoceanography*, *26*(3). https://doi.org/10.1029/2010PA002074

Rousselle, G., Beltran, C., Sicre, M.-A., Raffi, I., & De Rafélis, M. (2013). Changes in sea-surface conditions in the Equatorial Pacific during the middle Miocene–Pliocene as inferred from coccolith geochemistry. *Earth and Planetary Science Letters*, *361*, 412–421. https://doi.org/10.1016/j.epsl.2012.11.003

Sangiorgi, F., Bijl, P. K., Passchier, S., Salzmann, U., Schouten, S., McKay, R., et al. (2018). Southern Ocean warming and Wilkes Land ice sheet retreat during the mid-Miocene. *Nature Communications*, *9*(1), 317. https://doi.org/10.1038/s41467-017-02609-7

Sangiorgi, F., Quaijtaal, W., Donders, T. H., Schouten, S., & Louwye, S. (2021). Middle Miocene Temperature and Productivity Evolution at a Northeast Atlantic Shelf Site (IODP U1318, Porcupine Basin): Global and Regional Changes. *Paleoceanography and Paleoclimatology*, *36*(7), e2020PA004059. https://doi.org/10.1029/2020PA004059

Schouten, S., Hopmans, E. C., Schefuß, E., & Sinninghe Damsté, J. S. (2002). Distributional variations in marine crenarchaeotal membrane lipids: a new tool for reconstructing ancient sea water temperatures? *Earth and Planetary Science Letters*, *204*(1), 265–274. https://doi.org/10.1016/S0012-821X(02)00979-2

Schuster, M., Duringer, P., Ghienne, J.-F., Vignaud, P., Mackaye, H. T., Likius, A., & Brunet, M. (2006). The Age of the Sahara Desert. *Science*, *311*(5762), 821–821. https://doi.org/10.1126/science.1120161

Seki, O., Foster, G. L., Schmidt, D. N., Mackensen, A., Kawamura, K., & Pancost, R. D. (2010). Alkenone and boron-based Pliocene pCO_2 records. *Earth and Planetary Science Letters*, *292*(1), 201–211. https://doi.org/10.1016/j.epsl.2010.01.037

Seki, O., Schmidt, D. N., Schouten, S., Hopmans, E. C., Sinninghe Damsté, J. S., & Pancost, R. D. (2012). Paleoceanographic changes in the Eastern Equatorial Pacific over the last 10 Myr. *Paleoceanography*, *27*(3). https://doi.org/10.1029/2011PA002158

Shevenell, A. E., Ingalls, A. E., Domack, E. W., & Kelly, C. (2011). Holocene Southern Ocean surface temperature variability west of the Antarctic Peninsula. *Nature*, *470*(7333), 250–254. https://doi.org/10.1038/nature09751

Shevenell, Amelia E., Kennett, J. P., & Lea, D. W. (2004). Middle Miocene Southern Ocean Cooling and Antarctic Cryosphere Expansion. *Science*, *305*(5691), 1766–1770. https://doi.org/10.1126/science.1100061

Sluijs, A., Schouten, S., Pagani, M., Woltering, M., Brinkhuis, H., Damsté, J. S. S., et al. (2006). Subtropical Arctic Ocean temperatures during the Palaeocene/Eocene thermal maximum. *Nature*, *441*(7093), 610–613. https://doi.org/10.1038/nature04668

Sosdian, S. M., Greenop, R., Hain, M. P., Foster, G. L., Pearson, P. N., & Lear, C. H. (2018). Constraining the evolution of Neogene ocean carbonate chemistry using the boron isotope pH proxy. *Earth and Planetary Science Letters*, *498*, 362–376. https://doi.org/10.1016/j.epsl.2018.06.017

Spector, P., & Balco, G. (2020). Exposure-age data from across Antarctica reveal mid-Miocene establishment of polar desert climate. *Geology*, *49*(1), 91–95. https://doi.org/10.1130/G47783.1

Steinthorsdottir, M., Jardine, P. E., & Rember, W. C. (2021). Near-Future pCO_2 During the Hot Miocene Climatic Optimum. *Paleoceanography and Paleoclimatology*, *36*(1), e2020PA003900. https://doi.org/10.1029/2020PA003900

Steinthorsdottir, M., Coxall, H. K., de Boer, A. M., Huber, M., Barbolini, N., Bradshaw, C. D., et al. (2021). The Miocene: The Future of the Past. *Paleoceanography and Paleoclimatology*, *36*(4), e2020PA004037. https://doi.org/10.1029/2020PA004037

Super, J. R., Thomas, E., Pagani, M., Huber, M., O'Brien, C., & Hull, P. M. (2018). North Atlantic temperature and pCO_2 coupling in the early-middle Miocene. *Geology*, *46*(6), 519–522. https://doi.org/10.1130/G40228.1

Super, J. R., Thomas, E., Pagani, M., Huber, M., O'Brien, C. L., & Hull, P. M. (2020). Miocene Evolution of North Atlantic Sea Surface Temperature. *Paleoceanography and Paleoclimatology*, *35*(5), e2019PA003748. https://doi.org/10.1029/2019PA003748

Tanner, T., Hernández-Almeida, I., Drury, A. J., Guitián, J., & Stoll, H. (2020). Decreasing Atmospheric CO_2 During the Late Miocene Cooling. *Paleoceanography and Paleoclimatology*, *35*(12), e2020PA003925. https://doi.org/10.1029/2020PA003925

Taylor, K. W. R., Huber, M., Hollis, C. J., Hernandez-Sanchez, M. T., & Pancost, R. D. (2013). Re-evaluating modern and Palaeogene GDGT distributions: Implications for SST reconstructions. *Global and Planetary Change*, *108*, 158–174. https://doi.org/10.1016/j.gloplacha.2013.06.011

Thiede, J., & Myhre, A. M. (1996). The paleoceanographic history of the North Atlantic-Arctic gateways: Synthesis of the Leg 151 drilling results. *Proceedings of the Ocean Drilling Program, Scientific Results*, *151*.

Tierney, J. E., & Tingley, M. P. (2014). A Bayesian, spatially-varying calibration model for the TEX_{86} proxy. *Geochimica et Cosmochimica Acta*, *127*, 83–106. https://doi.org/10.1016/j.gca.2013.11.026

Tierney, J. E., & Tingley, M. P. (2018). BAYSPLINE: A New Calibration for the Alkenone Paleothermometer. *Paleoceanography and Paleoclimatology*, *33*(3), 281–301. https://doi.org/10.1002/2017PA003201

Uda, I., Sugai, A., Itoh, Y. H., & Itoh, T. (2001). Variation in molecular species of polar lipids from Thermoplasma acidophilum depends on growth temperature. *Lipids*, *36*(1), 103–105. https://doi.org/10.1007/s11745-001-0914-2

Verret, M., Trinh-Le, C., Dickinson, W., Norton, K., Lacelle, D., Christl, M., et al. (2023). Late Miocene onset of hyper-aridity in East Antarctica indicated by meteoric beryllium-10 in permafrost. *Nature Geoscience*, *16*(6), 492–498. https://doi.org/10.1038/s41561-023-01193-4

Wang, K. J., Huang, Y., Majaneva, M., Belt, S. T., Liao, S., Novak, J., et al. (2021). Group 2i Isochrysidales produce characteristic alkenones reflecting sea ice distribution. *Nature Communications*, *12*(1), 15. https://doi.org/10.1038/s41467-020-20187-z

Wang, Yang, Cerling, T. E., & MacFadden, B. J. (1994). Fossil horses and carbon isotopes: new evidence for Cenozoic dietary, habitat, and ecosystem changes in North America. *Palaeogeography, Palaeoclimatology, Palaeoecology*, *107*(3), 269–279. https://doi.org/10.1016/0031-0182(94)90099-X

Wang, Yuqing, Momohara, A., Wang, L., Lebreton-Anberrée, J., & Zhou, Z. (2015). Evolutionary History of Atmospheric CO_2 during the Late Cenozoic from Fossilized

Metasequoia Needles. *PLOS ONE*, *10*(7), e0130941. https://doi.org/10.1371/journal.pone.0130941

Warny, S., Askin, R. A., Hannah, M. J., Mohr, B. A. R., Raine, J. I., Harwood, D. M., et al. (2009). Palynomorphs from a sediment core reveal a sudden remarkably warm Antarctica during the middle Miocene. *Geology*, *37*(10), 955–958. https://doi.org/10.1130/G30139A.1

Warny, S., Kymes, C. M., Askin, R., Krajewski, K. P., & Tatur, A. (2019). Terrestrial and marine floral response to latest Eocene and Oligocene events on the Antarctic Peninsula. *Palynology*, *43*(1), 4–21. https://doi.org/10.1080/01916122.2017.1418444

Westerhold, T., Marwan, N., Drury, A. J., Liebrand, D., Agnini, C., Anagnostou, E., et al. (2020). An astronomically dated record of Earth's climate and its predictability over the last 66 million years. *Science*, *369*(6509), 1383–1387. https://doi.org/10.1126/science.aba6853

Willard, D. A., Donders, T. H., Reichgelt, T., Greenwood, D. R., Sangiorgi, F., Peterse, F., et al. (2019). Arctic vegetation, temperature, and hydrology during Early Eocene transient global warming events. *Global and Planetary Change*, *178*, 139–152. https://doi.org/10.1016/j.gloplacha.2019.04.012

Williams, C. J., Mendell, E. K., Murphy, J., Court, W. M., Johnson, A. H., & Richter, S. L. (2008). Paleoenvironmental reconstruction of a Middle Miocene forest from the western Canadian Arctic. *Palaeogeography, Palaeoclimatology, Palaeoecology*, *261*(1), 160–176. https://doi.org/10.1016/j.palaeo.2008.01.014

Witkowski, C. R., Von Der Heydt, A. S., Valdes, P. J., Van Der Meer, M. T. J., Schouten, S., & Sinninghe Damsté, J. S. (2024). Continuous sterane and phytane $\delta^{13}C$ record reveals a substantial pCO_2 decline since the mid-Miocene. *Nature Communications*, *15*(1), 5192. https://doi.org/10.1038/s41467-024-47676-9

Zachos, J., Pagani, M., Sloan, L., Thomas, E., & Billups, K. (2001). Trends, Rhythms, and Aberrations in Global Climate 65 Ma to Present. *Science*, *292*(5517), 686–693. https://doi.org/10.1126/science.1059412

Zhang, Y. G., Zhang, C. L., Liu, X.-L., Li, L., Hinrichs, K.-U., & Noakes, J. E. (2011). Methane Index: A tetraether archaeal lipid biomarker indicator for detecting the instability of marine gas hydrates. *Earth and Planetary Science Letters*, *307*(3), 525–534. https://doi.org/10.1016/j.epsl.2011.05.031

Zhang, Y. G., Pagani, M., Liu, Z., Bohaty, S. M., & DeConto, R. (2013). A 40-million-year history of atmospheric CO_2. *Philosophical Transactions of the Royal Society A: Mathematical, Physical and Engineering Sciences*, *371*(2001), 20130096. https://doi.org/10.1098/rsta.2013.0096

Zhang, Y. G., Pagani, M., & Liu, Z. (2014). A 12-Million-Year Temperature History of the Tropical Pacific Ocean. *Science*, *344*(6179), 84–87. https://doi.org/10.1126/science.1246172

Zhang, Y. G., Pagani, M., & Wang, Z. (2016). Ring Index: A new strategy to evaluate the integrity of TEX86 paleothermometry. *Paleoceanography*, *31*(2), 220–232. https://doi.org/10.1002/2015PA002848

Zhang, Y. G., Pagani, M., Henderiks, J., & Ren, H. (2017). A long history of equatorial deep-water upwelling in the Pacific Ocean. *Earth and Planetary Science Letters*, *467*, 1–9. https://doi.org/10.1016/j.epsl.2017.03.016

CHAPTER 2

North Pacific warmth synchronous with the Miocene Climatic Optimum

Jared E. Nirenberg[1] and Timothy D. Herbert[1]

[1]Department of Earth, Environmental, and Planetary Sciences, Brown University, Providence, Rhode Island 02912, USA

Published in 2024 in *Geology*

Abstract

Peak Neogene warmth and minimal polar ice volumes occurred during the Miocene Climatic Optimum (MCO, ~16.95-13.95 Ma), followed by cooling and ice sheet expansion during the Middle Miocene Climate Transition (MMCT, ~13.95-12.8 Ma). Previous records of northern high-latitude sea surface temperatures (SSTs) during these global climatic transitions are limited to Atlantic sites, and none resolve orbital-scale variability. Here, we present an orbital-resolution alkenone SST proxy record from the subpolar North Pacific that establishes a local maximum of SSTs during the MCO up to 16°C warmer than modern with rapid warming initiating the MCO, cooling synchronous with Antarctic ice sheet expansion during the MMCT, and high variability on orbital timescales. Persistently cooler North Pacific SST anomalies than Atlantic at equivalent latitudes throughout the Miocene suggest enhanced Atlantic northward heat transport under a globally warm climate. We conclude that a global forcing mechanism, likely elevated greenhouse gas concentrations, is the most parsimonious explanation for synchronous global high-latitude warmth during the Miocene.

Introduction

The Middle Miocene is distinguished as the major warm anomaly in the Cenozoic transition from global greenhouse conditions to the modern icehouse world (Westerhold et al., 2020). During the Miocene Climatic Optimum (MCO, ~16.95-13.95 Ma) ice sheets retreated, leaving Antarctica at least partially deglaciated and occupied with temperate and tundra ecosystems (Lewis et al., 2008; Warny et al., 2009). Cooling and ice sheet growth intensified during the Middle Miocene Climate Transition (MMCT, ~13.95-12.8 Ma), culminating in the reestablishment and expansion of the East Antarctic Ice Sheet during the Mi-3 glaciation (~13.8-

13.9 Ma, Miller et al., 1991). Outside of Antarctica, global ecosystems shifted from equable MCO conditions towards stronger meridional gradients and terrestrial aridity (Pound et al., 2012).

While qualitative warmth during the MCO and cooling during the MMCT are well-supported by geologic evidence, the quantitative evolution of global surface temperatures during these periods remains unclear. Benthic foraminiferal oxygen isotope records (benthic $\delta^{18}O$) have provided high-resolution information on global climate throughout the Early and Middle Miocene (Holbourn et al., 2014, 2015), but surface temperature proxy records at similar resolution are lacking. As a result of this gap, estimates of Middle Miocene global warmth range anywhere from ~5°C (Westerhold et al., 2020) to over 10°C above modern (Burls et al., 2021; Herbert et al., 2022).

Existing Northern Hemisphere SST records are limited to sites in the eastern North Atlantic and North Sea (Herbert et al., 2016, 2020; Super et al., 2020; Sangiorgi et al., 2021; Fig. 1). These sites are influenced by regional dynamics of the North Atlantic Current, so SSTs at these sites may not be representative of broader Miocene Northern Hemisphere temperatures. In addition, the temporal resolution of these records do not resolve orbital-scale SST variability. Higher resolution records from other regions are needed to constrain the Miocene evolution of Northern Hemisphere SSTs.

Here, we present high-resolution SST proxy data from the North Pacific spanning the entire MCO and MMCT. We measure the unsaturation ratios of alkenones ($U^{k'}_{37}$) from Ocean Drilling Program (ODP) Site 884 in the northwest Pacific (Rea et al., 1993; see Supplemental Materials for site description). $U^{k'}_{37}$ SST reconstructions are largely robust to species effects

(Villanueva et al., 2002), assumptions of past seawater chemistry, and methods of calibration to SST (Müller et al., 1998; Tierney & Tingley, 2018), and this proxy has been successfully applied to quantifying global mean annual SSTs in the Late Miocene (Herbert et al., 2016). High core recovery (>90%) and magnetic reversal stratigraphy (Table S1) provide a continuous and well-dated section for high-resolution records of the MCO and MMCT at Site 884 (see Supplemental Materials for age model). Our record extends continuous records of SSTs in the North Pacific to span the past 18 million years.

Results and Discussion

Our measurements of $U^{k'}_{37}$ at Site 884 provide a continuous high-resolution (6 kyr average sampling interval) record of SSTs in the subpolar North Pacific from 18.2 to 12.6 Ma, with lower resolution (54 kyr) data to 8.8 Ma. After column chromatography, alkenones were analyzed using gas chromatographic or high performance liquid chromatographic methods (see Supplemental Materials for analytical methods). $U^{k'}_{37}$ varied between 0.393 and 0.882, providing reconstructed SSTs between 10.6 and 25.4°C. We apply the calibration of Müller et al. (1998), though other choices of calibration do not significantly affect the reconstructed SSTs for the range of $U^{k'}_{37}$ obtained (Tierney & Tingley, 2018).

Previous work suggests seasonal biases in the modern application of the $U^{k'}_{37}$ proxy in the subpolar North Pacific, although the implications for Miocene interpretations are uncertain. The majority of alkenone production in the region occurs between July and November (Harada et al., 2006), which average 2.9°C warmer than mean annual SSTs at Site 884 (Huang et al., 2021). Regional core-top $U^{k'}_{37}$ correlates most strongly with June through August monthly SSTs

(Tierney & Tingley, 2018), which are 2.3°C warmer than mean annual SSTs at Site 884 (Huang et al., 2021).While winter light limitation was similar, differences in the seasonal variation of SSTs and nutrient availability between the Miocene and modern are unknown, complicating any assumption of similar biases in $U^{k'}_{37}$ as well.

In addition, alkenone concentrations were strongly anti-correlated with $U^{k'}_{37}$, with warmer proxy values corresponding to exponentially lower alkenone concentrations (Fig. S1). Our Miocene anti-correlation implies higher production of alkenones associated with cooler temperatures at Site 884, potentially biasing reconstructed SSTs towards colder values. Because of conflicting directions for potential biases, we interpret $U^{k'}_{37}$ at Site 884 as representative of mean annual SSTs during the Miocene, though we acknowledge the potential for some bias (<3°C) towards warmer seasonal temperatures.

Early-Middle Miocene temperature evolution in the North Pacific

We find a pronounced SST maximum in the North Pacific synchronous within age uncertainties to the MCO as defined by benthic $\delta^{18}O$ records (Holbourn et al., 2014, 2015). Long-term mean temperatures during the MCO peak above 22°C, over 16°C warmer than the modern mean annual SST at Site 884. Though changes in SSTs at high-latitudes were likely amplified compared to the global mean (Liu et al., 2022), these temperatures are more consistent with high-end estimates of MCO global warmth of at least 10°C warmer than modern (Herbert et al. 2022 ~12°C; Burls et al. 2021 ~11.5°C) than more modest estimates (Westerhold et al., 2020 ~5°C).

The coincident timing of Miocene warmth and subsequent cooling in the North Pacific with analogous changes in benthic $\delta^{18}O$ establishes a globally synchronous evolution of Miocene ocean temperatures. The benthic $\delta^{18}O$ signal originates from the Southern high-latitudes as the source of both bottom water formation and terrestrial ice volume during the Early-Middle Miocene (Shevenell et al., 2008), controlling both deep sea temperatures and seawater $\delta^{18}O$. Geologic records from Antarctica and the polar Southern Ocean (Lewis et al., 2008; Pierce et al., 2017; Warny et al., 2009) corroborate reduced MCO ice volume and ice sheet expansion during the MMCT interpreted from benthic $\delta^{18}O$ (Holbourn et al., 2014, 2015). While previous temperature records have found high-latitude cooling events during the MMCT, either preceding or coincident with the Mi-3 glaciation between 13.8 and 14.2 Ma (Sangiorgi et al., 2021; Shevenell et al., 2004; Super et al., 2020), ours captures the significant warming at the onset of the MCO as well as MMCT cooling in a continuous record at a single site.

In light of ice-distal SST records from both the North Atlantic and North Pacific, the Miocene decay and subsequent growth of ice sheets in Antarctica cannot be attributed primarily to regional dynamics (Hou et al., 2023; Shevenell et al., 2008) but rather as part of global temperature changes. Direct ice sheet feedbacks (ice-albedo, positions of Southern Hemisphere frontal zones, etc.) from the Antarctic would be insufficient to explain high-latitude warmth in both the North Pacific and North Atlantic. Changes in greenhouse gas concentrations likely provided this global forcing, though direct evidence for synchronous changes in atmospheric pCO_2 proxy records have yielded widely varying results (The Cenozoic CO_2 Proxy Integration Project (CENCO$_2$PIP) Consortium, 2023 and references therein; Fig. 2A). While pCO_2 proxies show a local maximum coinciding with the MCO, the increase in atmospheric pCO_2 appears to lag the increase in SSTs at Site 884 and benthic $\delta^{18}O$ (Fig. 2). However, we caution this may be an artifact of low pCO_2 proxy data density covering the Early Miocene before the MCO. The eruption of the Columbia River Flood Basalts is often considered the source of this inorganic carbon to the ocean-atmosphere system (Holbourn et al., 2015; Sosdian et al., 2020), but this mechanism is challenged by the later timing of eruptions with respect to warming (Kasbohm & Schoene, 2018) and questions regarding the ability for these emissions to cause such long-sustained (~3 Myr) warmth. While flood volcanism may have contributed to peak warmth early during the MCO, elevated tectonic degassing (Herbert et al., 2022) provides a more sustained mechanism of greenhouse gas emissions on million-year timescales. The beginning of long-term cooling after 15 Ma aligns with declining seafloor spreading rates (Fig. S2). Slowing mantle degassing could explain the initiation of cooling, culminating in passing a glaciation threshold (DeConto et al., 2008) during the Mi-3 glaciation. However, our temperature records alone cannot distinguish between the importance of reductions in CO_2 sources to the atmosphere and increasing weathering sinks, such as the uplift of highly weatherable silicates in the tropics (Park et al., 2020). Changes in carbon cycling within the ocean-atmosphere system (Holbourn et al., 2015) were associated with climate variability on shorter timescales (10-100s kyr) imposed on these longer-term (Myr) tectonic forcings.

High resolution records reveal rapid transitions and orbital-scale variability

Our high-resolution data reveal rapid warming at the beginning of the MCO as well as cooling synchronous with East Antarctic Ice Sheet expansion during the MMCT. SSTs at Site 884 warm over 7°C within 50 kyr after 17 Ma (Fig. 3), shorter than tectonic processes could force. Although our reported timing of this warming is younger than that observed in the benthic $\delta^{18}O$ records (Holbourn et al., 2015), we interpret these as synchronous within error of our age model (Supplemental Material). In addition, SSTs in the North Pacific cool 4°C after 14 Ma, though a gap in sediment recovery between cores prevents precise determination of the duration of cooling. This cooling event aligns with the abrupt expansion of the East Antarctic Ice Sheet observed in Antarctic geologic records (Lewis et al., 2008; Pierce et al., 2017) and in benthic $\delta^{18}O$ records (Holbourn et al., 2014; Shevenell et al., 2004), as well as decreasing atmospheric pCO_2 observed in some proxy records (Badger et al., 2013; Raitzsch et al., 2021; Witkowski et al., 2024).

North Pacific SSTs during the MCO were highly variable, with glacial-interglacial cycles up to 6°C in amplitude (Fig. 3) and a longer cooler interval surrounding the Mi-2 glaciation (Miller et al., 1991) after 16 Ma (Fig. 2). Significant periodicities correspond to orbital frequencies near eccentricity (109 kyr, 99% confidence level) and obliquity (43 kyr, 90% confidence level) across the high-resolution record (Fig. S3). The large amplitude of orbital-scale temperature variability, particularly during the MCO, is consistent with large variability found in contemporaneous $\delta^{18}O$ (Holbourn et al., 2014, 2015), atmospheric pCO_2 proxies (Greenop et al., 2014), and Antarctic ice sheet extent (Levy et al., 2016) on orbital timescales. Our record confirms that temperature variability in the high-latitudes distant from Southern Hemisphere ice sheets accompanied these changes as well.

Enhanced North Atlantic Current during Miocene global warmth

To assess the context of North Pacific temperatures within the Northern subpolar regions, we compile Miocene $U^{k'}_{37}$ records from sites between 50 and 60°N (Herbert et al., 2016, 2020; Super et al., 2020; Sangiorgi et al., 2021; Fig. 4; Fig S4). SST anomalies in the North Atlantic relative to modern mean annual SST were persistently higher than in the North Pacific throughout the Miocene, resulting in a larger than modern gradient between the basins. While the gradient appears to reduce during the MCO, we caution that this may be an artifact of proxy saturation ($U^{k'}_{37}$ approaches 1) at North Atlantic sites. The proxy response to further SST variability at these high temperatures is likely truncated, whereas North Pacific $U^{k'}_{37}$ is much further from saturation. Because reconstructed SSTs in the North Atlantic depend more on the choice of linear (Müller et al., 1998) or non-linear (Tierney & Tingley, 2018) calibrations, our reconstructed inter-basin gradient has higher uncertainty during the MCO.

The gradient between North Pacific and North Atlantic SST anomalies (Fig. 4) suggests persistent differences in poleward oceanic heat transport between the two basins. While the modern North Atlantic is warmer than the North Pacific due to the greater poleward influence of the North Atlantic Current (NAC) compared to the North Pacific Current (Fig. 1), these differences were enhanced throughout the Miocene (Fig. S5). Super et al. (2020) hypothesized an invigorated NAC as responsible for extreme North Atlantic warmth, extending into the mid-latitudes as well, and our North Pacific record confirms this warmth was exaggerated in the Atlantic basin. These proxy records contradict predictions from model simulations (Burls et al., 2021) of a reduced or even reversed Miocene temperature gradient between the northern ocean basins (Fig. S6). A stronger inter-basin gradient during the Miocene, when the Central American Seaway was open, also challenges the idea of a weaker NAC prior to its closure during the Pliocene (Haug & Tiedemann, 1998). While these paleotemperature records alone cannot directly rule out effects of other possible mechanisms, such as cloud radiative feedbacks and atmospheric heat transport, greater northward oceanic heat transport in the Atlantic basin provides a compelling potential mechanism for enhanced Miocene warmth observed in the North Atlantic.

Conclusions

Our high-resolution SST proxy record spanning the entire MCO and MMCT at a single site extends our understanding of continuous temperature evolution in the North Pacific over the past 18 million years. Elevated temperatures in the Northern high-latitudes coincide with minimal Antarctic Ice Sheet volumes and higher bottom water temperatures, showing that the MCO was a globally synchronous climate interval in the high-latitudes. The bipolar nature of warmth between about 17 and 14 Ma suggests a global forcing mechanism, likely elevated greenhouse gas concentrations, though proxy constraints on these concentrations vary widely (CENCO$_2$PIP Consortium, 2023). The coincidence of high SST variability on orbital timescales in the North Pacific with similarly large variations in benthic $\delta^{18}O$ implies either large changes in atmospheric pCO_2 on these timescales or high sensitivity of Miocene climate to smaller changes in greenhouse gas concentrations or orbital forcing. While high-resolution temperature records from more regions are needed to assess the global pattern and magnitude of temperature variability, the synchronous timing of Early-Middle Miocene warmth in both the North Pacific and Antarctic provides strong circumstantial evidence for a common forcing.

Acknowledgements

This study used samples and data provided by the International Ocean Discovery Program (IODP) and its predecessors. Funding for this research was provided by NSF Grants 1635127 and 2202760 to Herbert. We thank Jonah Bernstein-Schalet, Emily Clements, and Sofía Gilroy for their assistance in sample extraction and preparation.

Figures

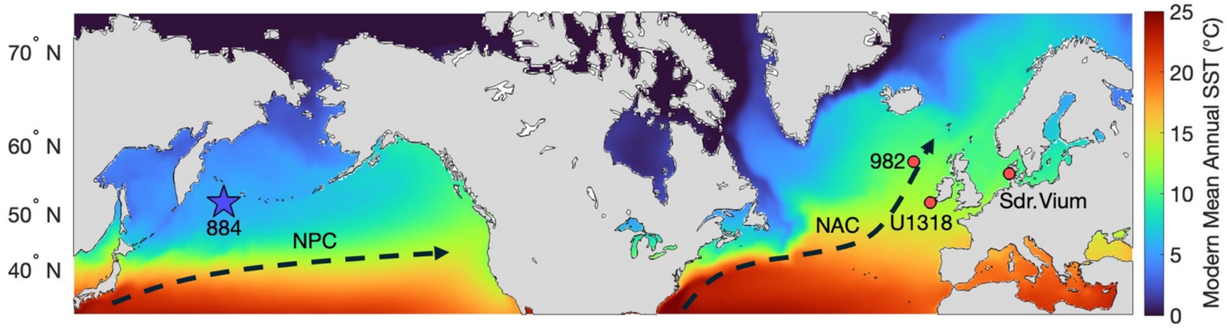

Figure 1. Site locations of Northern subpolar $U^{k'}_{37}$ records during the Early-Middle Miocene. Data from ODP Site 884 (blue star) was generated in this study and from Herbert et al., (2016). Data from ODP Site 982, IODP Site U1318, and Sdr. Vium (red circles) are from Herbert et al. (2016; 2020), Sangiorgi et al. (2021), and Super et al. (2020). Generalized paths of the North Atlantic Current (NAC) and North Pacific Current (NPC) are shown as dashed arrows.

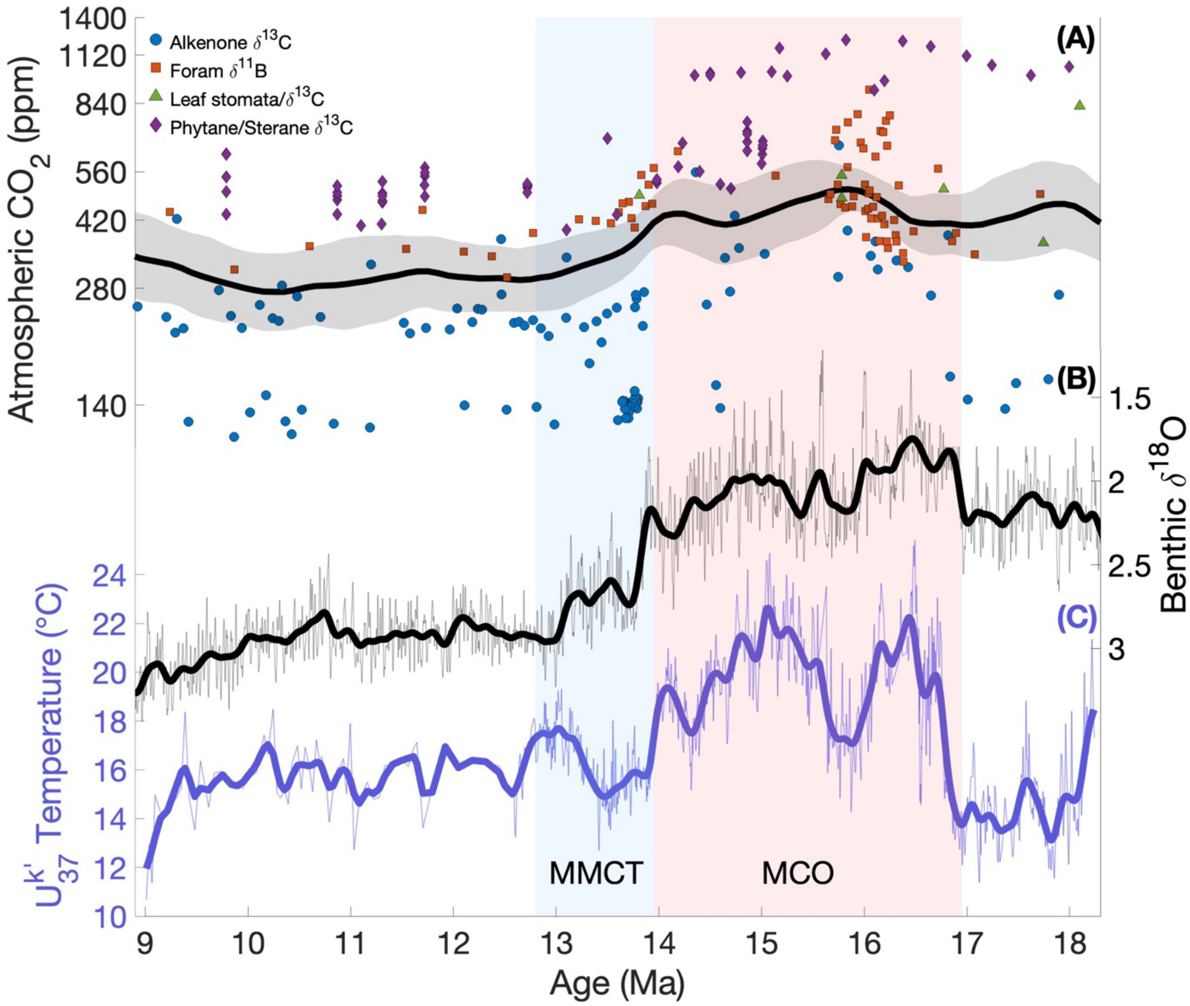

Figure 2. (A) Category 1 pCO_2 proxy estimates and 100 kyr smoothed average (black line) from CENCO$_2$PIP Consortium, (2023) along with phytane and sterane data from Witkowski et al., (2024). (B) Benthic $\delta^{18}O$ from Westerhold et al. (2020). (C) Alkenone-derived SSTs produced in this work from ODP Site 884. Individual data (thin line) are shown along with a Gaussian-weighted smoothed average (thick line).

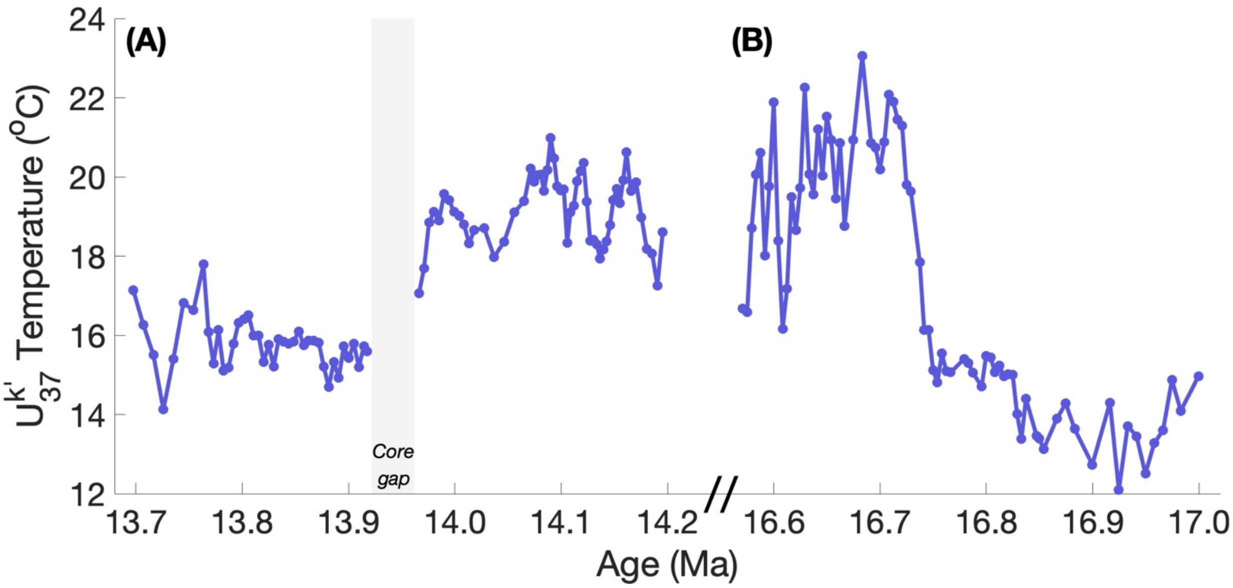

Figure 3. High-resolution alkenone-derived SSTs from ODP Site 884 during two key climatic transitions. (A) Mi-3 glaciation during the MMCT, where SSTs cool ~4°C after 14 Ma and (B) the onset of the MCO, when SSTs abruptly warm ~7°C after 17 Ma. Discrepancies between the timing of these transitions and those in benthic $\delta^{18}O$ are within the error of the age model for Site 884.

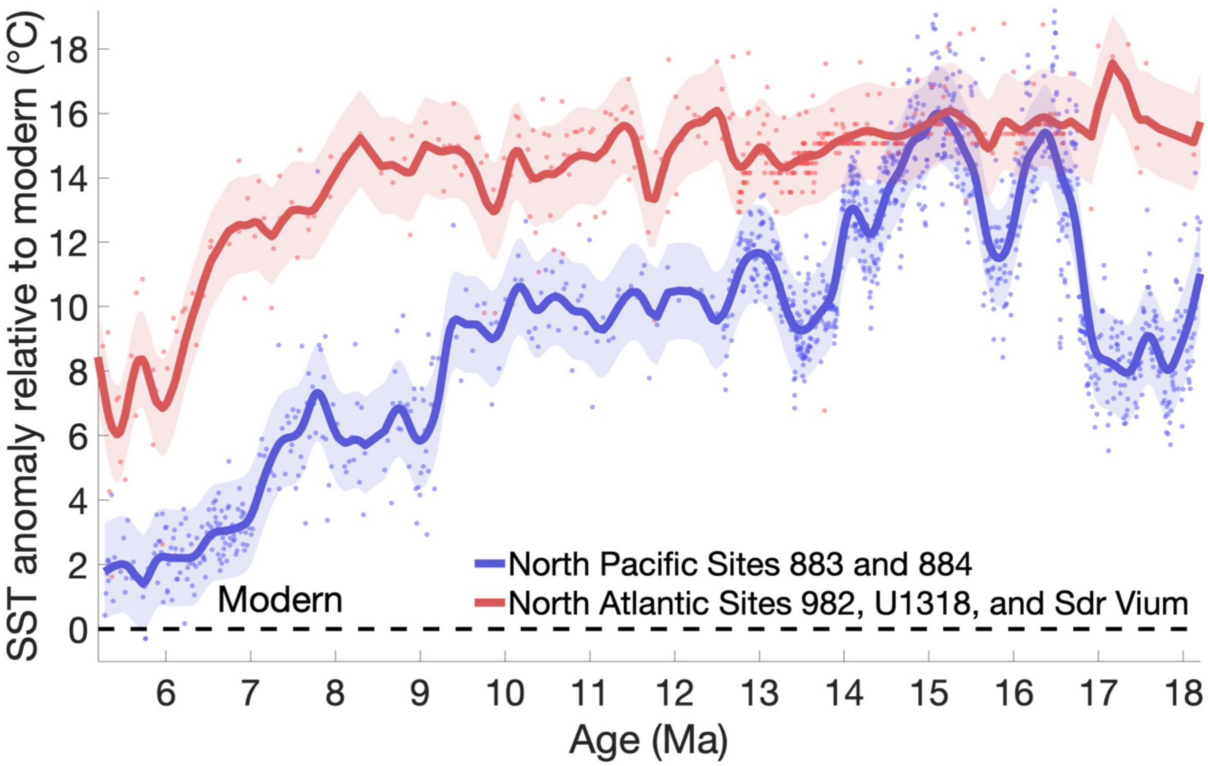

Figure 4. Miocene SST anomalies relative to modern mean annual SSTs for high-latitude Northern Hemisphere sites. Data from ODP Sites 883 and 884 are from this study and Herbert et al. (2016). Data from ODP Site 982, IODP Site U1318, and borehole Sdr. Vium are from Herbert et al. (2016; 2020), Sangiorgi et al. (2021), and Super et al. (2020). Individual data are shown as points with a Gaussian-weighted smoothed average.

Supplementary Information

Alkenone analytical methods

Between 3 and 10 grams of dry sediment were extracted using a Dionex Accelerated Solvent Extractor 350 with 3 static cycles at 150°C and 1600 psi using a solvent mixture of 9:1 dichloromethane:methanol. The total lipid extracts were separated using flash silica gel column chromatography through eluting with 4 mL hexane, dichloromethane, and methanol. The dichloromethane fraction was then further separated chromatographically into saturated and unsaturated fractions using 10% silver nitrate on silica gel and eluting with 8 mL dichloromethane and then 4 mL ethyl acetate, respectively. The unsaturated fraction, containing the alkenones, was then evaporated under N_2 and redissolved in toluene containing internal standards of *n*-hexatriacontane and *n*-heptatriacontane for quantification.

The samples were analyzed using an Agilent 7890 or 8890 gas chromatograph with a flame ionization detector (GC-FID), equipped with an Agilent DB-1 column (60 m length, 0.32 mm diameter, 0.10 μm film thickness). The oven ramp was as follows: hold at 90°C for 2 minutes, ramp to 255°C at 40°C/min, ramp to 300°C at 1°C/min, ramp to 320°C at 10°C/min, and hold at 320°C for 11 minutes. The PTV inlet ramp was as follows: hold at 110°C for 0.85 minutes, ramp to 290°C at 720°C/min, hold for 5 minutes, ramp to 320°C at 720°C/min, and hold at 320°C. Alkenone peaks were assigned through comparison with a laboratory standard, and all data was screened to ensure sufficient peak areas and chromatographic separation from other matrix compounds. In-house laboratory alkenone standards were measured before, during, and after each run to ensure data quality, and only data from runs with standard reproducibility within 0.01 $U^{k'}_{37}$ units, or about 0.3°C according to the calibration of Müller et al. (1998), were used. About 30% of samples have replicate measurements, which were generally within 0.01 $U^{k'}_{37}$ units, or about 0.3°C.

A small number of samples (~5% of total) were unable to produce reliable alkenone quantification using GC-FID due to low alkenone concentrations below the limit of detection and/or poor separation of alkenones from other matrix compounds even after column chromatography. These samples were analyzed using high-performance liquid chromatography with mass spectrometry (HPLC-MS) using the method of Liao et al., (2023). Briefly, alkenones were dissolved in acetone and separated using a Zorbax Eclipse PAH column (2.1 by 100 mm by 3.5 μm) using the solvent scheme of Liao et al., (2023). Masses of ammonia-adducts to alkenones (m/z 547 and 549) were monitored using selected ion monitoring (SIM). Alkenone peaks were integrated in SIM chromatograms, and the $U^{k'}_{37}$ derived from the HPLC peak areas were calibrated to FID $U^{k'}_{37}$ using a set of 10 standards of known $U^{k'}_{37}$ between 0.1 and 0.9 using a quadratic fit. Using this calibration method, the reproducibility of the laboratory alkenone standard was within 0.01 $U^{k'}_{37}$ units, or about 0.3°C. Selected samples which produced good quality data using GC-FID were also ran using HPLC-MS and produced statistically indistinguishable $U^{k'}_{37}$ between the two methods.

Site description and age model

ODP Site 884 was drilled on the eastern flank of the Detroit Seamount at 51°27'N, 168°20'E and 3836 m water depth (Rea et al., 1993). The modern (1990-2021) mean annual SST is 5.8°C with monthly averages between 2.8 and 10.6°C (Huang et al., 2021). Tectonic backtracking places the site near 48°N, 177°E at 15 Ma, with a modern mean annual SST of

6.5°C (Herbert et al., 2016). Core recovery was between 92.7% and 104% throughout the sections studied, though gaps between cores prevented the recovery of a complete stratigraphy. The lack of continuous presence of benthic foraminifera in the siliceous sediments at Site 884 prevents direct stratigraphic correlation between our alkenone records and benthic isotope records from other sites. Instead, age controls were provided by paleomagnetic reversals guided by diatom biostratigraphy (Barron & Gladenkov, 1995). The magnetic reversal stratigraphy was revised here (Table S1), and reversal ages were assigned according to APTS 2012 (Hilgen et al., 2012). Age estimates carry uncertainties on the order of 100 kyr for most sections. The sedimentation rate over the period sampled varied between 0.59 and 3.23 cm per kyr with an average of 1.87 cm per kyr.

The age model for Site 884 was constructed using linear interpolation between observed paleomagnetic reversals, as described in Barron & Gladenkov (1995) and revised here (Table S1). The assignment of specific magnetic chrons to observed reversals were informed by biostratigraphy and correlation with ODP Site 887 in the Northeastern Pacific (Rea et al., 1993). Ages for paleomagnetic reversals were assigned using APTS 2012 (Hilgen et al., 2012).

Not all magnetic reversals expected in the section were observed, particularly during the MCO interval. Reversals in Chrons C5Dr through C5Bn.2n were not observed at Site 884, which we interpret as due to the lithology of this section, with very high biogenic silica and low magnetic susceptibility, rather than stratigraphic discontinuity. The identification of a complete sequence of all Neogene North Pacific diatom zones in Hole 884B (Barron & Gladenkov, 1995) also supports continuous deposition throughout the section despite lacking evidence of some reversals. Reversals between Chrons C5Cn.1n through C5Cr were not observed due to the lack of reported magnetic measurements from Core 64X. For both of these intervals, our age model interpolates between the closest observed reversals above and below using a constant sedimentation rate, and we note that age estimates during these intervals are associated with higher uncertainties than the rest of the section. The base of Chron C5En was not observed, providing a maximum possible age for the bottom of the section, and ages below the lowest observed reversal were estimated by extrapolating the sedimentation rate directly above.

The presence of 7 gaps between the 8 cores studied at high-resolution here also prevented a continuous sequence of expected magnetic reversals. In contrast to the interpretation of Barron & Gladenkov (1995), we interpret the bases of chrons C5Ar.1n and C5Ar.2r as missing in the core gap between cores 57X and 58X. This shifts our reversal assignments above as well, which produces less variable implied sedimentation rates on the relatively short (~100 kyr) timescales between these reversals. The base of chron C5ABr is missing in the core gap between cores 59X and 60X, so a depth was not assigned.

Calculation of SST anomalies

Miocene SST anomalies for each site were calculated relative to the modern mean annual SST at the current site location. Modern mean annual SSTs were calculated using monthly averaged data between 1990 and 2021 from NOAA OISST v2.1 (Huang et al., 2021). The modern mean annual SST for each site was calculated by interpolating from the 0.25° by 0.25° gridded data. For the site Sdr. Vium, which is currently above sea level, the mean annual SST at the nearest grid point was used for the calculations of SST anomalies. In Figure 4, site-specific SST anomalies were calculated for each North Atlantic site prior to smoothing to remove the effects of differences in modern mean annual SSTs when comparing to Miocene $U^{k'}_{37}$ SST reconstructions.

Supplementary figures and tables

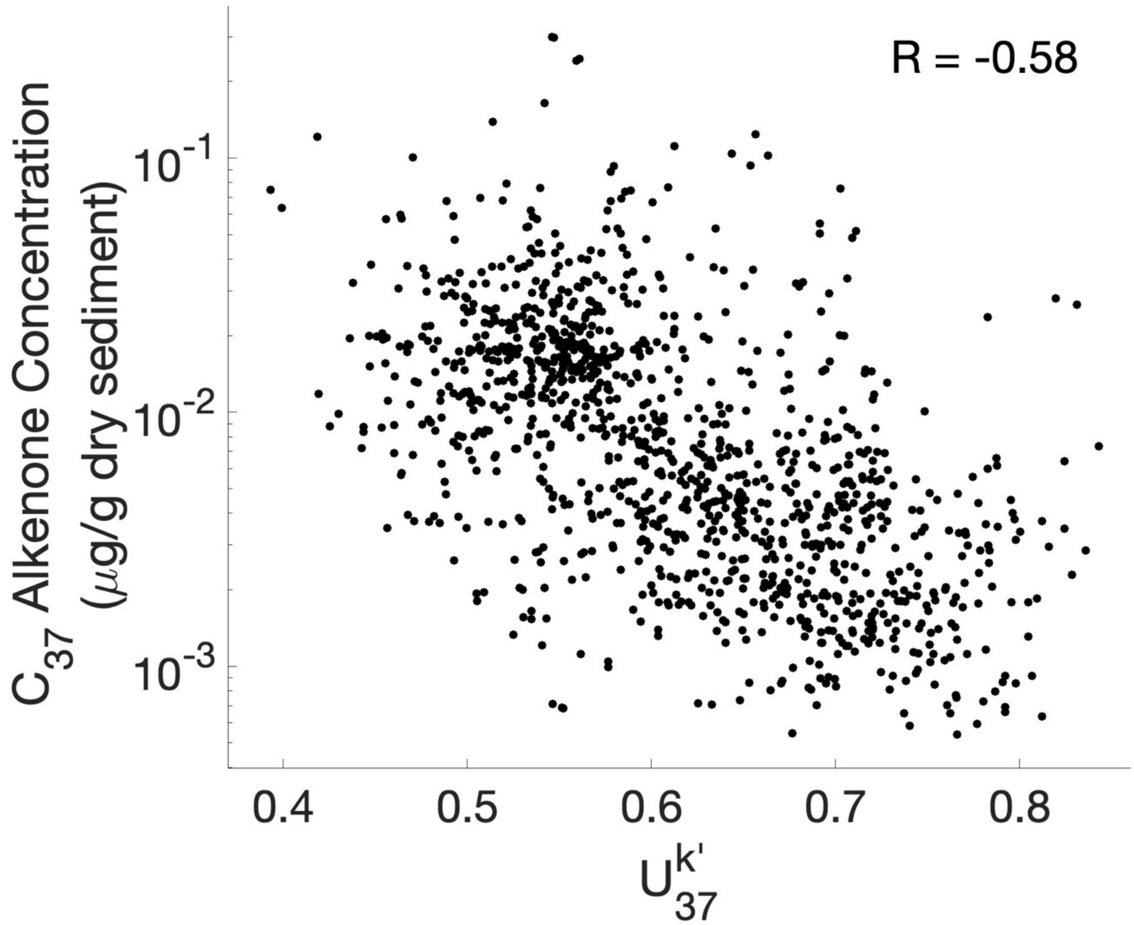

Figure S1. Concentrations of C_{37} alkenones versus $U^{k'}_{37}$ for every sample measured using GC-FID from Site 884 in this study. Log_{10} of alkenone concentrations show a statistically significant ($p<<0.001$) negative linear correlation with $U^{k'}_{37}$.

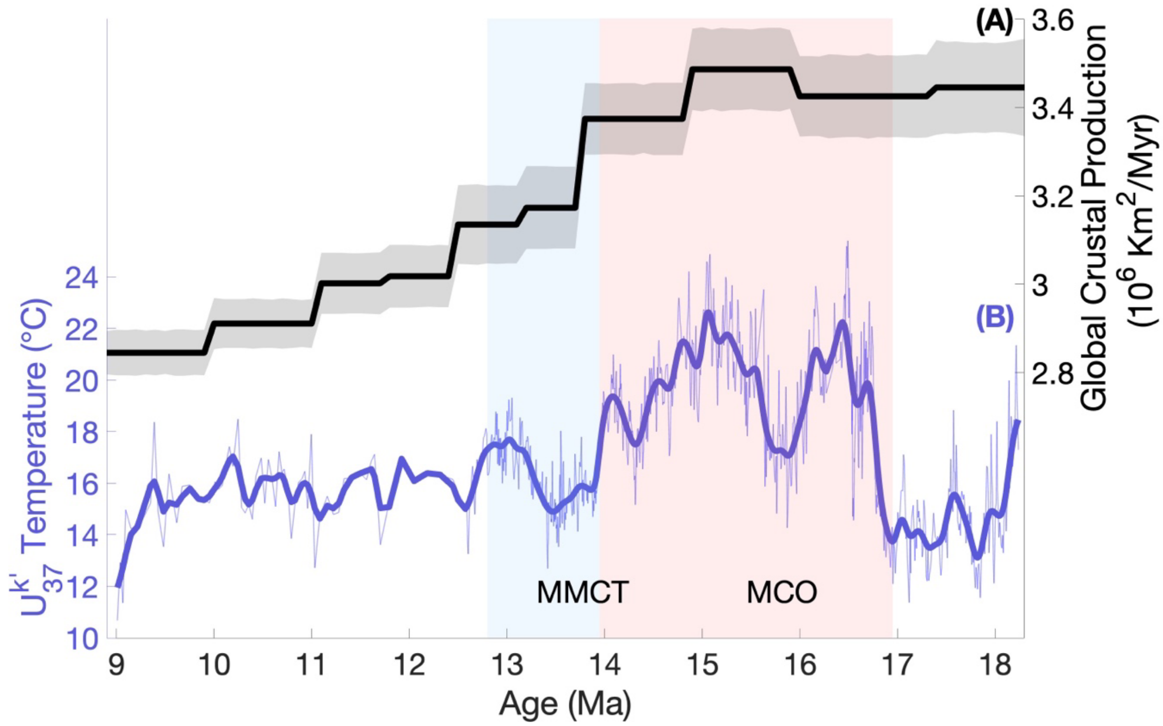

Figure S2. (A) Global oceanic crustal production rates from Dalton et al. (2022). Mean values are shown as black line while upper and lower limits of uncertainty as shaded areas. (B) Alkenone-derived SSTs produced in this work from ODP Site 884. Individual data and the smoothed average are shown using a Gaussian-weighted smoothed average with a standard deviation of 50 kyr.

(A)

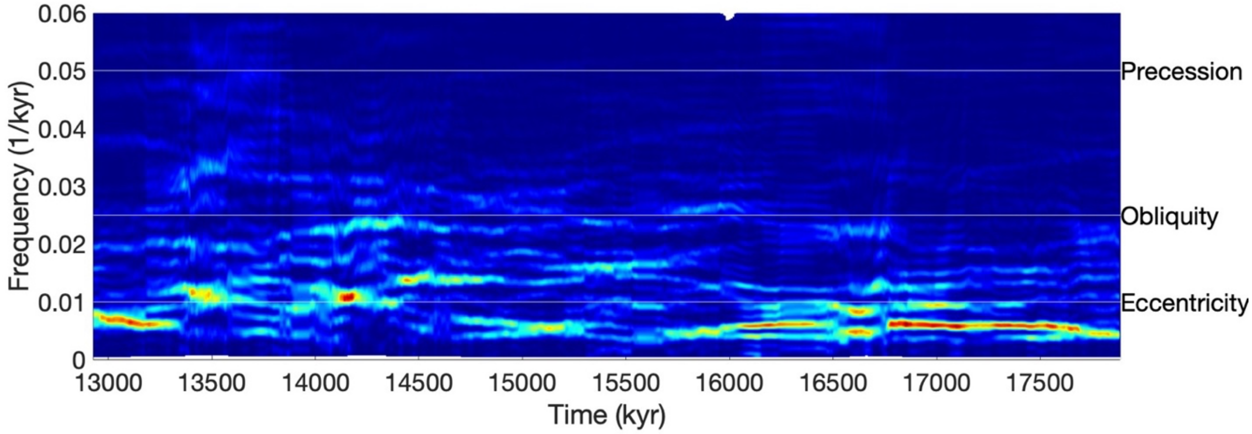

(B)

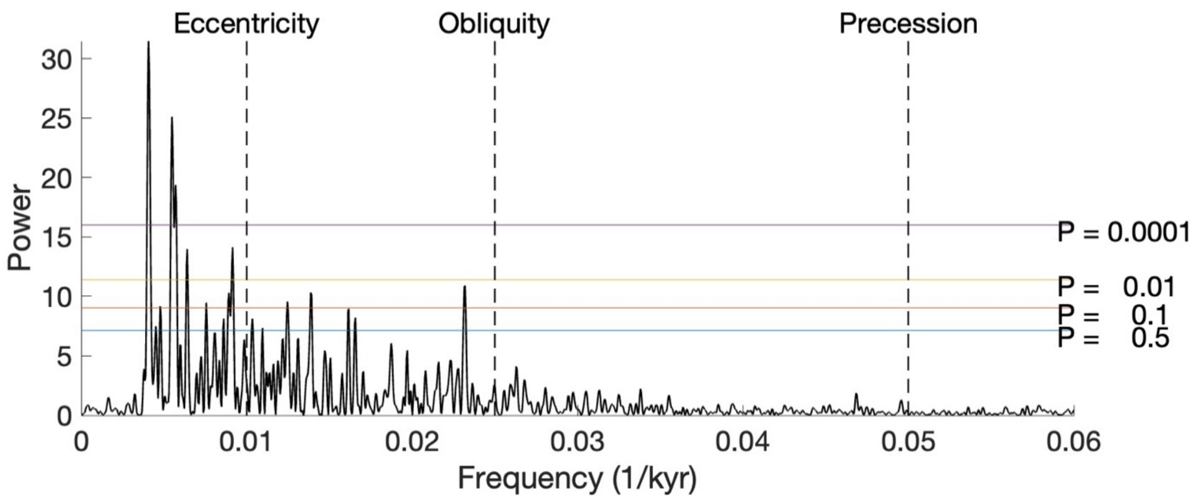

Figure S3. Spectral analysis of high-resolution alkenone SSTs at Site 884. (A) Evolutive Lomb-Scargle spectrum of our high-resolution $U^{k'}_{37}$ record between 12.575 and 18.240 Ma at Site 884 using a moving window of 90 points. Data were filtered using a low-pass filter to remove frequencies with periods longer than 250 kyr prior to analysis. (B) Lomb-Scargle peridogram for the entire high-resolution record. Significant (>90% confidence level) frequencies across the entire record had periods of 246 kyr (99.99% confidence), 182 kyr (99.99% confidence), 175 kyr (99.99% confidence), 156 kyr (99% confidence), 132 kyr (90% confidence), 112 kyr (90% confidence), 109 kyr (99% confidence), 80 kyr (90% confidence), 72 kyr (90% confidence), 60 kyr (90% confidence), and 43 kyr (90% confidence). Spectra were generated from code modified from Trauth (2021).

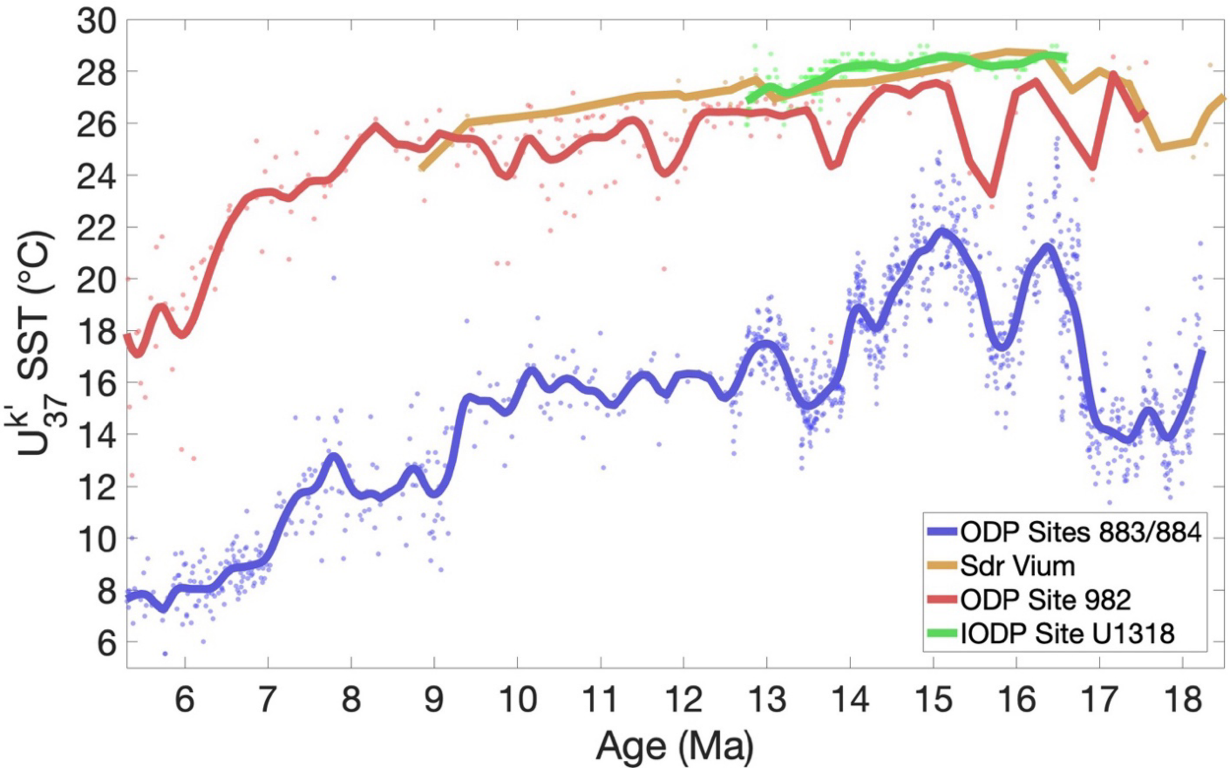

Figure S4. SSTs from Miocene $U^{k'}_{37}$ (calibration of Müller et al., 1998) from Northern subpolar sites (50-60ºN) compiled in this study. Individual sample SSTs are shown as points, and long-term smoothed averages (Gaussian-weighted, standard deviation of 120 kyr) are shown as lines. North Atlantic SSTs from Sdr Vium (Herbert et al., 2020), ODP Site 982 (Herbert et al., 2016; Super et al., 2020), and IODP Site U1318 (Sangiorgi et al., 2021) are persistently greater than North Pacfic SSTs from ODP Sites 883 and 884 (this study and Herbert et al., (2016).

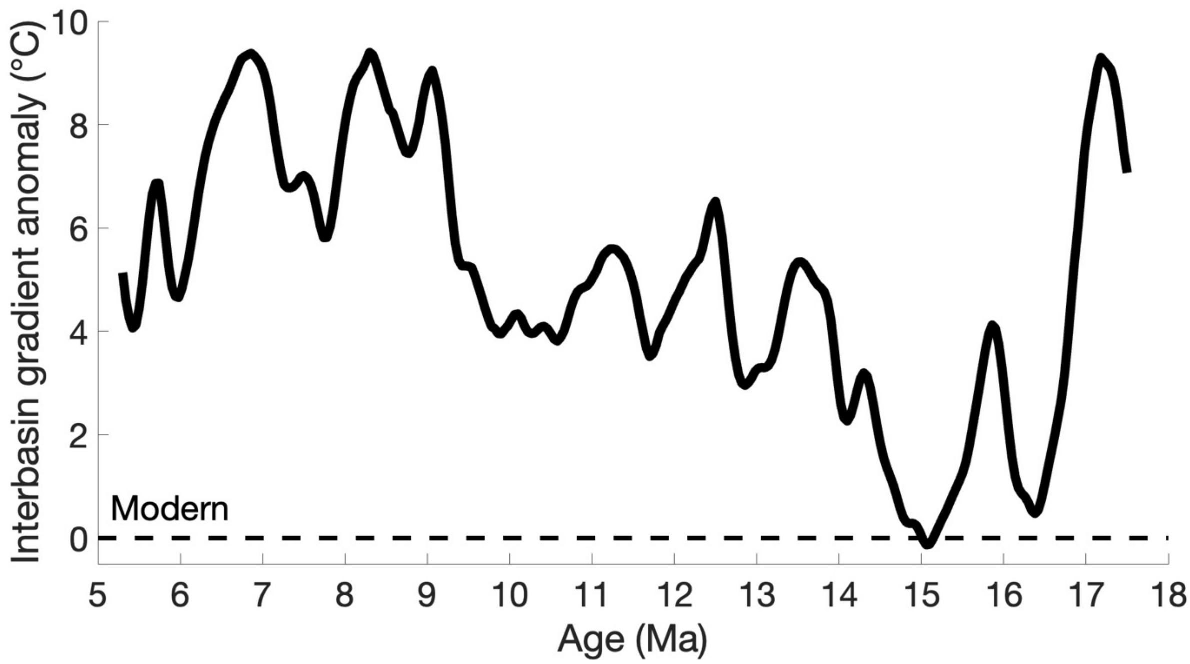

Figure S5. Change in the North Atlantic-North Pacific subpolar SST gradient relative to modern between 5.3 and 18.2 Ma, calculated as the difference between the Gaussian-weighted smoothed averages with a standard deviation of 120 kyr of our North Atlantic and Pacific compilations (Fig. 4). The near-modern gradient found during the MCO is associated with the greatest uncertainty due to the near-saturation of the $U^{k'}_{37}$ proxy at the North Atlantic sites.

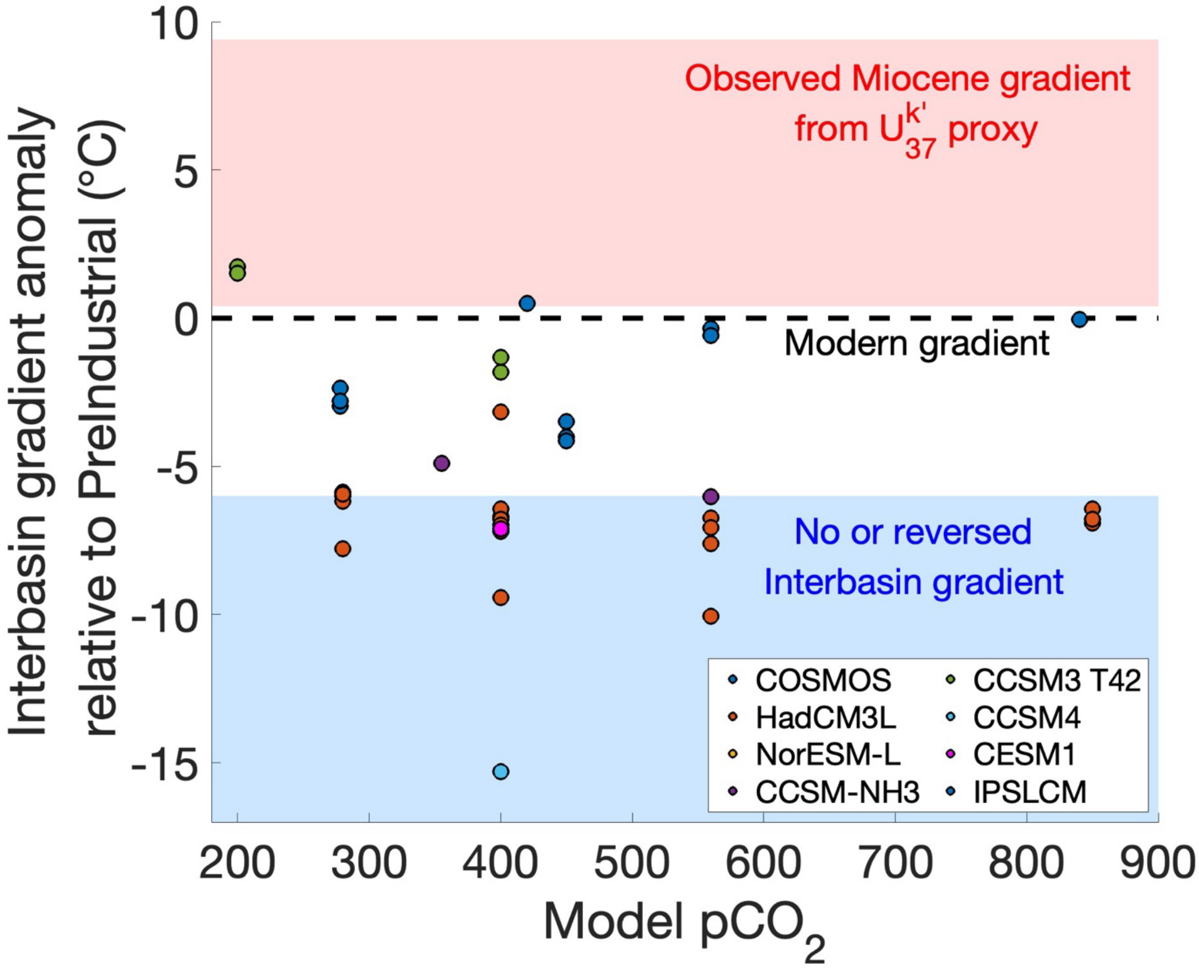

Figure S6. Difference in calculated North Atlantic-North Pacific subpolar SST gradient observed in MioMIP1 models (Burls et al., 2021) over the modeled atmospheric pCO_2. The gradients were calculated using the same site locations as $U^{k'}_{37}$ proxy records, and is either near or lower than modern for Miocene simulation, independent of atmospheric CO_2 concentrations used in the simulations.

Table S1. Revised magnetostratigraphy for ODP Site 884.

Polarity Chron	Depth of base (mbsf)	APTS 2012 Age (Ma)
C4r.2r	418.45	8.771
C4An	436.15	9.105
C4Ar.1r	440.65	9.311
C4Ar.1n	445.2	9.426
C4Ar.2r	451.1	9.647
C4Ar.2n	453.1	9.721
C4Ar.3r	453.5	9.786
C5n.1n	457.3	9.937
C5n.1r	458.75	9.984
C5n.2n	502.5	11.056
C5r.2r	513	11.592
C5r.2n	516	11.657
C5r.3r	520.6	12.049
C5An.1n	522	12.174
C5An.1r	523.1	12.272
C5An.2n	525.4	12.474
C5Ar.1r	528.9	12.735
C5Ar.2n	529.8	12.887
C5Ar.3r	531	13.032
C5AAn	532.1	13.183
C5AAr	535	13.363
C5ABn	542.3	13.608
C5ACn	547.2	14.07
C5ACr	550.2	14.163
C5ADn	559.1	14.609
C5Br	580.3	15.985
C5Dn	598.9	17.533
C5Dr.1r	600.2	17.717
C5Dr.1n	600.45	17.74
C5Dr.2r	602.6	18.056

References

Badger, M. P. S., Lear, C. H., Pancost, R. D., Foster, G. L., Bailey, T. R., Leng, M. J., & Abels, H. A. (2013). CO_2 drawdown following the middle Miocene expansion of the Antarctic Ice Sheet. *Paleoceanography*, *28*(1), 42–53. https://doi.org/10.1002/palo.20015

Barron, J., & Gladenkov, A. (1995). Early Miocene to Pleistocene Diatom Stratigraphy of Leg 145. *Proceedings of the Ocean Drilling Program, Scientific Results*, *145*. https://doi.org/10.2973/odp.proc.sr.145.101.1995

Burls, N. J., Bradshaw, C. D., De Boer, A. M., Herold, N., Huber, M., Pound, M., et al. (2021). Simulating Miocene Warmth: Insights From an Opportunistic Multi-Model Ensemble (MioMIP1). *Paleoceanography and Paleoclimatology*, *36*(5), e2020PA004054. https://doi.org/10.1029/2020PA004054

Cenozoic CO_2 Proxy Integration Project (CENCO$_2$PIP) Consortium. (2023). Toward a Cenozoic history of atmospheric CO_2. *Science*, *382*(6675), eadi5177. https://doi.org/10.1126/science.adi5177

DeConto, R. M., Pollard, D., Wilson, P. A., Pälike, H., Lear, C. H., & Pagani, M. (2008). Thresholds for Cenozoic bipolar glaciation. *Nature*, *455*(7213), 652–656. https://doi.org/10.1038/nature07337

Greenop, R., Foster, G. L., Wilson, P. A., & Lear, C. H. (2014). Middle Miocene climate instability associated with high-amplitude CO_2 variability. *Paleoceanography*, *29*(9), 845–853. https://doi.org/10.1002/2014PA002653

Harada, N., Sato, M., Shiraishi, A., & Honda, M. C. (2006). Characteristics of alkenone distributions in suspended and sinking particles in the northwestern North Pacific.

Geochimica et Cosmochimica Acta, *70*(8), 2045–2062. https://doi.org/10.1016/j.gca.2006.01.024

Haug, G. H., & Tiedemann, R. (1998). Effect of the formation of the Isthmus of Panama on Atlantic Ocean thermohaline circulation. *Nature*, *393*(6686), 673–676. https://doi.org/10.1038/31447

Herbert, T. D., Lawrence, K. T., Tzanova, A., Peterson, L. C., Caballero-Gill, R., & Kelly, C. S. (2016). Late Miocene global cooling and the rise of modern ecosystems. *Nature Geoscience*, *9*(11), 843–847. https://doi.org/10.1038/ngeo2813

Herbert, T. D., Rose, R., Dybkjær, K., Rasmussen, E. S., & Śliwińska, K. K. (2020). Bihemispheric Warming in the Miocene Climatic Optimum as Seen From the Danish North Sea. *Paleoceanography and Paleoclimatology*, *35*(10), e2020PA003935. https://doi.org/10.1029/2020PA003935

Herbert, T. D., Dalton, C. A., Liu, Z., Salazar, A., Si, W., & Wilson, D. S. (2022). Tectonic degassing drove global temperature trends since 20 Ma. *Science*, *377*(6601), 116–119. https://doi.org/10.1126/science.abl4353

Hilgen, F. J., Lourens, L. J., Van Dam, J. A., Beu, A. G., Boyes, A. F., Cooper, R. A., et al. (2012). The Neogene Period. In *The Geologic Time Scale* (pp. 923–978). Elsevier. https://doi.org/10.1016/B978-0-444-59425-9.00029-9

Holbourn, A., Kuhnt, W., Lyle, M., Schneider, L., Romero, O., & Andersen, N. (2014). Middle Miocene climate cooling linked to intensification of eastern equatorial Pacific upwelling. *Geology*, *42*(1), 19–22. https://doi.org/10.1130/G34890.1

Holbourn, A., Kuhnt, W., Kochhann, K. G. D., Andersen, N., & Sebastian Meier, K. J. (2015). Global perturbation of the carbon cycle at the onset of the Miocene Climatic Optimum. *Geology*, *43*(2), 123–126. https://doi.org/10.1130/G36317.1

Hou, S., Stap, L. B., Paul, R., Nelissen, M., Hoem, F. S., Ziegler, M., et al. (2023). Reconciling Southern Ocean fronts equatorward migration with minor Antarctic ice volume change during Miocene cooling. *Nature Communications*, *14*(1), 7230. https://doi.org/10.1038/s41467-023-43106-4

Huang, B., Liu, C., Banzon, V., Freeman, E., Graham, G., Hankins, B., et al. (2021). Improvements of the Daily Optimum Interpolation Sea Surface Temperature (DOISST) Version 2.1. *Journal of Climate*, *34*(8), 2923–2939. https://doi.org/10.1175/JCLI-D-20-0166.1

Kasbohm, J., & Schoene, B. (2018). Rapid eruption of the Columbia River flood basalt and correlation with the mid-Miocene climate optimum. *Science Advances*, *4*(9), eaat8223. https://doi.org/10.1126/sciadv.aat8223

Levy, R., Harwood, D., Florindo, F., Sangiorgi, F., Tripati, R., Eynatten, H. von, et al. (2016). Antarctic ice sheet sensitivity to atmospheric CO_2 variations in the early to mid-Miocene. *Proceedings of the National Academy of Sciences*, *113*(13), 3453–3458. https://doi.org/10.1073/pnas.1516030113

Lewis, A. R., Marchant, D. R., Ashworth, A. C., Hedenäs, L., Hemming, S. R., Johnson, J. V., et al. (2008). Mid-Miocene cooling and the extinction of tundra in continental Antarctica. *Proceedings of the National Academy of Sciences*, *105*(31), 10676–10680. https://doi.org/10.1073/pnas.0802501105

Liao, S., Liu, X.-L., Manz, K. E., Pennell, K. D., Novak, J., Santos, E., & Huang, Y. (2023). Comprehensive analysis of alkenones by reversed-phase HPLC-MS with unprecedented selectivity, linearity and sensitivity. *Talanta*, *260*, 124653. https://doi.org/10.1016/j.talanta.2023.124653

Liu, X., Huber, M., Foster, G. L., Dessler, A., & Zhang, Y. G. (2022). Persistent high latitude amplification of the Pacific Ocean over the past 10 million years. *Nature Communications*, *13*(1), 7310. https://doi.org/10.1038/s41467-022-35011-z

Miller, K. G., Wright, J. D., & Fairbanks, R. G. (1991). Unlocking the Ice House: Oligocene-Miocene oxygen isotopes, eustasy, and margin erosion. *Journal of Geophysical Research: Solid Earth*, *96*(B4), 6829–6848. https://doi.org/10.1029/90JB02015

Müller, P. J., Kirst, G., Ruhland, G., von Storch, I., & Rosell-Melé, A. (1998). Calibration of the alkenone paleotemperature index $U_{37}^{K'}$ based on core-tops from the eastern South Atlantic and the global ocean (60°N-60°S). *Geochimica et Cosmochimica Acta*, *62*(10), 1757–1772. https://doi.org/10.1016/S0016-7037(98)00097-0

Park, Y., Maffre, P., Goddéris, Y., Macdonald, F. A., Anttila, E. S. C., & Swanson-Hysell, N. L. (2020). Emergence of the Southeast Asian islands as a driver for Neogene cooling. *Proceedings of the National Academy of Sciences*, *117*(41), 25319–25326. https://doi.org/10.1073/pnas.2011033117

Pierce, E. L., van de Flierdt, T., Williams, T., Hemming, S. R., Cook, C. P., & Passchier, S. (2017). Evidence for a dynamic East Antarctic ice sheet during the mid-Miocene climate transition. *Earth and Planetary Science Letters*, *478*, 1–13. https://doi.org/10.1016/j.epsl.2017.08.011

Pound, M. J., Haywood, A. M., Salzmann, U., & Riding, J. B. (2012). Global vegetation dynamics and latitudinal temperature gradients during the Mid to Late Miocene (15.97–5.33Ma). *Earth-Science Reviews*, *112*(1), 1–22. https://doi.org/10.1016/j.earscirev.2012.02.005

Raitzsch, M., Bijma, J., Bickert, T., Schulz, M., Holbourn, A., & Kučera, M. (2021). Atmospheric carbon dioxide variations across the middle Miocene climate transition. *Climate of the Past*, *17*(2), 703–719. https://doi.org/10.5194/cp-17-703-2021

Rea, D. K., Basov, La., Janecek, T. R., Palmer-Julson, A., & et al. (Eds.). (1993). *Proceedings of the Ocean Drilling Program|145 Initial Reports* (Vol. 145). Ocean Drilling Program. https://doi.org/10.2973/odp.proc.ir.145.1993

Sangiorgi, F., Quaijtaal, W., Donders, T. H., Schouten, S., & Louwye, S. (2021). Middle Miocene Temperature and Productivity Evolution at a Northeast Atlantic Shelf Site (IODP U1318, Porcupine Basin): Global and Regional Changes. *Paleoceanography and Paleoclimatology*, *36*(7), e2020PA004059. https://doi.org/10.1029/2020PA004059

Shevenell, A. E., Kennett, J. P., & Lea, D. W. (2004). Middle Miocene Southern Ocean Cooling and Antarctic Cryosphere Expansion. *Science*, *305*(5691), 1766–1770. https://doi.org/10.1126/science.1100061

Shevenell, A. E., Kennett, J. P., & Lea, D. W. (2008). Middle Miocene ice sheet dynamics, deep-sea temperatures, and carbon cycling: A Southern Ocean perspective. *Geochemistry, Geophysics, Geosystems*, *9*(2). https://doi.org/10.1029/2007GC001736

Sosdian, S. M., Babila, T. L., Greenop, R., Foster, G. L., & Lear, C. H. (2020). Ocean Carbon Storage across the middle Miocene: a new interpretation for the Monterey Event. *Nature Communications*, *11*(1), 134. https://doi.org/10.1038/s41467-019-13792-0

Super, J. R., Thomas, E., Pagani, M., Huber, M., O'Brien, C. L., & Hull, P. M. (2020). Miocene Evolution of North Atlantic Sea Surface Temperature. *Paleoceanography and Paleoclimatology*, *35*(5), e2019PA003748. https://doi.org/10.1029/2019PA003748

Tierney, J. E., & Tingley, M. P. (2018). BAYSPLINE: A New Calibration for the Alkenone Paleothermometer. *Paleoceanography and Paleoclimatology*, *33*(3), 281–301. https://doi.org/10.1002/2017PA003201

Villanueva, J., Flores, J. A., & Grimalt, J. O. (2002). A detailed comparison of the $U^{k'}_{37}$ and coccolith records over the past 290 kyears: implications to the alkenone paleotemperature method. *Organic Geochemistry*, *33*(8), 897–905. https://doi.org/10.1016/S0146-6380(02)00067-0

Warny, S., Askin, R. A., Hannah, M. J., Mohr, B. A. R., Raine, J. I., Harwood, D. M., et al. (2009). Palynomorphs from a sediment core reveal a sudden remarkably warm Antarctica during the middle Miocene. *Geology*, *37*(10), 955–958. https://doi.org/10.1130/G30139A.1

Westerhold, T., Marwan, N., Drury, A. J., Liebrand, D., Agnini, C., Anagnostou, E., et al. (2020). An astronomically dated record of Earth's climate and its predictability over the last 66 million years. *Science*, *369*(6509), 1383–1387. https://doi.org/10.1126/science.aba6853

Witkowski, C. R., Von Der Heydt, A. S., Valdes, P. J., Van Der Meer, M. T. J., Schouten, S., & Sinninghe Damsté, J. S. (2024). Continuous sterane and phytane $\delta^{13}C$ record reveals a substantial pCO_2 decline since the mid-Miocene. *Nature Communications*, *15*(1), 5192. https://doi.org/10.1038/s41467-024-47676-9

CHAPTER 3

Controls on subpolar North Pacific productivity during the Early-Middle Miocene

Jared E. Nirenberg[1], Sofía Gilroy[1], Jordan T. Abell[2], and Timothy D. Herbert[1]

[1]Department of Earth, Environmental, and Planetary Sciences, Brown University, Providence, Rhode Island 02912, USA

[2]Department of Earth and Environmental Sciences, Lehigh University, Bethlehem, PA 18015, USA

Abstract

The North Pacific experienced dramatic changes in sedimentation during the Early and Middle Miocene with the rise of biosiliceous deposition during the Miocene Climatic Optimum (MCO) and intervals of substantial calcite accumulation prior to the MCO in regions where calcite is not preserved in recent sediments. While qualitatively suggestive of major oceanographic changes in the region, little is known about the drivers of these changes. Here, we present high-resolution data from X-ray fluorescence (XRF) core scanning from ODP Site 884 spanning the Early-Middle Miocene from 12.6 to 18.2 Ma to quantitatively reconstruct the evolution of sedimentation in the subpolar North Pacific. After calibration of XRF elemental count ratios using discrete geochemical measurements, we calculate accumulation rates of biogenic silica, calcium carbonate, and detrital material over this interval. We apply a multi-proxy approach to interpreting surface productivity using accumulation rates of biogenic material and C_{37} alkenones as well as barium to titanium count ratios as an approximation for biogenic barium concentrations. Comparison of these productivity proxies with surface temperature proxies at the same site constrains the relationship between Miocene climate and productivity in the western subpolar North Pacific. While we do not find a simple, consistent relationship between surface temperatures and productivity throughout the Early-Middle Miocene, periods of elevated biogenic accumulation rates of silica and calcite coincide with colder intervals of the Miocene Climatic Optimum and Early Miocene, respectively, which contrasts with findings from the Quaternary. Our findings highlight the complexity of the relationship between climate and high-latitude productivity as well as the utility of understanding a wide range of warm climate states prior to Northern Hemisphere glaciation.

Introduction

For much of the global ocean, phytoplankton nearly completely utilize available macronutrients, leaving most surface waters depleted in nitrate and phosphate (Sarmiento & Gruber, 2006). However, in certain 'high nutrient, low chlorophyll' (HNLC) regions, phytoplankton macronutrient utilization cannot keep up with the supply of these nutrients from the deep ocean due to other limiting factors such as low light availability or lacking micronutrients such as iron (Harrison et al., 1999; Martin et al., 1990; Mitchell et al., 1991; Tsuda et al., 2003). The major HNLC regions in the modern ocean are located within the Southern Ocean, Equatorial Pacific, and subpolar North Pacific. The unused nutrients in these regions represent major 'leaks' in the global biological pump where phytoplankton productivity could potentially sequester further carbon into the deep ocean, but currently do not. As such, the role of export productivity to the deep ocean in these regions is of particular interest due to their outsized impact on atmospheric carbon dioxide concentrations.

Sedimentation in the modern subpolar North Pacific (SNP) reflects both export productivity as well as preservation. Deposition in the open ocean region of the SNP is characterized by high fluxes of biogenic opal reflecting surface productivity of siliceous organisms, yet moderate to low fluxes of organic carbon due to relatively low export production (Hayes et al., 2021; Serno et al., 2014). Calcium carbonate is generally low or absent in these sediments due to dissolution from the corrosivity of deep waters in the North Pacific (Hayes et al., 2021). While opal concentrations are high relative to the rest of the modern ocean, detrital material comprises the majority of surface sediment composition in the SNP (Hayes et al., 2021; Jaccard et al., 2010). However, this was not always the case.

During the Middle Miocene, sedimentation in the SNP was dominated by higher than modern rates of opal deposition (Rea et al., 1993). This was part of a larger pattern of opal deposition across the North Pacific, with elevated opal accumulation rates observed in marine sediments of the California margin (Lyle et al., 2000) and in the Monterey Formation (Anttila et al., 2023). In addition, calcium carbonate was the dominant sediment composition in the SNP during intervals the Early Miocene and Pliocene (Rea et al., 1993). Together, these departures from modern-like sediment compositions imply that Neogene surface and/or deep ocean conditions in the SNP were quite different from modern, but the mechanism, timing, and relationship to global climate surrounding these changes in sediment deposition are unclear.

In this work, we explore sediment accumulation and productivity reconstructions within the HLNC region of the subpolar North Pacific during the dramatic global warmth of the Early and Middle Miocene. Surface productivity and resulting biogenic sedimentary fluxes in the SNP have important broader implications for global thermohaline circulation (Woodruff & Savin, 1989) and deep ocean carbon storage (Haug et al., 1999). While there has been abundant work reconstructing these changes during the Quaternary glacial-interglacial cycles (Brunelle et al., 2010; Gray et al., 2018; Jaccard et al., 2005) and during the warmer Pliocene and latest Miocene (Abell & Winckler, 2023; Burls et al., 2017; Haug et al., 1999), little is known during the more extreme warmth of the Early and Middle Miocene. Much of the quantitative work in the Pacific across the Neogene has focused on accumulation of biogenic calcite on the seafloor (Lyle, 2003), whereas biogenic silica accumulation has been mostly described through qualitative core descriptions (Woodruff & Savin, 1989) prior to the late Miocene. Fully quantitative biogenic fluxes are needed to describe the evolution of productivity in the SNP prior to late Neogene cooling (Herbert et al., 2016).

The Early and Middle Miocene contain the warmest interval over the past 23 million years, the Miocene Climatic Optimum (MCO, ~17-14 Ma), as well as subsequent global cooling and ice sheet expansion during the Middle Miocene Climate Transition (Nirenberg & Herbert, 2024; Shevenell et al., 2004; Westerhold et al., 2020). These intervals represent a range of warmer than modern climate states with high, though uncertain, atmospheric carbon dioxide concentrations (Cenozoic CO_2 Proxy Integration Project (CENCO$_2$PIP) Consortium, 2023; Witkowski et al., 2024) that may be analogous to long-term future climate under mid and high greenhouse gas emission scenarios (Steinthorsdottir et al., 2021). Surface waters in the western SNP were up to 18°C warmer than modern, though highly variable, during these intervals (Nirenberg & Herbert, 2024). As such, the evolution of productivity in the SNP during the Early-Middle Miocene furthers our understanding of the response of this region to a wider range of warming and atmospheric CO_2 concentrations than experienced during the late Neogene and Quaternary alone.

Leg 145 of the Ocean Drilling Program (ODP) recovered several Miocene sections from the western to eastern SNP across a range of water depths (Rea et al., 1993). We analyze the Early-Middle Miocene section at ODP Site 884 here due to its lack of hiatuses (Barron & Gladenkov, 1995), providing a continuous, well-dated stratigraphy back to 18.2 Ma as well as the availability of sea surface temperature (SST) records from previous work (Nirenberg & Herbert, 2024). Site 884 is located on the flank of the Detroit Seamount, within the HNLC zone of the SNP (Figure 1), at a water depth of 3825 m (Rea et al., 1993). Its paleolocation during the Early-Middle Miocene was to the southeast of its modern location, but still within the modern HNLC region (Herbert et al., 2016). Miocene sedimentation rates at Site 884, averaging 1.87 cm per kyr, allow for reconstructions at the orbital scale (Nirenberg & Herbert, 2024).

X-ray fluorescence (XRF) scanning of sediment cores provides a non-destructive, low-cost, and time-efficient method of producing high-resolution data on sediment composition. Raw element counts from XRF core scanning are only semi-quantitative due to different excitation responses of different elements and the dependence of counts on sediment density and composition (Oyedotun, 2018). However, ratios between elemental counts from the same measurement can often be calibrated using geochemical measurements on discrete samples to provide fully quantitative data on sediment composition. We apply this methodology here to generate an orbital-scale record of sediment composition at Site 884 during the Early and Middle Miocene.

We partition sediment composition into 3 components, biogenic silica, calcite, and detrital material, and use age model-derived mass accumulation rates to calculate the accumulation rates of these components between 12.6 and 18.2 Ma. We employ a multi-proxy approach to assessing export productivity at Site 884 using biogenic sediment accumulation rates, phytoplankton biomarker (C_{37} alkenone) accumulation rates, and XRF-derived barium to titanium count ratios. Comparison with surface temperature proxies at the same site reveals a complex and changing relationship between climate and export productivity in the western SNP throughout the Early-Middle Miocene. Together, our results demonstrate a fundamentally different response of export productivity to climate forcings in this HNLC region during these warmest intervals of the Neogene than previously observed during the colder Quaternary.

Methods

XRF scanning

XRF core scanning was performed at the IODP Gulf Coast Repository using an Avaatech core scanner. All core sections were scanned using the same instrument. Core sections were scanned at an average resolution of about 2 cm at both 10 kVp (no filter) and 50 kVp (Cu filter). Due to the age and dry condition of the cores, core sections often contained large cracks and some completely crumbled sections. Care was taken to manually select scanning locations to avoid these problematic intervals and to produce scanning surfaces as flat and smooth as possible. Measurements with Ar counts greater than 0 were removed due to significant interference from air. We report XRF counts for Al, Ar, Ca, Fe, K, Mn, S, Si, and Ti from the 10 kV scan and counts for Ba from the 50 kV scan.

Biogenic silica measurements

Measurements of biogenic silica concentrations on 70 samples were done using a modified version of the method of Russell & Johnson (2005) adapted to photometric analysis using an Automated Discrete Analyzer SmartChem 200 from KPM Analytics. Briefly, 30-40 mg of dry, pulverized sediment samples were digested in 40 mL of 0.5 M NaOH in a water bath maintained at 85°C. After precisely 4 hours for each sample, 1 mL aliquots were removed and transferred into separate containers containing 4 mL Milli-Q water. Silicon concentrations were then analyzed using a colorimetric (molybdenum blue) method on the Automated Discrete Analyzer SmartChem 200.

Briefly, 35 μL of sample was added to 280 μL of Milli-Q water. After 36 seconds, 140 μL of 6.9 μM ammonium molybdate in 0.288 M HCl was added. After reacting for 144 seconds, 210 μL of reducing solution was added. The reducing solution was comprised of 20% 9.4 M sulfuric acid, 20% 0.55 M oxalic acid, 33.3% 5.8 μM metol in 9.5 μM sodium sulfite, and 26.7% Milli-Q water. After reacting for 576 seconds, the color absorption was measured at 880 nm. Absorption was calibrated to silicon concentrations using a dilution series of a standard of 3000 μM sodium hexafluorosilicate with a quadratic fit. To avoid silica contamination, all reagents were prepared using Milli-Q water and were handled in HDPE bottles. Reagent and digestion blanks were run every 10 and 35 samples, respectively, to monitor potential contamination. Silicon concentrations of all blanks were below the limit of detection.

Percent mass of biogenic silica was calculated from silicon concentrations according to the equation below, assuming 8% water in biogenic silica. The volume of NaOH was 0.040 L, and the dilution factor was 5.

$$\%BSi = \frac{Silicon\ concentration\ (\mu M) * volume\ NaOH(L) * dilution\ factor * 65.3g/mol}{mass\ dry\ sediment(\mu g)} * 100\%$$

Calcium carbonate measurements

Weight percents of $CaCO_3$ were measured on 252 samples using a CM5014 CO_2 coulometer. 3-15 mg of dry, pulverized sediment were added to capsules, which were acidified using 4 N sulfuric acid. The mass of inorganic carbon was measured after 8 minutes. Pure calcium carbonate standards and blanks were run every 8 and 19 samples, respectively, for quality control. Amounts of inorganic carbon in the blanks for each run were averaged, and this amount was subtracted from each sample. In some cases, the amount of inorganic carbon from samples was less than that of the average of the blanks, leading to a calculation of %$CaCO_3$ slightly less than 0. We instead report these as 0% $CaCO_3$. Sample replicates and pure $CaCO_3$ standards indicate measurement precision within 1% $CaCO_3$.

Calibrating XRF to carbonate concentrations

XRF scanning data was calibrated to discrete sample measurements of weight percents of calcium carbonate using the logarithm of the ratio of counts of calcium to titanium. This ratio was interpolated to the midpoint of sample depth intervals using a Gaussian process regression fitted with a combined Matern 3/2 and exponential kernel calculated using MATLAB. Only samples within 2 cm of an XRF scanning measurement were used for calibration to minimize the uncertainty associated with this interpolation.

A quadratic curve was used to fit the nonlinear relationship between $\log_{10}$(Ca/Ti) and %$CaCO_3$ (Figure 2). This fit estimates %$CaCO_3$ less than 0 to a minimum of -0.24% for Ca/Ti less than 1.82. To correct this, we revise this to estimate 0% $CaCO_3$ for Ca/Ti less than 1.82 ($\log_{10}$(Ca/Ti) less than 0.26) and the quadratic fit for Ca/Ti above 1.82. The root means squared error (RMSE) for this calibration is 3.74% $CaCO_3$. XRF-derived values closely match measured %$CaCO_3$ (Figure S1).

Calibrating XRF to biogenic silica measurements

After calculating % CaCO3, the remaining mass percent at each XRF scanning measurement was partitioned between biogenic opal and detrital material using the ratio of counts of titanium to silicon (Ti/Si).

$$\left(\frac{Si}{Ti}\right)_{total} = \frac{Si_{det} + Si_{bio}}{Ti_{det} + Ti_{bio}} = \frac{Si_{det} + Si_{bio}}{Ti_{det}} = \left(\frac{Si}{Ti}\right)_{det} + \frac{Si_{bio}}{Ti_{det}} = \left(\frac{Si}{Ti}\right)_{det} + \frac{Si_{bio}}{Ti_{det}} * \frac{Si_{det}}{Si_{det}}$$

$$= \left(\frac{Si}{Ti}\right)_{det} + \frac{Si_{det}}{Ti_{det}} * \frac{Si_{bio}}{Si_{det}} = \left(\frac{Si}{Ti}\right)_{det} * \left(1 + \frac{Si_{bio}}{Si_{det}}\right)$$

This assumes all titanium is from detrital sources and that the detrital source has a constant ratio of silicon to titanium. We can now define the ratio, R, of the Si/Ti measured from XRF (total) to Si/Ti of the detrital source.

$$\frac{\left(\frac{Si}{Ti}\right)_{total}}{\left(\frac{Si}{Ti}\right)_{det}} = R = 1 + \frac{Si_{bio}}{Si_{det}}$$

We now define the fractions of silicon counts from detrital and biogenic sources.

$f_{bio} + f_{det} = 1$, where $f_{bio} = \frac{Si_{bio}}{Si_{total}}$ and $f_{det} = \frac{Si_{det}}{Si_{total}}$

$$R - 1 = \frac{Si_{bio}}{Si_{det}} = \frac{f_{bio}}{1 - f_{bio}}$$

$$f_{bio} = (R - 1)(1 - f_{bio}) = R - R * f_{bio} - 1 + f_{bio}$$

$$1 = R * (1 - f_{bio})$$

$$f_{bio} = 1 - \frac{1}{R} = 1 - \frac{\left(\frac{Si}{Ti}\right)_{det}}{\left(\frac{Si}{Ti}\right)_{total}} = 1 - \left(\frac{Si}{Ti}\right)_{det} * \left(\frac{Ti}{Si}\right)_{total}$$

Therefore, the fraction of silicon counts from biogenic silica is linearly related to Ti/Si measured from XRF. This is consistent with an assumed detrital and biogenic endmember approach, as f_{bio} should be zero when measured Si/Ti equals that of the detrital source and pure biogenic silica ($f_{bio} = 1$) should theoretically result in zero measured titanium counts (Ti/Si = 0).

However, the fraction of silicon counts from biogenic silica is related to the mole fraction of biogenic silica relative to all silicon, not the mass fraction which we measure. Therefore, the mass fractions of biogenic silica must be converted to mole fractions of silicon in order to calibrate the XRF data.

$$f_{bio} = \frac{mass\ silicon_{bio}}{mass\ silicon_{bio} + mass\ silicon_{det}} = \frac{\%Si_{bio} * mass_{bio}}{\%Si_{bio} * mass_{bio} + \%Si_{det} * mass_{det}}$$

We can then define mass fractions of sediment only considering the biogenic silica and detrital fractions (the silicon bearing sources). Note that these are not mass fractions of total core material, but rather the partitioning of the non-carbonate mass between biogenic silica and detrital fractions.

$$100\% = \%M_{bio} + \%M_{det}$$

$$f_{bio} = \frac{\%Si_{bio} * \%M_{bio}}{\%Si_{bio} * \%M_{bio} + \%Si_{det} * \%M_{det}} = \frac{\%Si_{bio} * \%M_{bio}}{\%Si_{bio} * \%M_{bio} + \%Si_{det} * (100\% - \%M_{bio})}$$

The mass fraction of biogenic silica is therefore not linearly related to the mole fraction (Figure 3). To calculate the mole fraction from the mass fraction, the mass percents of silicon in the detrital and biogenic silica fractions must be assumed. Assuming the biogenic silica is 8% water by mass, as was done for calculating mass percent biogenic silica of the bulk sediment, biogenic silica is 43% silicon. A value of 17% silicon was chosen for the detrital fraction in order to force the intercept of XRF Ti/Si to f_{bio} to 1 (Figure 4). The resulting slope of the linear regression is the empirically-derived Si/Ti of detrital material, which is 3.274 +/- 0.095 (1 standard error) in this case. We emphasize that this ratio, and all count ratios we report from XRF, are not quantitative concentration ratios due to different excitation responses of different elements using XRF.

For the final calibration to sample measurements, only samples within 2 cm of an XRF scanning measurement were used to minimize bias from interpolating the Ti/Si signal between measurement points. First, %$CaCO_3$ was estimated using log_{10}(Ca/Ti), and the measured percent biogenic silica was converted to mass percent of the non-carbonate fraction. Then, this mass percent was converted to mole fraction of silicon using the relationship above. When converted back to mass percent silica of the non-carbonate fraction, the calibration with outliers removed has a RMSE of 3.36%.

Samples deposited before the onset of the MCO, below 589.7 mbsf, provided anomalously low fractions of biogenic silica (Figure 4) and were removed from the calibration. The reason for potential analytical underestimation of biogenic silica relative to XRF scanning Si/Ti in these samples is unclear. This interval before the MCO also contains the most calcareous-rich sediments, containing upwards of 60% $CaCO_3$ (Figure 7), and the carbonate is primarily in the form of fine-grained microfossils (Rea et al., 1993). Samples for biogenic silica analysis were not acidified to remove carbonate prior to silica digestion in NaOH, so coatings of fine-grained carbonate material may have inhibited complete dissolution of biogenic silica. In addition, radiolarian and sponge spicules, which are more resistant to dissolution, are significant biogenic components in these sections, but it is unlikely they account for up to 50% of the biogenic silica in a sample to fully account for the discrepancy between analytical and XRF-estimated biogenic silica fractions.

Alternatively to analytical underestimation, the discrepancy could represent a limit of our assumption of a constant detrital endmember. A shift in the composition of the detrital source to Site 884 across the onset of the MCO may have been significant, but cannot be directly constrained here. A synchronous decrease in K/Ti (Figure S2) may reflect changing clay mineral compositions, which could also coincide with shifts in detrital silicon content. However, other elemental ratios which could indicate detrital composition shifts, such as Fe/Ti, are constant across the onset of the MCO (Figure S3). While future mineralogical work is needed to further constrain the effects of changing detrital source composition, the strong linearity of our calibration under the assumption of a constant detrital endmember suggests that these effects are relatively small in most of the section studied here. As such, we apply the same calibration to all depths, including those below 589.7 mbsf.

After the determination of first %$CaCO_3$ using $\log_{10}$(Ca/Ti) and then percent biogenic silica using Ti/Si, the remaining mass is assigned as detrital material according to our 3 endmember framework. This satisfies the following equation.

$$100\% = \%CaCO_3 + \%SiO_2 \circ 0.29H_2O + \%detrital$$

Calculating mass accumulation rates

Wet bulk density was estimated from shipboard GRAPE density measurements (Rea et al., 1993). GRAPE density measurements of less than 1.15 g/cc were removed, as these are indicative of cracks in the cores or poor measurement quality. To reduce the effects of noise, we smoothed the GRAPE density measurements using a Gaussian process regression (GPR) with a combined Matern 3/2 and exponential kernel. We then used this GPR to predict the wet bulk density at all depths which were scanned using XRF.

To calculate dry bulk density from wet bulk density, the following equation was used (Herbert & Mayer, 1991).

$$DBD = GD * \left(1 - \frac{GD - WBD}{GD - 1.025}\right) + 0.025 * \frac{GD - WBD}{GD - 1.025}$$

In this equation, DBD is dry bulk density, WBD is wet bulk density, and GD is grain density. Grain density was estimated for every depth with an XRF measurement by weighting the grain densities of 3 major sediment components (carbonate, opal, and detrital), which were assigned values of 2.65, 2.0, and 2.65 g/cm^3, respectively. The weights for each end member were assigned according to fractions determined by XRF calibration presented in the following section (Figure 7).

Mass accumulation rates (MAR) were calculated using the following equation, where LSR is linear sedimentation rate, which was calculated by linear interpolation between magnetic polarity reversals in the age model of Nirenberg & Herbert (2024). MARs were calculated for each sedimentary source (MAR_x) by weighting the total MAR by the fraction of the sediment from each source (f_x).

$$MAR_x = f_x * DBD\left(\frac{g}{cm^3}\right) * LSR\left(\frac{cm}{kyr}\right)$$

Results and Discussion

Using XRF counts from just 3 elements (Ca, Si, and Ti), we partition the 3 major sedimentary lithologic sources to Site 884 between 12.57 and 18.23 Ma, a span of over 5.6 million years, at 1.3 kyr median sampling resolution (Figure 7). These results highlight the power of XRF core scanning to generate high-resolution geochemical records, even in older legacy cores such as from Site 884, where the dry and cracked cores provide less than ideal conditions for such scanning. These high-resolution geochemical records can then be compared with other proxy measurements, such as sea surface temperature and productivity proxies from organic biomarkers (Nirenberg & Herbert, 2024), to interpret the drivers of sedimentation in the subpolar North Pacific and their relation to surface and deep ocean conditions.

While diatoms are present and generally abundant throughout the record (Barron & Gladenkov, 1995), biogenic opal is only the most abundant sedimentary component during some intervals during the MCO. Instead, detrital components, composed predominantly of clays (Rea et al., 1993) generally dominate the sediment composition at Site 884 prior to 16 Ma and after 14 Ma. Biogenic calcium carbonate, primarily in the form of microfossils but also some benthic foraminifera (Rea et al., 1993), is generally a minor or absent sedimentary component. This is perhaps unsurprising given the water depth (3825 m) of Site 884 below the relatively shallow carbonate compensation depth (CCD), or water depth below which calcite is favored to dissolve, of the modern North Pacific (Berger et al., 1976). However, intervals prior to the MCO that are dominantly calcareous suggest a periodically deeper, but variable, North Pacific CCD during the Early Miocene. While volcanic ash is a significant sedimentary component in some intervals at Site 884, no ash layers are found in the stratigraphic intervals measured here (Rea et al., 1993). As such, a 3-component model of sedimentation comprised of biogenic opal, carbonate, and detrital material is sufficient. However, our 3 endmember representation cannot account for the potential presence of diffuse ash in low concentrations.

Implications for Si/Ti from XRF as a biogenic silica proxy

A distinction of this work is the application of Ti/Si to partition the non-carbonate fraction of sediment between biogenic silica and detrital concentrations. In contrast, previous work, including at sites elsewhere in the Pacific during the Miocene (Holbourn et al., 2014, 2024; Kochhann et al., 2016) has directly applied Si/Ti or its logarithm as a proxy for biogenic silica concentration of bulk sediment. However, this elemental ratio is unaffected by the presence of biogenic $CaCO_3$, while percentages of biogenic silica are affected by $CaCO_3$ due to dilution. To account for this, %$CaCO_3$ must first be estimated prior to partitioning the remaining sediment between biogenic silica and detrital material. While this distinction may seem pedantic, it can completely change the interpretation of biogenic silica concentrations with variable %$CaCO_3$. As an example from this work, we more closely examine the interval prior to the MCO.

During intervals of high %$CaCO_3$, Si/Ti also increases (Figure 8). Previous interpretations of Si/Ti would conclude that the percentages of both biogenic components, carbonate and silica, are tightly positively correlated during these intervals. However, this is not the case as mass percents of biogenic silica are either constant or decrease slightly during high carbonate intervals. Rather, percentages of detrital material decrease during these intervals, so biogenic silica is a larger portion of the non-carbonate fraction, but a smaller or constant portion of bulk sediment.

As a result, we caution against the interpretation of Si/Ti directly as a proxy for biogenic silica concentrations of bulk sediment. While it may be a reasonable approximation where %$CaCO_3$ remains relatively constant, this is often not the case. Rather, the effects of dilution from other sedimentary components which do not contain silicon or titanium, such as calcium carbonate, must be accounted for when interpreting percent biogenic silica of bulk sediment from Si/Ti.

Mass accumulation rates

Percentages of each component are susceptible to effects of dilution from changing fluxes from other components. For example, the mass percent of detrital material can be lowered by either decreased delivery of lithogenous material or increased deposition of biogenic opal or carbonate. We calculate the mass accumulation rates for each component to account for these effects.

Our MAR calculations cannot account for the effects of lateral sediment redistribution on sediment MARs, which may be substantial considering that Site 884 is from a proposed drift deposit (Rea et al., 1993). As such, potential discrepancies between bulk sediment and vertical fluxes are an uncertainty in our analyses. Future work applying a constant flux proxy, such as extraterrestrial helium-3, as has been previously applied to the subpolar North Pacific (Abell et al., 2021; Abell & Winckler, 2023) would constrain these effects.

An additional uncertainty with MAR calculation is the limited number of age model constraints, as the age model for Site 884 is derived from observed magnetic polarity reversals in magnetic inclination (Nirenberg & Herbert, 2024). We assume constant sedimentation rates between reversals (Figure 6), as is typically done for age model-based MAR calculations. As such, the resulting MARs cannot account for likely variable sedimentation rates within a magnetic polarity chron. In addition, our sediment accumulation rates cannot account for missing sediment that was not recovered between cores, and incomplete core recovery also prevented a complete sequence of paleomagnetic reversals, leading to some additional age model uncertainty. Our step-function representation of sedimentation rates results in some abrupt and discontinuous shifts in accumulation rates, which are particularly evident between 13 and 14.2 Ma (Figures 6 and 9). We caution against overinterpretation of sharp changes in accumulation rates surrounding age model control points as changes in sedimentation were very likely more gradual. An alternative age model using more smooth changes in sedimentation rates would produce smoother changes in accumulation rates, but the broad patterns would remain unchanged from those shown in Figure 9.

To discuss the drivers of sediment accumulation at Site 884, we focus on 3 distinct climatic and sedimentary intervals of the record: prior to the MCO (>16.7 Ma), during the MCO (14-16.7 Ma), and after the MCO (<14 Ma).

Early Miocene

Sediment deposited at Site 884 prior to the onset of the MCO, below 589.7 mbsf, contains visual variations on the meter scale between carbonate-dominated (diatom-bearing chalk) and carbonate-free (diatom-bearing clay) lithologies. Large variations in %$CaCO_3$ are confirmed with analytical measurements and XRF-derived Ca/Ti as well (Figures 2 and 7). The presence of periodic intervals of up to 60% $CaCO_3$ during the Early Miocene stands in stark contrast with the modern deep subpolar North Pacific, where the CCD is much shallower than the depth (3825 m) at Site 884.

However, the presence of carbonate alone does not constrain the mechanism for its deposition. Carbonate accumulation on the seafloor is influenced by both production in the surface ocean as well as preservation in the deep ocean where the carbonate saturation state is lower. Increased carbonate accumulation in the subpolar North Pacific during the Pliocene has been previously attributed to either increased surface productivity of calcareous phytoplankton (Novak et al., 2024) or increased preservation in the deep ocean due to better ventilated bottom water conditions (Burls et al., 2017).

To evaluate the relationship between sedimentary accumulation rates and surface productivity, we apply two additional proxies for surface productivity, which include the accumulation rates of C_{37} alkenones and barium to titanium count ratios (Ba/Ti) from XRF core scanning. Modern core-top sedimentary concentrations of C_{37} alkenones are strongly correlated with overlying sea surface chlorophyll-*a* concentrations (Raja & Rosell-Melé, 2021), providing a proxy for past phytoplankton productivity. However, the effects of past phytoplankton ecological shifts, as alkenone producers are a small subset of phytoplankton, and temperature and bottom water oxygen effects on preservation of organic matter are unconstrained, presenting potential complications for this proxy. In addition to biomarker concentrations, we examine Ba/Ti as an estimate for sedimentary biogenic barium concentrations, as has been previously applied to other subarctic North Pacific sites during the Pleistocene (Jaccard et al., 2005) and late Neogene (Abell & Winckler, 2023; Chen et al., 2022). Barium sulfate precipitates as organic matter decomposes while sinking through the water column, providing a proxy for export productivity from the surface ocean (Dymond et al., 1992; Francois et al., 1995). Barium can also be derived from detrital sources, so we interpret the ratio of barium to titanium, the latter of which we assume only comes from detrital sources, as reflective of biogenic barium. While we cannot calculate quantitative concentrations of barium from XRF scanning data alone, we can interpret relative inputs of barium from biogenic and detrital sources through normalizing to titanium counts. These two paleoproductivity proxies provide a multi-proxy approach using both organic and inorganic proxies to complement productivity interpretations from biogenic sediment accumulation.

Comparison of $CaCO_3$ accumulation and other productivity proxies show limited coherence. We find little correspondence between $CaCO_3$ and C_{37} alkenone MARs (Figure 10). While portions of carbonate intervals 2 and 4 overlap with elevated C_{37} alkenone MAR, the increases and decreases in the cyclicity are not synchronous. In addition, carbonate interval 1, which is particularly microfossil-rich, aligns with the lowest C_{37} alkenone MAR prior to the MCO. There is some correspondence between $CaCO_3$ MAR and elevated Ba/Ti in carbonate intervals 1-3, but the relationship is not observed during the rest of the carbonate intervals. In carbonate intervals 3 and 4, the accumulation rates of both $CaCO_3$ and biogenic opal are correlated, which could indicate surface productivity affecting both fluxes, but biogenic opal fluxes are relatively constant across the other carbonate intervals. While there are some sporadic correlations between surface productivity proxies and $CaCO_3$ accumulation rates, we find no consistent line of evidence to suggest that elevated surface productivity was the primary driver of carbonate accumulation in the subpolar North Pacific during the Early Miocene.

Instead, changes in the carbonate preservation are a more likely explanation for such large changes in $CaCO_3$ MAR. This explanation is also more intuitive as $\%CaCO_3$ drops to 0 between the carbonate intervals, and it is unlikely that surface productivity of calcareous phytoplankton completely collapsed during these carbonate-free intervals. This is further supported by the continuous presence of C_{37} alkenones, which are produced by calcareous phytoplankton, throughout the record at Site 884 even in sections that are devoid of $CaCO_3$. While increased surface productivity may have enhanced the magnitude of $CaCO_3$ accumulation during some of the carbonate intervals, we interpret changing preservation as the dominant control on such variable carbonate accumulation during this interval.

While we do not observe a clear one-to-one relationship between SSTs and $CaCO_3$ MAR at Site 884, all of the carbonate intervals occur during when SSTs were below the average SST during the Early Miocene, under 16°C. As such, bottom water in the North Pacific during glacial intervals before the MCO may have been better ventilated and less corrosive, allowing for carbonate preservation at 3825 meters water depth. Similar enhanced carbonate preservation during Early Miocene glacials has been found across the deep Eastern Equatorial Pacific (Kochhann et al., 2016). In addition, cyclicity of $\%CaCO_3$ across carbonate intervals 2-4 may have been paced by 100 kyr eccentricity, as was found in the Equatorial Pacific (Kochhann et al., 2016). A common, northward-flowing deep water mass across the North and Equatorial Pacific, similar to that suggested during the MCO (Holbourn et al., 2024), with enhanced ventilation during glacial conditions prior to the MCO may explain intervals of enhanced carbonate preservation in both the SNP and Equatorial Pacific. Future work is needed to assess the potential synchroneity of these intervals between site locations as well as provide further constraints on deep ocean conditions in the SNP.

Miocene Climatic Optimum

Biogenic silica deposition in the subpolar North Pacific reached its maximum during the MCO, but its relationship with SSTs reveals that increasing opal MAR was not synchronous with ocean warming. The onset of increased biogenic silica MAR lagged the onset of the MCO by over 700 kyr (Figure 11). The transition in lithology at the onset of the MCO from nannofossil carbonate-dominated to clay-dominated was driven by the total elimination of carbonate accumulation, likely due to dissolution, rather than changes in detrital or opal MAR, which were similar to their pre-MCO values across the onset of the MCO.

Our reported timing of the onset of elevated silica deposition in the North Pacific is broadly synchronous with declining silica deposition in the North Atlantic (Woodruff & Savin, 1989) and its appearance in the equatorial Pacific (Keller & Barron, 1983). This 'silica switch' from the North Atlantic to North Pacific and Indian Oceans has been previously interpreted as reflective of shifts in global thermohaline circulation towards more modern-like patterns (Keller & Barron, 1983; Woodruff & Savin, 1989). While this switch may have occurred during the MCO, we show that it did not coincide with ocean warming associated with the onset of the MCO, but rather with cooling that occurred hundreds of thousands of years after the onset.

Peak opal MARs occurred during the colder intervals of the MCO. These intervals at ~16 Ma and ~14.8 Ma coincide with temporary enrichments of benthic $\delta^{18}O$, indicating glacial expansion and/or bottom water cooling, denoted as Mi2 and Mi3a (Holbourn et al., 2024; Miller et al., 1991), which are observed globally. The later phase of increased opal deposition also aligns with what is sometimes referred to as the initiation of the Middle Miocene Climate Transition (MMCT) about 1 Myr prior to the global cooling step and Antarctic ice sheet expansion during Mi3 at ~13.8 Ma (Holbourn et al., 2014).

Biogenic opal accumulation during the MCO shows little to no correspondence with C_{37} alkenone accumulation or Ba/Ti, which may be reflective of non-productivity influences on the latter two proxies. While we cannot constrain potential preservation biases on biogenic opal accumulation, we find these unlikely to be significant at Site 884. Ba/Ti is somewhat elevated during the interval of increased biogenic opal accumulation between about 14.7 and 14.9 Ma, but is relatively constant during the other phases. C_{37} alkenone concentrations and accumulation rates reach their minimum observed values during the MCO, with some brief intervals of elevated accumulation between 14.3 and 14.7 Ma. While low alkenone MAR could reflect decreased surface productivity, it could also result from increased microbial respiration of organic matter at higher temperatures either in the water column or during early stages of burial (Li et al., 2023). Alternatively, shifts in phytoplankton ecology favoring diatoms over alkenone-producing coccolithophores during the MCO may also explain the discrepancy between high opal accumulation rates and low alkenone accumulation rates. Though the discordance between productivity proxies highlights potential pitfalls of overreliance on any single productivity proxy, we favor the interpretation of biogenic sediment accumulation rates as the most broadly reflective of export productivity in the SNP during the MCO.

The mechanism linking increased biogenic silica deposition, and likely surface productivity as well, with cooler SSTs during the warmest interval over the past 18 million years is unclear. If colder SSTs occurred while bottom water temperatures remained similarly warm throughout the MCO (Leutert et al., 2021; Modestou et al., 2020), a decreased temperature gradient between the surface and deep subpolar North Pacific may have reduced the upper ocean density gradient and resulting stratification, allowing for enhanced upward transport of nutrients to sustain higher diatom productivity. Increased nutrient supply from the deep ocean to the surface SNP is consistent with reduced nutrient utilization observed during the same interval (after 16 Ma) from depleted bulk sedimentary $\delta^{15}N$ at nearby Site 883 (Sigman et al., 2004).

The strong halocline of the modern subpolar North Pacific inhibits deep mixing (Yuan & Talley, 1996), but changes in surface hydrology, resulting in increased sea surface salinity (SSS), during the MCO may have further contributed to reduced stratification. This is observed in some climate model simulations, with SSS in the subpolar Northwest Pacific increasing with increasing model atmospheric CO_2 concentrations, but this is not a universal result among MCO model simulations (Burls et al., 2021; Hutchinson et al., 2025). However, these effects are unconstrained by data and are therefore speculative. Evidence such as surface seawater isotope reconstructions would be needed to constrain Miocene changes in SSS relative to the modern North Pacific. Alternatively, a reduction in the vertical salinity gradient of the SNP may not be as necessary for reduced stratification during the warm Miocene as it was during the Quaternary due to the increased influence of temperature changes on water density at warmer temperatures (Sigman et al., 2004), as was observed in both the surface and deep ocean during the MCO (Leutert et al., 2021; Modestou et al., 2020; Nirenberg & Herbert, 2024).

Our finding of peak biogenic opal accumulation rates during the colder periods within the MCO contrasts with previous findings from the SNP during the Plio-Pleistocene. The onset of stratification in the SNP, resulting in declining productivity, is traditionally ascribed to the intensification of Northern Hemisphere glaciation during the Plio-Pleistocene transition (Haug et al., 1999), an interval of global cooling. Productivity in the SNP later declined to its lowest extent during glacial maxima of the Late Pleistocene (Brunelle et al., 2010; Jaccard et al., 2005). As such, cold climate intervals are associated with increased stratification and reduced productivity in the SNP (Sigman et al., 2004), which is the opposite of our findings during the

MCO. These contrasting results suggest an important role of Northern Hemisphere ice sheets in forcing the SNP halocline and resulting stratification. During the Early-Middle Miocene, continental-scale ice sheets were limited to Antarctica with no evidence for continental-scale glaciation in the Northern Hemisphere until the late Miocene (Larsen et al., 1994; Rea et al., 1993). The discrepancy of the response of SNP productivity to cooling during the warmer Miocene and colder Plio-Pleistocene suggest either a non-monotonic response of polar stratification to lower global temperatures or the unique influence of direct ice sheet forcings in the Northern Hemisphere.

Middle Miocene Climate Transition

Opal accumulation rates at Site 884 decline at the end of the MCO and beginning of the MMCT. However, the transition from diatom-dominated to clay-dominated bulk lithology, driven by this opal crash, occurs stratigraphically below and therefore prior to surface cooling associated with global cooling and Antarctic ice sheet expansion during the Mi3 glacial event (Miller et al., 1991). Our age model places the opal crash ~100-150 kyr prior to surface cooling, though more precise timing of cooling at Site 884 is obscured by a gap in sediment recovery between cores.

The rapid nature of declining opal MAR, and perhaps surface productivity more broadly, in the SNP suggests a potential shift in oceanographic frontal zones prior to surface cooling. In the case of the SNP, this was likely a southward shift of the Subarctic frontal zone, where mixing of water from the cold Oyashio and warm Kuroshio currents result in increased nutrients and surface productivity (Yasunaka et al., 2014), from north of Site 884 to south of it. Crossing of the

Subarctic front over the paleolocation of Site 884 represents a location of this frontal zone at least 5° northward of its modern location (Nishikawa et al., 2021; Yuan & Talley, 1996), consistent with more poleward positions of frontal zones during the globally warm Miocene. Our findings in the SNP are analogous to previous findings in the Southern Hemisphere, where Southern Ocean frontal zones shifted northward prior to global cooling and glacial expansion during the MMCT by ~300 and 100 kyr in the South Atlantic and Tasman Sea, respectively (Kuhnert et al., 2009; Shevenell et al., 2004). A synchronous, bi-hemispheric nature of these frontal shifts towards the equator would suggest global forcings, rather than Southern Hemisphere forcings directly related to Antarctic ice sheet expansion, were the likely cause.

The most pronounced feature in our records after the MCO is elevated accumulation rates of all components between ~13.2 and 13.6 Ma, peaking between 13.36 and 13.6 Ma. At first, these elevated rates may appear to be an artifact of total MAR derived from our linearly-interpolated age model between paleomagnetic reversals, which indicate elevated sedimentation rates in magnetic chrons C5AA and C5AB. Because the MARs we report here assume no changes in sediment focusing or winnowing at Site 884, we cannot rule out that elevated accumulation rates during this interval were solely due to elevated sediment focusing at the seafloor. In fact, the location of Site 884 within the "Meiji Tongue", in which sediments may be deposited by contour currents (Kerr et al., 2005; VanLaningham et al., 2009), could be conducive to large changes in sediment focusing. However, the timing of the onset of contourite sedimentation in the Meiji Tongue is unknown, and the method of sedimentation may have been quite different from modern during the Miocene due to differences in ocean circulation, particularly as the Bering Strait was closed (Marincovich & Gladenkov, 1999).

Elevated surface productivity during this interval of the MMCT is an alternative explanation for such high accumulation rates. Biogenic accumulation rates of both opal and carbonate spiked during this interval, though a synchronous increase in detrital MAR seems unlikely from this explanation alone. Elevated Ba/Ti from XRF scanning, which is independent of the age model and total MAR, supports increased export production during this interval. In addition, accumulation rates of C_{37} alkenones also greatly increase during this interval, providing further support for increased surface productivity. The convergence of multiple productivity proxies with elevated biogenic sediment accumulation rates supports a surface origin of the signal reflecting increased surface productivity, and organic carbon burial as well, between 13.2 and 13.6 Ma.

The timing of this highly productive interval occurs after global cooling during the MMCT and also after the termination of the final benthic carbon isotope maximum (Holbourn et al., 2014) of the Monterey Event, which is traditionally interpreted as reflective of increased global organic carbon burial (Flower & Kennett, 1993; Vincent & Berger, 1985). The interval at Site 884 coincides with sustained cold SSTs after Mi3 cooling and terminates synchronously with warming SSTs after 13.2 Ma. This is consistent with either similar climate and oceanographic forcings as the periods of elevated biogenic opal accumulation rates during the MCO or a transition from carbon burial from shallow marginal seas to the deep ocean with eustatic sea level fall after Mi3, as has been suggested for the North Pacific Monterey Formation (Anttila et al., 2023). Through either mechanism, the lagged timing of increased surface productivity and carbon burial from temperature forcing agrees with the interpretation of Anttila et al. (2023) that oceanic organic carbon burial acted in response to, rather than as a driver of, global climate change during the Miocene.

Conclusions

Our quantification of different sources of sediment deposition to Site 884 provides novel constraints on the rise of heightened opal deposition in the subpolar North Pacific at ~16 Ma as well as its decline slightly prior to global cooling and ice sheet expansion at ~14 Ma. While this occurred during the MCO, we show that opal accumulation did not increase with warming at the onset of the MCO, but rather with cooling hundreds of thousands of years after. In addition, we find that the intervals of carbonate accumulation at Site 884 occurred during the relatively cold Early Miocene glacials prior to the MCO. Both of these findings caution against simple interpretations of North Pacific surface and deep ocean conditions to warmer than modern conditions. Carbonate in the deep North Pacific was preserved during the moderately-warm mid-Pliocene and Early Miocene, but not during the more extreme warmth of the MCO, which provides evidence against a single, linear response of deep ocean circulation to warming.

Our results demonstrate a fundamentally different oceanographic response within the western SNP during the warmer climates of the Early-Middle Miocene than observed during the colder late Pliocene and Quaternary. Stratification and nutrient supply to the SNP during the MCO responded to temperature forcing in the opposite manner to that observed during the Quaternary, with less stratification during cooler intervals of the MCO. However, we do not find a clear one-to-one relationship between SSTs and surface productivity consistently throughout the Miocene, highlighting the spatial and temporal complexity of SNP paleoceanography, as was also found during the late Miocene and Pliocene (Abell & Winckler, 2023). These lessons from the Miocene exhibit the value of paleoclimatic observations over a wider range of climate forcings, such as those observed over the past 18 million years, beyond the limits of the better-studied Quaternary glacial-interglacial cycles. The distinct climate-productivity relationship between the Neogene and Quaternary in the SNP imply that productivity in this HNLC region exhibits either a non-monotonic response to temperature forcing or was more directly forced by Northern Hemisphere ice sheet extent during the Quaternary.

Finally, this study highlights the power of XRF core scanning calibrated using geochemical measurements to produce quality sedimentation reconstructions using mostly non-destructive and low cost means. A record of this length and resolution would not have been practical using only traditional geochemical measurements performed on discrete samples, which would have also removed a significant amount of irreplaceable core material. While our work here is limited to a specific interval at one ocean drilling site, our methodology could be feasibly applied at other sites in the subpolar North Pacific to further understand controls on sedimentation across a range of warm climate intervals, water depths, and locations within this region.

Acknowledgements

We thank Jesse Yeon and the IODP Gulf Coast Repository for their generous assistance in collecting XRF core scanning data and providing sample material. We thank the scientists and crew of ODP Expedition 145 for collecting the sample material and providing initial core descriptions. This study used data from the International Ocean Discovery Program (IODP) and its predecessors. We acknowledge funding from NSF grant GR5260822.

Figures

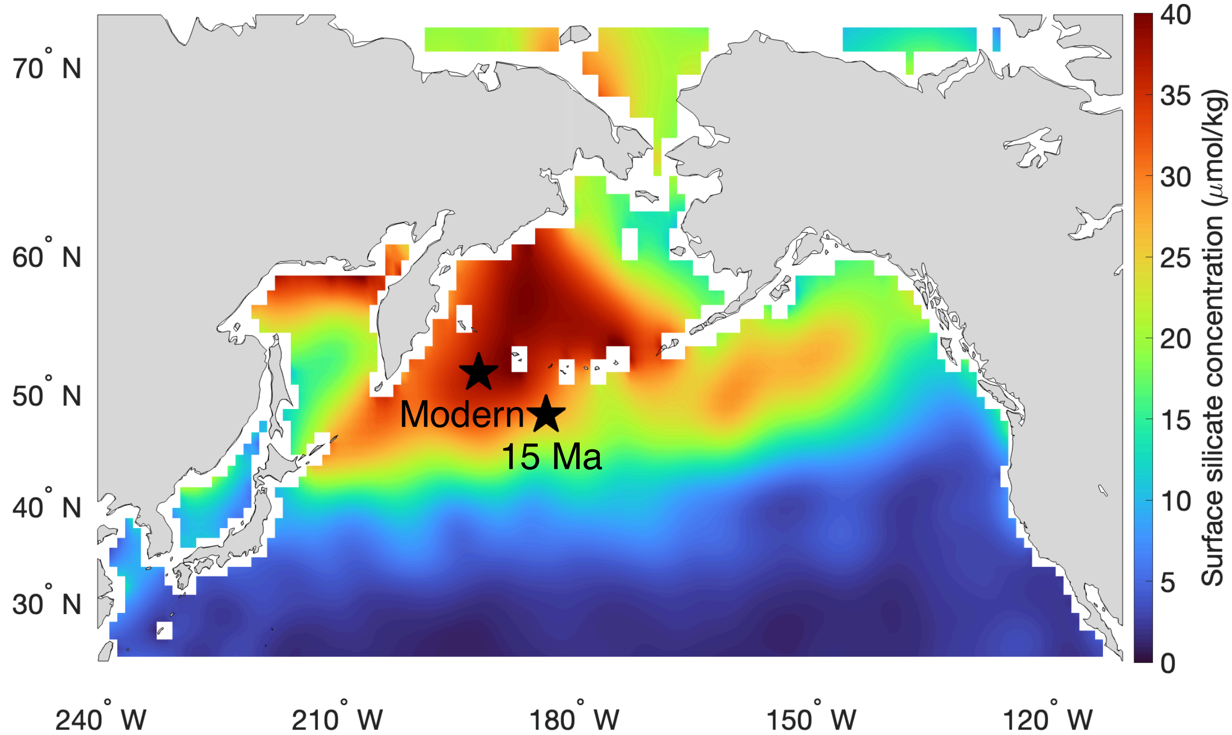

Figure 1. Mean annual surface silicate concentrations in the North Pacific Ocean from World Ocean Atlas 2023 (Garcia et al., 2024). ODP Site 884 is located within the HNLC region of the western SNP. Its paleolocation during the Middle Miocene (15 Ma) was also within the modern HNLC region.

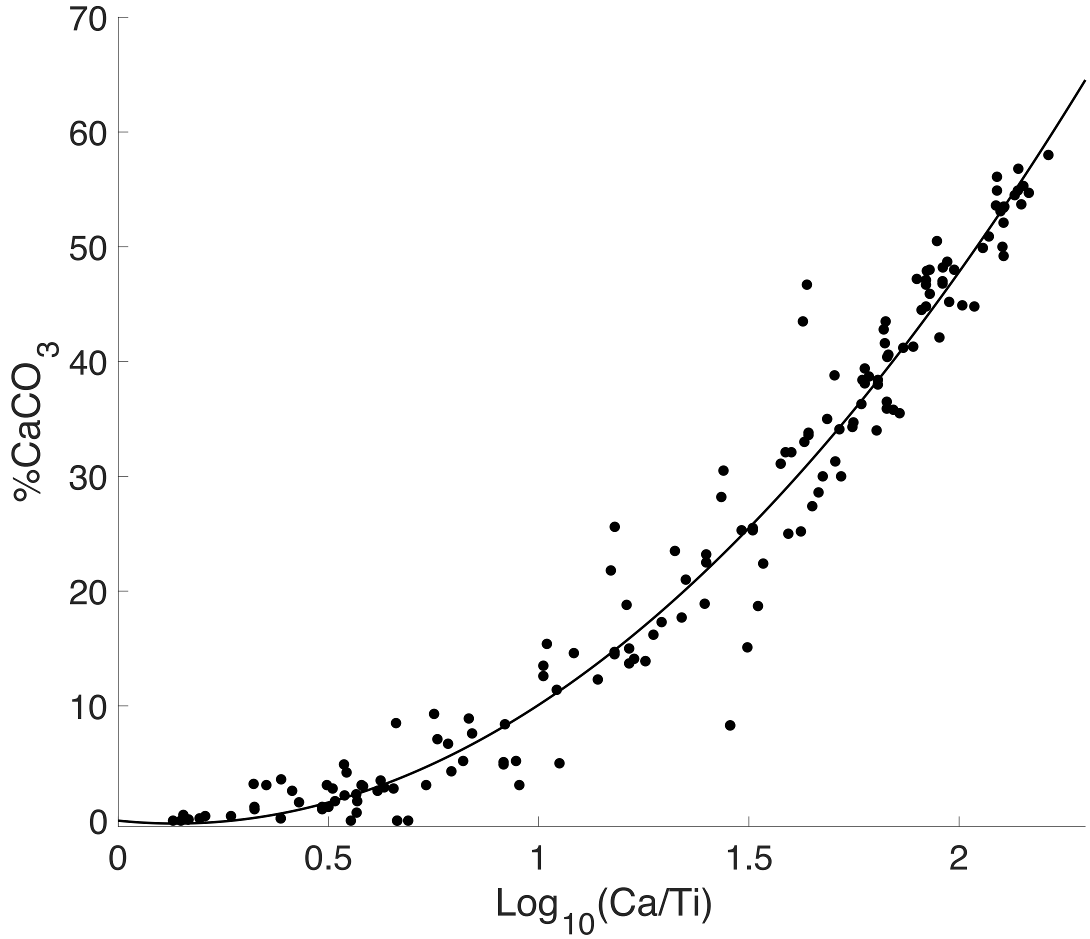

Figure 2. Mass percent calcium carbonate of measured discrete samples versus interpolated $\log_{10}$ of calcium to titanium count ratios from XRF scanning. Sample measurements (black circles) are shown with a quadratic regression (black line).

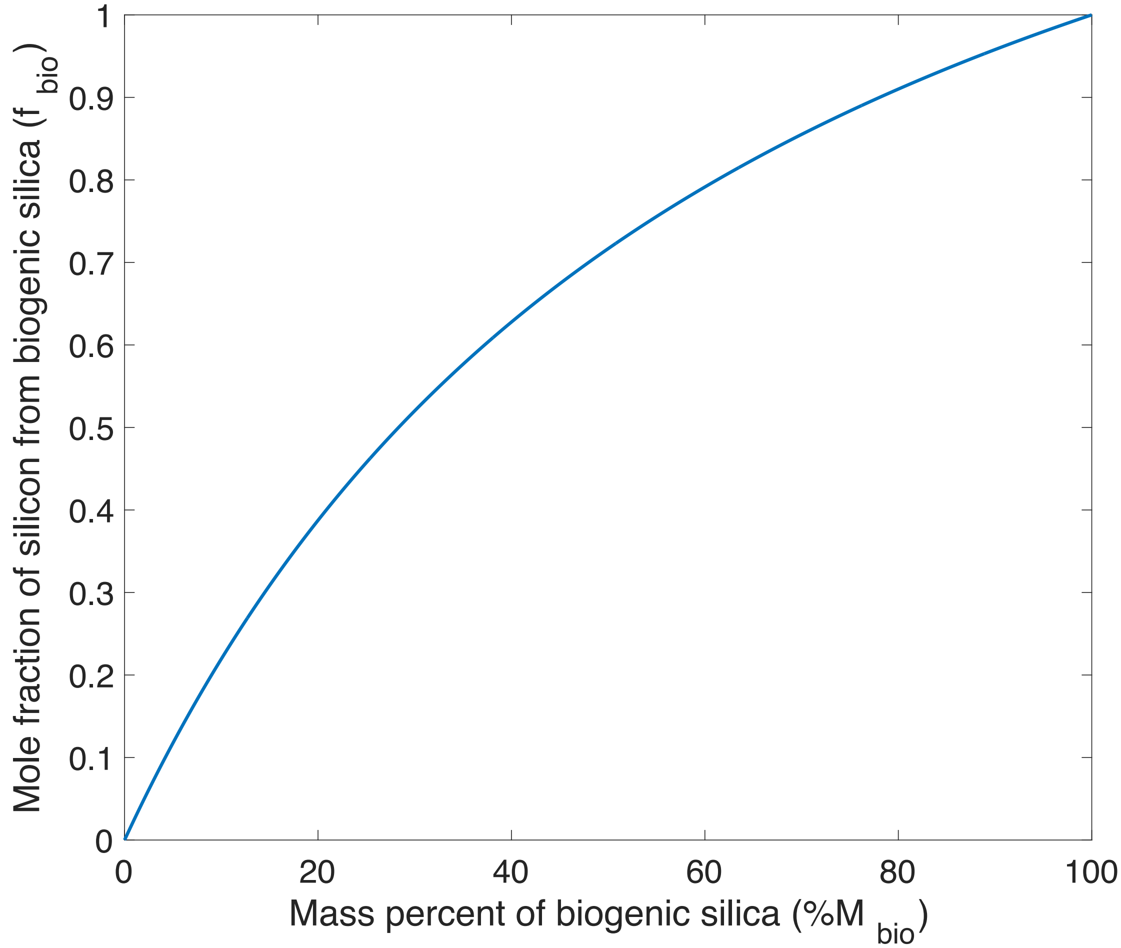

Figure 3. Nonlinearity of the relationship between mass percent biogenic silica relative to detrital material and the fraction of silicon atoms from biogenic silica. The nonlinear mixing arises from different mass percents of silicon between the two end-members.

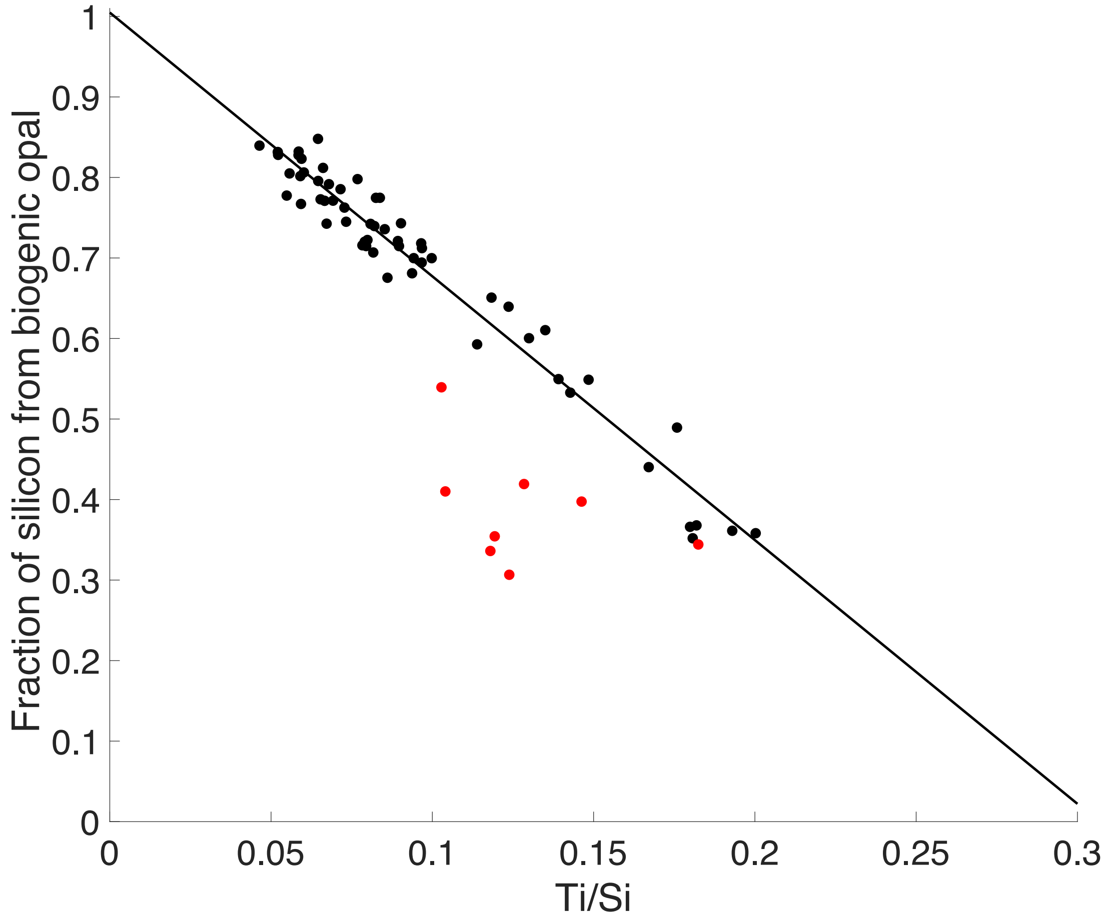

Figure 4. Fraction of silicon atoms from biogenic silica measured in samples versus interpolated titanium to silicon count ratios from XRF scanning. Sample measurements (black dots) are shown with a least-squares linear regression (black line). Measurements from samples below 589.7 mbsf (red dots) were removed from the calibration, as explained in the main text.

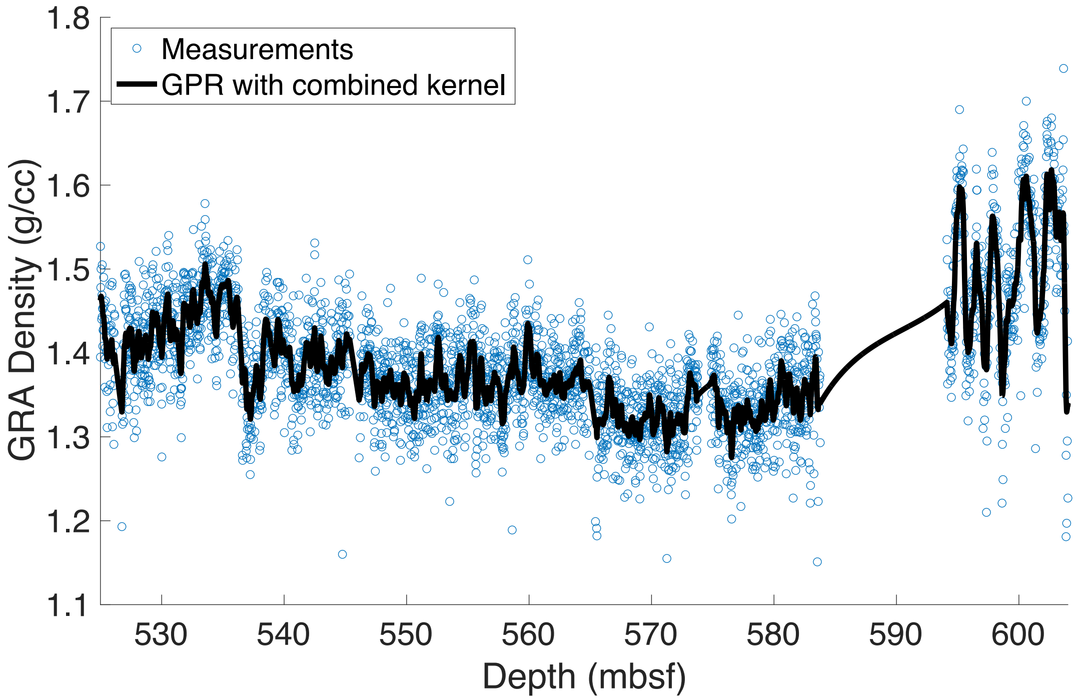

Figure 5. Shipboard GRAPE density measurements (Rea et al., 1993) from ODP Site 884B (blue circles) interpolated to any depth using a Gaussian process regression (black line). No data was reported from Core 64X between 584.4 and 592.7 mbsf.

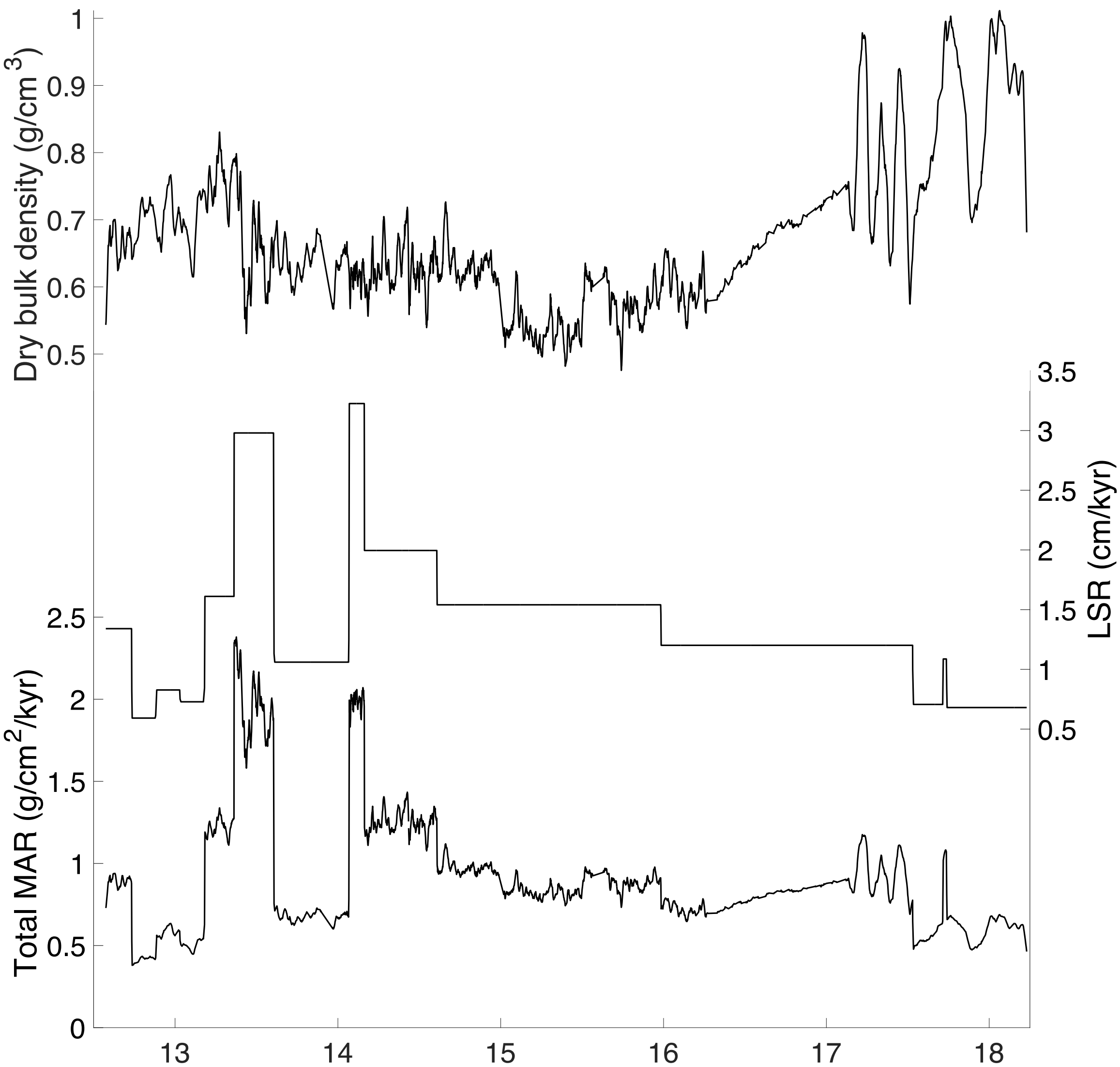

Figure 6. (a) Dry bulk density estimates from GRAPE density and lithology (b) Linear sedimentation rate (LSR) derived from the age model (Nirenberg & Herbert, 2024) and (c) Total sediment mass accumulation rates at Site 884 between 12.57 and 18.23 Ma.

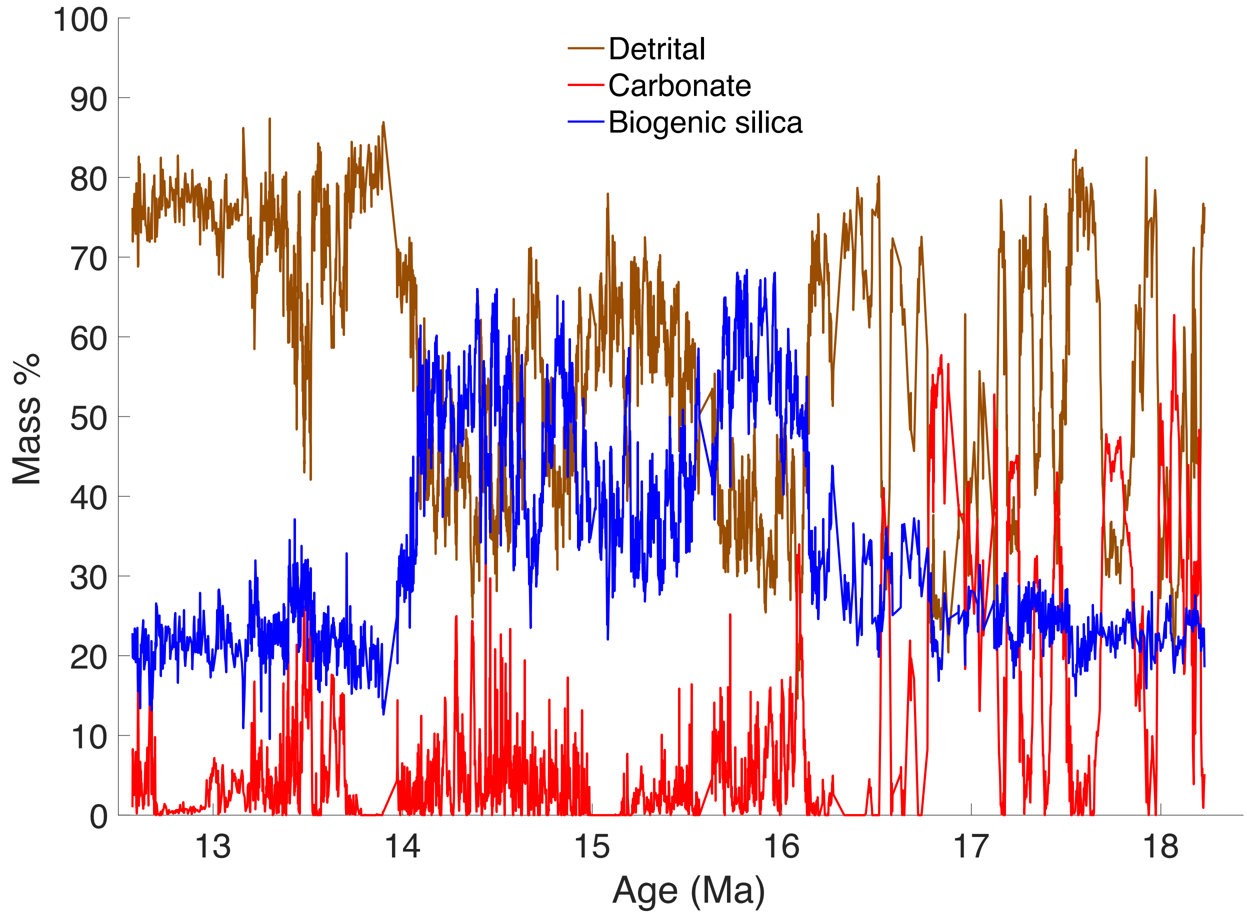

Figure 7. Mass percent contributions of sediment sources at Site 884 during the Early-Middle Miocene showing partitioning between calcium carbonate (red), biogenic silica (blue), and detrital material (brown).

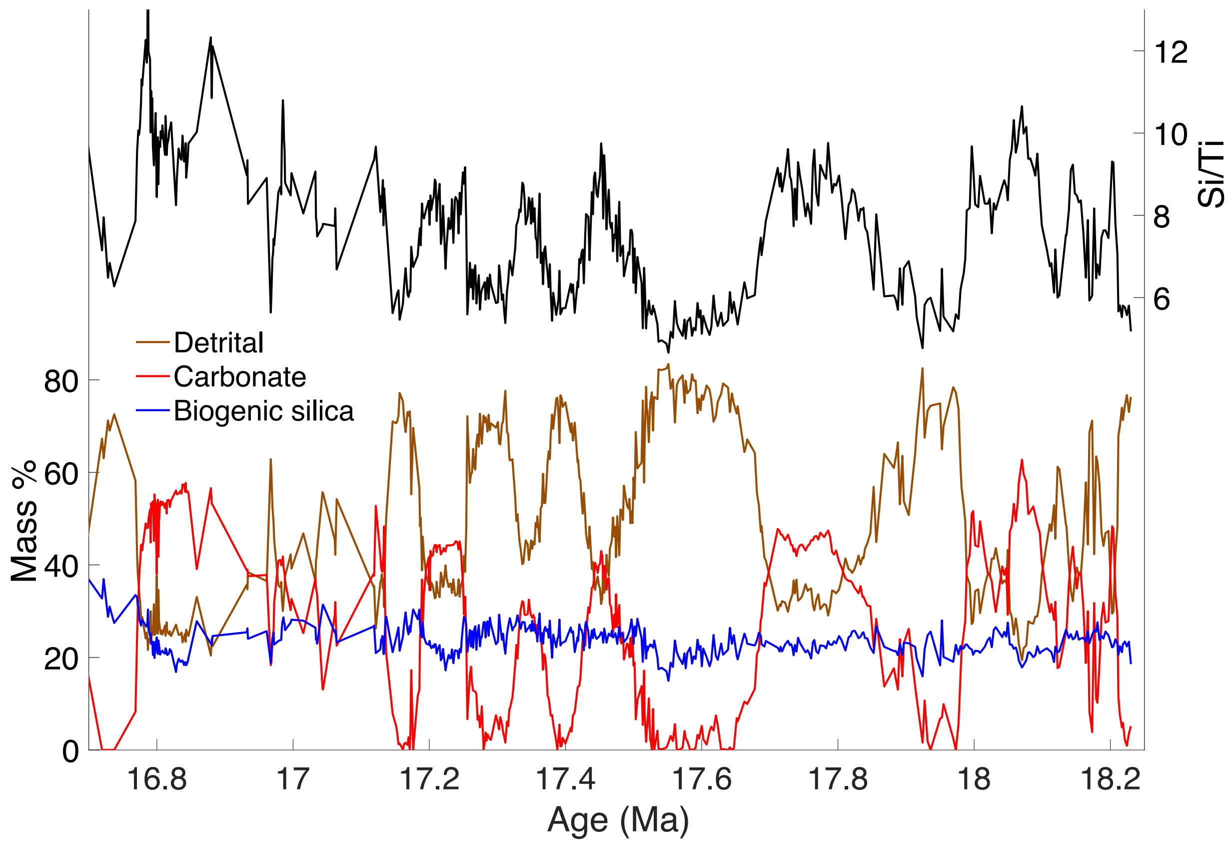

Figure 8. (a) Ratios of silicon to titanium counts and (b) sediment mass partitioning by source showing calcium carbonate (red), biogenic silica (blue), and detrital material (brown) during the Early Miocene between 16.7 and 18.23 Ma.

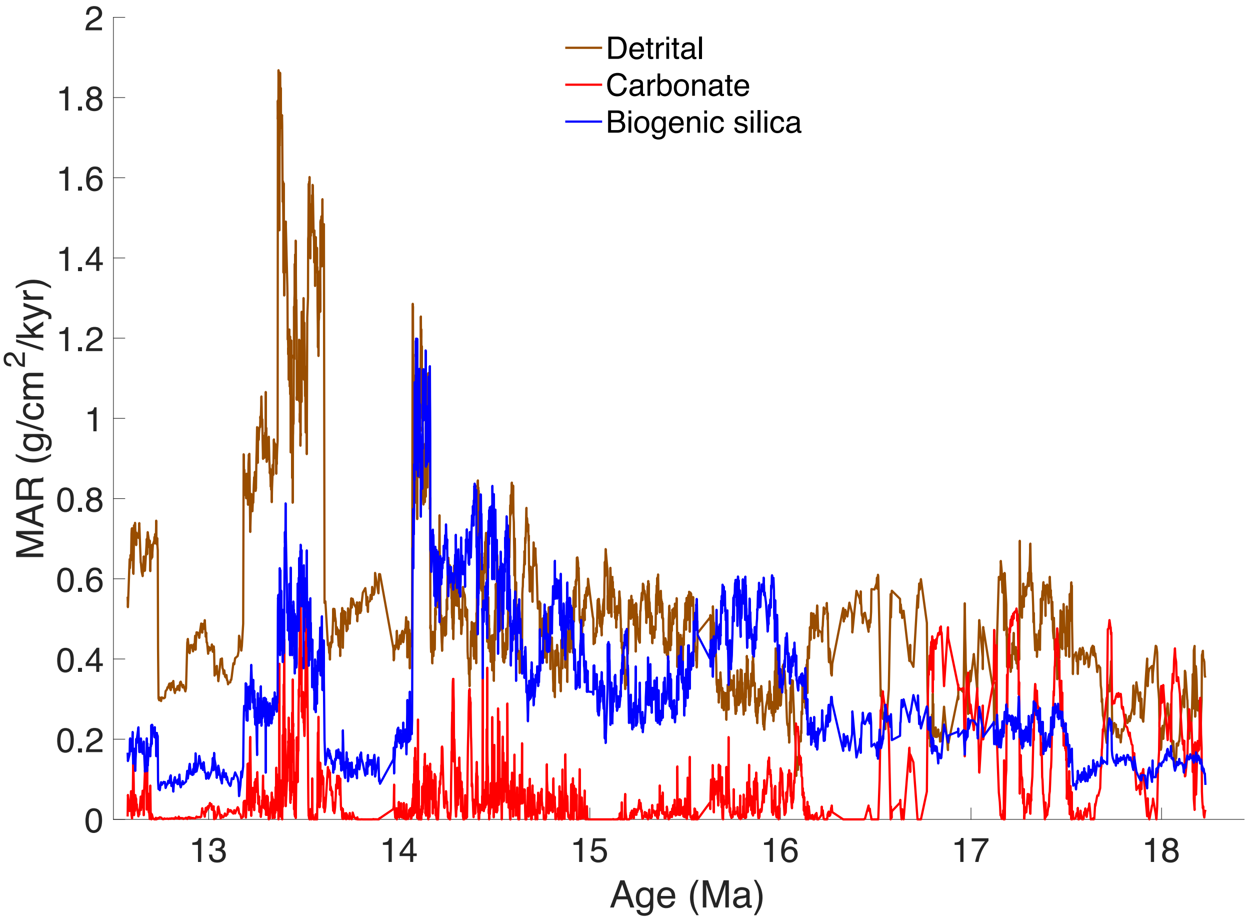

Figure 9. Mass accumulation rates of sediment sources, calcium carbonate (red), biogenic silica (blue), and detrital material (brown), at Site 884.

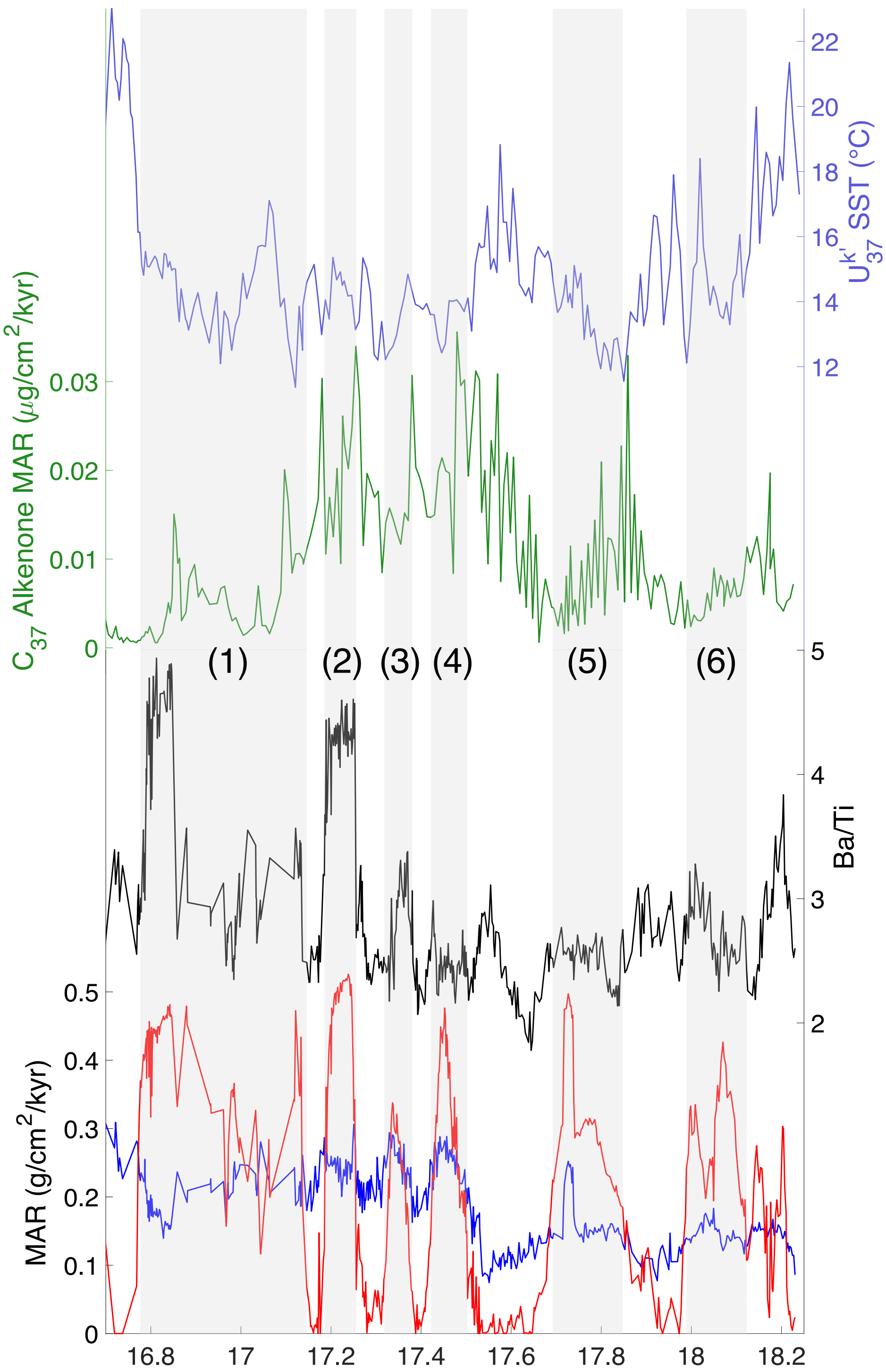

Figure 10. (a) $U^{k'}_{37}$ SSTs and (b) C_{37} alkenone accumulation rates at Site 884 from Nirenberg & Herbert (2024) (c) Ratio of barium to titanium counts and (d) mass accumulation rates of calcium carbonate (red) and biogenic silica (blue) between 16.7 and 18.23 Ma.

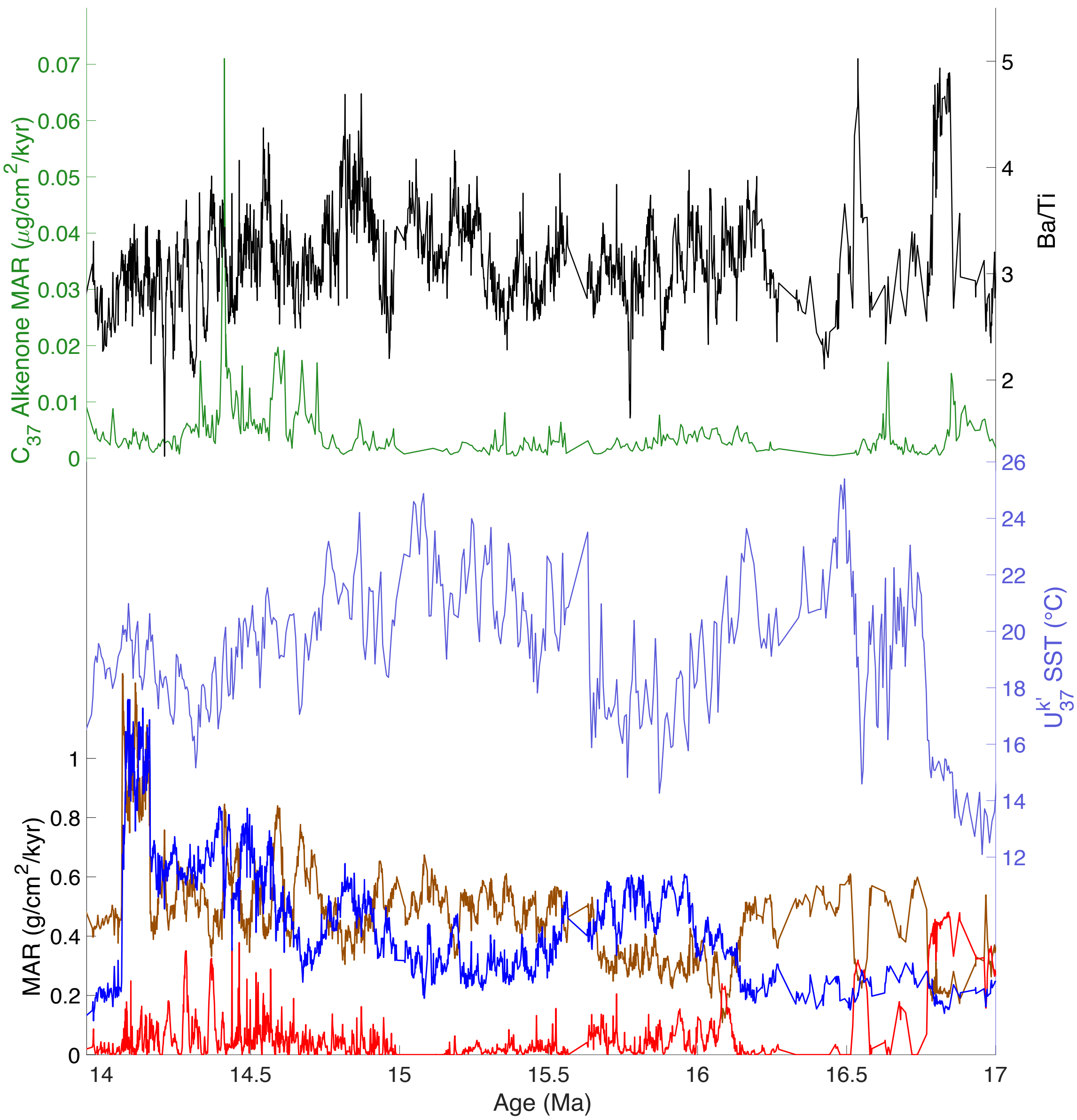

Figure 11. (a) Barium to titanium count ratios (b) C$_{37}$ alkenone accumulation rates (c) U$^{k'}_{37}$ SSTs from Nirenberg & Herbert (2024) and (d) mass accumulation rates of sediment sources to Site 884, calcium carbonate (red), biogenic silica (blue), and detrital material (brown) between 13.7 and 17 Ma.

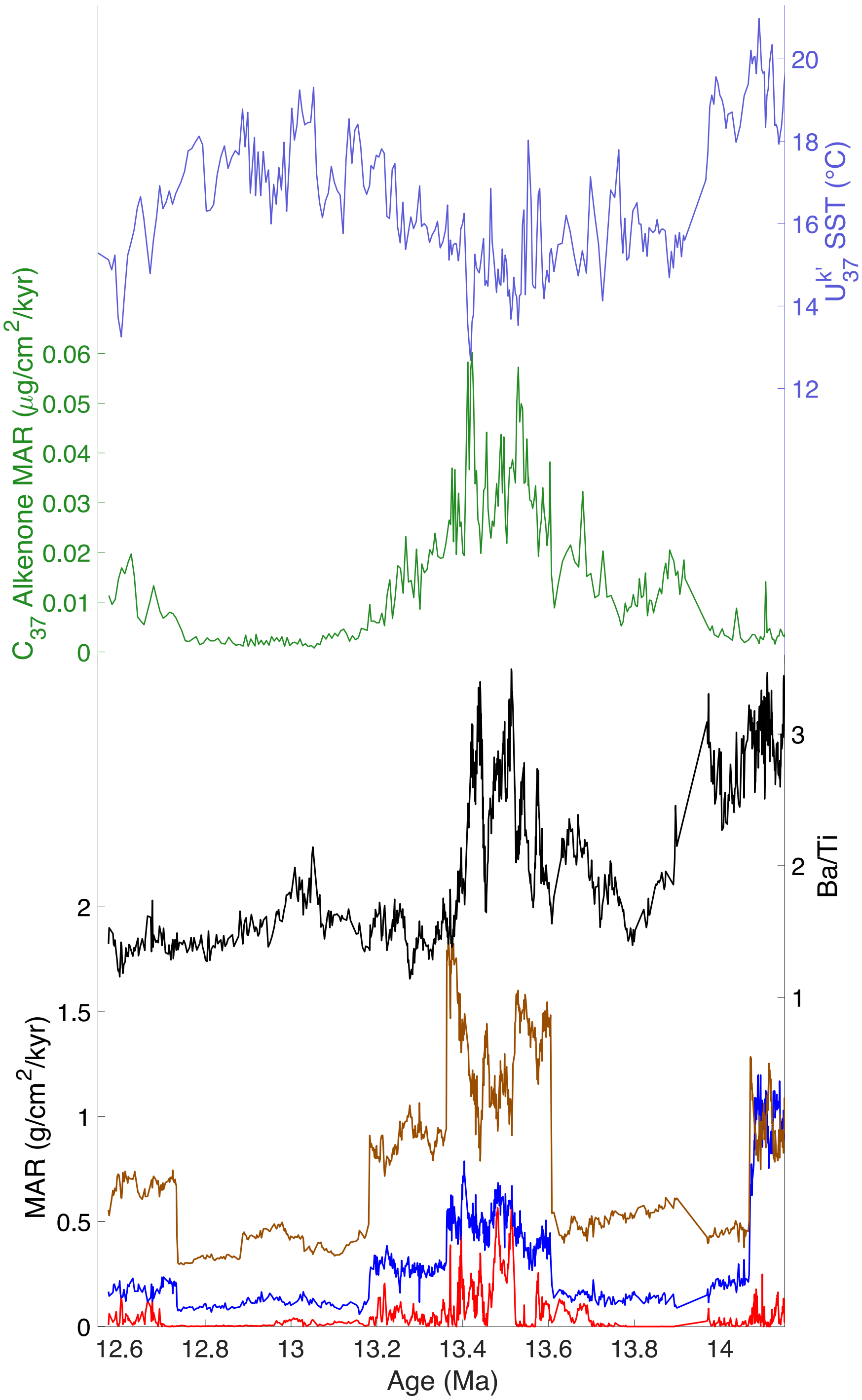

Figure 12. (a) $U^{k'}_{37}$ SSTs and (b) C_{37} alkenone accumulation rates at Site 884 from Nirenberg & Herbert (2024) (c) Ratio of barium to titanium counts and (d) mass accumulation rates of calcium carbonate (red), biogenic silica (blue), and detrital material (brown) between 12.57 and 14.15 Ma.

Supplementary figures

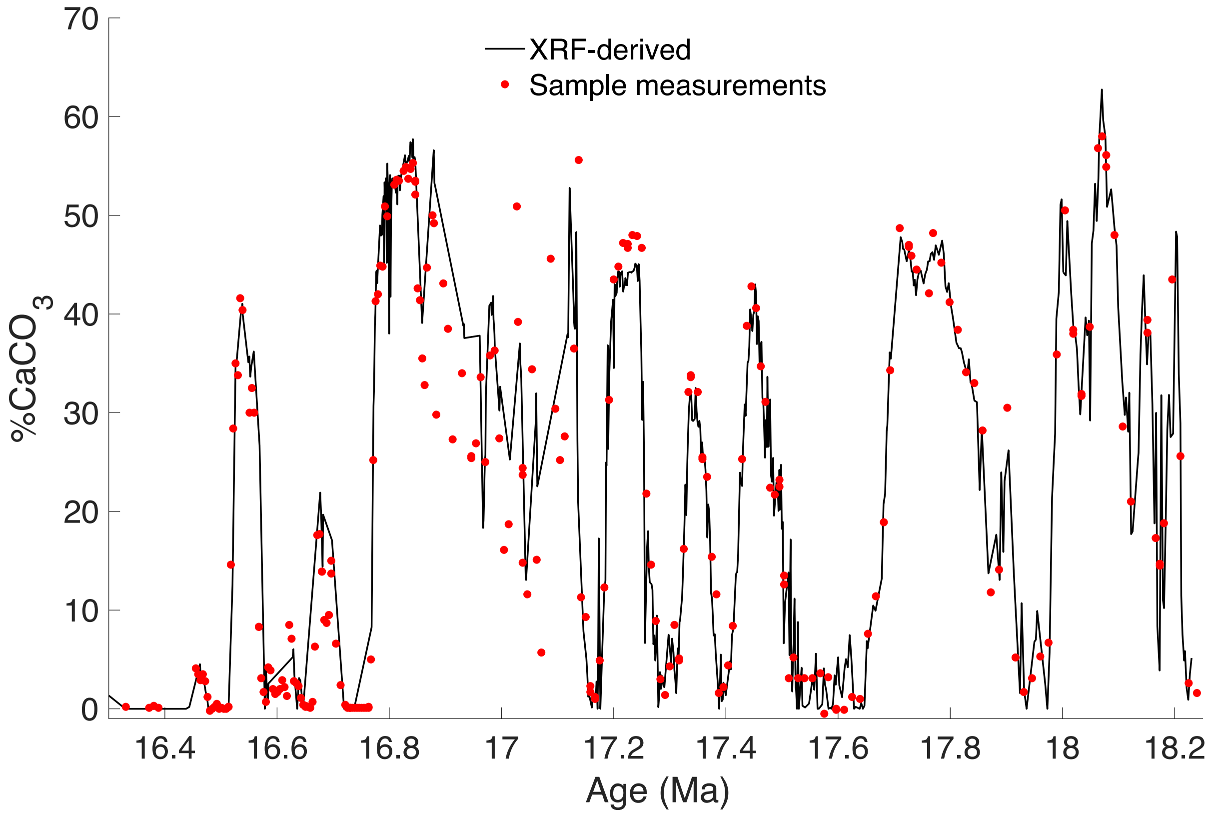

Figure S1. Comparison of estimated $\%CaCO_3$ from XRF $\log_{10}(Ca/Ti)$ (black line) and measured $\%CaCO_3$ on samples using coulometry (red points).

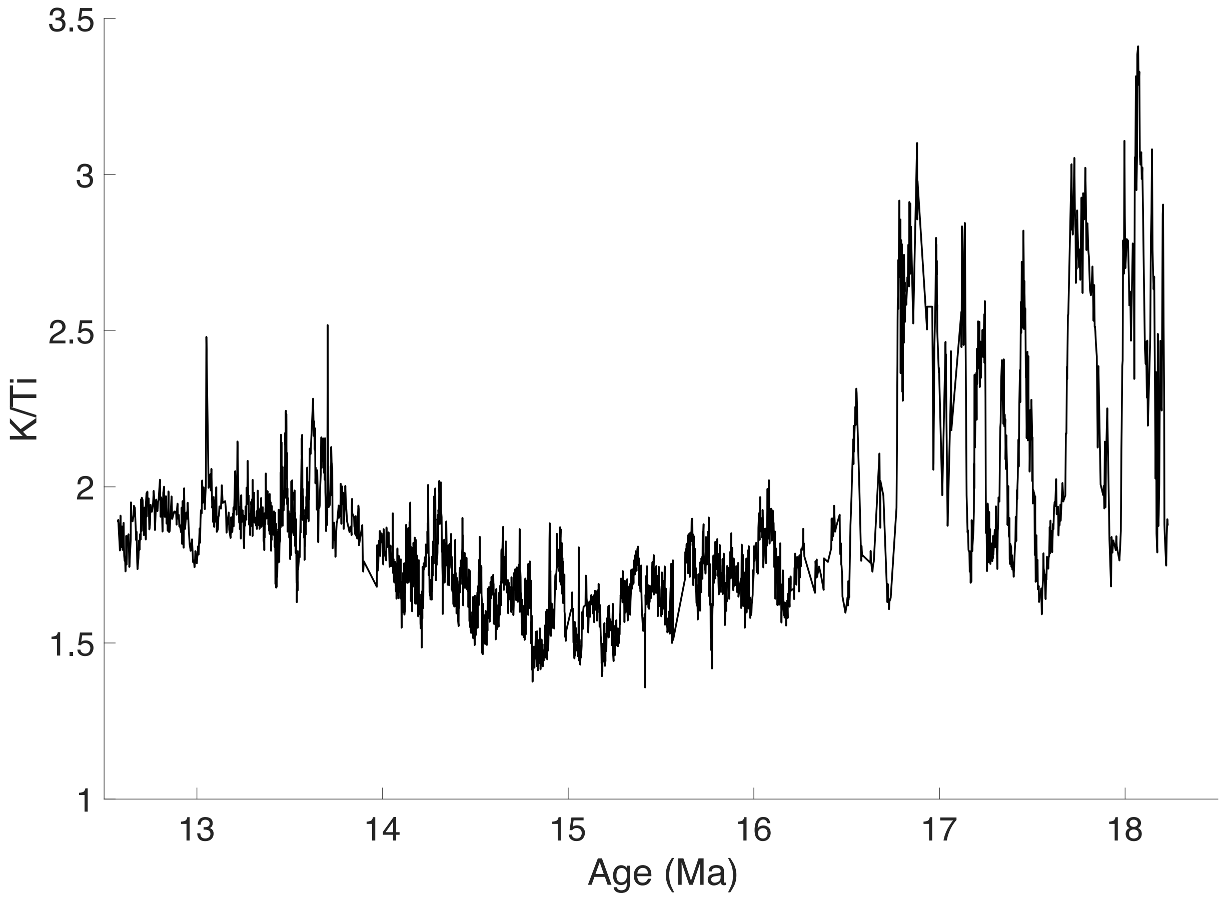

Figure S2. Potassium to titanium count ratios at Site 884.

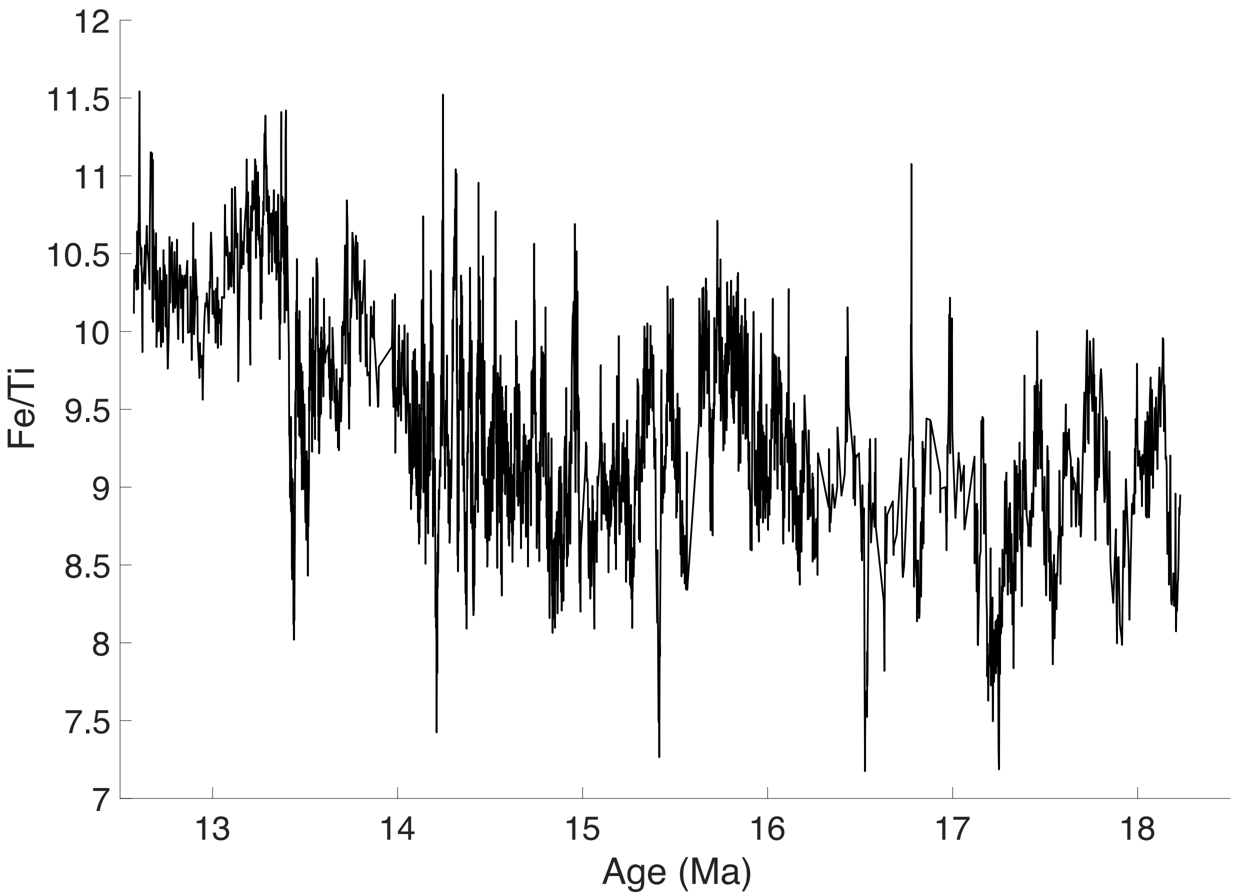

Figure S3. Iron to titanium count ratios at Site 884.

References

Abell, J. T., & Winckler, G. (2023). Long-Term Variability in Pliocene North Pacific Ocean Export Production and Its Implications for Ocean Circulation in a Warmer World. *AGU Advances*, *4*(4), e2022AV000853. https://doi.org/10.1029/2022AV000853

Abell, J. T., Winckler, G., Anderson, R. F., & Herbert, T. D. (2021). Poleward and weakened westerlies during Pliocene warmth. *Nature*, *589*(7840), 70–75. https://doi.org/10.1038/s41586-020-03062-1

Anttila, E. S. C., Macdonald, F. A., Szymanowski, D., Schoene, B., Kylander-Clark, A., Danhof, C., & Jones, D. S. (2023). Timing and tempo of organic carbon burial in the Monterey Formation of the Santa Barbara Basin and relationships with Miocene climate. *Earth and Planetary Science Letters*, *620*, 118343. https://doi.org/10.1016/j.epsl.2023.118343

Barron, J., & Gladenkov, A. (1995). Early Miocene to Pleistocene Diatom Stratigraphy of Leg 145. *Proceedings of the Ocean Drilling Program, Scientific Results*, *145*. https://doi.org/10.2973/odp.proc.sr.145.101.1995

Berger, W. H., Adelseck Jr., C. G., & Mayer, L. A. (1976). Distribution of carbonate in surface sediments of the Pacific Ocean. *Journal of Geophysical Research (1896-1977)*, *81*(15), 2617–2627. https://doi.org/10.1029/JC081i015p02617

Brunelle, B. G., Sigman, D. M., Jaccard, S. L., Keigwin, L. D., Plessen, B., Schettler, G., et al. (2010). Glacial/interglacial changes in nutrient supply and stratification in the western subarctic North Pacific since the penultimate glacial maximum. *Quaternary Science Reviews*, *29*(19), 2579–2590. https://doi.org/10.1016/j.quascirev.2010.03.010

Burls, N. J., Bradshaw, C. D., De Boer, A. M., Herold, N., Huber, M., Pound, M., et al. (2021). Simulating Miocene Warmth: Insights From an Opportunistic Multi-Model Ensemble

(MioMIP1). *Paleoceanography and Paleoclimatology*, *36*(5), e2020PA004054. https://doi.org/10.1029/2020PA004054

Burls, Natalie J., Fedorov, A. V., Sigman, D. M., Jaccard, S. L., Tiedemann, R., & Haug, G. H. (2017). Active Pacific meridional overturning circulation (PMOC) during the warm Pliocene. *Science Advances*, *3*(9), e1700156. https://doi.org/10.1126/sciadv.1700156

Cenozoic CO_2 Proxy Integration Project (CENCO$_2$PIP) Consortium. (2023). Toward a Cenozoic history of atmospheric CO_2. *Science*, *382*(6675), eadi5177. https://doi.org/10.1126/science.adi5177

Chen, T., Liu, Q., & Wang, X. (2022). Enhanced direct ventilation in the subarctic Pacific Ocean during 3.5–2.73 Ma: New evidence of elemental results from ODP Site 882. *Global and Planetary Change*, *215*, 103867. https://doi.org/10.1016/j.gloplacha.2022.103867

Dymond, J., Suess, E., & Lyle, M. (1992). Barium in Deep-Sea Sediment: A Geochemical Proxy for Paleoproductivity. *Paleoceanography*, *7*(2), 163–181. https://doi.org/10.1029/92PA00181

Flower, B. P., & Kennett, J. P. (1993). Relations between Monterey Formation deposition and middle Miocene global cooling: Naples Beach section, California. *Geology*, *21*(10), 877–880. https://doi.org/10.1130/0091-7613(1993)021%253C0877:RBMFDA%253E2.3.CO;2

Francois, R., Honjo, S., Manganini, S. J., & Ravizza, G. E. (1995). Biogenic barium fluxes to the deep sea: Implications for paleoproductivity reconstruction. *Global Biogeochemical Cycles*, *9*(2), 289–303. https://doi.org/10.1029/95GB00021

Garcia, H. E., Bouchard, C., Cross, S. L., Paver, C. R., Reagan, J. R., Boyer, T. P., et al. (2024). World Ocean Atlas 2023, Volume 4: Dissolved Inorganic Nutrients (phosphate, nitrate and nitrate+nitrite, silicate). https://doi.org/10.25923/39QW-7J08

Gray, W. R., Rae, J. W. B., Wills, R. C. J., Shevenell, A. E., Taylor, B., Burke, A., et al. (2018). Deglacial upwelling, productivity and CO_2 outgassing in the North Pacific Ocean. *Nature Geoscience*, *11*(5), 340–344. https://doi.org/10.1038/s41561-018-0108-6

Harrison, P. J., Boyd, P. W., Varela, D. E., Takeda, S., Shiomoto, A., & Odate, T. (1999). Comparison of factors controlling phytoplankton productivity in the NE and NW subarctic Pacific gyres. *Progress in Oceanography*, *43*(2), 205–234. https://doi.org/10.1016/S0079-6611(99)00015-4

Haug, G. H., Sigman, D. M., Tiedemann, R., Pedersen, T. F., & Sarnthein, M. (1999). Onset of permanent stratification in the subarctic Pacific Ocean. *Nature*, *401*(6755), 779–782. https://doi.org/10.1038/44550

Hayes, C. T., Costa, K. M., Anderson, R. F., Calvo, E., Chase, Z., Demina, L. L., et al. (2021). Global Ocean Sediment Composition and Burial Flux in the Deep Sea. *Global Biogeochemical Cycles*, *35*(4), e2020GB006769. https://doi.org/10.1029/2020GB006769

Herbert, T. D., & Mayer, L. A. (1991). Long climatic time series from sediment physical property measurements. *Journal of Sedimentary Research*, *61*(7), 1089–1108. https://doi.org/10.1306/D4267843-2B26-11D7-8648000102C1865D

Herbert, T. D., Lawrence, K. T., Tzanova, A., Peterson, L. C., Caballero-Gill, R., & Kelly, C. S. (2016). Late Miocene global cooling and the rise of modern ecosystems. *Nature Geoscience*, *9*(11), 843–847. https://doi.org/10.1038/ngeo2813

Holbourn, A., Kuhnt, W., Lyle, M., Schneider, L., Romero, O., & Andersen, N. (2014). Middle Miocene climate cooling linked to intensification of eastern equatorial Pacific upwelling. *Geology*, *42*(1), 19–22. https://doi.org/10.1130/G34890.1

Holbourn, A., Kuhnt, W., Kulhanek, D. K., Mountain, G., Rosenthal, Y., Sagawa, T., et al. (2024). Re-organization of Pacific overturning circulation across the Miocene Climate Optimum. *Nature Communications*, *15*(1), 8135. https://doi.org/10.1038/s41467-024-52516-x

Hutchinson, D. K., Meissner, K. J., Menviel, L., Wright, N. M., Berg, J., & Acosta, R. P. (2025). Pacific and Atlantic Modes of Overturning in the Miocene Climatic Optimum. *Paleoceanography and Paleoclimatology*, *40*(11), e2025PA005220. https://doi.org/10.1029/2025PA005220

Jaccard, S. L., Haug, G. H., Sigman, D. M., Pedersen, T. F., Thierstein, H. R., & Röhl, U. (2005). Glacial/Interglacial Changes in Subarctic North Pacific Stratification. *Science*, *308*(5724), 1003–1006. https://doi.org/10.1126/science.1108696

Jaccard, S. L., Galbraith, E. D., Sigman, D. M., & Haug, G. H. (2010). A pervasive link between Antarctic ice core and subarctic Pacific sediment records over the past 800 kyrs. *Quaternary Science Reviews*, *29*(1), 206–212. https://doi.org/10.1016/j.quascirev.2009.10.007

Keller, G., & Barron, J. A. (1983). Paleoceanographic implications of Miocene deep-sea hiatuses. *GSA Bulletin*, *94*(5), 590–613. https://doi.org/10.1130/0016-7606(1983)94%253C590:PIOMDH%253E2.0.CO;2

Kerr, B. C., Scholl, D. W., & Klemperer, S. L. (2005). Seismic stratigraphy of Detroit Seamount, Hawaiian-Emperor seamount chain: Post-hot-spot shield-building volcanism and deposition of the Meiji drift. *Geochemistry, Geophysics, Geosystems*, *6*(7). https://doi.org/10.1029/2004GC000705

Kochhann, K. G. D., Holbourn, A., Kuhnt, W., Channell, J. E. T., Lyle, M., Shackford, J. K., et al. (2016). Eccentricity pacing of eastern equatorial Pacific carbonate dissolution cycles during the Miocene Climatic Optimum. *Paleoceanography*, *31*(9), 1176–1192. https://doi.org/10.1002/2016PA002988

Kuhnert, H., Bickert, T., & Paulsen, H. (2009). Southern Ocean frontal system changes precede Antarctic ice sheet growth during the middle Miocene. *Earth and Planetary Science Letters*, *284*(3), 630–638. https://doi.org/10.1016/j.epsl.2009.05.030

Larsen, H. C., Saunders, A. D., Clift, P. D., Beget, J., Wei, W., & Spezzaferri, S. (1994). Seven Million Years of Glaciation in Greenland. *Science*, *264*(5161), 952–955. https://doi.org/10.1126/science.264.5161.952

Leutert, T. J., Modestou, S., Bernasconi, S. M., & Meckler, A. N. (2021). Southern Ocean bottom-water cooling and ice sheet expansion during the middle Miocene climate transition. *Climate of the Past*, *17*(5), 2255–2271. https://doi.org/10.5194/cp-17-2255-2021

Li, Z., Zhang, Y. G., Torres, M., & Mills, B. J. W. (2023). Neogene burial of organic carbon in the global ocean. *Nature*, *613*(7942), 90–95. https://doi.org/10.1038/s41586-022-05413-6

Lyle, M., Koizumi, I., Richter, C., Moore, T. C., & Jr. (Eds.). (2000). *Proceedings of the Ocean Drilling Program, 167 Scientific Results* (Vol. 167). Ocean Drilling Program. https://doi.org/10.2973/odp.proc.sr.167.2000

Lyle, Mitchell. (2003). Neogene carbonate burial in the Pacific Ocean. *Paleoceanography*, *18*(3). https://doi.org/10.1029/2002PA000777

Marincovich, L., & Gladenkov, A. Y. (1999). Evidence for an early opening of the Bering Strait. *Nature*, *397*(6715), 149–151. https://doi.org/10.1038/16446

Martin, J. H., Fitzwater, S. E., & Gordon, R. M. (1990). Iron deficiency limits phytoplankton growth in Antarctic waters. *Global Biogeochemical Cycles*, *4*(1), 5–12. https://doi.org/10.1029/GB004i001p00005

Miller, K. G., Wright, J. D., & Fairbanks, R. G. (1991). Unlocking the Ice House: Oligocene-Miocene oxygen isotopes, eustasy, and margin erosion. *Journal of Geophysical Research: Solid Earth*, *96*(B4), 6829–6848. https://doi.org/10.1029/90JB02015

Mitchell, B. G., Brody, E. A., Holm-Hansen, O., McClain, C., & Bishop, J. (1991). Light limitation of phytoplankton biomass and macronutrient utilization in the Southern Ocean. *Limnology and Oceanography*, *36*(8), 1662–1677. https://doi.org/10.4319/lo.1991.36.8.1662

Modestou, S. E., Leutert, T. J., Fernandez, A., Lear, C. H., & Meckler, A. N. (2020). Warm Middle Miocene Indian Ocean Bottom Water Temperatures: Comparison of Clumped Isotope and Mg/Ca-Based Estimates. *Paleoceanography and Paleoclimatology*, *35*(11), e2020PA003927. https://doi.org/10.1029/2020PA003927

Nirenberg, J. E., & Herbert, T. D. (2024). North Pacific warmth synchronous with the Miocene Climatic Optimum. *Geology*. https://doi.org/10.1130/G52432.1

Nishikawa, H., Mitsudera, H., Okunishi, T., Ito, S., Wagawa, T., Hasegawa, D., et al. (2021). Surface water pathways in the subtropical–subarctic frontal zone of the western North Pacific. *Progress in Oceanography*, *199*, 102691. https://doi.org/10.1016/j.pocean.2021.102691

Novak, J. B., Caballero-Gill, R. P., Rose, R. M., Herbert, T. D., & Dowsett, H. J. (2024). Isotopic evidence against North Pacific Deep Water formation during late Pliocene warmth. *Nature Geoscience*, *17*(8), 795–802. https://doi.org/10.1038/s41561-024-01500-7

Oyedotun, T. D. T. (2018). X-ray fluorescence (XRF) in the investigation of the composition of earth materials: a review and an overview. *Geology, Ecology, and Landscapes*, *2*(2), 148–154. https://doi.org/10.1080/24749508.2018.1452459

Raja, M., & Rosell-Melé, A. (2021). Appraisal of sedimentary alkenones for the quantitative reconstruction of phytoplankton biomass. *Proceedings of the National Academy of Sciences*, *118*(2), e2014787118. https://doi.org/10.1073/pnas.2014787118

Rea, D. K., Basov, La., Janecek, T. R., Palmer-Julson, A., & et al. (Eds.). (1993). *Proceedings of the Ocean Drilling Program|145 Initial Reports* (Vol. 145). Ocean Drilling Program. https://doi.org/10.2973/odp.proc.ir.145.1993

Russell, J. M., & Johnson, T. C. (2005). A high-resolution geochemical record from Lake Edward, Uganda Congo and the timing and causes of tropical African drought during the late Holocene. *Quaternary Science Reviews*, *24*(12), 1375–1389. https://doi.org/10.1016/j.quascirev.2004.10.003

Sarmiento, J. L., & Gruber, N. (2006). *Ocean biogeochemical dynamics*. Princeton: Princeton University Press.

Serno, S., Winckler, G., Anderson, R. F., Hayes, C. T., Ren, H., Gersonde, R., & Haug, G. H. (2014). Using the natural spatial pattern of marine productivity in the Subarctic North Pacific to evaluate paleoproductivity proxies. *Paleoceanography*, *29*(5), 438–453. https://doi.org/10.1002/2013PA002594

Shevenell, A. E., Kennett, J. P., & Lea, D. W. (2004). Middle Miocene Southern Ocean Cooling and Antarctic Cryosphere Expansion. *Science*, *305*(5691), 1766–1770. https://doi.org/10.1126/science.1100061

Sigman, D. M., Jaccard, S. L., & Haug, G. H. (2004). Polar ocean stratification in a cold climate. *Nature*, *428*(6978), 59–63. https://doi.org/10.1038/nature02357

Steinthorsdottir, M., Coxall, H. K., de Boer, A. M., Huber, M., Barbolini, N., Bradshaw, C. D., et al. (2021). The Miocene: The Future of the Past. *Paleoceanography and Paleoclimatology*, *36*(4), e2020PA004037. https://doi.org/10.1029/2020PA004037

Tsuda, A., Takeda, S., Saito, H., Nishioka, J., Nojiri, Y., Kudo, I., et al. (2003). A Mesoscale Iron Enrichment in the Western Subarctic Pacific Induces a Large Centric Diatom Bloom. *Science*, *300*(5621), 958–961. https://doi.org/10.1126/science.1082000

VanLaningham, S., Pisias, N. G., Duncan, R. A., & Clift, P. D. (2009). Glacial–interglacial sediment transport to the Meiji Drift, northwest Pacific Ocean: Evidence for timing of Beringian outwashing. *Earth and Planetary Science Letters*, *277*(1), 64–72. https://doi.org/10.1016/j.epsl.2008.09.033

Vincent, E., & Berger, W. H. (1985). Carbon Dioxide and Polar Cooling in the Miocene: The Monterey Hypothesis. In *The Carbon Cycle and Atmospheric CO_2: Natural Variations Archean to Present* (pp. 455–468). American Geophysical Union (AGU). https://doi.org/10.1029/GM032p0455

Westerhold, T., Marwan, N., Drury, A. J., Liebrand, D., Agnini, C., Anagnostou, E., et al. (2020). An astronomically dated record of Earth's climate and its predictability over the last 66 million years. *Science*, *369*(6509), 1383–1387. https://doi.org/10.1126/science.aba6853

Witkowski, C. R., Von Der Heydt, A. S., Valdes, P. J., Van Der Meer, M. T. J., Schouten, S., & Sinninghe Damsté, J. S. (2024). Continuous sterane and phytane $\delta^{13}C$ record reveals a substantial pCO_2 decline since the mid-Miocene. *Nature Communications*, *15*(1), 5192. https://doi.org/10.1038/s41467-024-47676-9

Woodruff, F., & Savin, S. M. (1989). Miocene deepwater oceanography. *Paleoceanography*, *4*(1), 87–140. https://doi.org/10.1029/PA004i001p00087

Yasunaka, S., Nojiri, Y., Nakaoka, S., Ono, T., Whitney, F. A., & Telszewski, M. (2014). Mapping of sea surface nutrients in the North Pacific: Basin-wide distribution and seasonal to interannual variability. *Journal of Geophysical Research: Oceans*, *119*(11), 7756–7771. https://doi.org/10.1002/2014JC010318

Yuan, X., & Talley, L. D. (1996). The subarctic frontal zone in the North Pacific: Characteristics of frontal structure from climatological data and synoptic surveys. *Journal of Geophysical Research: Oceans*, *101*(C7), 16491–16508. https://doi.org/10.1029/96JC01249

CHAPTER 4

East Antarctic ocean-ice sheet interactions during Miocene warmth

Jared E. Nirenberg[1] and Timothy D. Herbert[1]

[1]Department of Earth, Environmental, and Planetary Sciences, Brown University, Providence, Rhode Island 02912, USA

Abstract

Regions of Antarctica were most recently ice-free during the Miocene Climatic Optimum (MCO, ~17-14 Ma). During this warm interval, the East Antarctic Ice Sheet (EAIS) exhibited highly dynamic behavior and episodic wide-scale retreat associated with global sea level rise. During the subsequent Middle Miocene Climate Transition (MMCT), the EAIS expanded and stabilized with contemporaneous global cooling. However, little is directly known about drivers of EAIS behavior during the Miocene due to a lack of continuous, high-resolution climate records near Antarctica. Here, we present multi-proxy biomarker records of sea surface temperatures (SSTs) from the polar Southern Ocean spanning 5 to 19 Ma, with high-resolution data spanning the MMCT, to constrain ocean-ice sheet interactions. We find peak SSTs during the MCO up to 18°C warmer than modern as well as cooling synchronous with the establishment of permanent Antarctic glaciation and broader global cooling during the MMCT and Late Miocene. Ice rafting to the same site disappeared when SSTs warmed above 12°C, demonstrating the vulnerability of marine-based ice to ocean warming. However, terrestrial-based ice exhibited threshold behavior as transient cooling during the MMCT crossed a tipping point for terrestrial ice sheet growth and stabilization, which subsequent warming was not sufficient to reverse.

Introduction

The East Antarctic Ice Sheet (EAIS) contains the majority of modern global ice volume, estimated at 53.3 meters of sea level equivalent (Fretwell et al., 2013). As such, ice mass loss from the EAIS represents the largest potential contributor to sea level rise due to anthropogenic warming, several times the total possible contributions from ice loss in Greenland and West

Antarctica. However, terrestrial-based ice in East Antarctica is considered more resilient to warming than other more sensitive areas, such as the portions of the EAIS grounded below sea level (e.g. Wilkes basin, Aurora basin) and the West Antarctic Ice Sheet. While model simulations show that high elevation areas of East Antarctica are the first regions to glaciate with cooling and the most resilient to warming (DeConto et al., 2008; DeConto & Pollard, 2003), geologic observations are needed to constrain the response of Antarctic ice sheets to warming beyond conditions observed in instrumental records and to temperatures during past intervals as analogues for future warmth.

The Miocene Epoch (5.33 to 23 Ma) is a primary target interval for these geologic constraints as Antarctic ice sheet extent was highly variable during a wide range of warmer than modern climate states. The Miocene Climatic Optimum (MCO) was the warmest interval since the initiation of wide-scale Antarctic glaciation during the Eocene-Oligocene transition (Westerhold et al., 2020). MCO global surface temperatures averaged 5-12°C warmer than modern (Burls et al., 2021; Herbert et al., 2022; Westerhold et al., 2020), and atmospheric CO_2 concentrations were likely near or higher than modern (Cenozoic CO_2 Proxy Integration Project (CENCO$_2$PIP) Consortium, 2023 and references therein). Polar amplification and a reduced meridional temperature gradient were fundamental aspects of Miocene global warmth (Herbert et al., 2016; Liu et al., 2022; Nirenberg & Herbert, 2024; Super et al., 2020).

Geologic records from Antarctica demonstrate striking MCO warmth and periodic wide-scale retreat of the EAIS. Conifers and southern beech trees related to those found in modern subantarctic and austral-alpine regions vegetated portions of both East and West Antarctica during the MCO (Anderson et al., 2011; Feakins et al., 2012; Sangiorgi et al., 2018; Warny et al., 2009). Mosses, insects, and ostracods thrived in lakes in the Transantarctic Mountains (Lewis et al., 2008). Expansion of these Antarctic terrestrial ecosystems coincided with negative excursions in benthic foraminiferal oxygen isotope records (benthic $\delta^{18}O$), demonstrating association with warming and ice sheet retreat (Feakins et al., 2012; Holbourn et al., 2014, 2015).

After the MCO, the Antarctic environment transitioned towards modern cold polar desert conditions during the MMCT and late Miocene global cooling interval. During the Mi3 glaciation (~13.8 Ma, Miller et al., 1991), the EAIS expanded to the coast as large pulses of ice-rafted debris (IRD) accumulated around the Antarctic margin (Pierce et al., 2017) coincident with a positive excursion in benthic $\delta^{18}O$ reflecting ice sheet expansion (Holbourn et al., 2014; Shevenell et al., 2004) and lowered sea level (John et al., 2011; Miller et al., 2020). Tundra and woodland biomes on Antarctica were reduced with ice sheet expansion (Lewis et al., 2008; Warny et al., 2009), though local refugia for Antarctic vegetation persisted throughout the Neogene (Anderson et al., 2011; Rees-Owen et al., 2018). EAIS volume also stabilized after expansion during the MMCT, with orbital-scale variations in sea level and benthic $\delta^{18}O$ decreasing by half from the MCO (Miller et al., 2020).

However, the quantitative evolution of Antarctic surface temperatures and resulting forcings of ice sheet behavior during these periods were unclear. While sedimentary records from the sub-Antarctic have provided Miocene temperature reconstructions using a variety of proxies (Herbert et al., 2016; Hou et al., 2023; Kuhnert et al., 2009; Leutert et al., 2020; Shevenell et al., 2004), contemporaneous temperature records south of the polar front are scarce and discontinuous. Ice-proximal records from the Ross Sea shelf (ANDRILL-2A) capture snapshots of MCO warmth (Levy et al., 2016), but unconformities due to glacial expansion onto the shelf prevent continuous records across the MMCT (Acton et al., 2008). Poor core recovery prevents a continuous stratigraphic section from the continental rise offshore Wilkes Land (IODP U1356).

Here, we analyze a stratigraphic section spanning most of the Miocene (5-21 Ma) that was recovered at Ocean Drilling Program (ODP) Site 1165 (O'Brien et al., 2001) in Prydz Bay with good core recovery (>85%) and no significant hiatuses. The site location proximal to the Amery Ice Shelf allowed for the accumulation of sediments both from the marine surface as well as IRD from the nearby ice margin.

We utilize the record from Site 1165 to quantify the continuous evolution of polar Southern Ocean SSTs from 5 to 19 Ma using multiple biomarker proxy reconstructions. $U^{k'}_{37}$ and TEX_{86} show good agreement throughout the long-term records with peak temperatures during the MCO and cooling during the MMCT and Late Miocene in accordance with global trends. In addition, we present orbital resolution $U^{k'}_{37}$ data during the MMCT to constrain the climatic drivers of EAIS expansion during this interval. We find 10°C cooling over 120 kyr, synchronous with EAIS expansion, though SSTs nearly return to warm MCO-like values within 400 kyr after glaciation. Comparison of IRD and SSTs at Site 1165 show that the marine margin of the ice sheet was highly sensitive to nearby ocean thermal forcing both before and after EAIS expansion during the MMCT. However, benthic $\delta^{18}O$ show a more stepwise, monotonic increase in terrestrial ice volume during MMCT cooling with no return to wide-scale deglaciation in East Antarctica after 13.8 Ma, despite polar SSTs warming to near-MCO values. Our results support a theorized tipping point for terrestrial ice volume in East Antarctica, where cooling surpassed a threshold for East Antarctic ice sheet expansion and stabilization during the MMCT that subsequent warming was not sufficient to reverse.

Multi-proxy SST reconstruction in the polar Southern Ocean

Our measurements of $U^{k'}_{37}$ and TEX_{86} on 409 and 181 samples, respectively, from Site 1165 provide records of these biomarker SST proxies from 5 to 19 Ma. Median sample resolution was 5 kyr during the high-resolution interval spanning 13.2 to 15.1 Ma and 100 kyr otherwise. Lack of core recovery between 11 and 12 Ma (O'Brien et al., 2001) precludes reconstruction during this interval. This site is the only one known to consistently yield quantifiable alkenones for $U^{k'}_{37}$ estimates in the polar Southern Ocean, where alkenones are not typically found in modern surface sediments (Sikes et al., 1997). Our successful application of $U^{k'}_{37}$ at Site 1165 throughout the Miocene suggest this proxy, which carries less significantly less calibration uncertainty than GDGT-based proxies (Kim et al., 2010; Müller et al., 1998), might also be applicable at other Antarctic sites during past warm intervals. Careful chromatographic separation from complex matrices (see methods) and new analytical methods (Liao et al., 2023) may help produce further $U^{k'}_{37}$ records from the Southern high-latitudes.

For both proxies, quality control of data used for SST reconstructions was rigorous. For $U^{k'}_{37}$ data produced using GC-FID, we screened each sample for C_{37} alkenones that were distinguishable from the baseline and other matrix compounds to ensure positive alkenone identification and lack of co-eluting interfering compounds. Analytically challenging samples were run using HPLC-MS (Liao et al., 2023) for its mass selectivity and relative immunity to co-eluting compounds (see alkenone methods).

For TEX_{86}, we calculated the BIT index (Hopmans et al., 2004), methane index (Zhang et al., 2011), and ring index (Zhang et al., 2016) to assess each sample's suitability for SST reconstruction (see GDGT methods and Figure S1). After quality control, 40% (73 out of 181) of samples analyzed for GDGTs provided suitable data for SST reconstruction using TEX_{86}, though we report GDGT data for all samples.

We apply the core-top calibrations of Müller et al. (1998) for $U^{k'}_{37}$ and Kim et al. (2010) using the TEX_{86}^{L} index. While the original TEX_{86} index shows a weak linear relationship with mean annual SSTs below 10°C, the TEX_{86}^{L} index shows a stronger correlation (Kim et al., 2010), though the applicability of the global calibration to the Southern Ocean is debated (Fietz et al., 2016; Ho et al., 2014).

Biomarker SST proxies provide reliable estimates of past ocean temperatures, but their application at Site 1165 at 64°S is complicated by seasonal variation in production of biomarkers. Alkenone production is limited to when light is available, which is between September and March at Site 1165. The modern mean annual SST at Site 1165 is -1.1°C (Huang et al., 2021) with monthly averages between -1.7°C and 0.6°C. The seasonal range of modern temperature variability is low (<2°C) due to proximity to the freezing point of seawater providing a lower bound. However, Miocene seasonal temperature ranges may have been greater than modern, particularly during the warmest intervals where sea ice may have been absent. Modern productivity in Prydz Bay is highest during the austral spring and summer months as sea ice cover reduces (Roden et al., 2013), but differences in the precise timing of peak seasonal productivity between modern and the Miocene are unknown. Here, we interpret the temperature derived from $U^{k'}_{37}$ as average summer (September through March) surface ocean temperature.

In addition, production of GDGTs is not limited to the photic zone and significant subsurface production occurs (Ho & Laepple, 2016); therefore TEX_{86} represents an integrated signal across a range of water depths, typically about 0-200 m. Vertical ocean temperature variations near Site 1165 are small (<2°C) in the modern ocean (Locarnini et al., 2024), making depth-integrated ocean temperatures nearly equivalent to surface temperatures at this site. Whether similar conditions applied during the Miocene would depend on water column mixing.

Results and Discussion

Polar warmth and ice sheet retreat during the Miocene Climatic Optimum

Our record demonstrates that surface ocean temperatures near Antarctica reached their maximum over the past 19 million years during the MCO (Figure 2), broadly coincident with minimal EAIS extent. Long-term average summer SSTs during the MCO were between 10 and 16°C warmer than modern (Figure 2), consistent with polar-amplified warming and retreat of the adjacent EAIS. This range of SSTs is higher than simulated from any existing Miocene global climate model simulation (Burls et al., 2021), even those run with concentrations of atmospheric CO_2 as high as 850 ppm (Figure S3). This model-data discrepancy further highlights the challenges of model simulations to reproduce the large degree of polar amplification observed from proxy records during past warm climates, including the MCO.

While Antarctic ice sheets were dynamic during the Early Miocene prior to the MCO (Marschalek et al., 2021; Smellie et al., 2024; Williams & Handwerger, 2005), ice volume declined to its minimum extent over the past 34 million years during the warmest MCO interglacials (Westerhold et al., 2020). We find that elevated polar temperatures coincided with these glacial retreats and the expansion of Antarctic terrestrial ecosystems (Warny et al., 2009) and that peak polar warmth was near the beginning of the MCO (Figure 2), when these wide-scale glacial retreats initiated. Our warm range of reconstructed SSTs during the MCO is consistent with coastal Antarctic temperatures above freezing, at least during the summer. Coastal summer air temperatures consistently above freezing would explain ice sheet retreat to the higher-elevation continental interior and the growth of cool temperate forest ecosystems on Antarctica during the MCO (Sangiorgi et al., 2018; Warny et al., 2009).

We emphasize that variations from the long-term average of individual samples in Figure 2 represent large temperature variability on orbital timescales, rather than analytical or calibration errors, which are much smaller (0.15 and 1.5°C, respectively) than orbital-scale variability. Our record fully resolves this orbital-scale variability between 13.2 and 15.1 Ma and demonstrates that these SST variations were cyclical and coherent, not random noise.

Our multi-proxy SST records from Site 1165 greatly extend the span of continuous Southern polar SST records during the Miocene and provide a novel application of $U^{k'}_{37}$ to a region where previously only GDGT-based proxies have been applied. TEX_{86}^{L} from the continental rise of Prydz Bay and Wilkes Land at Site U1356 (Sangiorgi et al., 2018) at similar latitudes provides very similar SST reconstructions during the intervals of overlap (Figure 3). However, TEX_{86}^{L} in the Ross Sea at ANDRILL-2A (Levy et al., 2016) reconstructs much colder SSTs than other sites, though with temporal trends almost identical to Site 1165 from 16 to 18 Ma. This large SST gradient during the Miocene between the Ross Sea and continental rise sites contrasts with the negligible modern SST gradient between these site locations (Figure 1), perhaps due to the more isolated position of the Ross Sea and/or potential southward movement of frontal zones between these site latitudes (64 and 77°S). Together, these multi-proxy temperature records from multiple sites across the Antarctic margin span 5 to 19 Ma almost continuously, providing novel insight into the climatic forcings surrounding the emergence of Earth’s largest ice sheets.

Southern Ocean cooling synchronous with Miocene global cooling intervals

We find that long-term Miocene cooling in the polar Southern Ocean occurred in two main phases: during the MMCT (13.8-13.9 Ma) and late Miocene cooling interval (6-7.5 Ma), synchronous with global cooling during these intervals. Cooling during the MMCT was transient, with a return to long-term average SSTs similar to the later MCO and pre-MCO during the Tortonian between 9 and 10.5 Ma. The magnitude of the Tortonian reversal is unique to the polar Southern Ocean as SSTs in other high-latitude regions do not return to levels as warm as the MCO during the Late Miocene (Herbert et al., 2016; Hou et al., 2023; Nirenberg & Herbert, 2024; Super et al., 2020). The driver of this discrepancy between the polar Southern Ocean and other high-latitude regions is unknown.

Polar summer SSTs below 8°C became permanent during the Late Miocene cooling interval after 8 Ma. Our results confirm that the polar Southern Ocean cooled synchronously with Southern mid-latitudes (Figure 3) and the Northern Hemisphere as well (Herbert et al., 2016), providing further evidence for the global nature of cooling during this interval. The synchronized timing and polar-amplified (4.5°C in mid-latitudes, 7°C at 64°S) nature of global cooling is consistent with declining greenhouse gas concentrations (Tanner et al., 2020). The synchronous development of the Antarctic Circumpolar Current to modern or higher strength during this interval (Evangelinos et al., 2024; Wegwerth et al., 2025) may have further contributed to Southern high-latitude cooling, perhaps in tandem with greenhouse gas forcing.

High-resolution MMCT record

Our high-resolution SST record shows a large degree of orbital-scale variability and indicates a dynamic marine ice margin driven by ocean thermal forcing through comparison with ice rafting. Cold SSTs coincided with delivery of IRD to Site 1165, indicating ice sheet expansion to the marine margin, whereas IRD was absent when summer SSTs rose above 12°C, indicating retreat and possible collapse of the marine ice margin due to ocean warming (Figure 4). These observations at Site 1165 provide empirical evidence supporting the results of model simulations that show the presence of marine-based ice in East Antarctic subglacial basins only during the coldest Middle Miocene conditions (Halberstadt et al., 2021) as well as the collapse of ice shelves within thousands of years after ocean warming driven by marine ice sheet and ice cliff instabilities (DeConto & Pollard, 2016; Halberstadt et al., 2024). The complete absence of ice rafting to Site 1165 during intervals of summer SSTs above 12°C provides quantitative evidence for an ocean temperature threshold above which extensive grounding line retreat occurred and the Amery Ice Shelf may have fully collapsed.

However, benthic $\delta^{18}O$ shows substantial orbital-scale variability that cannot be explained by changes in polar SSTs alone (Figure 4). The discordance between oscillations in SSTs and benthic $\delta^{18}O$ indicates that terrestrial ice volume may have primarily responded to local insolation changes on orbital timescales, rather than strictly to nearby SSTs, both during the MCO and after. The conjunction of favorable orbital configuration for ice sheet growth (Holbourn et al., 2005) and SST cooling below 8°C may together explain the large increase in ice volume during the MMCT.

We find pronounced cooling of polar Southern Ocean SSTs synchronous with EAIS expansion and stabilization during the Mi3 glaciation. SSTs cooled ~10°C within 120 kyr (Figure 4). This cooling event occurred synchronously with large pulses of IRD accumulation at the same site and others around the East Antarctic margin (Pierce et al., 2017), a ~1‰ enrichment in benthic $\delta^{18}O$ observed globally (Holbourn et al., 2005, 2014; Shevenell et al., 2004), as well as ice sheet expansion and >8°C cooling in the Transantarctic Mountains (Lewis et al., 2008). The timing of cooling in the polar Southern Ocean at Site 1165 also coincides with surface cooling in the sub-Antarctic (Kuhnert et al., 2009; Shevenell et al., 2004), and the magnitude of cooling was amplified closer to Antarctica (~6°C at 48° and 55°S, ~10°C at 64°S). The synchronous timing of polar-amplified Southern Ocean cooling is consistent with a decrease in atmospheric greenhouse gas concentrations as found in some pCO_2 proxy records (Badger et al., 2013; Raitzsch et al., 2021). Additional temperature forcing directly related to Antarctic ice sheet expansion may have also contributed to the larger magnitude of cooling observed in the Southern high-latitudes across Mi3 than in the Northern subpolar regions (Nirenberg & Herbert, 2024).

Implications for sensitivity of EAIS volume

Comparison of our SST record with benthic $\delta^{18}O$ supports a tipping point for terrestrial EAIS volume where cooling passed a stability threshold during the Mi3 glaciation. Glacial-interglacial SST variability as high as 8-9°C was present both before and after cooling and EAIS expansion during Mi3 (Figure 4). Large orbital-scale variations in benthic $\delta^{18}O$ were characteristic of the MCO (Holbourn et al., 2014; Westerhold et al., 2020), which reflect large changes in global ice volume from a highly dynamic EAIS (Levy et al., 2016; Warny et al., 2009), but decrease substantially after 13.8 Ma (Westerhold et al., 2020). Subsequent variations in sea level were reduced, implying a more stable EAIS near modern ice volume (John et al., 2011; Miller et al., 2020). The observation that temperature variations in the southern high-latitudes remain large both before and after Mi3 supports the conclusion that the reduction in benthic $\delta^{18}O$ variability represents a stabilization of EAIS volume and resulting effects on seawater $\delta^{18}O$ rather than reduced temperature effects on benthic $\delta^{18}O$. Therefore, cooling in the polar Southern Ocean not only coincided with EAIS expansion, but also a tipping point of EAIS terrestrial ice volume into a state less sensitive to temperature variability and orbital insolation changes after Mi3.

This ice sheet stabilization occurred when cooling in the polar Southern Ocean during Mi3 exceed glacial minima prior to 14 Ma. SST minima prior to Mi3 were consistently 8-10°C, whereas summer SSTs cooled to ~6°C during Mi3 (Figure 4). Polar Southern Ocean SSTs warmed to near-MCO values within 400 kyr after Mi3 (Figure 4), yet there is no evidence for subsequent widescale EAIS retreat in benthic $\delta^{18}O$ or in Antarctic geologic records during this interval. Together, this provides evidence that the majority of EAIS volume remained more stable to subsequent ocean warming and orbital forcings after its expansion during the Mi3 glaciation, exhibiting a different response than observed during the MCO when ice volume was more variable. Therefore, our results support a fundamental change in the stability state of the EAIS to polar summer SST cooling below 8°C. Though these cool SSTs between ~13.5 and 13.8 Ma were transient, the effects on global ice volume were resilient through the rest of the Miocene.

Subsequent warming and high SST variability between 9 and 10.7 Ma at Site 1165 (Figure 2) was contemporaneous with fluctuating glacial extent in the nearby Lambert Graben and periodic retreat of over 250 km from modern grounding line (Whitehead et al., 2003).

Correspondence of warm and variable ocean temperatures with highly dynamic glacial extent in this region of East Antarctica demonstrates that marine-based ice remained highly responsive to ocean thermal forcing. However, the notable absence of any significant changes in Late Miocene benthic $\delta^{18}O$ (Figure 2) implies that changes in global ice volume during this interval were negligible. Therefore, we suggest that Antarctic terrestrial ice volume was largely resilient to Tortonian warming despite the polar Southern Ocean returning to MCO-like temperatures. This provides further support for a threshold effect for terrestrial ice volume that was not surpassed after intense, but transient, Southern Ocean cooling during the MMCT.

While our records alone cannot constrain the physical mechanisms underlying this terrestrial ice volume stabilization, changes in the hydrologic regime of Antarctic glaciers likely contributed. High-elevation glaciers in the Transantarctic Mountains shifted from wet-based to dry-based conditions with cooling during Mi3 (Lewis et al., 2007). The complete absence of weathering processes observed in some areas of Antarctica after 13.8 Ma (Lewis et al., 2008; Spector & Balco, 2020) further support the establishment of permanent hyperarid conditions at high elevations during the MMCT. However, sedimentology at other locations suggests polythermal basal ice sheet conditions with some basal meltwater returned periodically in the Transantarctic Mountains after the MMCT (McKay et al., 2009; Smellie et al., 2014) as well as in lower elevation areas of the Lambert Graben (Hambrey & McKelvey, 2000). It is unknown whether similar conditions applied in other high-elevation areas of East Antarctica such as the Gamburtsev Mountains, where the EAIS likely originated (DeConto & Pollard, 2003). While subglacial thermal regimes were likely regionally variable across the EAIS, broad shifts towards cold- and dry-based glaciation may have stabilized EAIS volume on a larger scale after the MMCT and prevented as extensive retreats as occurred during the MCO.

Conclusions

The transition from ephemeral to permanent continental-scale glaciation in East Antarctica during the Miocene represents a fundamental development of Earth's modern cryosphere. While previous climate reconstructions from the Southern polar region are hindered by stratigraphic discontinuity common in glacially-influenced depositional environments, ODP Site 1165 provided a stratigraphic section spanning these critical climate transitions with continuous sedimentation and abundant, contemporaneous biomarkers at the East Antarctic continental margin. Our SST proxy records reveal peak temperatures during the MCO as high as 18°C warmer than modern near Antarctica surrounding episodic wide-scale EAIS retreat, further demonstrating the global nature of MCO high-latitude warmth. We quantify the degree and timing of polar Southern Ocean cooling during the Miocene and show that the two main cooling phases were synchronous with broader global cooling events at ~13.8 and ~7.5 Ma. Our high-resolution data, the first of its kind to continuously span the MMCT proximal to EAIS growth, reveal ocean-ice sheet interactions which provide geologic evidence for a tipping point and threshold behavior of terrestrial East Antarctic ice volume, while the marine-based ice margin remained highly sensitive to ocean thermal forcing.

Integrating records of paleotemperature and ice sheet behavior during past warm periods is critical for providing empirical constraints on the response of the largest potential contributor to global sea level rise to warming ocean temperatures, which we observe today and project in the coming centuries. While we find increased stability of terrestrial EAIS volume to orbital and ocean temperature forcings after the MMCT, we caution that these global sea level variations on orbital timescales were still tens of meters (Miller et al., 2020), which would have drastic impacts on modern communities. In addition, the modern EAIS contains 19.2 m of sea level equivalent grounded below sea level (Fretwell et al., 2013), and estimates of this potential source of sea level rise only continue to grow with increasing constraints on bed topography (Pritchard et al., 2025). The vulnerability of East Antarctic marine-based ice to ocean warming, as now found during past global warmth at the Amery Ice Shelf in this work and at other subglacial basins (Gulick and Shevenell et al., 2017), represent a significant potential contributor to future sea level rise.

Methods

Up to 15 grams of dry sediment were extracted using a Dionex Accelerated Solvent Extractor 350 with 3 static cycles at 150°C and 1600 psi using a solvent mixture of 9:1 dichloromethane (DCM):methanol. The total lipid extracts were desulfurized using activated copper wires and then separated using aminopropyl-modified silica gel chromatography into neutral and acid fractions through eluting with 4 mL 2:1 DCM:isopropanol and 4 mL 4:96 acetic acid:diethyl ether, respectively. The neutral fractions were then further separated using silica gel column chromatography through eluting with 4 mL pure hexane, 7:3 hexane:DCM, pure DCM, and 1:1 DCM:ethyl acetate.

Alkenone analytical methods

The pure DCM fraction was then further separated chromatographically into saturated and unsaturated fractions using 10% silver nitrate on silica gel and eluting with 4 mL DCM and then 4 mL ethyl acetate, respectively. The unsaturated fraction, containing the alkenones, was then evaporated under N_2 and redissolved in toluene containing internal standards of *n*-hexatriacontane and *n*-heptatriacontane for quantification.

Alkenones were analyzed using an Agilent 7890 or 8890 gas chromatograph with a flame ionization detector (GC-FID), equipped with an Agilent DB-1 column (60 m length, 0.32 mm diameter, 0.10 µm film thickness). The oven ramp was as follows: hold at 90°C for 2 minutes, ramp to 255°C at 40°C/min, ramp to 300°C at 1°C/min, ramp to 320°C at 10°C/min, and hold at 320°C for 11 minutes. The PTV inlet ramp was as follows: hold at 110°C for 0.85 minutes, ramp to 290°C at 720°C/min, hold for 5 minutes, ramp to 320°C at 720°C/min, and hold at 320°C. Alkenone peaks were assigned through comparison with a laboratory standard, and all data was screened to ensure sufficient peak areas and chromatographic separation from other matrix compounds. In-house laboratory alkenone standards were measured before, during, and after each run to ensure data quality, and only data from runs with standard reproducibility within 0.01 $U^{k'}_{37}$ units, or about 0.3°C according to the calibration of Müller et al. (1998), were used. About 30% of samples have replicate measurements, which were generally within 0.01 $U^{k'}_{37}$ units, or about 0.3°C.

Some samples were analyzed using high-performance liquid chromatography with mass spectrometry (HPLC-MS) using the method of Liao et al., (2023). Briefly, alkenones were dissolved in acetone and separated using a Zorbax Eclipse PAH column (2.1 by 100 mm by 3.5 µm) using the solvent scheme of Liao et al., (2023). Masses of ammonia-adducts to $C_{37:3}$ and $C_{37:2}$ alkenones (m/z 547 and 549) were monitored using selected ion monitoring (SIM). Peaks were integrated in SIM chromatograms, and the $U^{k'}_{37}$ derived from the HPLC peak areas were calibrated to FID $U^{k'}_{37}$ using a set of 10 standards of known $U^{k'}_{37}$ between 0.1 and 0.9 using a quadratic fit. Using this calibration method, the reproducibility of the laboratory alkenone standard was within 0.01 $U^{k'}_{37}$ units, or about 0.3°C. Selected samples which produced good quality data using GC-FID were also ran using HPLC-MS and produced statistically indistinguishable $U^{k'}_{37}$ between the two methods.

GDGT analytical methods

The polar fraction from silica gel column chromatography, eluted with 1:1 DCM:ethyl acetate, was blown down under N_2, redissolved in 99:1 hexane:isopropanol, and passed through a 0.45 μm PTFE filter. GDGTs were analyzed using high performance liquid chromatography coupled with atmospheric pressure chemical ionization with selective ion monitoring (SIM) at m/z 1302, 1300, 1298, 1296, 1292, 1050, 1048, 1046, 1036, 1034, 1032, 1022, 1020, and 1018. Two silica columns (Acquity UPLC BEH HILIC 1.7 μm, 2.1 by 150 mm) were run in series at 30°C with a flow rate of 0.2 mL/min with mobile phases as in Hopmans et al. (2016). Areas for GDGT peaks were integrated manually using the SIM signals, and a laboratory standard was run before and after samples to ensure measurement quality. Peak areas for hydroxylated GDGTs (OH-GDGTs) were integrated using the mass of the molecular ion after dehydration (M-18) in m/z 1300, 1298, and 1296.

GDGT quality control

Samples with ring indices offset from those expected from TEX_{86} (ΔRI) greater than 0.4 were not used for SST reconstruction, as these indicate anomalous isoGDGT distributions (Zhang et al., 2016). Samples with methane indices greater than 0.4 were not used for SST reconstruction due to significant impact from methanogenic archaeal input (Zhang et al., 2011).

Samples with a GDGT 2/3 ratio greater than 7 were not used for SST reconstruction as these values are indicative of significant input from archaea at deep depths, which are not representative of SST (Taylor et al., 2013). Finally, samples with BIT (Hopmans et al., 2004) greater than 0.6 were not used for SST reconstruction, and samples with BIT between 0.3 and 0.6 were only used for SST reconstruction if all other quality control indices were in ideal ranges. The values of these quality control indices at Site 1165 over time are shown in Figure S1, and many of them were correlated with each other, which is shown in Figure S2 for BIT and ΔRI.

Age model

To construct an age model for Site 1165, we applied the program rBacon (Blaauw et al., 2017) using available biostratigraphic (O'Brien et al., 2001) and magnetic reversal (Florindo et al., 2003) datums. In addition, we stratigraphically aligned the main pulse of IRD between 289.2 and 293.4 meters below seafloor (mbsf) with the Mi3 glaciation (ages defined by Holbourn et al. (2014)), as supported by Pierce et al. (2017) and found in multiple sites around the Antarctic continental margin. The input for the rBacon age model is found in Table S1. Briefly, biostratigraphic and magnetic reversal datums were assigned base age uncertainties of 200 and 20 kyr, respectively. Additional age uncertainty was added in quadrature according to the uncertainty with the depth of the datums where present. Ages for magnetic reversals were assigned using APTS 2012 (Hilgen et al., 2012).

Acknowledgments

We thank Emily Clements and Sofía Gilroy for their assistance with sample preparation. We thank the Gulf Coast Repository and the scientists and crew of ODP Leg 188 for providing sample material and core descriptions. This study used samples and data provided by the International Ocean Discovery Program (IODP) and its predecessors. This study was funded by the Schlanger Ocean Drilling Fellowship Program from the US Science Support Program as well as NSF Grant GR5260690.

Figures

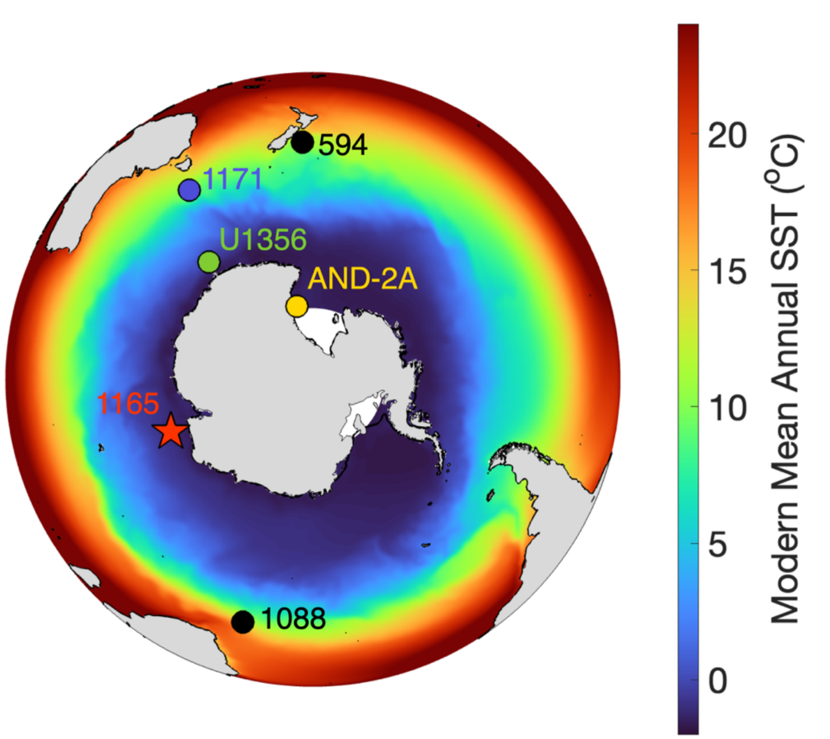

Figure 1. Site locations of Early-Middle Miocene Southern Ocean temperature records. New data presented here is from Site 1165, red star, in Prydz Bay adjacent to the Amery Ice Shelf. We compare to existing TEX_{86} records from polar sites U1356 (green circle, (Sangiorgi et al., 2018)) and Andrill-2A (AND-2A, yellow circle (Levy et al., 2016)), Mg/Ca of planktic foraminifera from sub-Antarctic sites 1171 (blue circle (Shevenell et al., 2004)), and $U^{k'}_{37}$ from Southern mid-latitude sites 1088 and 594 (black circles, (Herbert et al., 2016)). Surface ocean is colored according to mean annual SST from 1991-2021 from NOAA OISST v2.1 (Huang et al., 2021).

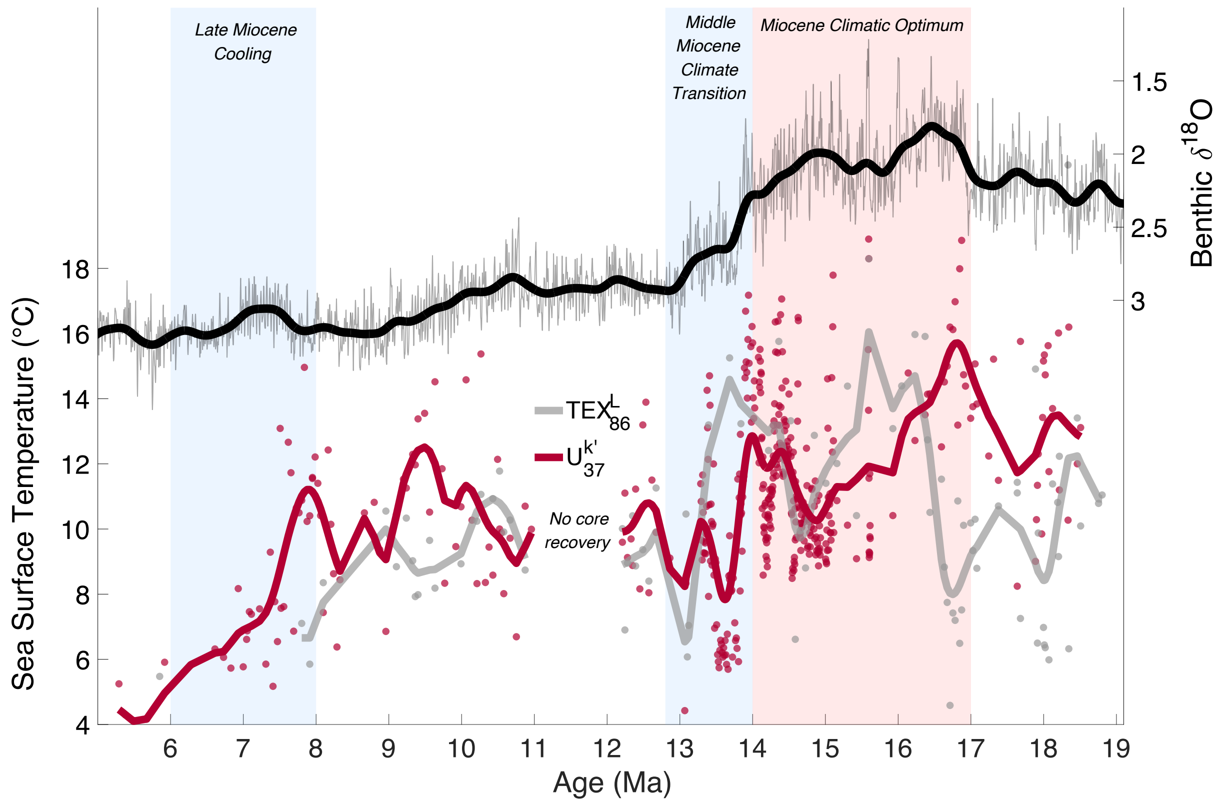

Figure 2. Comparison of (a) benthic $\delta^{18}O$, reflecting deep ocean temperature and global ice volume and (b) summer SSTs at Site 1165 reconstructed from $U^{k'}_{37}$ (red) and TEX_{86}^{L} (orange) from this work. Circles represent individual data points, and thick lines are smoothed averages calculated using a Gaussian-weighting with a standard deviation of 200 kyr.

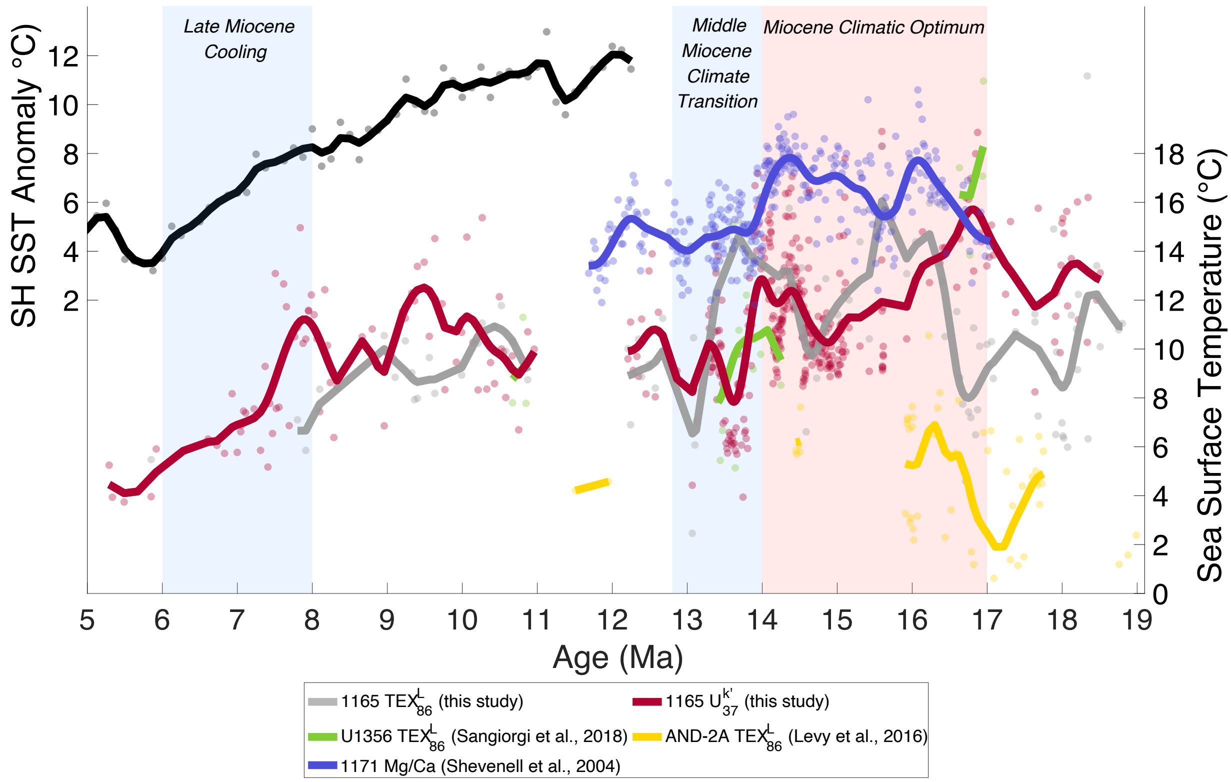

Figure 3. Comparison of SST records from Site 1165 ($U^{k'}_{37}$ red, TEX_{86}^{L} orange, this work) with other polar TEX_{86}^{L} records (U1356 green (Sangiorgi et al., 2018), ANDRILL-2A yellow (Levy et al., 2016)), subantarctic SST from planktic foraminifera Mg/Ca at Site 1171 (blue, (Shevenell et al., 2004)), and stacked $U^{k'}_{37}$ SST anomalies from Southern Hemisphere mid-latitude Sites 594 and 1088 (black, (Herbert et al., 2016)). Points are individual data measurements and lines are smoothed averages using a Gaussian-weighting with a standard deviation of 200 kyr.

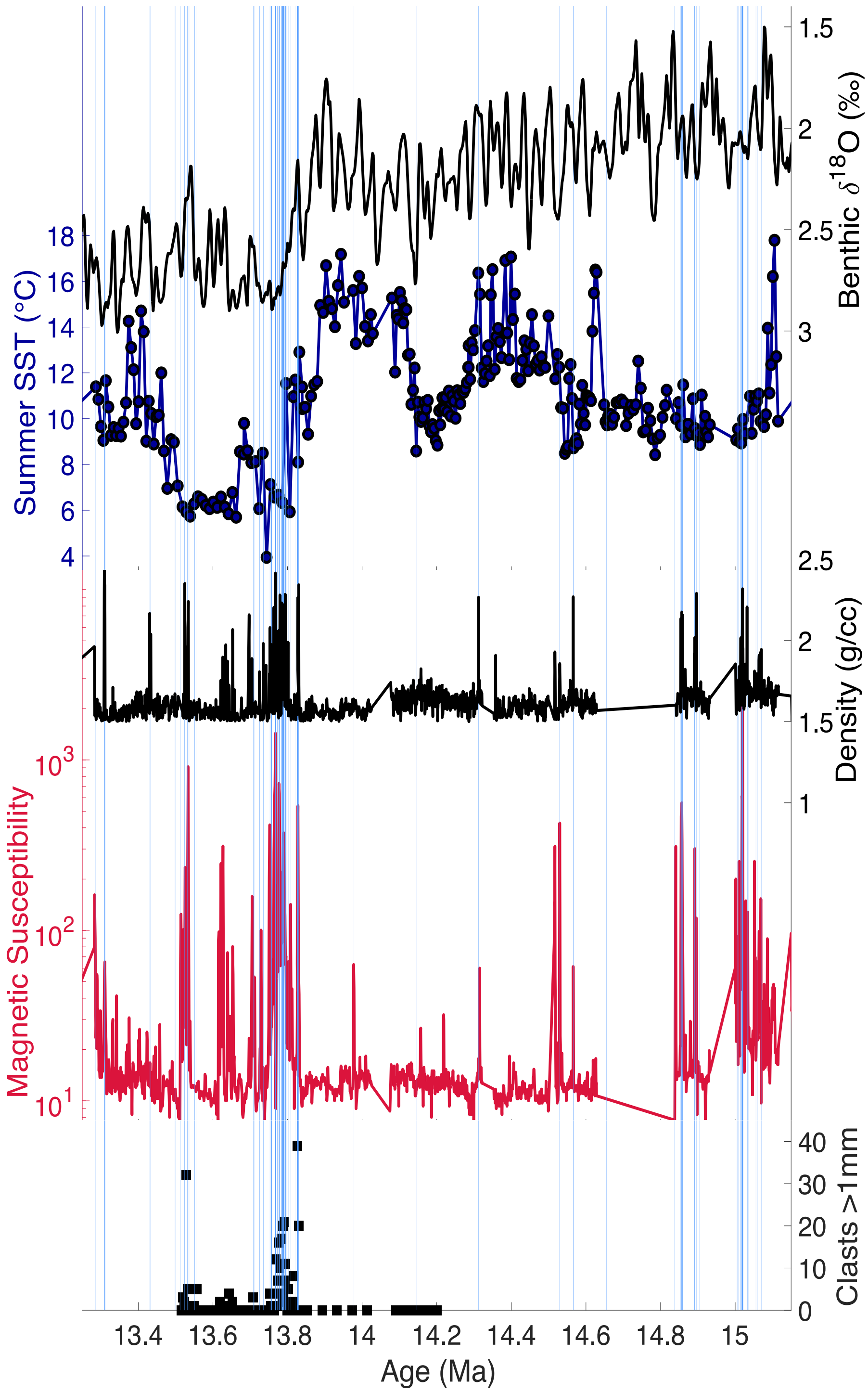

Figure 4. Comparison of global ice volume/deep ocean temperatures, polar ocean surface summer temperatures, and IRD at Site 1165. (a) Global benthic δ^{18}O from Cenozoic megasplice of (Westerhold et al., 2020). (b) Summer SSTs at Site 1165 from $U^{k'}_{37}$. Shipboard measurements of (c) GRA density and (d) magnetic susceptibility from (O'Brien et al., 2001). (e) Counts of clasts > 1mm from individual samples from (Pierce et al., 2017). Blue bars indicate intervals

containing clasts > 5mm from visual inspection of core photos. Note that (b-e) are from the same site and are aligned stratigraphically regardless of age model, while comparison with (a) carries age model uncertainties.

Supplementary figures and tables

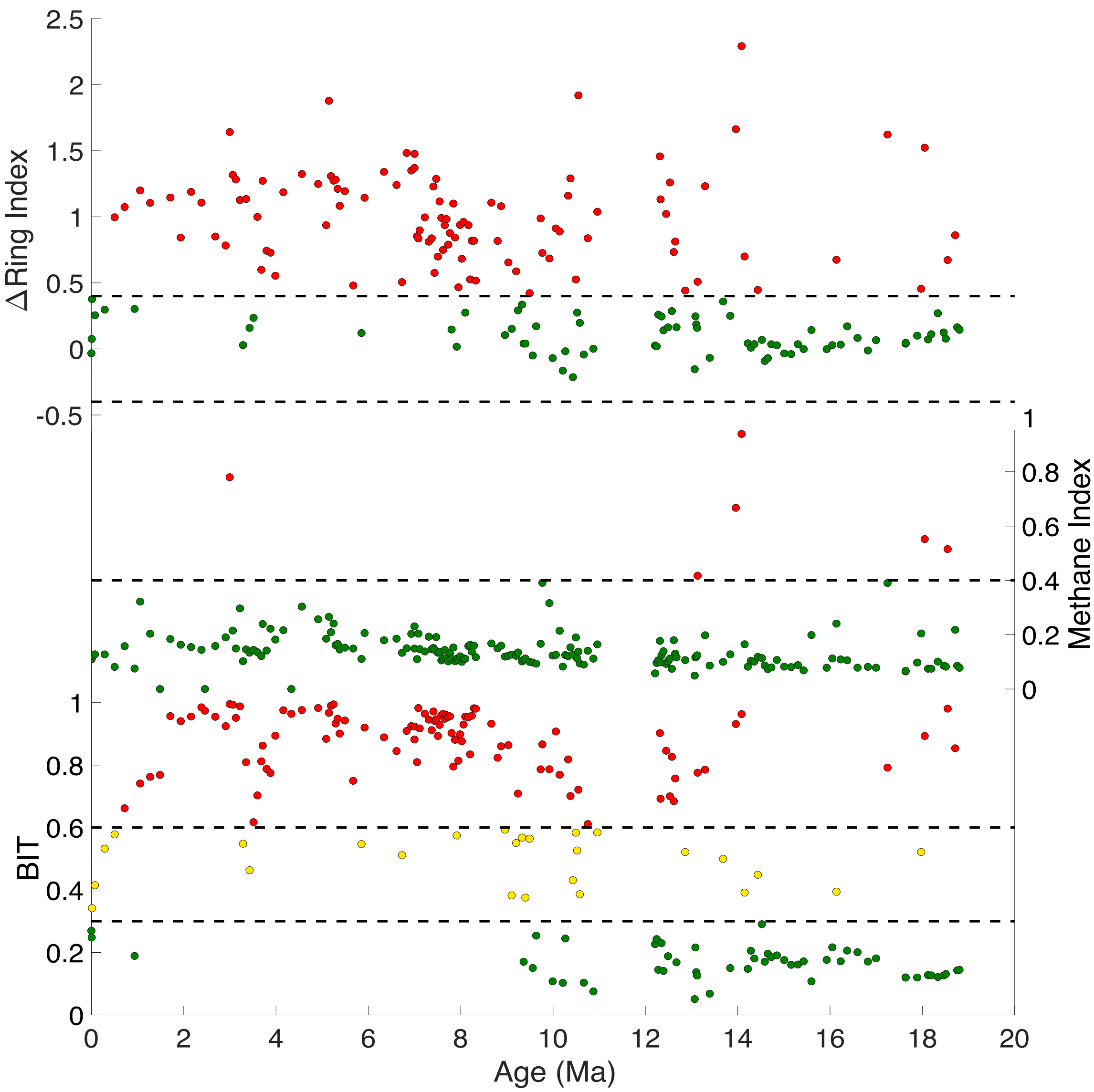

Figure S1. Deviation in ring index (ΔRI) from that expected from TEX_{86} (Zhang et al., 2016), methane index (Zhang et al., 2011), and BIT (Hopmans et al., 2004) of isoprenoid GDGT distributions at Site 1165. Green points indicate samples with values suitable for SST interpretation, while red points indicate samples with index values outside of the acceptable range. For BIT, yellow points indicate samples with intermediate values, which were only used for SST interpretation if all other indices were also in the suitable range.

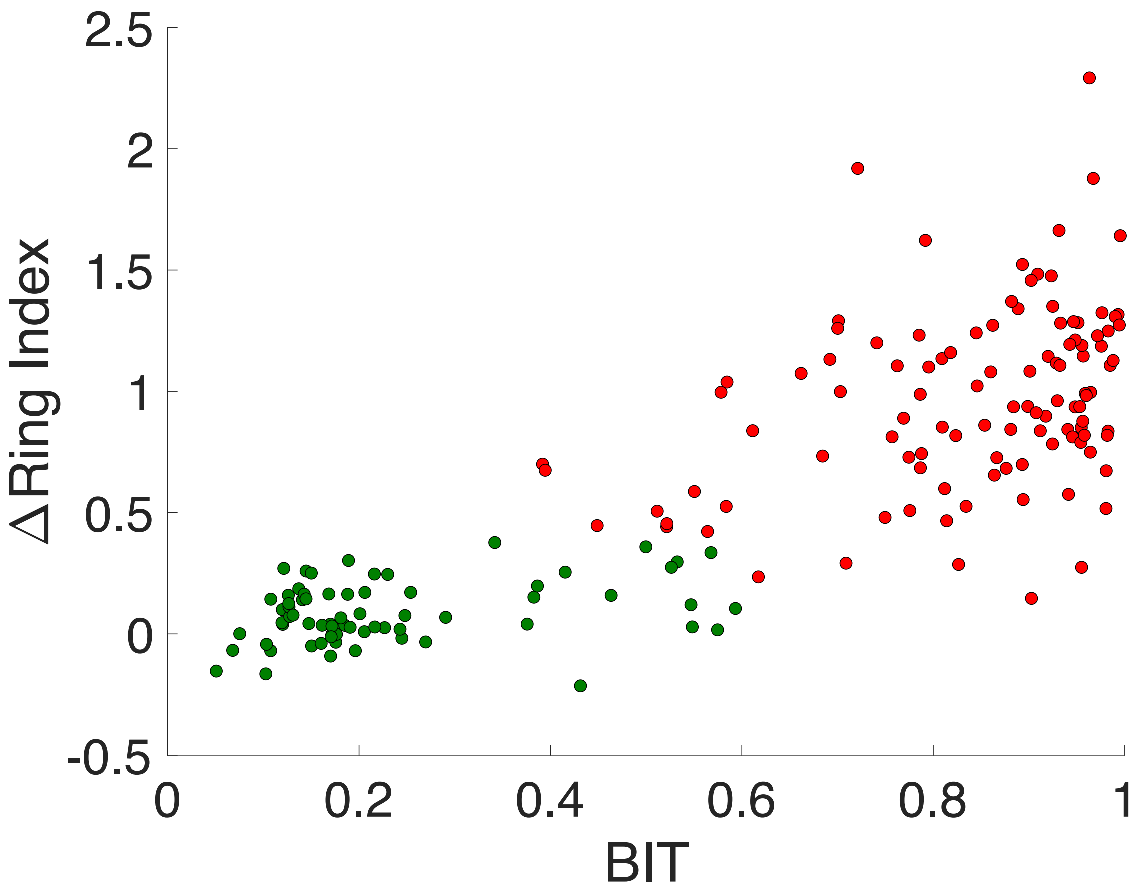

Figure S2. Deviation in ring index (ΔRI) from that expected from TEX_{86} (Zhang et al., 2016), versus BIT (Hopmans et al., 2004). Green points indicate samples which were used for SST reconstruction while red points indicate samples which were not. Note the positive correlation between the two quality control indices, as samples with high BIT also had generally higher ΔRI as well.

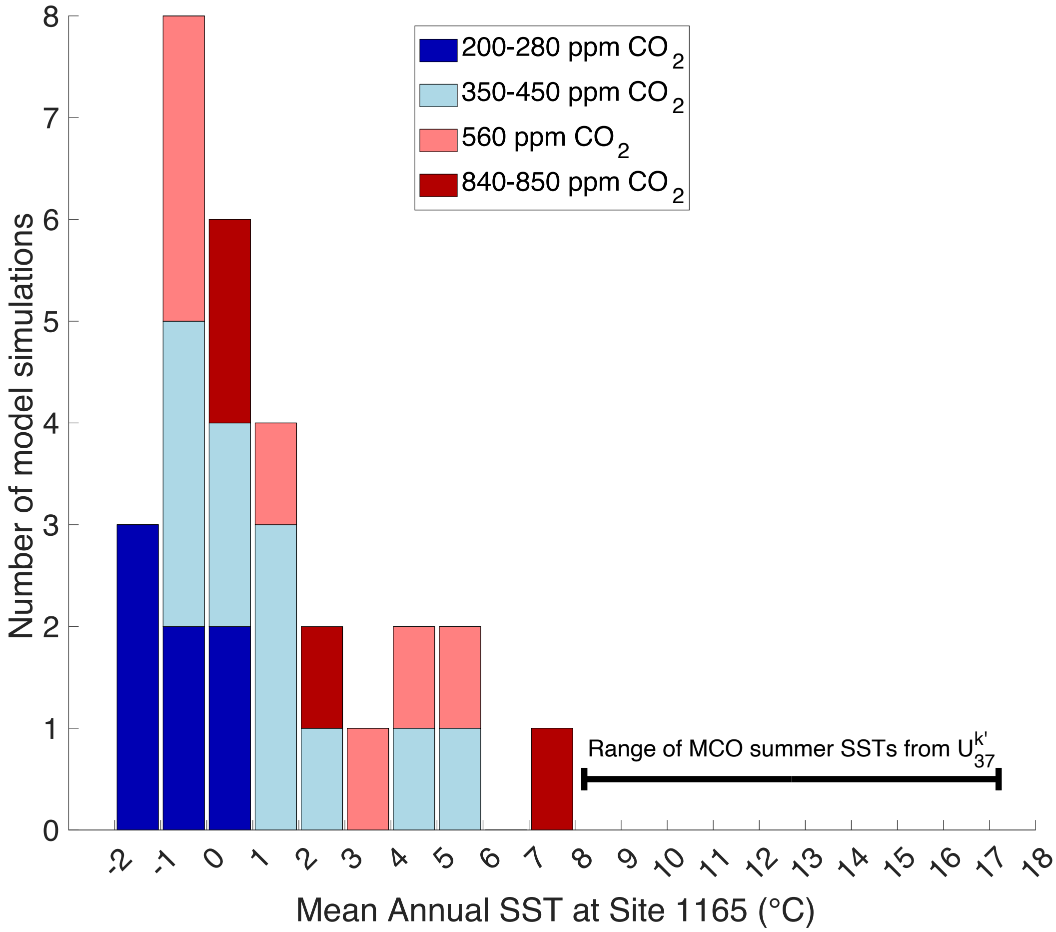

Figure S3. Annually-averaged sea surface temperatures at the site location of Site 1165 in the MioMIP1 model simulations compiled by Burls et al. (2021). Colored bars represent models ran with different atmospheric carbon dioxide concentrations, ranging from 200 ppm to 850 ppm. The range of MCO summer SSTs at Site 1165 from $U^{k'}_{37}$ is uniformly higher than all mean annual SSTs in MioMIP1 simulations. Seasonally-averaged data from model simulations is not available for comparison.

Table S1. Input for rBacon age model. All diatom datums (such as PD1) are named according to Florindo et al. (2003). The depth given for magnetic reversal datums is the base of the chron. For biostratigraphic datums, the depth given is the average between the sample depths where this datum was found.

Datum	Age (ka)	Error (ka)	Depth (mbsf)
CoreTop	0	10	0
PD1	650	214.937095	3.95
C1n	773	10	5.37
C1r.3r	1775	10	6.97
PD2	1350	253.396792	7.73
PD3	1900	248.369408	13.25
C2n	1934	10	14.1
PD4	2300	282.845941	17.52
PD5	2600	223.610881	17.92
PD6	2600	223.610881	18.42
C2An.1n	3032	10	19.23
THV	2420	202.318374	19.87
C2An.1r	3116	10	20.91
PD7	2950	320.429998	25.51
C2An.2n	3207	10	25.96
C2An.2r	3330	10	30.76
C2An.3n	3596	10	36.46
PD9	3750	206.158116	38.01
PD10	4200	200.004565	38.02
PD11	4250	206.161659	41.84
C2Ar	4187	10	42.06
C3n.1n	4300	10	43.19
C3n.2n	4631	10	45.75
C3n.2r	4799	10	46.96
C3n.3n	4896	10	48.8
C3n.3r	4997	10	49.12
PD12	4900	223.610881	49.62
BHV	4690	206.353431	51.37
C3n.4n	5235	10	54.56
MD1	5800	201.57325	55.52
MD2	6100	225.076077	62.65
TcLG	5020	206.7587	65.09
TAC	6100	209.11934	65.45

BAC	6650	203.447999	72.87
C3An.2n	6730	20	73.52
MD3	6400	201	73.63
C3Ar	7100	20	89.2
MD4	8600	226	100.62
MD5	8700	203	100.62
BAL	7800	238	103.22
MD6	8900	225	107.25
TCS	9120	220.782194	114.45
BAA	10370	212.255789	182.07
MD7	10200	225	189.05
TAG	10770	255	190.54
MD8	10700	200	192.43
MD9	11500	287	206.28
MD10	11800	304	206.28
BCS	12550	756.119616	225.62
MD11	12450	322	232.63
MD12	12300	204	232.63
MD13	12850	207	240.05
MD14	13100	202	272.93
MD15	13450	206	281.1
CHZ	13815	415.450529	286.64
Mi3end	13780	10	289.2
Mi3begin	13900	10	293.4
MD16	14200	203	298.73
MD17	14400	224	318.98
MD18	15300	224	390.43
C5Br	15985	20	418.84
C5Cn.1n	16268	20	449.4
MD19	16200	212	451.8
C5Cn.2n	16472	50	458.8
C5Cn.3n	16721	50	467.5
MD20	16750	220	489.88
C5Dr	18056	50	512.62
MD21	17850	252	513.83
MD22	18300	244	564.61
C5En	18524	50	588.08
C5Er	18724	50	655.48

C6n	19535	50	824.15
C6r	19979	50	858.96
C6An.1n	20182	50	874.3
C6An.1r	20448	50	903
C6An.2n	20765	50	933.4
C6Ar	21130	50	992.9
C6AAn	21204	50	996

References

Acton, G., Crampton, J., Vincenzo, G. D., Fielding, C., Florindo, F., Hannah, M., et al. (2008). Preliminary Integrated Chronostratigraphy of the AND-2A Core, ANDRILL Southern McMurdo Sound Project, Antarctica. *ANDRILL Research and Publications*. Retrieved from https://digitalcommons.unl.edu/andrillrespub/6

Anderson, J. B., Warny, S., Askin, R. A., Wellner, J. S., Bohaty, S. M., Kirshner, A. E., et al. (2011). Progressive Cenozoic cooling and the demise of Antarctica's last refugium. *Proceedings of the National Academy of Sciences*, *108*(28), 11356–11360. https://doi.org/10.1073/pnas.1014885108

Badger, M. P. S., Lear, C. H., Pancost, R. D., Foster, G. L., Bailey, T. R., Leng, M. J., & Abels, H. A. (2013). CO_2 drawdown following the middle Miocene expansion of the Antarctic Ice Sheet. *Paleoceanography*, *28*(1), 42–53. https://doi.org/10.1002/palo.20015

Blaauw, M., Christen, J. A., & Aquino Lopez, M. A. (2017). rbacon: Age-Depth Modelling using Bayesian Statistics [Data set]. https://doi.org/10.32614/CRAN.package.rbacon

Burls, N. J., Bradshaw, C. D., De Boer, A. M., Herold, N., Huber, M., Pound, M., et al. (2021). Simulating Miocene Warmth: Insights From an Opportunistic Multi-Model Ensemble (MioMIP1). *Paleoceanography and Paleoclimatology*, *36*(5), e2020PA004054. https://doi.org/10.1029/2020PA004054

Cenozoic CO_2 Proxy Integration Project (CENCO$_2$PIP) Consortium. (2023). Toward a Cenozoic history of atmospheric CO_2. *Science*, *382*(6675), eadi5177. https://doi.org/10.1126/science.adi5177

DeConto, R. M., & Pollard, D. (2003). Rapid Cenozoic glaciation of Antarctica induced by declining atmospheric CO_2. *Nature*, *421*(6920), 245–249. https://doi.org/10.1038/nature01290

DeConto, R. M., & Pollard, D. (2016). Contribution of Antarctica to past and future sea-level rise. *Nature*, *531*(7596), 591–597. https://doi.org/10.1038/nature17145

DeConto, R. M., Pollard, D., Wilson, P. A., Pälike, H., Lear, C. H., & Pagani, M. (2008). Thresholds for Cenozoic bipolar glaciation. *Nature*, *455*(7213), 652–656. https://doi.org/10.1038/nature07337

Evangelinos, D., Etourneau, J., van de Flierdt, T., Crosta, X., Jeandel, C., Flores, J.-A., et al. (2024). Late Miocene onset of the modern Antarctic Circumpolar Current. *Nature Geoscience*, *17*(2), 165–170. https://doi.org/10.1038/s41561-023-01356-3

Feakins, S. J., Warny, S., & Lee, J.-E. (2012). Hydrologic cycling over Antarctica during the middle Miocene warming. *Nature Geoscience*, *5*(8), 557–560. https://doi.org/10.1038/ngeo1498

Fietz, S., Ho, S. L., Huguet, C., Rosell-Melé, A., & Martínez-García, A. (2016). Appraising GDGT-based seawater temperature indices in the Southern Ocean. *Organic Geochemistry*, *102*, 93–105. https://doi.org/10.1016/j.orggeochem.2016.10.003

Florindo, F., Bohaty, S. M., Erwin, P. S., Richter, C., Roberts, A. P., Whalen, P. A., & Whitehead, J. M. (2003). Magnetobiostratigraphic chronology and palaeoenvironmental history of Cenozoic sequences from ODP sites 1165 and 1166, Prydz Bay, Antarctica. *Palaeogeography, Palaeoclimatology, Palaeoecology*, *198*(1), 69–100. https://doi.org/10.1016/S0031-0182(03)00395-X

Fretwell, P., Pritchard, H. D., Vaughan, D. G., Bamber, J. L., Barrand, N. E., Bell, R., et al. (2013). Bedmap2: improved ice bed, surface and thickness datasets for Antarctica. *The Cryosphere*, *7*(1), 375–393. https://doi.org/10.5194/tc-7-375-2013

Gulick, S. P. S., Shevenell, A. E., Montelli, A., Fernandez, R., Smith, C., Warny, S., et al. (2017). Initiation and long-term instability of the East Antarctic Ice Sheet. *Nature*, *552*(7684), 225–229. https://doi.org/10.1038/nature25026

Halberstadt, A. R. W., Chorley, H., Levy, R. H., Naish, T., DeConto, R. M., Gasson, E., & Kowalewski, D. E. (2021). CO_2 and tectonic controls on Antarctic climate and ice-sheet evolution in the mid-Miocene. *Earth and Planetary Science Letters*, *564*, 116908. https://doi.org/10.1016/j.epsl.2021.116908

Halberstadt, A. R. W., Gasson, E., Pollard, D., Marschalek, J., & DeConto, R. M. (2024). Geologically constrained 2-million-year-long simulations of Antarctic Ice Sheet retreat and expansion through the Pliocene. *Nature Communications*, *15*(1), 7014. https://doi.org/10.1038/s41467-024-51205-z

Hambrey, M. J., & McKelvey, B. (2000). Major Neogene fluctuations of the East Antarctic ice sheet: Stratigraphic evidence from the Lambert Glacier region. *Geology*, *28*(10), 887–890. https://doi.org/10.1130/0091-7613(2000)28%253C887:MNFOTE%253E2.0.CO;2

Herbert, T. D., Lawrence, K. T., Tzanova, A., Peterson, L. C., Caballero-Gill, R., & Kelly, C. S. (2016). Late Miocene global cooling and the rise of modern ecosystems. *Nature Geoscience*, *9*(11), 843–847. https://doi.org/10.1038/ngeo2813

Herbert, T. D., Dalton, C. A., Liu, Z., Salazar, A., Si, W., & Wilson, D. S. (2022). Tectonic degassing drove global temperature trends since 20 Ma. *Science*, *377*(6601), 116–119. https://doi.org/10.1126/science.abl4353

Hilgen, F. J., Lourens, L. J., Van Dam, J. A., Beu, A. G., Boyes, A. F., Cooper, R. A., et al. (2012). The Neogene Period. In *The Geologic Time Scale* (pp. 923–978). Elsevier. https://doi.org/10.1016/B978-0-444-59425-9.00029-9

Ho, S. L., & Laepple, T. (2016). Flat meridional temperature gradient in the early Eocene in the subsurface rather than surface ocean. *Nature Geoscience*, *9*(8), 606–610. https://doi.org/10.1038/ngeo2763

Ho, S. L., Mollenhauer, G., Fietz, S., Martínez-Garcia, A., Lamy, F., Rueda, G., et al. (2014). Appraisal of TEX_{86} and TEX_{86}^{L} thermometries in subpolar and polar regions. *Geochimica et Cosmochimica Acta*, *131*, 213–226. https://doi.org/10.1016/j.gca.2014.01.001

Holbourn, A., Kuhnt, W., Schulz, M., & Erlenkeuser, H. (2005). Impacts of orbital forcing and atmospheric carbon dioxide on Miocene ice-sheet expansion. *Nature*, *438*(7067), 483–487. https://doi.org/10.1038/nature04123

Holbourn, A., Kuhnt, W., Lyle, M., Schneider, L., Romero, O., & Andersen, N. (2014). Middle Miocene climate cooling linked to intensification of eastern equatorial Pacific upwelling. *Geology*, *42*(1), 19–22. https://doi.org/10.1130/G34890.1

Holbourn, A., Kuhnt, W., Kochhann, K. G. D., Andersen, N., & Sebastian Meier, K. J. (2015). Global perturbation of the carbon cycle at the onset of the Miocene Climatic Optimum. *Geology*, *43*(2), 123–126. https://doi.org/10.1130/G36317.1

Hopmans, E. C., Weijers, J. W. H., Schefuß, E., Herfort, L., Sinninghe Damsté, J. S., & Schouten, S. (2004). A novel proxy for terrestrial organic matter in sediments based on branched and isoprenoid tetraether lipids. *Earth and Planetary Science Letters*, *224*(1), 107–116. https://doi.org/10.1016/j.epsl.2004.05.012

Hou, S., Lamprou, F., Hoem, F. S., Hadju, M. R. N., Sangiorgi, F., Peterse, F., & Bijl, P. K. (2023). Lipid-biomarker-based sea surface temperature record offshore Tasmania over the last 23 million years. *Climate of the Past*, *19*(4), 787–802. https://doi.org/10.5194/cp-19-787-2023

Huang, B., Liu, C., Banzon, V., Freeman, E., Graham, G., Hankins, B., et al. (2021). Improvements of the Daily Optimum Interpolation Sea Surface Temperature (DOISST) Version 2.1. *Journal of Climate*, *34*(8), 2923–2939. https://doi.org/10.1175/JCLI-D-20-0166.1

John, C. M., Karner, G. D., Browning, E., Leckie, R. M., Mateo, Z., Carson, B., & Lowery, C. (2011). Timing and magnitude of Miocene eustasy derived from the mixed siliciclastic-carbonate stratigraphic record of the northeastern Australian margin. *Earth and Planetary Science Letters*, *304*(3), 455–467. https://doi.org/10.1016/j.epsl.2011.02.013

Kim, J.-H., van der Meer, J., Schouten, S., Helmke, P., Willmott, V., Sangiorgi, F., et al. (2010). New indices and calibrations derived from the distribution of crenarchaeal isoprenoid tetraether lipids: Implications for past sea surface temperature reconstructions. *Geochimica et Cosmochimica Acta*, *74*(16), 4639–4654. https://doi.org/10.1016/j.gca.2010.05.027

Kuhnert, H., Bickert, T., & Paulsen, H. (2009). Southern Ocean frontal system changes precede Antarctic ice sheet growth during the middle Miocene. *Earth and Planetary Science Letters*, *284*(3), 630–638. https://doi.org/10.1016/j.epsl.2009.05.030

Leutert, T. J., Auderset, A., Martínez-García, A., Modestou, S., & Meckler, A. N. (2020). Coupled Southern Ocean cooling and Antarctic ice sheet expansion during the middle

Miocene. *Nature Geoscience*, *13*(9), 634–639. https://doi.org/10.1038/s41561-020-0623-0

Levy, R., Harwood, D., Florindo, F., Sangiorgi, F., Tripati, R., Eynatten, H. von, et al. (2016). Antarctic ice sheet sensitivity to atmospheric CO_2 variations in the early to mid-Miocene. *Proceedings of the National Academy of Sciences*, *113*(13), 3453–3458. https://doi.org/10.1073/pnas.1516030113

Lewis, Adam R., Marchant, D. R., Ashworth, A. C., Hedenäs, L., Hemming, S. R., Johnson, J. V., et al. (2008). Mid-Miocene cooling and the extinction of tundra in continental Antarctica. *Proceedings of the National Academy of Sciences*, *105*(31), 10676–10680. https://doi.org/10.1073/pnas.0802501105

Lewis, A.R., Marchant, D. R., Ashworth, A. C., Hemming, S. R., & Machlus, M. L. (2007). Major middle Miocene global climate change: Evidence from East Antarctica and the Transantarctic Mountains. *GSA Bulletin*, *119*(11–12), 1449–1461. https://doi.org/10.1130/0016-7606(2007)119%255B1449:MMMGCC%255D2.0.CO;2

Liao, S., Liu, X.-L., Manz, K. E., Pennell, K. D., Novak, J., Santos, E., & Huang, Y. (2023). Comprehensive analysis of alkenones by reversed-phase HPLC-MS with unprecedented selectivity, linearity and sensitivity. *Talanta*, *260*, 124653. https://doi.org/10.1016/j.talanta.2023.124653

Liu, X., Huber, M., Foster, G. L., Dessler, A., & Zhang, Y. G. (2022). Persistent high latitude amplification of the Pacific Ocean over the past 10 million years. *Nature Communications*, *13*(1), 7310. https://doi.org/10.1038/s41467-022-35011-z

Locarnini, R. A., Mishonov, A. V., Baranova, O. K., Reagan, J. R., Boyer, T. P., Seidov, D., et al. (2024). World Ocean Atlas 2023, Volume 1: Temperature. https://doi.org/10.25923/54BH-1613

Marschalek, J. W., Zurli, L., Talarico, F., van de Flierdt, T., Vermeesch, P., Carter, A., et al. (2021). A large West Antarctic Ice Sheet explains early Neogene sea-level amplitude. *Nature*, *600*(7889), 450–455. https://doi.org/10.1038/s41586-021-04148-0

McKay, R., Browne, G., Carter, L., Cowan, E., Dunbar, G., Krissek, L., et al. (2009). The stratigraphic signature of the late Cenozoic Antarctic Ice Sheets in the Ross Embayment. *GSA Bulletin*, *121*(11–12), 1537–1561. https://doi.org/10.1130/B26540.1

Miller, K. G., Feigenson, M. D., Wright, J. D., & Clement, B. M. (1991). Miocene isotope reference section, Deep Sea Drilling Project Site 608: An evaluation of isotope and biostratigraphic resolution. *Paleoceanography*, *6*(1), 33–52. https://doi.org/10.1029/90PA01941

Miller, K. G., Browning, J. V., Schmelz, W. J., Kopp, R. E., Mountain, G. S., & Wright, J. D. (2020). Cenozoic sea-level and cryospheric evolution from deep-sea geochemical and continental margin records. *Science Advances*, *6*(20), eaaz1346. https://doi.org/10.1126/sciadv.aaz1346

Müller, P. J., Kirst, G., Ruhland, G., von Storch, I., & Rosell-Melé, A. (1998). Calibration of the alkenone paleotemperature index $U_{37}^{K'}$ based on core-tops from the eastern South Atlantic and the global ocean (60°N-60°S). *Geochimica et Cosmochimica Acta*, *62*(10), 1757–1772. https://doi.org/10.1016/S0016-7037(98)00097-0

Nirenberg, J. E., & Herbert, T. D. (2024). North Pacific warmth synchronous with the Miocene Climatic Optimum. *Geology*. https://doi.org/10.1130/G52432.1

O'Brien, P. E., Cooper, A. K., Richter, C., & et al. (Eds.). (2001). *Proceedings of the Ocean Drilling Program, 188 Initial Reports* (Vol. 188). Ocean Drilling Program. https://doi.org/10.2973/odp.proc.ir.188.2001

Pierce, E. L., van de Flierdt, T., Williams, T., Hemming, S. R., Cook, C. P., & Passchier, S. (2017). Evidence for a dynamic East Antarctic ice sheet during the mid-Miocene climate transition. *Earth and Planetary Science Letters*, *478*, 1–13. https://doi.org/10.1016/j.epsl.2017.08.011

Pritchard, H. D., Fretwell, P. T., Fremand, A. C., Bodart, J. A., Kirkham, J. D., Aitken, A., et al. (2025). Bedmap3 updated ice bed, surface and thickness gridded datasets for Antarctica. *Scientific Data*, *12*(1), 414. https://doi.org/10.1038/s41597-025-04672-y

Raitzsch, M., Bijma, J., Bickert, T., Schulz, M., Holbourn, A., & Kučera, M. (2021). Atmospheric carbon dioxide variations across the middle Miocene climate transition. *Climate of the Past*, *17*(2), 703–719. https://doi.org/10.5194/cp-17-703-2021

Rees-Owen, R. L., Gill, F. L., Newton, R. J., Ivanović, R. F., Francis, J. E., Riding, J. B., et al. (2018). The last forests on Antarctica: Reconstructing flora and temperature from the Neogene Sirius Group, Transantarctic Mountains. *Organic Geochemistry*, *118*, 4–14. https://doi.org/10.1016/j.orggeochem.2018.01.001

Roden, N. P., Shadwick, E. H., Tilbrook, B., & Trull, T. W. (2013). Annual cycle of carbonate chemistry and decadal change in coastal Prydz Bay, East Antarctica. *Marine Chemistry*, *155*, 135–147. https://doi.org/10.1016/j.marchem.2013.06.006

Sangiorgi, F., Bijl, P. K., Passchier, S., Salzmann, U., Schouten, S., McKay, R., et al. (2018). Southern Ocean warming and Wilkes Land ice sheet retreat during the mid-Miocene. *Nature Communications*, *9*(1), 317. https://doi.org/10.1038/s41467-017-02609-7

Shevenell, A. E., Kennett, J. P., & Lea, D. W. (2004). Middle Miocene Southern Ocean Cooling and Antarctic Cryosphere Expansion. *Science*, *305*(5691), 1766–1770. https://doi.org/10.1126/science.1100061

Sikes, E. L., Volkman, J. K., Robertson, L. G., & Pichon, J.-J. (1997). Alkenones and alkenes in surface waters and sediments of the Southern Ocean: Implications for paleotemperature estimation in polar regions. *Geochimica et Cosmochimica Acta*, *61*(7), 1495–1505. https://doi.org/10.1016/S0016-7037(97)00017-3

Smellie, J. L., Panter, K. S., McIntosh, W. C., & Licht, K. J. (2024). Landscape evolution in the southern Transantarctic Mountains during the early Miocene (c. 20–17 Ma) and evidence for a highly dynamic East Antarctic Ice Sheet margin from the southernmost volcanoes in the world (87°S). *Global and Planetary Change*, *238*, 104465. https://doi.org/10.1016/j.gloplacha.2024.104465

Smellie, John L., Rocchi, S., Wilch, T. I., Gemelli, M., Di Vincenzo, G., McIntosh, W., et al. (2014). Glaciovolcanic evidence for a polythermal Neogene East Antarctic Ice Sheet. *Geology*, *42*(1), 39–41. https://doi.org/10.1130/G34787.1

Spector, P., & Balco, G. (2020). Exposure-age data from across Antarctica reveal mid-Miocene establishment of polar desert climate. *Geology*, *49*(1), 91–95. https://doi.org/10.1130/G47783.1

Super, J. R., Thomas, E., Pagani, M., Huber, M., O'Brien, C. L., & Hull, P. M. (2020). Miocene Evolution of North Atlantic Sea Surface Temperature. *Paleoceanography and Paleoclimatology*, *35*(5), e2019PA003748. https://doi.org/10.1029/2019PA003748

Tanner, T., Hernández-Almeida, I., Drury, A. J., Guitián, J., & Stoll, H. (2020). Decreasing Atmospheric CO_2 During the Late Miocene Cooling. *Paleoceanography and Paleoclimatology*, *35*(12), e2020PA003925. https://doi.org/10.1029/2020PA003925

Taylor, K. W. R., Huber, M., Hollis, C. J., Hernandez-Sanchez, M. T., & Pancost, R. D. (2013). Re-evaluating modern and Palaeogene GDGT distributions: Implications for SST reconstructions. *Global and Planetary Change*, *108*, 158–174. https://doi.org/10.1016/j.gloplacha.2013.06.011

Warny, S., Askin, R. A., Hannah, M. J., Mohr, B. A. R., Raine, J. I., Harwood, D. M., et al. (2009). Palynomorphs from a sediment core reveal a sudden remarkably warm Antarctica during the middle Miocene. *Geology*, *37*(10), 955–958. https://doi.org/10.1130/G30139A.1

Wegwerth, A., Arz, H. W., Kaiser, J., Winckler, G., Lembke-Jene, L., Rigalleau, V., et al. (2025). South Pacific sea surface temperature and global ocean circulation changes since the late Miocene. *Nature Communications*, *16*(1), 6593. https://doi.org/10.1038/s41467-025-62037-w

Westerhold, T., Marwan, N., Drury, A. J., Liebrand, D., Agnini, C., Anagnostou, E., et al. (2020). An astronomically dated record of Earth's climate and its predictability over the last 66 million years. *Science*, *369*(6509), 1383–1387. https://doi.org/10.1126/science.aba6853

Whitehead, J. M., Harwood, D. M., & McMinn, A. (2003). Ice-distal Upper Miocene marine strata from inland Antarctica. *Sedimentology*, *50*(3), 531–552. https://doi.org/10.1046/j.1365-3091.2003.00563.x

Williams, T., & Handwerger, D. (2005). A high-resolution record of early Miocene Antarctic glacial history from ODP Site 1165, Prydz Bay. *Paleoceanography*, *20*(2). https://doi.org/10.1029/2004PA001067

Zhang, Y. G., Zhang, C. L., Liu, X.-L., Li, L., Hinrichs, K.-U., & Noakes, J. E. (2011). Methane Index: A tetraether archaeal lipid biomarker indicator for detecting the instability of marine gas hydrates. *Earth and Planetary Science Letters*, *307*(3), 525–534. https://doi.org/10.1016/j.epsl.2011.05.031

Zhang, Y. G., Pagani, M., & Wang, Z. (2016). Ring Index: A new strategy to evaluate the integrity of TEX_{86} paleothermometry. *Paleoceanography*, *31*(2), 220–232. https://doi.org/10.1002/2015PA002848

CHAPTER 5

Plant waxes record East Antarctic hydroclimate during Miocene global warmth

Jared E. Nirenberg[1], Daniel E. Ibarra[1], and Timothy D. Herbert[1]

[1]Department of Earth, Environmental, and Planetary Sciences, Brown University, Providence, Rhode Island 02912, USA

Abstract

East Antarctica experienced a dramatic transformation in hydroclimate during the Miocene, from warm and wet conditions during the Miocene Climatic Optimum (MCO, ~14-17 Ma) to the establishment of polar desert conditions with cooling and ice sheet expansion during the Middle Miocene Climate Transition (MMCT, ~13.9 Ma) and late Miocene cooling interval (~6-7.5 Ma). During Miocene warmth, retreat of Antarctic ice sheets allowed for the rise of vascular plant ecosystems on Antarctica, which preserved information on terrestrial hydroclimate through their epicuticular waxes. Here, we investigate molecular biomarkers of plant waxes from East Antarctica preserved in the polar Southern Ocean at Ocean Drilling Program Site 1165. We quantify the abundances and isotopic composition of long-chain *n*-alkanoic acids, providing records between 5 and 19 Ma. In addition, we present high-resolution (5 kyr) data spanning the late MCO and MMCT between 13.2 and 15.1 Ma. We compare plant wax isotopes to sea surface temperature (SST) proxies measured in the same samples to constrain interactions between ocean temperatures and terrestrial hydroclimate. Our records reveal a timescale-dependent relationship between SSTs and plant wax δD, with opposing isotopic responses to temperature forcing on orbital versus longer timescales. Our results demonstrate a complex response of Antarctic precipitation isotopes during the Miocene, with plant wax δD not only reflecting temperature changes, but also changes in vapor transport to Antarctica, aridity, and/or ecology. We conclude that our constraints on Antarctic precipitation isotopes have broader implications for the past isotopic composition of the East Antarctic Ice Sheet.

Introduction

Today, harsh conditions present extreme challenges to terrestrial vegetation on Antarctica. Less than 0.2% of the land surface is ice-free and therefore available as a substrate for vegetation growth (Burton-Johnson et al., 2016). Temperatures below freezing and hyperaridity make liquid water nearly inaccessible in these few ice-free areas. Yet, certain organisms have developed traits to survive and reproduce under these extreme conditions. Modern Antarctic vegetation is dominated by bryophytes, lichen, algae, and cyanobacteria, with only two species of native vascular plants in a narrow ecosystem along the Antarctic Peninsula (Colesie et al., 2023). However, this was not always the case.

During intervals of past global warmth, warmer and wetter conditions on Antarctica (Passchier et al., 2013) allowed for the expansion of more diverse terrestrial ecosystems than observed today. Cool temperate forests thrived across the continent from the Eocene through the Miocene (Anderson et al., 2011; Warny et al., 2009, 2019). These ecosystems were dominated by *Nothofagus* (Southern beech) trees and *Podocarp* conifers, analogous to ecosystems found in modern Southern South America and alpine New Zealand (Warny et al., 2009). Neogene cooling and ice sheet expansion led to a decline in these Antarctic terrestrial ecosystems (Anderson et al., 2011; Lewis et al., 2008), but local refugia for Antarctic vascular plants persisted at least through the Pliocene (Rees-Owen et al., 2018).

These ancient ecosystems were preserved through the accumulation of macrofossils, pollen, and epicuticular waxes (plant waxes) in sedimentary records across Antarctica (Francis & Hill, 1996; Lewis et al., 2008) and in marine records drilled from the continental margin (Hannah, 2006; Sangiorgi et al., 2018; Warny et al., 2009). Pollen assemblages have provided information about ecosystem changes and qualitative temperature reconstructions (Rees-Owen et al., 2018; Sangiorgi et al., 2018; Warny et al., 2009). Plant wax abundances and isotopic compositions provide complimentary information about processes such as plant water use efficiency and hydrologic cycling (Diefendorf et al., 2010; Sachse et al., 2012).

Plant waxes incorporate the isotopic composition of local precipitation (Sachse et al., 2012). In the modern high-latitudes, precipitation isotopes are strongly correlated with air temperature, with isotopic depletion reflecting colder temperatures (Dansgaard, 1964; Masson-Delmotte et al., 2008), known as the 'temperature effect'. Ice cores provide direct archives of past polar precipitation, and through the temperature effect, their isotopic composition has reconstructed Antarctic temperatures continuously over the past 800 kyr (Parrenin et al., 2007). While snapshots of ice from warmer climates prior to the Pleistocene have been captured (Shackleton et al., 2025), sedimentary records of plant wax isotopes present the most promising opportunity for continuous polar precipitation isotope records during intervals of past global warmth beyond the Pleistocene. However, Antarctic precipitation isotopes also reflect changing moisture sources to Antarctica (Masson-Delmotte et al., 2010; Stenni et al., 2010; Vimeux et al., 2001), and plant wax isotopes are also influenced by changing fractionation from source precipitation due to ecological and environmental shifts (Polissar & Freeman, 2010; Sachse et al., 2012). We hereafter refer to these effects as 'non-thermal' to distinguish from the dominant polar temperature effect, but we note that they are often coupled to changes in climate. A previous record of Antarctic plant wax hydrogen isotopes (δD hereafter) from the Miocene (Feakins et al., 2012) has been interpreted to reflect changes in polar air temperatures according to the temperature effect and analogous to ice core records, but this record lacks direct comparison to temperature proxy data measured in the same cores to distinguish between temperature and non-thermal influences on plant wax δD.

Here, we investigate the abundance and isotopic composition of plant waxes from East Antarctica preserved at Ocean Drilling Program (ODP) Site 1165 in the polar Southern Ocean. We create the first continuous record spanning much of the Miocene (5 to 19 Ma) to capture the rise of warm conditions during the Miocene Climatic Optimum (MCO), as well as the subsequent transition to cold polar conditions during the Middle Miocene Climate Transition (MMCT) and Late Miocene cooling interval. In addition, we present a high-resolution record between 13.2 and 15.1 Ma to resolve orbital-scale cyclicity in δD during the transition from MCO warmth to permanent East Antarctic glaciation during the MMCT. We compare plant wax isotopes with sea surface temperature (SST) proxies measured in the same samples to directly distinguish between temperature effects and non-thermal influences on plant wax δD. We find that ocean temperatures and plant wax δD mostly varied coherently on orbital timescales with depleted δD corresponding to colder SSTs, consistent with the modern temperature effect in polar regions. However, averaging over orbital cyclicity (>500 kyr) reveals that long-term SSTs and δD were correlated inversely to the modern temperature effect, with average δD enrichment during cooling intervals. These conflicting influences on Antarctic plant wax δD across the Miocene prevent the application of modern temperature-precipitation isotope relationships to reconstructing Antarctic air temperatures using plant wax δD.

Methods

Up to 15 grams of dry sediment were extracted using a Dionex Accelerated Solvent Extractor 350 with 3 static cycles at 150°C and 1600 psi using a solvent mixture of 9:1 dichloromethane (DCM):methanol. The total lipid extracts were desulfurized using activated copper wires and then separated using aminopropyl-modified silica gel chromatography into neutral and acid fractions through eluting with 4 mL 2:1 DCM:isopropanol and 4 mL 4:96 acetic acid:diethyl ether, respectively.

Free fatty acids were methylated to fatty acid methyl esters (FAMEs) for analysis. Acid fractions were dissolved in a small amount (<500 μL) of toluene, and about 1 mL of acidified methanol (5% acetyl chloride added dropwise to methanol) of known isotopic composition was added to each sample. Each vial was flushed with N_2 and set on a heating block to 60°C for 12 hours. After cooling to room temperature, about 2 mL of 5% sodium chloride in water was added to each sample to separate the sample mixture into an organic and aqueous layer. 1 mL of hexane was added, the vial was vortexed for about 20 seconds, and the organic (top) layer was carefully removed into a separate vial. This was repeated 4 times for every sample to extract the FAMEs from the methanol-water mixture. The fractions were then blown down under N_2 and reconstituted in a small amount (~500 μL) of hexane.

The FAME fractions were then further purified using silica gel flash chromatography. After conditioning in 4 mL DCM and then 4 mL hexane, the samples were loaded onto the column in hexane and further hexane was added until a total volume of 4 mL hexane was eluted. FAMEs were then eluted in 4 mL DCM. FAME fractions were then blown down under N_2 and reconstituted in 210 μL toluene containing an internal standard of hexatricontane (C_{36} *n*-alkane) of known concentration for quantification.

FAMEs were then quantified using gas chromatography with a flame ionization detector (GC-FID). Samples were analyzed using an Agilent 7890 or 8890 GC-FID equipped with a DB-1 column. FAMEs were identified through comparison with a FAME standard containing C_{16}, C_{18},

C_{22}, C_{24}, and C_{28} FAME. Blanks from ASE extractions, the methylation process, and both columns were run every 22 samples to monitor for potential contamination. C_{16} and C_{18} FAMEs were ubiquitous contaminants from the extraction process in significant quantities, preventing reliable sample isotopic measurements of these compounds. However, blank concentrations of longer-chain FAMEs, including the C_{28} FAME focused on in this work, ranged from negligible (under 2% of sample quantities) to undetectable.

Compound specific isotopes were measured using gas chromatography coupled to an isotope ratio mass spectrometer (GC-IRMS). Samples with sufficient FAME concentrations were measured in triplicate for δD or duplicate for $\delta^{13}C$. A standard mixture of C_{16}, C_{18}, C_{22}, C_{24}, and C_{28} FAMEs was run before, in between, and after sample injections. Sample isotopic compositions were corrected using the offset between the average of isotopic compositions of C_{28} FAME in all standards for each run and its known isotopic composition. A correction for the isotopic composition of the additional methyl group added during methylation was also applied. For δD, the instrument H_3 factor was determined twice a week at a minimum and each time after instrument maintenance. The standard deviation of replicate analyses of the C_{28} FAME standard was within 2‰ for δD and 0.2‰ for $\delta^{13}C$.

Data description

Our measurements of plant wax δD provide a record with an average sample resolution of 5 kyr during the high-resolution interval between 13.2 and 15.1 Ma and 124 kyr otherwise. Overall, 431 out of 471 (91.5%) of samples had sufficient C_{28} FAME concentrations for at least one measurement of δD. In addition, $\delta^{13}C$ was measured on 136 samples across the entire record, providing an average resolution of 138 kyr. We report all δD relative to VSMOW and $\delta^{13}C$ relative to VPDB.

C_{28} was the most abundant FAME chain length in the vast majority of samples, though C_{26} was the most abundant in some samples. A dominant chain length of C_{28} is consistent with other sites across the Antarctic margin during the Miocene, Oligocene, and Eocene (Feakins et al., 2012, 2014; Tibbett et al., 2021) which contain both pollen and plant waxes from vascular terrestrial plants. High carbon preference indices (CPI) for even over odd chain lengths support a source of fresh, thermally immature plant material for long-chain fatty acids (Bush & McInerney, 2013; Diefendorf et al., 2015). In addition, the lower energy and more ice-distal environment of the continental rise at Site 1165 also favors the preservation of contemporaneous, rather than reworked, plant waxes (Duncan et al., 2019). While limited work has been done on the palynology of Site 1165, pollen from terrestrial plants has been identified in this stratigraphic interval, along with minimal evidence for reworking (Hannah, 2006). As such, we interpret the plant wax signals as representative of contemporaneous conditions where plants were growing in East Antarctica during the Miocene.

$$CPI = \frac{0.5 * C_{24} + C_{26} + C_{28} + 0.5 * C_{30}}{C_{25} + C_{27} + C_{29}}$$

The isotope signals are likely biased towards the austral summer months due to a lack of light availability for plant growth during the polar winter. Light is primarily available during the months between September and March in regions south of the polar circle, limiting the growth season to those months.

Results and Discussion

Plant wax accumulation and preservation at Site 1165

We quantify accumulation rates of the most abundant long-chain plant wax at Site 1165, C_{28} FAME, which we interpret as roughly indicative of the extent of vascular plant growth in the Lambert subglacial catchment basin in East Antarctica, which drains into Prydz Bay (Figure 1). We caution that we cannot account for potential effects of changing catchment area, variable plant wax preservation due to changing burial rates, or dilution by changing marine sediment accumulation independent of the accumulation of terrigenous material. However, the accumulation of this molecular biomarker derived from plants at this marine site provides a continuous perspective of the response of vascular plant communities to Antarctic cooling and aridification over the Miocene independent of preservation of macrofossils or pollen, as commonly studied at other sites (Lewis et al., 2008; Warny et al., 2009).

We calculate mass accumulation rates of C_{28} acid in addition to sedimentary concentrations as concentrations are susceptible to dilution effects. To calculate accumulation rates, dry bulk density and linear sedimentation rates are needed. Linear sedimentation rates are derived from the age model for Site 1165, which uses biostratigraphic (O'Brien et al., 2001) and magnetic reversal datums (Florindo et al., 2003) integrated into a Bayesian framework using the package rBacon (Blaauw et al., 2017). Shipboard measurements using a gamma ray attenuation porosity evaluator (GRAPE) provide estimates of wet bulk density (O'Brien et al., 2001). To interpolate GRAPE density to sample depths and reduce measurement noise, we smooth the GRAPE density record using a Gaussian process regression fitted with a combined Matern 3/2 and exponential kernel, calculated using MATLAB (Figure 2). GRAPE density measurements less than 1.15 g/cm^3 were removed prior to smoothing, as these low densities are indicative of cracks in the cores and poor measurement quality.

To calculate dry bulk density from the smoothed GRAPE density record, the following equation (Herbert & Mayer, 1991) was used.

$$DBD = GD * \left(1 - \frac{GD - WBD}{GD - 1.025}\right) + 0.025 * \frac{GD - WBD}{GD - 1.025}$$

In this equation, DBD is dry bulk density, WBD is wet bulk density, and GD is grain density. Grain density was estimated as 2.52 g/cm^3 for every sample. This value was chosen by linearly mixing typical grain densities for detrital material (2.65 g/cm^3) and biogenic silica (2.0 g/cm^3) in a ratio of 80:20, which is a general estimate of bulk core composition from shipboard core descriptions of lithology (O'Brien et al., 2001). We lack further quantitative constraints on sediment composition in order to estimate changes in grain density across core depths. Finally, mass accumulation rates of C_{28} FAME were calculated using the following equation.

$$MAR_{C_{28}\,FAME} = [C_{28}\,FAME]\left(\frac{\mu g}{g\ dry\ sediment}\right) * DBD\left(\frac{g}{cm^3}\right) * LSR\left(\frac{cm}{kyr}\right)$$

Plant wax accumulation rates at Site 1165 peak during the Early and Middle Miocene and decline through the Late Miocene (Figure 3). While our age model cannot resolve changes in sedimentation rates on timescales shorter than hundreds of thousands of years due to the limited available datums, we can reasonably interpret changes in accumulation rates on broad timescales (>500 kyr). A pronounced local maximum coincides with the MCO between 14 and 17 Ma, though periods of elevated plant wax accumulation also occurred prior to the MCO. Plant wax accumulation sharply declined during the MMCT, though somewhat recovered within hundreds of thousands of years after East Antarctic Ice Sheet expansion at 13.8 Ma. Further declines occurred during the Late Miocene cooling interval (Herbert et al., 2016) after 8.5 Ma. These declines in plant wax accumulation that align with Miocene cooling and aridification in East Antarctica indicate a likely synchronous reduction in areas inhabited with vascular terrestrial plants on the continent.

However, long-chain *n*-alkanoic acids are detectible in almost every sample and C_{28} FAME accumulation rates do not decline to below detection limit. C_{28} acid is found in very low concentrations during the Plio-Pleistocene and even in the core top, despite the absence of vascular plant ecosystems in this region of East Antarctica today. The presence of these compounds suggests their origin is either from reworking of older material or long-range transport of plant waxes from another continent. The location of Site 1165 is not proximal to any other significant land masses, but atmospheric trajectory modeling of dust transport using data from 1979 to 2013 has shown that some trajectories of dust sourced from Southern Africa, and potentially Patagonia as well, can reach Prydz Bay within 10 days (Neff & Bertler, 2015). While samples with low CPI (less than 3) may indicate contributions from reworked, more thermally mature *n*-alkanoic acids, samples with very low C_{28} FAME concentrations but higher CPI, such as the core top, may reflect long-range transport of small, but detectable, quantities of plant waxes present from other continental sources.

Similarly to accumulation rates, CPI of long-chain fatty acids at Site 1165 also declines after the MCO (Figure 4). Persistently high CPI supports a contemporaneous plant source of these compounds during the Early and Middle Miocene. Despite large variations in concentrations between samples, CPI prior to 10 Ma is almost universally above 3, a commonly-used value as indicative of thermally-immature material from angiosperms (Bush & McInerney, 2013). The persistence of these well-preserved plant waxes through climate cooling and ice sheet expansion during the MMCT suggests that vascular plant communities in this region of East Antarctica likely retreated to coastal refugia (Duncan et al., 2025), but were not completely wiped out from the continent even during cold intervals. The disappearance of the highest CPI values after 12 Ma may indicate some contribution of reworked, thermally-mature acids, but CPI generally remained above 3 until Late Miocene Cooling after 8 Ma. After 8 Ma, CPI varies more evenly about an average of 3, with samples during the late Pliocene and Pleistocene having consistently lower CPI. While we note that these values are still consistently higher than a pure petrogenic end-member with a CPI of ~1, the decline in CPI along with declining plant wax accumulation rates since the late Miocene suggests that we cannot dismiss potentially significant influence of reworked material on plant wax isotopes after 8 Ma.

Production of long-chain fatty acids, including C_{28}, by microbes has been observed in modern Antarctic soils and lake sediments where no vascular plants are present (Chen et al., 2019, 2021, 2025). This alternative potential source of C_{28} acid raises uncertainty regarding the source organisms for C_{28} acid found at Site 1165. However, long-chain *n*-alkanoic acids in modern Antarctic lakes are chemically distinguished by their relatively enriched carbon isotopic composition, with $\delta^{13}C$ between -12.4‰ and -21.7‰ (Chen et al., 2019, 2025). At Site 1165, our measurements of $\delta^{13}C$ of C_{28} acid (Figure 5) vary between -26‰ and -30.1‰, which are typical values of C_3 vegetation and well outside of the range of observed microbially-produced values. While we cannot rule out potential trace amounts of microbially-produced C_{28} acid in Miocene sediments at Site 1165, $\delta^{13}C$ suggests that their influence is likely negligible relative to C_{28} acid produced by vascular plants. In addition, $\delta^{13}C$ of Plio-Pleistocene C_{28} acid are more depleted than Miocene values, which favors the interpretation of long-range transport of small amounts of plant waxes rather than a nearby microbial or thermally-mature source, both of which have more enriched $\delta^{13}C$ (Chen et al., 2019, 2025; Peters et al., 1981).

Orbital-scale temperature influences on precipitation isotopes

To assess the climatic drivers of plant wax δD variability, we directly compare with $U^{k'}_{37}$, a proxy for sea surface temperature independent of plant waxes that was measured in the same sample extracts. While not every sample was able to produce both proxy data due to lacking sufficient abundance of alkenones and/or C_{28} acid, both proxies were measured in over 90% of samples. The direct comparison between proxies derived from both marine and terrestrial organisms in the same sediment is a strength of ocean drilling sites with significant terrigenous input as the relationship between these proxies in the same stratigraphic intervals is unaffected by age model uncertainties, as they were deposited at the same time. However, differences in the transport time of biomarkers from production in the surface ocean and on the continent to sediment deposition at Site 1165 could result in stratigraphic offsets between the two signals. Alkenones are transported from the surface ocean to deeper depths on sub-seasonal timescales (see Herbert (2014) for a review of sediment trap studies), while terrigenous material in continental basins can have average transport times of hundreds of years (French et al., 2018). However, sediment samples were homogenized over approximately 2 cm depth intervals, so the biomarker signals measured represent an average of hundreds of years of deposition as sedimentation rates were 3-7 cm/kyr during our high-resolution interval. It is unlikely that the lag in deposition of terrigenous material from biomarkers produced at the same time is significant on the longer timescales of our records.

In our high-resolution record, we find mostly synchronous increases in SST and enrichment of plant wax δD between 14.1 and 15.1 Ma (Figure 6), near the end of the MCO. If the plant wax δD signal is interpreted as reflective of 1:1 changes in precipitation δD, the resulting relationship between surface temperatures in the polar Southern Ocean and East Antarctic precipitation δD during this interval of the MCO is analogous to modern Antarctic observations (Masson-Delmotte et al., 2008). The amplitude of temperature and δD variability that we observe on glacial-interglacial timescales (9°C and 60‰, respectively) are consistent with the modern air temperature and surface snow δD relationship of 6.34‰ per °C (Masson-Delmotte et al., 2008). However, if the slope of the temperature-δD relationship was lower than modern during the MCO, as some model simulations have suggested (Feakins et al., 2012), this would imply that air temperature variations in East Antarctica were amplified relative to changes in nearby SST. While quantification of changes in East Antarctic air temperatures from plant wax δD would require assumptions of precipitation to plant wax isotopic fractionation and a precipitation δD-air temperature relationship, which are both unconstrained, our results demonstrate the unambiguous influence of temperature on East Antarctic precipitation δD on orbital timescales during the MCO in a manner consistent with modern observed Antarctic relationships.

Cross-spectral coherence analysis (Figure 7) confirms that the strong visual correlations between plant wax δD and $U^{k'}_{37}$ prior to 14.1 Ma and after 13.6 Ma are statistically significant as well. The two signals are particularly coherent in the frequencies surrounding the characteristic oscillation of the obliquity, or degree of tilt, of Earth's axis with a period of 41 kyr. While our age model constraints are not precise enough for tuning to specific obliquity cycles from astronomical calculations (Laskar et al., 2004), the two proxies from the same samples are on the same age model as well, so their coherence to each other on these timescales is not as affected by uncertainties in absolute ages. Obliquity is the dominant influence on oscillations in mean annual insolation in the polar regions, so the coherence of Antarctic plant wax δD and polar Southern Ocean SST at the frequency of obliquity could be explained by local insolation forcing within both signals. While the cross-spectral coherence is most present near the frequency of obliquity oscillations, there is also significant coherence between plant wax δD and $U^{k'}_{37}$ at higher frequencies, perhaps related to precession cycles, prior to 14.5 Ma and at lower frequencies, perhaps related to 100 kyr eccentricity cycles, during some windows.

However, we note that we cannot explain all variability in plant wax δD during this interval through temperature effects alone. For example, between 14.15 and 14.25 Ma, SST and plant wax δD show opposing trends, and the variability of the two proxies appear relatively independent between 14.8 and 14.9 Ma. In addition, while the timing of high-frequency (<100 kyr period) cyclicity is generally synchronous between 14.3 and 14.75 Ma, lower frequency variability such as warming of average SSTs between 14.3 and ~14.53 Ma is not observed in plant wax δD.

After 14.1 Ma, variability in plant wax δD and $U^{k'}_{37}$ become discordant until a strong SST-δD relationship is reestablished around 13.5 Ma. SSTs at Site 1165 declined by ~10°C over 120 kyr synchronously with East Antarctic Ice Sheet expansion during the Mi3 glaciation between about 13.8 and 13.9 Ma (Figure 8). However, we do not observe depletion of plant wax δD during this interval as would be expected from temperature effects on precipitation δD. Rather, average plant wax δD becomes more enriched relative to the average prior to 14.1 Ma despite colder SSTs, and presumably air temperatures as well. While the departure from temperature effects on plant wax δD is most apparent during the Mi3 glaciation, the two proxies become decoupled prior to cooling and ice sheet expansion beginning around 14.1 Ma (Figure 8). This decoupling is also reflected in the disappearance of almost all cross-spectral coherence between plant wax δD and $U^{k'}_{37}$ after 14.1 Ma, particularly at the frequency of obliquity cycles (Figure 7).

The decoupling between SSTs and plant wax δD during the MMCT likely implies dominant influences of non-thermal effects on plant wax δD during this interval. While an alternative explanation could be that East Antarctic air temperatures and SSTs in the nearby polar Southern Ocean became decoupled during these intervals, this is unlikely. If interpreted as only affected by local/regional air temperatures, plant wax δD enrichment across the MMCT would imply warming continental air temperatures. Terrestrial records from Antarctica indicate cooling of at least 8°C and ice sheet expansion around 13.9 Ma (Lewis et al., 2008), which is synchronous with cooling SSTs at Site 1165 (Figure 8). Ice-rafted debris in marine records from around Antarctica show that ice sheets synchronously expanded to the marine-terminating margin in multiple basins, including the Prydz Bay region, during this glacial event as well (Pierce et al., 2017). We therefore rule out the possibility that decoupling of SSTs and plant wax δD across the MMCT was due to decoupling of continental and ocean surface temperatures, but rather is indicative of non-thermal influences on Antarctic plant wax δD that we discuss in the following section. The reemergence of synchronous warming of SSTs and plant wax δD enrichment according to the expected temperature effect after 13.5 Ma, as well as reappearance of significant cross-spectral coherence in the obliquity band (Figure 7), suggests that the non-thermal effects on plant wax δD only temporarily dominated high-frequency variability, reflecting a reorganization of either climatic processes or Antarctic ecosystems during the MMCT.

Miocene evolution of plant wax δD

Our measurements of plant wax isotopes at Site 1165 between 5 and 19 Ma provide a largely continuous record across most of the Miocene, save for an interval of no core recovery between about 11 and 12 Ma. While previous records have investigated Antarctic plant waxes during snapshots within the Miocene (Feakins et al., 2012; Tibbett et al., 2022), ours is the first to provide a continuous perspective spanning the rise of warm polar conditions with the onset of the MCO as well as the critical climate transitions of cooling and ice sheet growth during the MMCT and late Miocene cooling interval at a single location.

When averaged over orbital-scale cyclicity, plant wax δD during the warm MCO was more depleted on average, with depletion occurring with warming during the onset of the MCO and enrichment occurring with cooling during the MMCT. Plant wax δD and SSTs remain tightly coupled with δD enrichment with SST cooling until ~7.5 Ma, when little change in δD is observed during late Miocene cooling. This temperature-δD relationship is the opposite of what is observed in our orbital-resolution records spanning the Middle Miocene, when intervals of warming SSTs correspond to enriched plant wax δD in a manner consistent with the modern Antarctic air temperature-precipitation δD relationship. The correlation between SSTs in the polar Southern Ocean and plant wax δD on a multi-million year scale opposite to that observed on orbital timescales and in modern Antarctic spatial observations challenges a simplistic understanding of the drivers of high-latitude precipitation isotope variability and suggests a timescale-dependence of the plant wax δD response to temperature forcing.

The mechanisms driving enrichment of plant wax δD with Antarctic cooling and ice sheet expansion during the Miocene are unclear. One inherent challenge to reconstructing precipitation δD using plant wax isotopes is that plant waxes are not direct archives of past precipitation. Rather, they are affected by several processes which isotopically fractionate between the precipitation source of hydrogen and preserved plant waxes. The amount of fractionation between precipitation and plant wax δD is not necessarily constant over time, but cannot be directly constrained here. Instead, we explore potential mechanisms that could drive Antarctic plant wax δD enrichment with cooling during the Miocene. These mechanisms can be grouped into two broad categories: (1) those which assume the plant wax δD signal is representative of precipitation δD throughout the Miocene and (2) those which assume other processes independent of changes Antarctic precipitation δD drive the long-term plant wax δD variability observed in our record. We emphasize that both of these mechanisms can impact our measured plant wax δD at Site 1165 at the same time, but the relative influence between the two (precipitation vs non-precipitation δD forcings) may vary throughout the record.

If the evolution of plant wax δD at Site 1165 primarily reflects East Antarctic precipitation δD, large-scale changes in atmospheric circulation and poleward moisture transport would be needed to explain depletion of polar precipitation δD during the warm MCO. During the MCO, warm SSTs in the polar Southern Ocean would seem to suggest greater surface evaporation rates in the Southern Ocean and therefore a more proximal source of precipitation to Antarctica. However, a more proximal precipitation source would experience less distillation through rainout, leading to a more enriched isotopic composition, rather than more depleted as observed in our record (Figure 9). Therefore, large-scale atmospheric water vapor transport to Antarctica may have counterintuitively experienced a greater degree of rainout during the MCO. There are several lines of evidence which support a relatively expanded Hadley cell during the MCO (Groeneveld et al., 2017; Herold et al., 2011; Paknia et al., 2025). If a greater degree of distillation occurred as tropical moisture rained out over a larger transport path within an expanded Hadley cell, the precipitation isotope signature of moisture exported to higher latitudes would be more depleted. Alternatively, this greater degree of rainout of poleward moisture transport may have occurred even further from the tropics in the higher Southern latitudes where modern temperature gradients are steeper and storms transport more heat and moisture towards the poles. Further precipitation isotope reconstructions from other regions would help constrain global patterns of moisture transport during the MCO.

Conversely, shifts in atmospheric circulation may also explain Antarctic precipitation δD enrichment during the MMCT. Contraction of the Hadley cell along with equatorward shifts of other Southern Hemisphere frontal zones (Kuhnert et al., 2009; Shevenell et al., 2004) may have resulted in less distilled, and therefore more isotopically enriched, tropical-sourced water vapor transported to the high-latitudes. The timing of frontal shifts during the MMCT precedes ice sheet expansion by 100-300 kyr (Kuhnert et al., 2009; Shevenell et al., 2004), and this early timing of frontal shifts is synchronous with the decoupling of SSTs and plant wax δD ~120-200 kyr prior to cooling at Site 1165. Alternatively, direct forcings from an expanded and higher-elevation East Antarctic Ice Sheet may have significantly impacted polar atmospheric circulation and moisture sources to the Lambert basin. Direct forcing of Southern Hemisphere ice sheets on long-term Antarctic precipitation δD, rather than temperature itself, could be consistent with the lack of enrichment observed in plant wax δD during the late Miocene cooling interval after 7.5 Ma (Herbert et al., 2016), in which Southern Ocean SSTs declined but benthic $\delta^{18}O$ suggests little to no increase in global ice volume occurred (Westerhold et al., 2020).

Factors other than precipitation δD may have significant influences on the evolution of plant wax δD recorded at Site 1165. The plant waxes deposited at the open marine location of Site 1165 reflect an integration of all inputs over a catchment area. The modern drainage basin for the Lambert Glacier, which flows into Prydz Bay, spans over 20% of the area of East Antarctica (Figure 1). However, we cannot constrain past changes in catchment area or where plants were growing within the drainage basin. Changing areas suitable for plant growth in East Antarctica with highly variable ice sheet extent (Levy et al., 2016; McKay et al., 2024) during the Miocene may impact plant wax δD recorded at Site 1165 as the plant waxes, even if accurately recording changes in precipitation δD where the plants grew, may reflect precipitation δD integrated over different areas of East Antarctica over time. Modern Antarctic snowfall δD shows a large spatial gradient with depleted δD in the cold, high-elevation continental interior and more enriched δD in the lower elevation coastal areas (Masson-Delmotte et al., 2008). Vegetated areas likely expanded into higher-elevation areas and the continental interior during warm intervals of ice sheet retreat and towards ice-free areas in coastal refugia where conditions were milder when the ice sheet expanded. Even with a temporally-constant spatial gradient of precipitation δD, plant wax δD at Site 1165 would be expected to become more enriched during intervals with a larger EAIS and more depleted during intervals of reduced ice sheets, as we observe in our long-term record (Figure 9), simply due to where vascular plants were able to grow and produce waxes. Under this interpretation, our observed trend of longer-term δD over time could be reasonably be interpreted as an index of the extent of plant growth into the interior of East Antarctica, which could explain its tight correlation with nearby SST opposite to that expected from modern Antarctic relationships.

In addition, the net fractionation between δD of precipitation and plant waxes may have varied over time. Hyperarid conditions arose on Antarctica during Miocene cooling intervals (Lewis et al., 2008; Spector & Balco, 2020; Verret et al., 2023), transforming the continent into the cold polar desert we observe today. Drier surface conditions in East Antarctica may have enhanced evaporation rates within soil water, causing isotopic enrichment of soil water relative to precipitation. These potential aridity effects may explain the depleted plant wax δD during the wetter MCO and enrichment with cooling and drying during the MMCT. Similar mechanisms have been invoked to explain enrichment of Antarctic plant wax δD during earlier Cenozoic cooling intervals (Feakins et al., 2014; Tibbett et al., 2021). In addition, different types of vegetation have different net precipitation-wax isotopic fractionation factors (Sachse et al., 2012), so shifts in Antarctic vegetation throughout the Miocene may influence plant wax δD. While vegetation records consistently show primarily *Nothofagus* (Southern beech) trees and *Podocarp* conifers growing on Antarctica from the Oligocene through Pliocene (Rees-Owen et al., 2018; Sangiorgi et al., 2018; Warny et al., 2009, 2019), Miocene cooling and aridification of Antarctica could reasonably produce large-scale ecosystem shifts, though pollen data is not yet available at high enough resolution to constrain these shifts. The relatively small magnitude of variability in plant wax $\delta^{13}C$ throughout the Miocene at Site 1165 (Figure 5) also supports little change in vegetation types. While the genera of terrestrial plants populating Antarctica may not have changed much during the Miocene, changes in growth forms of these plants may have impacted δD of their waxes. Fossil wood found in the Transantarctic Mountains from the

Pliocene suggests that mature *Nothofagus* grew in a prostrate shrub form, with branches spreading out close to the ground, rather than the more familiar tree-like form with vertical trunk growth (Francis & Hill, 1996). While tree-like forms of *Nothofagus* are hypothesized to have grown during the warmest intervals of the MCO (Warny et al., 2009), changes in proportions of different growth forms over time cannot be reconstructed, and it is unknown whether different growth forms have different precipitation-wax isotopic fractionation factors. Changes in plant physiology and East Antarctic hydrology may have even combined to produce further effects on plant wax δD. The depth of the permafrost layer moved towards the surface with Miocene cooling (Verret et al., 2023), leaving soil water available at shallower depths. The prostrate shrub forms of *Nothofagus* may also have shallower root systems than tree forms, drawing on shallower water as a source of hydrogen for plant waxes. Greater soil evaporation due to increased aridity with cooling would affect shallow soil water the most. In combination, all 3 of these theorized effects would enrich plant water δD and could lead to enriched plant wax δD during Miocene cooling intervals independent of precipitation isotopes.

For all of these potential mechanisms, what drives opposing responses of δD to temperature changes on orbital versus longer timescales is unclear. Responses of vegetation, atmospheric circulation, and soil evaporation to temperature forcing all occur on even shorter timescales than orbital cyclicity (~20-100 kyr), so it is unknown why their influence would be dominant only on longer tectonic timescales.

Implications of precipitation isotopes in East Antarctica on benthic δ18O

In addition to providing information on hydroclimate response within East Antarctica to temperature forcing, the Miocene evolution of plant wax δD at Site 1165 has broader implications for the interpretation of global climate records. $\delta^{18}O$ of benthic foraminifera (benthic $\delta^{18}O$) are commonly interpreted as an index for global temperatures (Westerhold et al., 2020). Benthic $\delta^{18}O$ is influenced by both deep ocean temperatures and seawater $\delta^{18}O$, the latter of which is impacted by changing polar ice sheet volumes ('ice volume effect'). The magnitude of the ice volume effect on seawater $\delta^{18}O$ is directly related to both ice volume and the isotopic composition of the ice sheet. However, interpretations of benthic $\delta^{18}O$ generally assume a constant ice sheet isotopic composition over time. East Antarctica contained the vast majority of global ice volume prior to the intensification of Northern Hemisphere glaciation during the Plio-Pleistocene, and δD of modern Antarctic precipitation is tightly linearly related to $\delta^{18}O$ according to the local meteoric water line (Masson-Delmotte et al., 2008). If our record is representative of broader changes in East Antarctic precipitation δD, the evolution of plant wax δD at Site 1165 provides insight into changing $\delta^{18}O$ composition of the EAIS and the resulting ice volume effect on benthic $\delta^{18}O$ throughout the Miocene. These changes in EAIS $\delta^{18}O$ inferred from Miocene plant wax δD have dramatic potential consequences on the partition of changes in benthic $\delta^{18}O$ into ice volume and temperature components.

A relatively-depleted EAIS composition during the MCO would have increased the ice volume effect on benthic $\delta^{18}O$, potentially masking a larger reduction in ice volume than assumed from a constant ice sheet $\delta^{18}O$. At the onset of the MCO, a large degree of surface ocean warming observed at some high-latitude sites (Chapter 4, Nirenberg & Herbert, 2024) relative to depletion in benthic $\delta^{18}O$ would suggest mostly temperature effects on benthic $\delta^{18}O$ with little to no ice volume changes. However, plant wax δD shows a 25‰ depletion of δD across the onset of the MCO, which would translate to ~3.2‰ in $\delta^{18}O$ according to the modern Antarctic meteoric water line (Masson-Delmotte et al., 2008). If plant wax δD at Site 1165 is weighted towards coastal precipitation, the effects may have been amplified through Rayleigh distillation further inland and at higher elevations, where the ice sheet likely retreated during the MCO. While a reduction in ice volume during the MCO would have reduced the ice volume impact on benthic $\delta^{18}O$, a shift towards a more isotopically depleted EAIS would have counteracting effects, increasing the ice volume impact on benthic $\delta^{18}O$. As such, the combined impact of the two may have resulted in a negligible change in the total ice volume effect on benthic $\delta^{18}O$, despite a significant reduction in ice volume itself.

The converse may have also been true with EAIS expansion during the MMCT. During the Mi3 glaciation (~13.8-13.9 Ma), benthic $\delta^{18}O$ became enriched by ~1‰, but there is significant disagreement on the partition of this change between bottom water temperature and ice volume effects. Bottom water temperature records derived from the clumped isotopic composition of benthic foraminifera imply mostly temperature effects on the benthic $\delta^{18}O$ enrichment during the MMCT with little changes in ice volume (Hou et al., 2023). However, magnesium to calcium ratios of benthic foraminifera at other sites suggest little bottom water cooling during the MMCT and therefore a mostly ice volume effect on benthic $\delta^{18}O$ (Shevenell et al., 2008). Surface temperature records in the polar Southern Ocean, where bottom water forms, corroborate significant cooling during Mi3 (Chapter 4) and indirectly imply a large temperature effect on benthic $\delta^{18}O$, but geologic records from Antarctica (Lewis et al., 2008) and the polar Southern Ocean (Pierce et al., 2017) demonstrate dramatic ice sheet expansion. However, this ice sheet expansion may have had little impact on benthic $\delta^{18}O$ due to shifts in its isotopic composition. As the EAIS expanded from the higher elevation continental interior towards coastal lowlands, the ice sheet would incorporate more isotopically enriched precipitation near the coasts at the same time as Antarctic precipitation δD became more enriched by ~40‰ (Figure 10, equivalent to ~5.2‰ in $\delta^{18}O$). The isotopic enrichment of the EAIS synchronous with a large expansion in its volume may have combined to result in a negligible impact on benthic $\delta^{18}O$. As a result, shifts in the $\delta^{18}O$ of East Antarctic ice volume may explain the discrepancy between dramatic changes in Antarctic ice sheet extent observed through geologic records surrounding the MCO, yet little 'ice volume effect' within the benthic $\delta^{18}O$ record relative to temperature effects.

Conclusions

Our records of well-preserved Antarctic plant waxes from the deep polar Southern Ocean provide continuous information on vegetation growing in East Antarctica during most of the Miocene and serve as a geochemical complement to other physical remnants of these ancient ecosystems, such as pollen and macrofossils. Our measurements of these waxes in the same samples as for proxies for ocean surface temperature allow us to interpret the responses of hydroclimate and higher plant ecosystems in East Antarctica to thermal forcing from the adjacent polar Southern Ocean and/or orbital forcing during the warmer than modern climates of the Miocene. Our high-resolution record of plant wax δD confirms the existence of temperature effects on Antarctic precipitation δD similar to observed spatial patterns across modern

Antarctica. However, departure from the expected temperature effect during key climate transitions, such as the interval of East Antarctic Ice Sheet expansion after 14 Ma, and the reverse relationship between plant wax δD and SSTs in our long-term record indicate shifts in East Antarctic precipitation δD unexpected from modern temperature-isotope relationships alone and/or the influence of other factors such as large-scale atmospheric circulation changes, soil aridity, and ecological shifts on plant wax δD. The mechanisms driving depletion of plant wax δD with warming and enrichment with cooling in the long-term record remain unclear, but warrant further exploration with isotope-enabled Miocene climate model simulations.

As a result of the complex, and sometimes opposing, temperature effects on plant wax δD, we conclude that past Antarctic air temperatures cannot be quantitatively reconstructed using a single δD-air temperature transfer function. However, our high-resolution record suggests that plant wax δD can faithfully record relative changes in East Antarctic air temperatures on orbital timescales, but more complex effects can decouple the signals during some intervals, including the MMCT. While the ability to quantitatively reconstruct air temperature is limited, the evolution of Antarctic precipitation δD as implied by our plant wax record has significant implications for changes in the isotopic composition of the East Antarctic Ice Sheet, and its resulting impact on benthic $\delta^{18}O$, over the Miocene. Our findings highlight both the potential as well as the challenges of reconstructing Antarctic hydroclimate using sedimentary plant waxes during past warm climate intervals. With the emerging availability of samples of Antarctic ice from the Miocene (Shackleton et al., 2025), future work comparing isotopic signatures of both archives of past Antarctic precipitation during intervals of temporal overlap present an exciting possibility.

Acknowledgements

We thank Emily Clements and Sofía Gilroy for their assistance in sample preparation. We thank the Gulf Coast Repository as well as the scientists and crew of ODP Leg 188 for providing sample material. This study used samples and data from the International Ocean Discovery Program (IODP) and its predecessors. Funding was provided through the Schlanger Ocean Drilling Fellowship by the US Science Support Program and NSF Grant GR5260690.

Figures

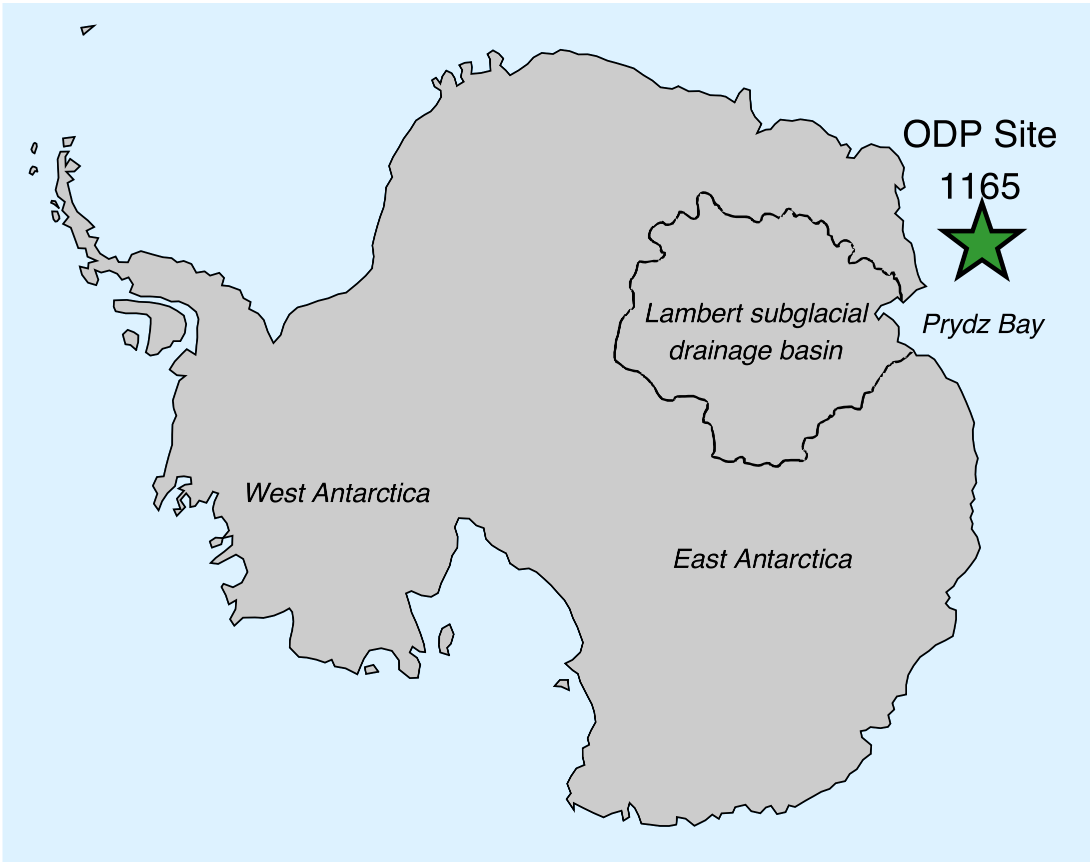

Figure 1. Stereographic projection map of Antarctica showing the modern Lambert subglacial drainage basin (Jamieson et al., 2005) and the location of ODP Site 1165.

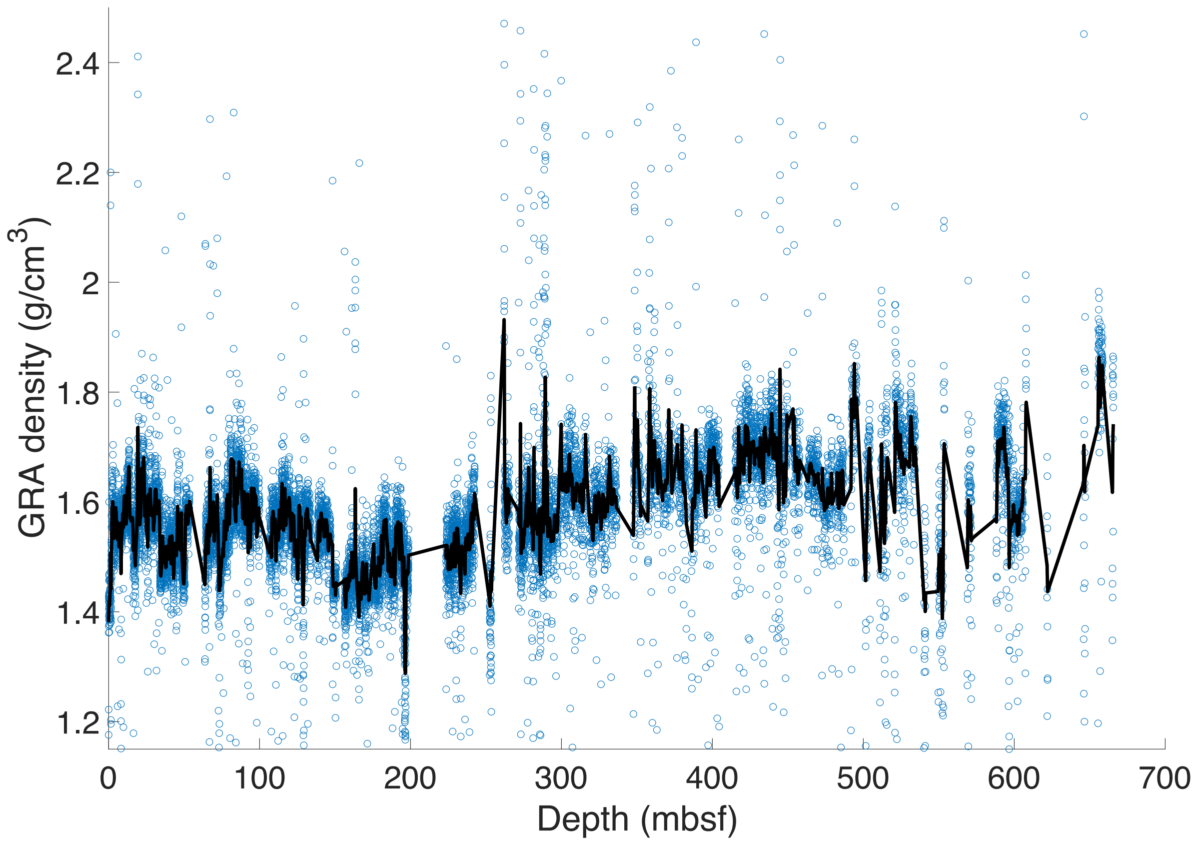

Figure 2. Wet bulk density from gamma ray attenuation porosity versus core depth in meters below seafloor (mbsf) for Hole 1165B. Blue circles are individual scanning measurements, and the black line represents predictions from a Gaussian process regression.

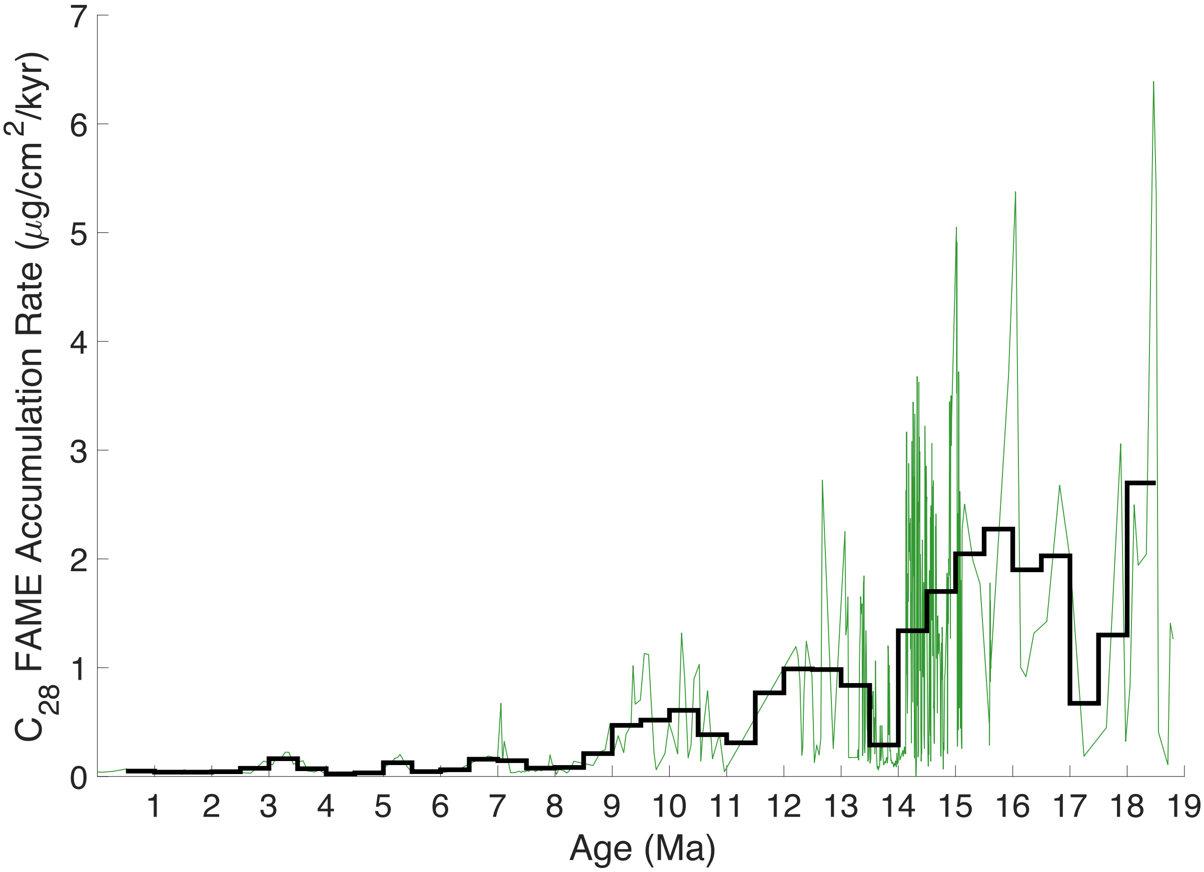

Figure 3. Accumulation rate of C_{28} FAME at Site 1165. Calculations from individual sample concentrations (green line) are shown along with integrated accumulation rates over 500 kyr bins (black line).

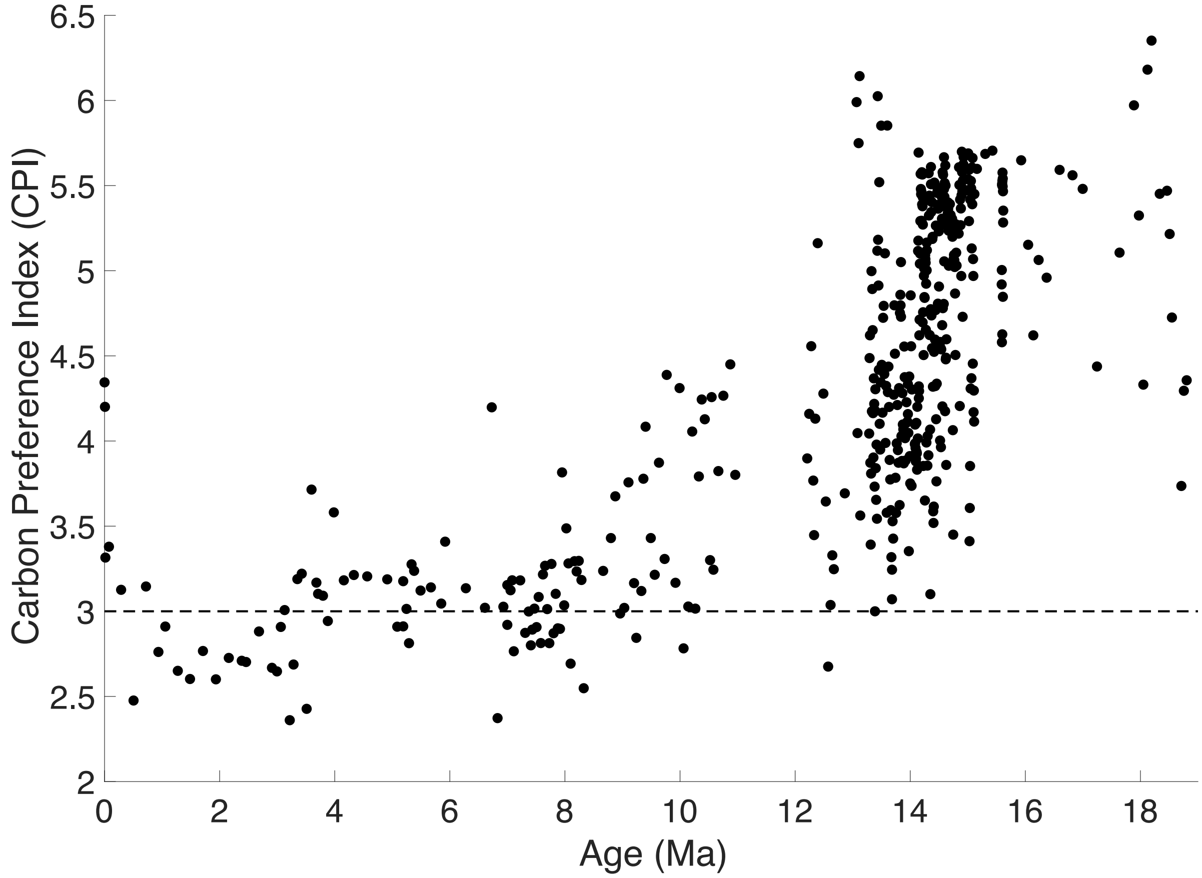

Figure 4. Carbon preference index of C_{24}-C_{30} fatty acids over time. Values above 3 are typical of fresh plant material whereas lower values may indicate contributions from thermally mature sources.

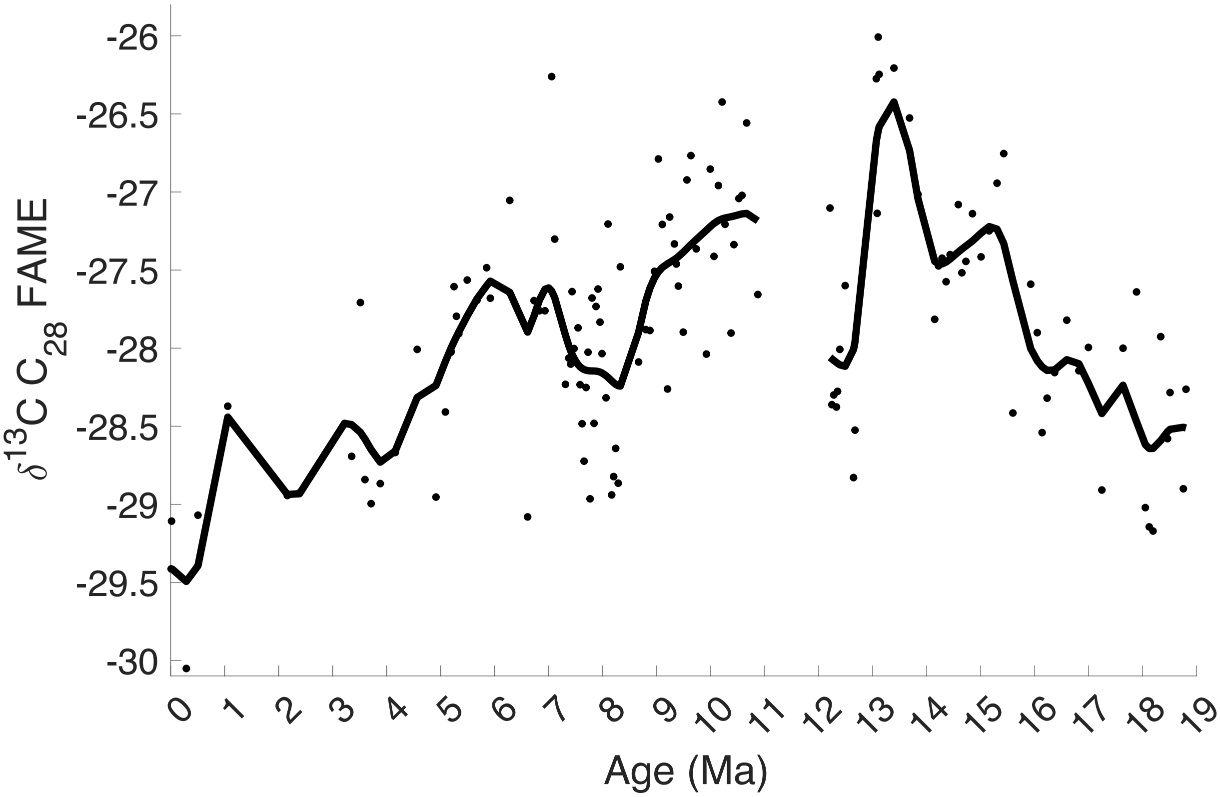

Figure 5. $\delta^{13}C$ vs. VPDB of C_{28} acid between 5 and 19 Ma. Black circles represent individual sample measurements, and the black line is a smoothed average using a Gaussian-weighting with a standard deviation of 250 kyr.

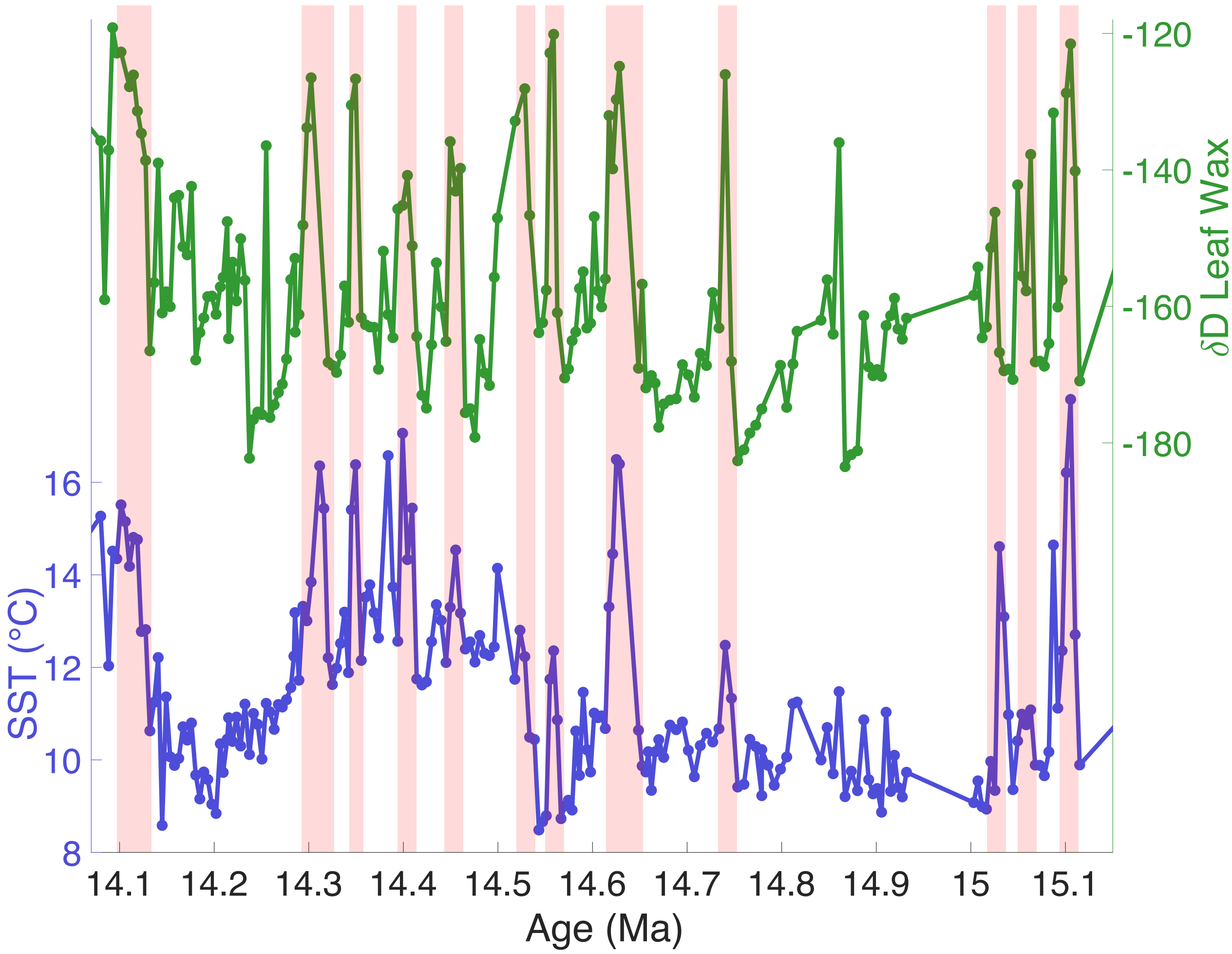

Figure 6. (a) Plant wax δD and (b) $U^{k'}_{37}$-derived SST from the calibration of Müller et al., (1998) during the high-resolution interval near the end of the Miocene Climatic Optimum. Red bars indicate intervals of synchronized SST warming and δD enrichment.

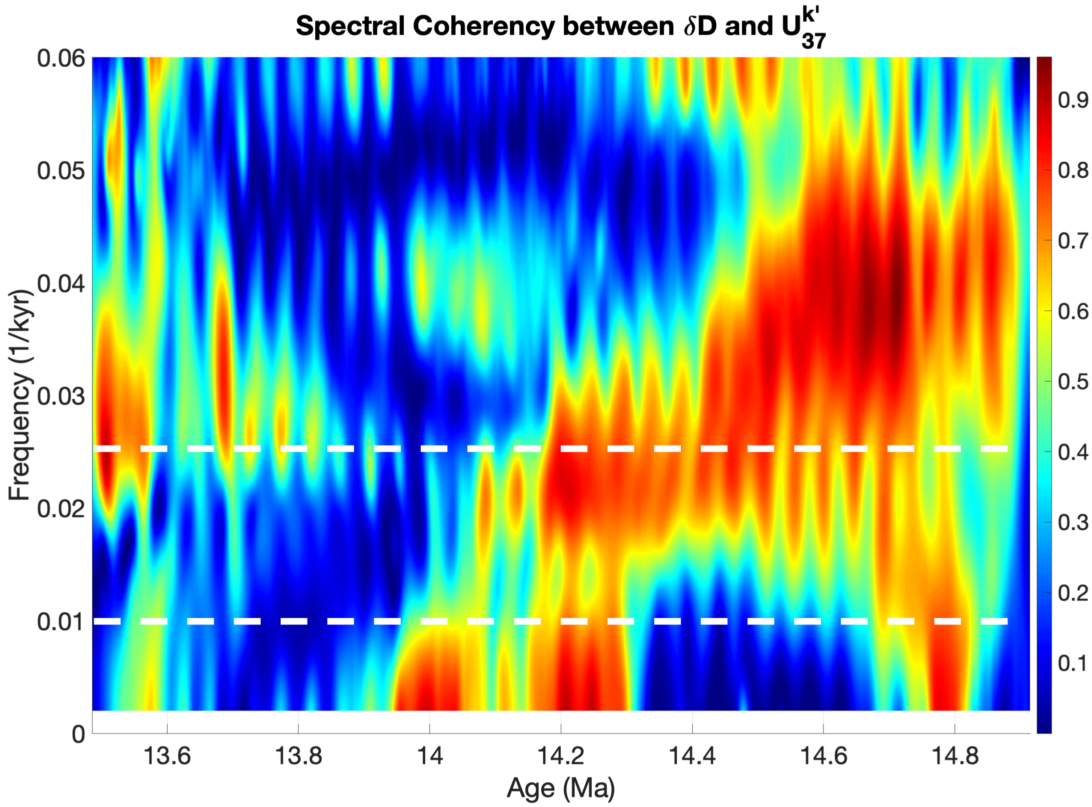

Figure 7. Evolutive cross-spectral coherence between plant wax δD and $U^{k'}_{37}$ during the orbital-resolution interval between 13.25 and 15.15 Ma. Moving windows of 400 kyr were used, and both records were resampled to a resolution of 1 kyr for the purposes of calculation. Within each window, both proxies were detrended prior to calculating coherence. Coherence was calculated using the mscohere function in MATLAB, which uses a magnitude-squared coherence function and estimates spectral power density using the periodogram function. White dashed lines represent characteristic frequencies of oscillations in the orbital parameters of obliquity (41 kyr period) and short-eccentricity (100 kyr period).

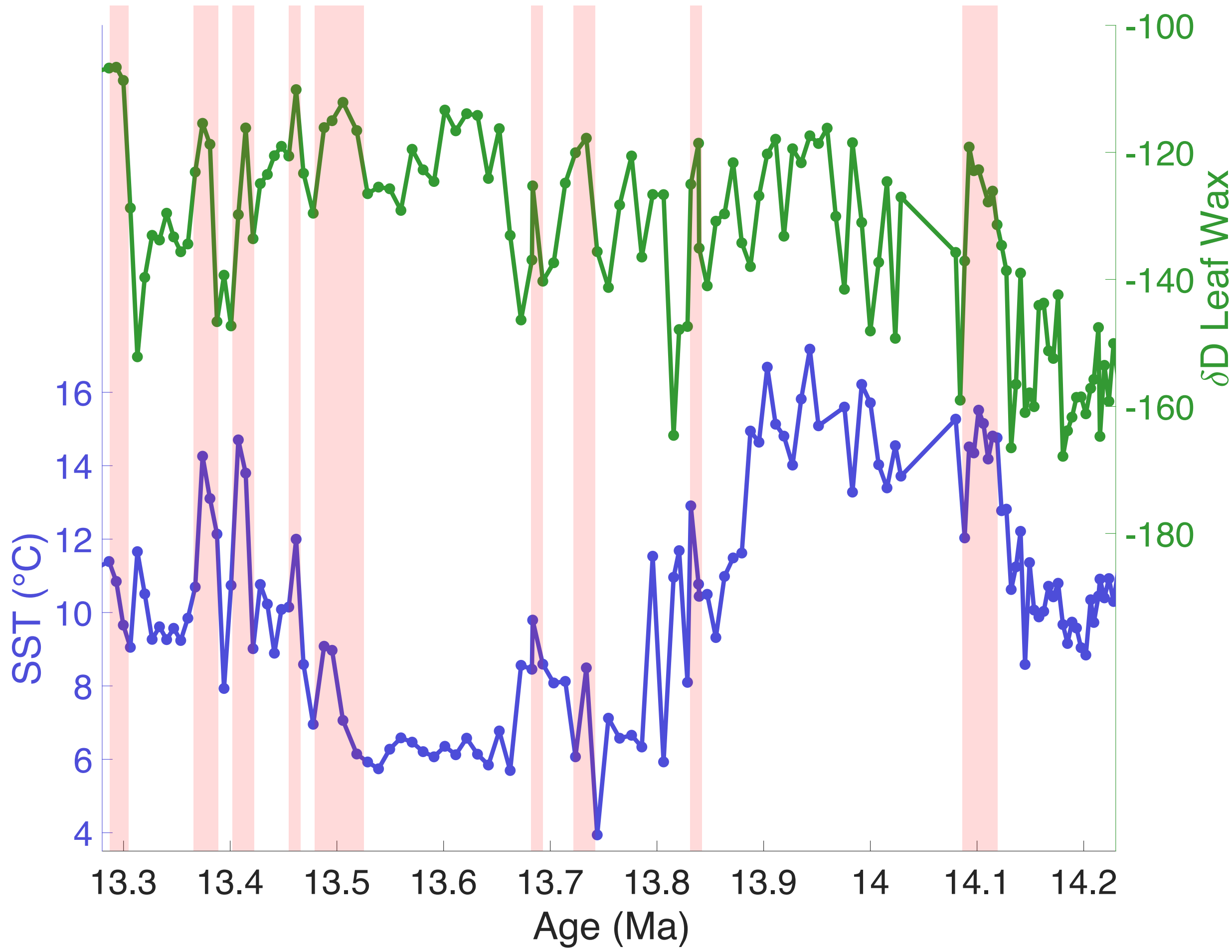

Figure 8. (a) Plant wax δD (green) and (b) $U^{k'}_{37}$-derived SST (blue) from the calibration of Müller et al., (1998) during the high-resolution interval spanning the Middle Miocene Climate Transition and Mi3 glaciation. Red bars indicate intervals of synchronized SST warming and δD enrichment.

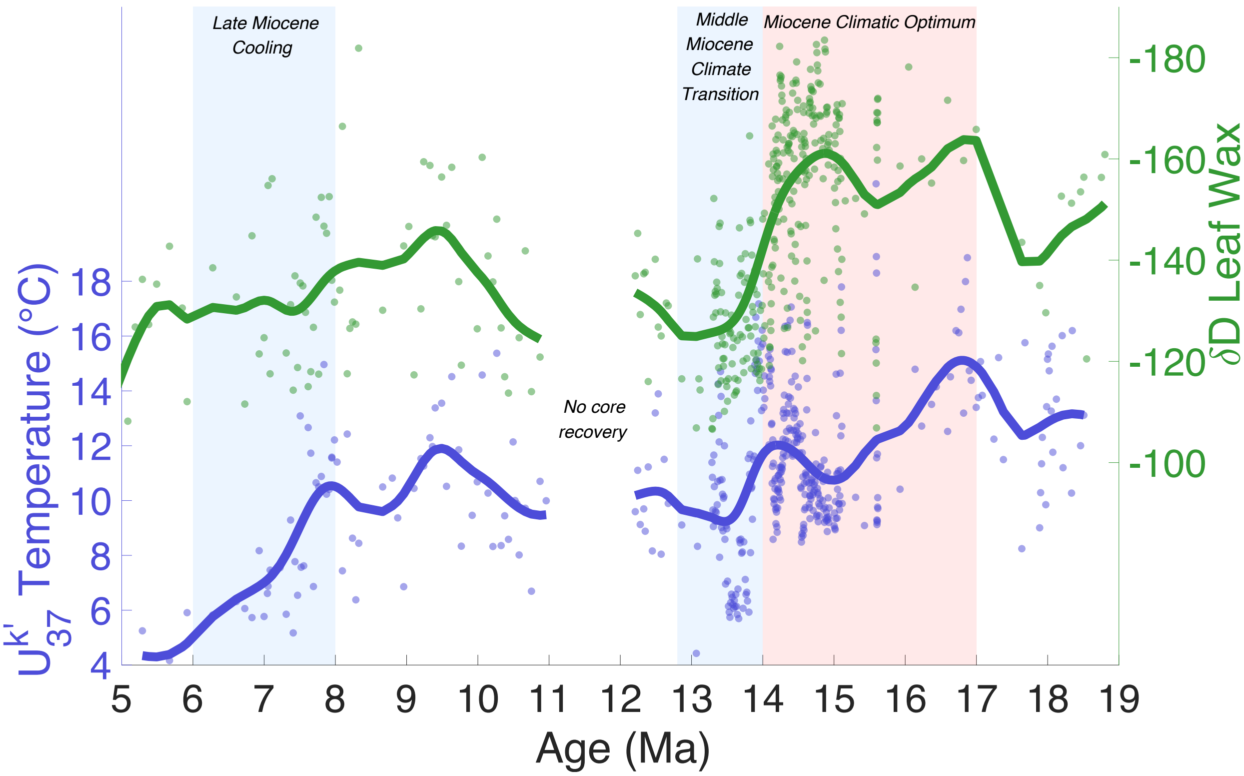

Figure 9. (a) Plant wax δD (green) and (b) $U^{k'}{}_{37}$-derived SST (blue) from the calibration of Müller et al., (1998) between 5 and 19 Ma. Individual sample data are shown as colored circles, and thick lines are a Gaussian-weighted smoothed-average with a standard deviation of 250 kyr.

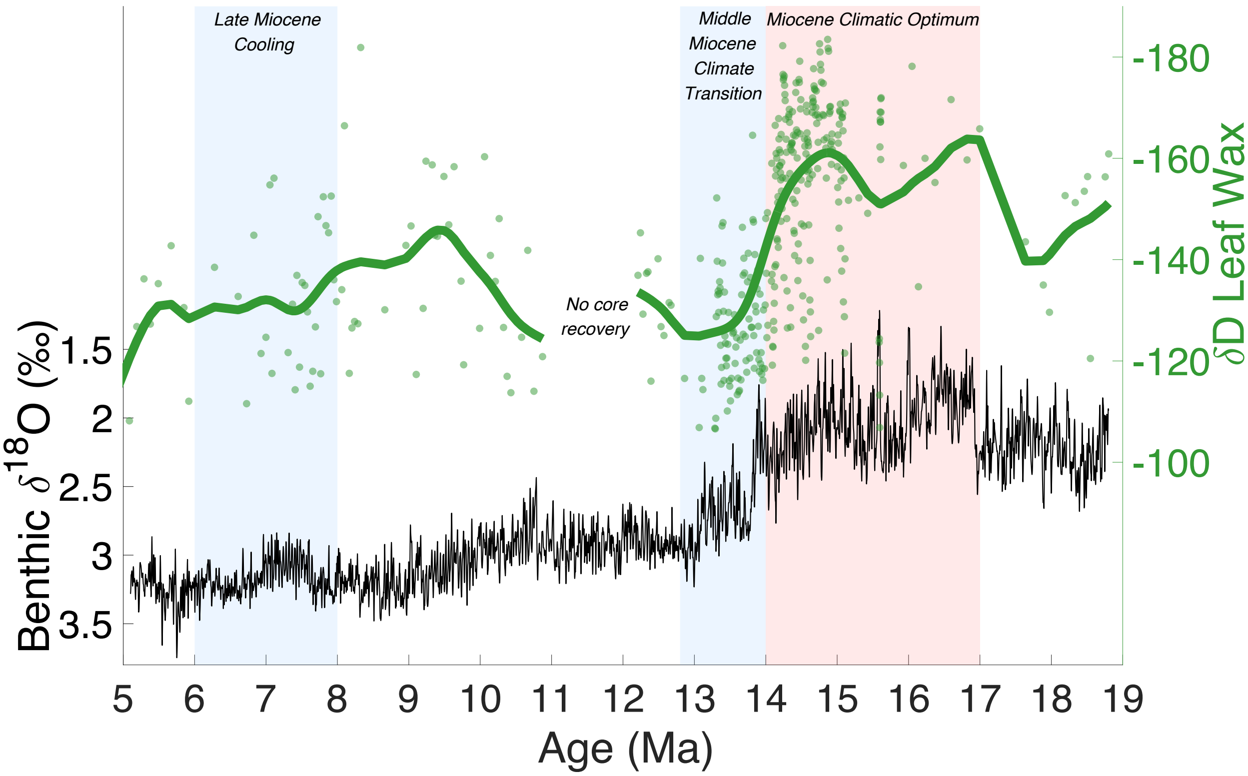

Figure 10. (a) Plant wax δD from Site 1165 and (b) benthic $\delta^{18}O$ (Westerhold et al., 2020) between 5 and 19 Ma.

References

Anderson, J. B., Warny, S., Askin, R. A., Wellner, J. S., Bohaty, S. M., Kirshner, A. E., et al. (2011). Progressive Cenozoic cooling and the demise of Antarctica's last refugium. *Proceedings of the National Academy of Sciences*, *108*(28), 11356–11360. https://doi.org/10.1073/pnas.1014885108

Blaauw, M., Christen, J. A., & Aquino Lopez, M. A. (2017). rbacon: Age-Depth Modelling using Bayesian Statistics [Data set]. https://doi.org/10.32614/CRAN.package.rbacon

Burton-Johnson, A., Black, M., Fretwell, P. T., & Kaluza-Gilbert, J. (2016). An automated methodology for differentiating rock from snow, clouds and sea in Antarctica from Landsat 8 imagery: a new rock outcrop map and area estimation for the entire Antarctic continent. *The Cryosphere*, *10*(4), 1665–1677. https://doi.org/10.5194/tc-10-1665-2016

Bush, R. T., & McInerney, F. A. (2013). Leaf wax *n*-alkane distributions in and across modern plants: Implications for paleoecology and chemotaxonomy. *Geochimica et Cosmochimica Acta*, *117*, 161–179. https://doi.org/10.1016/j.gca.2013.04.016

Chen, X., Liu, X., Wei, Y., & Huang, Y. (2019). Production of long-chain *n*-alkyl lipids by heterotrophic microbes: New evidence from Antarctic lakes. *Organic Geochemistry*, *138*, 103909. https://doi.org/10.1016/j.orggeochem.2019.103909

Chen, X., Liu, X., Jia, H., Jin, J., Kong, W., & Huang, Y. (2021). Inverse hydrogen isotope fractionation indicates heterotrophic microbial production of long-chain n-alkyl lipids in desolate Antarctic ponds. *Geobiology*, *19*(4), 394–404. https://doi.org/10.1111/gbi.12441

Chen, X., Liu, X., Feng, X., Kong, W., Wu, W., Liang, L., et al. (2025). $^{2}H/^{1}H$ variation in lipids traces late-Holocene lake microbial metabolism in Antarctica. *Geochimica et Cosmochimica Acta*. https://doi.org/10.1016/j.gca.2025.10.013

Colesie, C., Walshaw, C. V., Sancho, L. G., Davey, M. P., & Gray, A. (2023). Antarctica's vegetation in a changing climate. *WIREs Climate Change*, *14*(1), e810. https://doi.org/10.1002/wcc.810

Dansgaard, W. (1964). Stable isotopes in precipitation. *Tellus*, *16*(4), 436–468. https://doi.org/10.3402/tellusa.v16i4.8993

Diefendorf, A. F., Mueller, K. E., Wing, Scott. L., Koch, P. L., & Freeman, K. H. (2010). Global patterns in leaf ^{13}C discrimination and implications for studies of past and future climate. *Proceedings of the National Academy of Sciences*, *107*(13), 5738–5743. https://doi.org/10.1073/pnas.0910513107

Diefendorf, A. F., Sberna, D. T., & Taylor, D. W. (2015). Effect of thermal maturation on plant-derived terpenoids and leaf wax *n*-alkyl components. *Organic Geochemistry*, *89–90*, 61–70. https://doi.org/10.1016/j.orggeochem.2015.10.006

Duncan, B., McKay, R., Bendle, J., Naish, T., Inglis, G. N., Moossen, H., et al. (2019). Lipid biomarker distributions in Oligocene and Miocene sediments from the Ross Sea region, Antarctica: Implications for use of biomarker proxies in glacially-influenced settings. *Palaeogeography, Palaeoclimatology, Palaeoecology*, *516*, 71–89. https://doi.org/10.1016/j.palaeo.2018.11.028

Duncan, B. J., McKay, R., Levy, R., Prebble, J. G., Naish, T., Seki, O., et al. (2025). Survival strategies of Antarctic vegetation during extensive glacial expansion across the Oligocene/Miocene Transition. *EGUsphere*, 1–24. https://doi.org/10.5194/egusphere-2024-4021

Feakins, S. J., Warny, S., & Lee, J.-E. (2012). Hydrologic cycling over Antarctica during the middle Miocene warming. *Nature Geoscience*, *5*(8), 557–560. https://doi.org/10.1038/ngeo1498

Feakins, S. J., Warny, S., & DeConto, R. M. (2014). Snapshot of cooling and drying before onset of Antarctic Glaciation. *Earth and Planetary Science Letters*, *404*, 154–166. https://doi.org/10.1016/j.epsl.2014.07.032

Florindo, F., Bohaty, S. M., Erwin, P. S., Richter, C., Roberts, A. P., Whalen, P. A., & Whitehead, J. M. (2003). Magnetobiostratigraphic chronology and palaeoenvironmental history of Cenozoic sequences from ODP sites 1165 and 1166, Prydz Bay, Antarctica. *Palaeogeography, Palaeoclimatology, Palaeoecology*, *198*(1), 69–100. https://doi.org/10.1016/S0031-0182(03)00395-X

Francis, J. E., & Hill, R. S. (1996). Fossil Plants from the Pliocene Sirius Group, Transantarctic Mountains: Evidence for Climate from Growth Rings and Fossil Leaves. *PALAIOS*, *11*(4), 389–396. https://doi.org/10.2307/3515248

French, K. L., Hein, C. J., Haghipour, N., Wacker, L., Kudrass, H. R., Eglinton, T. I., & Galy, V. (2018). Millennial soil retention of terrestrial organic matter deposited in the Bengal Fan. *Scientific Reports*, *8*(1), 11997. https://doi.org/10.1038/s41598-018-30091-8

Groeneveld, J., Henderiks, J., Renema, W., McHugh, C. M., De Vleeschouwer, D., Christensen, B. A., et al. (2017). Australian shelf sediments reveal shifts in Miocene Southern Hemisphere westerlies. *Science Advances*, *3*(5), e1602567. https://doi.org/10.1126/sciadv.1602567

Hannah, M. J. (2006). The palynology of ODP site 1165, Prydz Bay, East Antarctica: A record of Miocene glacial advance and retreat. *Palaeogeography, Palaeoclimatology, Palaeoecology*, *231*(1), 120–133. https://doi.org/10.1016/j.palaeo.2005.07.029

Herbert, T. D. (2014). 8.15 - Alkenone Paleotemperature Determinations. In H. D. Holland & K. K. Turekian (Eds.), *Treatise on Geochemistry (Second Edition)* (pp. 399–433). Oxford: Elsevier. https://doi.org/10.1016/B978-0-08-095975-7.00615-X

Herbert, Timothy D., & Mayer, L. A. (1991). Long climatic time series from sediment physical property measurements. *Journal of Sedimentary Research*, *61*(7), 1089–1108. https://doi.org/10.1306/D4267843-2B26-11D7-8648000102C1865D

Herbert, Timothy D., Lawrence, K. T., Tzanova, A., Peterson, L. C., Caballero-Gill, R., & Kelly, C. S. (2016). Late Miocene global cooling and the rise of modern ecosystems. *Nature Geoscience*, *9*(11), 843–847. https://doi.org/10.1038/ngeo2813

Herold, N., Huber, M., & Müller, R. D. (2011). Modeling the Miocene Climatic Optimum. Part I: Land and Atmosphere*. *Journal of Climate*, *24*(24), 6353–6372. https://doi.org/10.1175/2011JCLI4035.1

Hou, S., Stap, L. B., Paul, R., Nelissen, M., Hoem, F. S., Ziegler, M., et al. (2023). Reconciling Southern Ocean fronts equatorward migration with minor Antarctic ice volume change during Miocene cooling. *Nature Communications*, *14*(1), 7230. https://doi.org/10.1038/s41467-023-43106-4

Jamieson, S. S. R., Hulton, N. R. J., Sugden, D. E., Payne, A. J., & Taylor, J. (2005). Cenozoic landscape evolution of the Lambert basin, East Antarctica: the relative role of rivers and ice sheets. *Global and Planetary Change*, *45*(1), 35–49. https://doi.org/10.1016/j.gloplacha.2004.09.015

Kuhnert, H., Bickert, T., & Paulsen, H. (2009). Southern Ocean frontal system changes precede Antarctic ice sheet growth during the middle Miocene. *Earth and Planetary Science Letters*, *284*(3), 630–638. https://doi.org/10.1016/j.epsl.2009.05.030

Laskar, J., Robutel, P., Joutel, F., Gastineau, M., Correia, A. C. M., & Levrard, B. (2004). A long-term numerical solution for the insolation quantities of the Earth. *Astronomy & Astrophysics*, *428*(1), 261–285. https://doi.org/10.1051/0004-6361:20041335

Levy, R., Harwood, D., Florindo, F., Sangiorgi, F., Tripati, R., Eynatten, H. von, et al. (2016). Antarctic ice sheet sensitivity to atmospheric CO_2 variations in the early to mid-Miocene. *Proceedings of the National Academy of Sciences*, *113*(13), 3453–3458. https://doi.org/10.1073/pnas.1516030113

Lewis, A. R., Marchant, D. R., Ashworth, A. C., Hedenäs, L., Hemming, S. R., Johnson, J. V., et al. (2008). Mid-Miocene cooling and the extinction of tundra in continental Antarctica. *Proceedings of the National Academy of Sciences*, *105*(31), 10676–10680. https://doi.org/10.1073/pnas.0802501105

Masson-Delmotte, V., Hou, S., Ekaykin, A., Jouzel, J., Aristarain, A., Bernardo, R. T., et al. (2008). A Review of Antarctic Surface Snow Isotopic Composition: Observations, Atmospheric Circulation, and Isotopic Modeling. *Journal of Climate*, *21*(13), 3359–3387. https://doi.org/10.1175/2007JCLI2139.1

Masson-Delmotte, V., Stenni, B., Blunier, T., Cattani, O., Chappellaz, J., Cheng, H., et al. (2010). Abrupt change of Antarctic moisture origin at the end of Termination II. *Proceedings of the National Academy of Sciences*, *107*(27), 12091–12094. https://doi.org/10.1073/pnas.0914536107

McKay, R., Cockrell, J., Shevenell, A. E., Laberg, J. S., Burns, J., Patterson, M., et al. (2024). Miocene ice sheet dynamics and sediment deposition in the central Ross Sea, Antarctica. *GSA Bulletin*, *137*(3–4), 1267–1291. https://doi.org/10.1130/B37613.1

Müller, P. J., Kirst, G., Ruhland, G., von Storch, I., & Rosell-Melé, A. (1998). Calibration of the alkenone paleotemperature index $U_{37}^{K'}$ based on core-tops from the eastern South Atlantic and the global ocean (60°N-60°S). *Geochimica et Cosmochimica Acta*, *62*(10), 1757–1772. https://doi.org/10.1016/S0016-7037(98)00097-0

Neff, P. D., & Bertler, N. A. N. (2015). Trajectory modeling of modern dust transport to the Southern Ocean and Antarctica. *Journal of Geophysical Research: Atmospheres*, *120*(18), 9303–9322. https://doi.org/10.1002/2015JD023304

Nirenberg, J. E., & Herbert, T. D. (2024). North Pacific warmth synchronous with the Miocene Climatic Optimum. *Geology*. https://doi.org/10.1130/G52432.1

O'Brien, P. E., Cooper, A. K., Richter, C., & et al. (Eds.). (2001). *Proceedings of the Ocean Drilling Program, 188 Initial Reports* (Vol. 188). Ocean Drilling Program. https://doi.org/10.2973/odp.proc.ir.188.2001

Paknia, M., Ballato, P., Bilardello, D., Zeeden, C., & Jackson, M. (2025). Rock Magnetic Signature of Red Beds From the Intermontane Tarom Basin (NW Iran): Insights Into Middle to Late Miocene Environmental Conditions and Possible Forcing Mechanisms. *Paleoceanography and Paleoclimatology*, *40*(1), e2023PA004811. https://doi.org/10.1029/2023PA004811

Parrenin, F., Barnola, J.-M., Beer, J., Blunier, T., Castellano, E., Chappellaz, J., et al. (2007). The EDC3 chronology for the EPICA Dome C ice core. *Climate of the Past*, *3*(3), 485–497. https://doi.org/10.5194/cp-3-485-2007

Passchier, S., Bohaty, S. M., Jiménez-Espejo, F., Pross, J., Röhl, U., van de Flierdt, T., et al. (2013). Early Eocene to middle Miocene cooling and aridification of East Antarctica. *Geochemistry, Geophysics, Geosystems*, *14*(5), 1399–1410. https://doi.org/10.1002/ggge.20106

Peters, K. E., Rohrback, B. G., & Kaplan, I. R. (1981). Carbon and Hydrogen Stable Isotope Variations in Kerogen During Laboratory-Simulated Thermal Maturation. *AAPG Bulletin*, *65*(3), 501–508. https://doi.org/10.1306/2F9197FB-16CE-11D7-8645000102C1865D

Pierce, E. L., van de Flierdt, T., Williams, T., Hemming, S. R., Cook, C. P., & Passchier, S. (2017). Evidence for a dynamic East Antarctic ice sheet during the mid-Miocene climate transition. *Earth and Planetary Science Letters*, *478*, 1–13. https://doi.org/10.1016/j.epsl.2017.08.011

Polissar, P. J., & Freeman, K. H. (2010). Effects of aridity and vegetation on plant-wax δD in modern lake sediments. *Geochimica et Cosmochimica Acta*, *74*(20), 5785–5797. https://doi.org/10.1016/j.gca.2010.06.018

Rees-Owen, R. L., Gill, F. L., Newton, R. J., Ivanović, R. F., Francis, J. E., Riding, J. B., et al. (2018). The last forests on Antarctica: Reconstructing flora and temperature from the Neogene Sirius Group, Transantarctic Mountains. *Organic Geochemistry*, *118*, 4–14. https://doi.org/10.1016/j.orggeochem.2018.01.001

Sachse, D., Billault, I., Bowen, G. J., Chikaraishi, Y., Dawson, T. E., Feakins, S. J., et al. (2012). Molecular Paleohydrology: Interpreting the Hydrogen-Isotopic Composition of Lipid Biomarkers from Photosynthesizing Organisms. *Annual Review of Earth and Planetary Sciences*, *40*(1), 221–249. https://doi.org/10.1146/annurev-earth-042711-105535

Sangiorgi, F., Bijl, P. K., Passchier, S., Salzmann, U., Schouten, S., McKay, R., et al. (2018). Southern Ocean warming and Wilkes Land ice sheet retreat during the mid-Miocene. *Nature Communications*, *9*(1), 317. https://doi.org/10.1038/s41467-017-02609-7

Shackleton, S., Hishamunda, V., Davidge, L., Brook, E., Peterson, J. M., Carter, A., et al. (2025). Miocene and Pliocene ice and air from the Allan Hills blue ice area, East Antarctica. *Proceedings of the National Academy of Sciences*, *122*(44), e2502681122. https://doi.org/10.1073/pnas.2502681122

Shevenell, A. E., Kennett, J. P., & Lea, D. W. (2004). Middle Miocene Southern Ocean Cooling and Antarctic Cryosphere Expansion. *Science*, *305*(5691), 1766–1770. https://doi.org/10.1126/science.1100061

Shevenell, A. E., Kennett, J. P., & Lea, D. W. (2008). Middle Miocene ice sheet dynamics, deep-sea temperatures, and carbon cycling: A Southern Ocean perspective. *Geochemistry, Geophysics, Geosystems*, *9*(2). https://doi.org/10.1029/2007GC001736

Spector, P., & Balco, G. (2020). Exposure-age data from across Antarctica reveal mid-Miocene establishment of polar desert climate. *Geology*, *49*(1), 91–95. https://doi.org/10.1130/G47783.1

Stenni, B., Masson-Delmotte, V., Selmo, E., Oerter, H., Meyer, H., Röthlisberger, R., et al. (2010). The deuterium excess records of EPICA Dome C and Dronning Maud Land ice cores (East Antarctica). *Quaternary Science Reviews*, *29*(1), 146–159. https://doi.org/10.1016/j.quascirev.2009.10.009

Tibbett, E. J., Scher, H. D., Warny, S., Tierney, J. E., Passchier, S., & Feakins, S. J. (2021). Late Eocene Record of Hydrology and Temperature From Prydz Bay, East Antarctica.

Paleoceanography and Paleoclimatology, *36*(4), e2020PA004204. https://doi.org/10.1029/2020PA004204

Tibbett, E. J., Warny, S., Tierney, J. E., Wellner, J. S., & Feakins, S. J. (2022). Cenozoic Antarctic Peninsula Temperatures and Glacial Erosion Signals From a Multi-Proxy Biomarker Study. *Paleoceanography and Paleoclimatology*, *37*(9), e2022PA004430. https://doi.org/10.1029/2022PA004430

Verret, M., Trinh-Le, C., Dickinson, W., Norton, K., Lacelle, D., Christl, M., et al. (2023). Late Miocene onset of hyper-aridity in East Antarctica indicated by meteoric beryllium-10 in permafrost. *Nature Geoscience*, *16*(6), 492–498. https://doi.org/10.1038/s41561-023-01193-4

Vimeux, F., Masson, V., Delaygue, G., Jouzel, J., Petit, J. R., & Stievenard, M. (2001). A 420,000 year deuterium excess record from East Antarctica: Information on past changes in the origin of precipitation at Vostok. *Journal of Geophysical Research: Atmospheres*, *106*(D23), 31863–31873. https://doi.org/10.1029/2001JD900076

Warny, S., Askin, R. A., Hannah, M. J., Mohr, B. A. R., Raine, J. I., Harwood, D. M., et al. (2009). Palynomorphs from a sediment core reveal a sudden remarkably warm Antarctica during the middle Miocene. *Geology*, *37*(10), 955–958. https://doi.org/10.1130/G30139A.1

Warny, S., Kymes, C. M., Askin, R., Krajewski, K. P., & Tatur, A. (2019). Terrestrial and marine floral response to latest Eocene and Oligocene events on the Antarctic Peninsula. *Palynology*, *43*(1), 4–21. https://doi.org/10.1080/01916122.2017.1418444

Westerhold, T., Marwan, N., Drury, A. J., Liebrand, D., Agnini, C., Anagnostou, E., et al. (2020). An astronomically dated record of Earth's climate and its predictability over the last 66 million years. *Science*, *369*(6509), 1383–1387. https://doi.org/10.1126/science.aba6853